Antisolvent Crystallisation in Oscillatory Baffled Crystallisers

A thesis presented for the degree of

Doctor of Philosophy

in the Faculty of Science of the University of Strathclyde

by

Sebastion Davidson

Strathclyde Institute of Pharmacy and Biomedical Sciences

September 2019

Declaration of Author's Rights

This thesis is the result of the author's original research. It has been composed by the author and has not been previously submitted for examination which has led to the award of a degree.

SIGNED: ----------

DATE: ----------

Acknowledgements

I wish to express my utmost thanks to my supervisor Professor Alastair Florence for the opportunity to undertake this PhD, for his guidance and patience during what has certainly been a tumultuous experience. My gratitude is extended to my second supervisor Professor Joop ter Horst for his regular input and suggestions throughout the course of my PhD.

Thanks go to the University of Strathclyde, Nanyang Technological University and CMAC for funding this research. The various academic and lay staff and students within CMAC have all had some form of contribution towards this work. Particular thanks are due to Dr Cameron Brown, who without doubt has been one of the most influential people to the success of this project, from academic discussion to practical aspects in the laboratory and many "quick questions".

Finally, to the person who has had to bear the brunt of the low points throughout this journey, a special dedication to my wife Gemma. From the many weekends she has had to entertain our children Francesca and Alexandra whilst I work on my thesis, to the encouragement and support she has provided throughout, I am immeasurably grateful.

Abstract

Continuous manufacturing finds application in a variety of disciplines. It demonstrates a number of advantages, such as more controllable processes and allows particle attributes to be attained that would otherwise be unattainable. Antisolvent crystallisation is a widely used method of crystallisation in both academia and industry. It is employed to crystallise compounds that are not amenable to other techniques such as cooling crystallisation and can be utilised to produce crystal products with unique properties.

Oscillatory baffled crystallisers (OBCs) are platforms that generate intense mixing by the oscillatory motion of fluid through periodic constrictions, referred to as baffles. The oscillatory motion generates eddy currents through these baffles and induce highly turbulent and efficient mixing. By the superimposition of a net flow, the process can operate at near plug-flow conditions and is the principle of the continuous oscillatory baffled crystalliser (COBC). OBCs have been extensively studied for cooling crystallisations, but their application in antisolvent crystallisation has been limited.

The continuous antisolvent crystallisation of anthranilic acid in a COBC has been investigated for the first time as a function of antisolvent volume fraction and flow conditions, demonstrating the effects of a number of process variables on product outcomes. Metastable form II polymorph of anthranilic acid was consistently produced in a continuous unseeded antisolvent crystallisation from an ethanol and water solvent system. The incorporation of process analytical technology (PAT) allowed for monitoring of various process conditions in real time, giving insight into the evolution of the antisolvent crystallisation process in continuous flow. Local mixing effects were deemed to be significant in the COBC at the point of contact of solution and antisolvent, such that variable flow rates at fixed antisolvent compositions resulted in different product sizes whilst resulting in the same final solution concentration.

Polymorph control in a moving baffle oscillatory baffled crystalliser (MBOBC) was demonstrated for the anthranilic acid system. By variation of seeding conditions and startup strategy, the continuous production of either stable form I or metastable form II polymorph could be controlled. This demonstrated a novel continuous nucleation platform for an antisolvent crystallisation process that could potentially be coupled with

a COBC or other platform for reliable continuous production of a specified polymorph with targeted crystal attributes.

Growth and secondary nucleation kinetic parameters were determined by means of isothermal seeded batch experiments in a batch moving fluid oscillatory baffled crystalliser (MFOBC). Models were developed from these determined parameters, and further refined by the incorporation of a solvent factor that improved the fit of the model predictions to the experimentally measured attributes. The determined parameters were applied to the optimisation of a 30 m DN15 COBC with multiple antisolvent addition points and demonstrates the first such strategy utilising experimentally determined kinetic parameters.

This work has demonstrated novel approaches for the development of antisolvent crystallisation processes in continuous flow in oscillatory baffled crystallisers, detailing a number of control strategies and advancing the knowledge and understanding of such processes for future implementation.

Table of Contents

Declaration of Author's Rights I

Acknowledgements II

Abstract III

Table of Contents V

List of Figures IX

List of Tables XVI

List of Abbreviations XVII

1 Introduction 1

1.1 Crystallisation from a Continuous Manufacturing Perspective 2

1.2 Solubility and Solvent Selection 3

1.3 Supersaturation 5

1.3.1 Mixing and Supersaturation 6

1.4 Nucleation 8

1.4.1 Primary Nucleation 9

1.4.2 Secondary Nucleation 12

1.5 Crystal Growth 13

1.6 Polymorphism and Solid Form 16

1.7 Crystallisation Techniques 18

1.7.1 Cooling Crystallisation 18

1.7.2 Evaporative Crystallisation 20

1.7.3 Melt Crystallisation 21

1.7.4 Reactive Crystallisation 21

1.7.5 Antisolvent Crystallisation 22

1.8 Platforms for Continuous Crystallisation 24

1.8.1 Mixed Suspension Mixed Product Removal Crystalliser 24

1.8.2 Continuous Oscillatory Baffled Crystalliser 25
1.8.3 Static Mixer Crystalliser 31
1.9 Summary 35
2 Aims and Objectives 36
2.1 Aims 37
2.2 Objectives 38
3 Materials and Methods 39
3.1 Materials 40
3.2 Methods 40
3.2.1 Solubility Measurements 40
3.2.2 X-ray powder diffraction 42
3.2.3 Ultraviolet-visible Spectroscopy 43
3.2.4 Microscopy 43
3.2.5 Particle Sizing 43
3.2.6 Sieving 46
3.2.7 Data Presentation and Analysis 46
4 Developing Antisolvent Crystallisations in a COBC 47
4.1 Introduction 48
4.1.1 Anthranilic Acid 50
4.2 Experimental 53
4.2.1 Isolation and Solubility of Anthranilic Acid Form I 53
4.2.2 COBC Platform for Continuous Antisolvent Crystallisation 54
4.2.3 Removal of Impurities from Raw Material 56
4.3 Results and Discussion 58
4.3.1 Phase Diagram 58
4.3.2 Modes of Addition of Antisolvent and Feed Solution 60
4.3.3 Effect of Total Flow Rate 62

4.3.4 Effect of Antisolvent Fraction 66
4.4 Limitations of the Unseeded COBC 69
4.4.1 Fouling 69
4.4.2 Gas Solubilities and Degassing 70
4.4.3 Mixing Conditions 73
4.5 Summary 75
5 Polymorphism in a Continuous Antisolvent Crystallisation 77
5.1 Introduction 78
5.2 Experimental 80
5.2.1 Moving Baffle Oscillatory Baffled Crystalliser (MBOBC) 80
5.2.2 Solubility Data for Anthranilic Acid at Varying Temperature and Antisolvent Fraction 83
5.2.3 Unseeded Startup Process Operation 84
5.2.4 Seeded Startup Process Operation 84
5.2.5 Quantification of Polymorphic Content 85
5.3 Results and Discussion 87
5.3.1 Effect of Unseeded versus Seeded Startup 87
5.3.2 Effect of Flow Rate 92
5.3.3 Effect of Seed Polymorph 99
5.4 Summary 103
6 Determination of Kinetic Parameters for the Optimisation of Continuous Antisolvent Crystallisations in a COBC 104
6.1 Introduction 105
6.2 Experimental Setup 106
6.3 Experimental Procedure 107
6.3.1 Phase Diagram and Experimental Parameters 107
6.3.2 Mixing and Addition Method 112

6.3.3 Induction Times and Modification of Initial Design Space 113
6.3.4 UV-Vis Spectroscopy Calibration and Measurement 114
6.3.5 Sizing by Laser Diffraction 116
6.4 Formulation of the Population Balance Model 116
6.4.1 Model Assumptions 117
6.4.2 Growth 117
6.4.3 Secondary Nucleation 118
6.4.4 Solubility Expression 118
6.5 Results and Discussion 119
6.5.1 Growth Parameter Estimation 119
6.5.2 Secondary Nucleation Parameter Estimation 129
6.5.3 Secondary Nucleation Parameter Uncertainty 139
6.5.4 Optimisation of a Multi-addition Plug Flow Antisolvent Process 141
6.5.5 Limitations of the Optimisation 152
6.6 Summary 154
7 Conclusions and Future Work 155
7.1 Conclusions 156
7.2 Future Work 159
7.2.1 Fouling Mitigation Strategies 159
7.2.2 Alternative Methods of Generating Supersaturation 160
7.2.3 Dissolved Gas Effects 160
7.2.4 Alternative Techniques for Targeting Polymorphs 161
7.2.5 Local Mixing versus Overall Mixing and Dispersion Effects 162
7.2.6 Development of the Multi-addition COBC 163
7.3 Overall Conclusions 164
8 References 165

List of Figures

Figure 1.1. The solubility of various pharmaceutical compounds in ethanol. Data sourced from [16]. 4
Figure 1.2: The saturation limits of a cooling crystallisation. 5
Figure 1.3: The variation in MSZW as a function of addition rate of antisolvent and impellor velocity with antisolvent addition near the impellor [28]. 7
Figure 1.4: The variation in MSZW as a function of addition rate of antisolvent and impellor velocity with antisolvent addition near the vessel wall [28]. 8
Figure 1.5: The different processes of nucleation. Adapted from [32]. 9
Figure 1.6: Energy diagram for formation of a critical nucleus. r_c must be exceeded for the free energy of the system to decrease [34] 10
Figure 1.7. An overview of Classical Nucleation Theory and Two-step Nucleation. Adapted from [38]. 12
Figure 1.8: The molecular process of crystal growth. Steps and kinks are more energetically favourable locations for crystal growth. Adapted from [51] 14
Figure 1.9: AFM image of an insulin crystal showing steps and kinks [52]. 14
Figure 1.10: Polymorphs of ROY [63]. 16
Figure 1.11. Energy states for a polymorphic system. Adapted from [69]. 17
Figure 1.12: Crystal structures of the stable form I and metastable form II of paracetamol. Image adapted from [72] 18
Figure 1.13: A representative phase diagram for cooling crystallisation [51]. 19
Figure 1.14: Various cooling profiles for seeded batch crystallisation from supersaturated K_2SO_4 solutions. Reproduced from [62]. 19
Figure 1.15: A representative phase diagram for evaporative crystallisation [51]. 20
Figure 1.16. Paracetamol polymorphs produced from the melt [77]. 21
Figure 1.17: A representative phase diagram for antisolvent crystallisation [51]. 22
Figure 1.18: An example of an MSMPR cascade with temperature difference as the driving force of crystal growth [11]. 25
Figure 1.19: Eddies are generated as a result of oscillatory motion between the baffles of a COBC [87] 26
Figure 1.20. Oscillatory flow patterns in a COBC. (a) low Re_o, unbaffled tube. (b) low Re_o, baffles present. (c) high Re_o, baffles present. [86] 27

Figure 1.21: The heat transfer for a smooth tube and a baffled tube with non-oscillatory flow [90] 28
Figure 1.22: The heat transfer for a smooth tube and a baffled tube with oscillation superimposed on net flow (Re_n = 160, Sr = 0.16) [90] 28
Figure 1.23: Schematic of a COBC [89]. 29
Figure 1.24: Antisolvent COBC setup for the generation of seed crystals [94]. 31
Figure 1.25: Antisolvent crystallisation in a plug flow crystalliser utilizing static mixer inserts [9]. 32
Figure 1.26: The influence of static mixers on the crystal size distribution of flufenamic acid. 33
Figure 3.1. Crystal16 solubility measurement apparatus [98] 40
Figure 3.2. Gravimetric solubility apparatus. 42
Figure 3.3. Malvern Mastersizer 3000 instrument and modules [101]. 44
Figure 3.4. Cutaway view of the FBRM probe with illustration of measurement. 44
Figure 3.5. FBRM laser reflecting off particles in an OBC. The laser operates at 785 nm, which is invisible to the naked eye 45
Figure 3.6. Fritsch Analysette 3 Pro sieve shaker 46
Figure 4.1. Structure of anthranilic acid showing the neutral (left) and zwitterionic (right) species. 50
Figure 4.2. Large single crystals of anthranilic acid. 51
Figure 4.3. Simulated XRPD patterns from single-crystal data obtained from the Cambridge Structural Database [106] for form I (AMBACO01), II (AMBACO03) and III (AMBACO06) 51
Figure 4.4. Crystal structures showing packing and hydrogen bonding for orthorhombic form I (top), orthorhombic form II (middle) and monoclinic form III (bottom) polymorphs of anthranilic acid 52
Figure 4.5. Schematic of the COBC setup for antisolvent crystallisation 54
Figure 4.6. Internal geometry of the COBC. 54
Figure 4.7. XRPD pattern for a known sample of NaCl and isolated impurity. 56
Figure 4.8. Isolated insoluble components from the anthranilic acid raw material. 57
Figure 4.9. Crystal16 and gravimetric solubility measurements of anthranilic acid in an ethanol/water solvent system, coveringa range of antisolvent (water) volume

fractions (φ) and temperatures. Open markers represent gravimetric measurements at φ = 0.6 – 0.1.....58
Figure 4.10. Solubility (c^*), dilution line (c), maximum yield ($c - c^*$) and supersaturation of anthranilic acid form I and II at 25 °C as a function of antisolvent (water) volume fraction (φ) in an ethanol/water solvent system.....59
Figure 4.11. FBRM total counts as a function of number of residence times for varying total flow rates and antisolvent volume fractions. (a) φ = 0.4, 100 ml/min; (b) φ = 0.4, 50 ml/min; (c) φ = 0.5, 100 ml/min.....60
Figure 4.12. FBRM total counts as a function of number of residence times for varying total flow rates, φ = 0.6. (a) 100 ml/min; (b) 50 ml/min; (c) 25 ml/min 62
Figure 4.13. FBRM mean chord length (square-weighted) as a function of number of residence times for varying total flow rates, φ = 0.6. (a) 100 ml/min; (b) 50 ml/min; (c) 25 ml/min.....63
Figure 4.14. XRPD patterns for samples of anthranilic acid taken at steady state. 64
Figure 4.15: FBRM total counts as a function of number of residence times for (a) φ = 0.6, 100 ml/min; (b) φ = 0.8, 100 ml/min; (c) φ = 0.6, 50 ml/min; (d) φ = 0.8, 50 ml/min. 65
Figure 4.16. Total counts as a function of number of residence times for varying antisolvent fractions. (a) φ = 0.6; (b) φ = 0.5; (c) φ = 0.8; (d) φ = 0.4. Total flow rate = 100 ml/min.....67
Figure 4.17. Mean chord length (square-weighted) as a function of number of residence times for varying antisolvent fractions. (a) φ = 0.6; (b) φ = 0.5; (c) φ = 0.8; (d) φ = 0.4. Total flow rate = 100 ml/min. 68
Figure 4.18. Localised fouling of the stainless steel inlet at the mixing location in the COBC. 70
Figure 4.19. Ostwald coefficients for the solubility of nitrogen, oxygen and helium in ethanol and water mixtures. Data sourced from [112], [113], [115] 71
Figure 4.20. Accumulation of gas in the COBC during antisolvent crystallisation, resulting in oscillation dampening and reduced mixing.....72
Figure 4.21. An in-line degassing module. Vacuum is applied to the shell side and the liquid to be degassed flows through a bundle of silicone fibres.....73

Figure 4.22. Crystals of anthranilic acid form II produced at S_I = 1.5 75
Figure 5.1. Schematic of the MBOBC setup used for antisolvent crystallisation studies. 80
Figure 5.2. Filter capsule used for in-line filtration of impurities..... 82
Figure 5.3. Gravimetric solubility data for anthranilic acid form I at 15, 25 and 35 °C across a range of antisolvent (water) volume fractions (φ) 83
Figure 5.4. XRPD patterns of anthranilic acid raw material from different suppliers and reference patterns from the Cambridge Structural Database. 85
Figure 5.5. Calibration line for anthranilic acid polymorphic content based on ratio of XRPD peak height for form I (2θ = 24.28°) to form II (2θ = 26.58°). 86
Figure 5.6. Concentration and S_I over time for φ = 0.46, 50 ml/min. Upper limit (red line): maximum possible concentration of mixture. Lower limit (green line): equilibrium concentration..... 87
Figure 5.7. FBRM total counts for φ = 0.46, 50 ml/min, unseeded. 88
Figure 5.8. FBRM total counts for φ = 0.46, 50 ml/min, 10% seed load..... 89
Figure 5.9. XRPD patterns for φ = 0.46, 50 ml/min, unseeded. The first sample at 20 minutes represents moving from the batch startup mode to continuous. 90
Figure 5.10. XRPD patterns for φ = 0.46, 50 ml/min, 10% seed load..... 91
Figure 5.11. Concentration and S_I data for φ = 0.46, 10% seed load. Upper limit (red line): maximum possible concentration of mixture. Lower limit (green line): equilibrium concentration..... 92
Figure 5.12. XRPD patterns for φ = 0.46, 100 ml/min, 10% seed load. 93
Figure 5.13. Polymorph dynamics in the continuous process between I and II. φ = 0.46, 100 ml/min, 10% seed load..... 94
Figure 5.14. Polymorphs of anthranilic acid as a function of supersaturation and antisolvent volume fraction. Reproduced from [24]. 95
Figure 5.15. Concentration and S_I data for φ = 0.60, 10% seed load. Upper limit (red line): maximum possible concentration of mixture. Lower limit (green line): equilibrium concentration..... 96
Figure 5.16. XRPD patterns for φ = 0.60, 50 ml/min, 10% seed load..... 97
Figure 5.17. XRPD patterns for φ = 0.60, 100 ml/min, 10% seed load..... 97

Figure 5.18. Polymorph dynamics in the continuous process; φ = 0.60, 100 ml/min, 10% seed load. 98
Figure 5.19. Concentration data for φ = 0.60, 50 ml/min, 100% seed load. Upper limit (red line): maximum possible concentration of mixture. Lower limit (green line): equilibrium concentration. 100
Figure 5.20. XRPD patterns for φ = 0.60, Form III seed, 50 ml/min, 100% seed load. 101
Figure 5.21. Relative solubility of the three polymorphs of anthranilic acid. Reproduced from [105]. 102
Figure 6.1. Batch moving fluid OBC for antisolvent crystallisation 106
Figure 6.2. Phase diagram for anthranilic acid in an ethanol/water solvent system. Arrows show trajectory from undersaturation to supersaturation by addition of antisolvent. Red arrows show initially planned trajectory. 110
Figure 6.3. Sieved seed fractions of anthranilic acid form I. 0-63 μm (top), 63-125 μm (middle) and 125-250 μm (bottom) 111
Figure 6.4. Particle size distributions for the three anthranilic acid sieve fractions. ..112
Figure 6.5. Seed, solution and antisolvent in preparation for mixing. 113
Figure 6.6. Induction time measurements for initial antisolvent fractions. From left to right: $X\mathrm{EtOH}$ = 0.2, 0.3, 0.4 and 0.6. 114
Figure 6.7. Representative unprocessed UV spectrum of anthranilic acid. 115
Figure 6.8. Representative first order derivative UV spectrum of anthranilic acid... 115
Figure 6.9. Concentration profile for mass transfer experiment 1. 119
Figure 6.10. Measured (solid lines) and predicted (dashed lines) concentration profiles for growth rate experiments. 120
Figure 6.11. Growth rate constant as a function of ethanol mass fraction. 121
Figure 6.12. Measured (solid lines) and predicted (dashed lines) concentration profiles for growth rate experiments incorporating a solvent factor. 123
Figure 6.13. Measured and predicted CSDs for crystal growth from small seed. (a) $X\mathrm{EtOH}$ = 0.6; (b) $X\mathrm{EtOH}$ = 0.5; (c) $X\mathrm{EtOH}$ = 0.36 125
Figure 6.14. Scatter plots showing the correlation between model parameters at $X\mathrm{EtOH}$ = 0.6. (a) kG vs $g2$; (b) kG vs g; (c) g vs $g2$. 128
Figure 6.15. Histogram of PSD from predicted growth at $X\mathrm{EtOH}$ = 0.6. 128

Figure 6.16. Concentration profiles for secondary nucleation rate experiments. Solid lines show measured concentrations. Dashed lines show predicted concentrations for a combined growth and secondary nucleation model. Dotted lines show predicted concentrations for a growth-only model. 131
Figure 6.17. Measured and predicted PSDs for secondary nucleation experiments. Solid lines (blue) show measured PSDs. Dashed lines (orange) show predicted PSD for a combined growth and secondary nucleation model. Dotted lines (black) show predicted PSDs for a growth-only model. 135
Figure 6.18. Microscopy of isolated crystal products from secondary nucleation experiments. (a) experiment 6; (b) experiment 9; (c) experiment 10; (d) experiment 14. 138
Figure 6.19. Histogram of the PSD from predicted secondary nucleation parameters from Experiment 9. 140
Figure 6.20. Schematic of a 30 m COBC with multiple antisolvent additions. 142
Figure 6.21. Results of unoptimised antisolvent addition at three equally spaced positions in a COBC, constrained on X_{EtOH}. Solid lines: c. Dashed lines: $c^{\star}$. Blue (upper) dotted line: S_{I}. Red (lower) dotted line: S_{II}. 144
Figure 6.22. Optimisation results for maximum yield with antisolvent addition at three equally spaced positions in a COBC, constrained on X_{EtOH}. Solid lines: c. Dashed lines: $c^{\star}$. Blue (upper) dotted line: S_{I}. Red (lower) dotted line: S_{II}. .. 145
Figure 6.23. Optimisation results for maximum D4,3 with antisolvent addition at three equally spaced positions in a COBC, constrained on X_{EtOH}. Solid lines: c. Dashed lines: $c^{\star}$. Blue (upper) dotted line: S_{I}. Red (lower) dotted line: S_{II}. .. 146
Figure 6.24. Optimisation results for minimum coefficient of variation with antisolvent addition at three equally spaced positions in a COBC, constrained on X_{EtOH}. Solid lines: c. Dashed lines: $c^{\star}$. Blue (upper) dotted line: S_{I}. Red (lower) dotted line: S_{II}. 147
Figure 6.25. Optimisation results for maximum D4,3 with antisolvent addition at three equally spaced positions in a COBC, constrained on X_{EtOH} and S_{II} in first segment. Solid lines: c. Dashed lines: $c^{\star}$. Blue (upper) dotted line: S_{I}. Red (lower) dotted line: S_{II}. 148

Figure 6.26. Optimisation results for maximum D4,3 with antisolvent addition at three equally spaced positions in a COBC, constrained on $X\mathrm{EtOH}$ and $S\mathrm{II}$ in first and second segment. Solid lines: c. Dashed lines: $c^\star$. Blue (upper) dotted line: $S\mathrm{I}$. Red (lower) dotted line: $S\mathrm{II}$. 149
Figure 6.27. Optimisation results for maximum yield for three antisolvent addition points at variable positions in a COBC, constrained on $X\mathrm{EtOH}$. Solid lines: c. Dashed lines: $c^\star$. Blue (upper) dotted line: $S\mathrm{I}$. Red (lower) dotted line: $S\mathrm{II}$. ..150
Figure 6.28. Optimisation results for maximum D4,3 for three antisolvent addition points at variable positions in a COBC, constrained on $X\mathrm{EtOH}$ and $S\mathrm{II}$ in first segment. Solid lines: c. Dashed lines: $c^\star$. Blue (upper) dotted line: $S\mathrm{I}$. Red (lower) dotted line: $S\mathrm{II}$. 151
Figure 6.29. Waterfall plot showing the evolution of PSD along the length of the COBC for Case H..... 152
Figure 7.1. Proposed continuous nucleation unit to feed into the COBC. 160

List of Tables

Table 1.1. Summary of common nucleation expressions. Adapted from [40]. 13
Table 1.2. Commonly used growth expressions. 15
Table 3.1. Temperature profile for Crystal16 41
Table 4.1: Antisolvent volume fraction (φ), supersaturation ratio with respect to form I of anthranilic acid (S_I), and total flow rates for antisolvent crystallisation in the COBC. 55
Table 4.2. The median value of the mean chord length (square-weighted) for varying antisolvent fractions and corresponding S_{II}, 100 ml/min total flow rate. 67
Table 5.1. Experimental conditions for the MBOBC experiments 81
Table 5.2. Polymorphic mass fractions of form I and II for preparation of calibration line. 86
Table 6.1. Experimental process parameters for kinetic studies. Highlighted rows show originally intended experiments before these conditions were deemed unfeasible by preliminary experiments. 109
Table 6.2. Kinetic parameters from initial parameter estimation when fitted to individual experiments. 121
Table 6.3. Growth kinetic parameters with and without solvent effects. 123
Table 6.4. Measured and predicted growth CSDs for varying X_{EtOH}. 125
Table 6.5. Variance-covariance matrix of growth kinetic parameters. 126
Table 6.6. Goodness of fit tests for growth-only and growth and secondary nucleation kinetic parameters. Highlighted cells are values that do not satisfy the null hypothesis for this test. 133
Table 6.7. Measured and predicted PSDs for combined growth and secondary nucleation for varying ethanol mass fraction, seed size and power density. 136
Table 6.8. Secondary nucleation kinetic parameters. 139
Table 6.9. Variance-covariance matrix of secondary nucleation kinetic parameters. 139
Table 6.10. Correlation matrix for secondary nucleation kinetic parameters. 140
Table 6.11. Summary of optimisation cases for antisolvent crystallisation in a 30 m COBC. 143

List of Abbreviations

API	Active Pharmaceutical Ingredient
ATR	Attenuated Total Reflectance
CLD	Chord Length Distribution
CM	Continuous Manufacturing
CNT	Classical Nucleation Theory
COBC	Continuous Oscillatory Baffled Crystalliser
CQA	Critical Quality Attribute
CSD	Crystal Size Distribution
CV	Coefficient of Variation
FBRM	Focused Beam Reflectance Measurement
HPLC	High Performance Liquid Chromatography
IDBC	Impeller Driven Batch Crystalliser
MBOBC	Moving Baffle Oscillatory Baffled Crystalliser
MFOBC	Moving Fluid Oscillatory Baffled Crystalliser
MSZW	Metastable Zone Width
OBC	Oscillatory Baffled Crystalliser
PAT	Process Analytical Technology
PBE	Population Balance Equation
PEEK	Polyether Ether Ketone
PVDF	Polyvinylidene fluoride
PVM	Process Video Microscopy
PSD	Particle Size Distribution
PTFE	Polytetrafluoroethylene
QbD	Quality by Design
QbT	Quality by Testing
UV-vis	Ultraviolet-visible
XRPD	X-ray Powder Diffraction

1 Introduction

1.1 Crystallisation from a Continuous Manufacturing Perspective

Crystallisation is an intriguing phenomenon that is important for a multitude of disciplines and areas. Fundamentally, it describes the formation of a solid with regular structure consisting of repeating units, be those atoms, ions or molecules. It is used as a process in food, chemical and pharmaceutical industries as a method of purification and isolation of chemical products, potentially separating hazardous starting materials and intermediates from impure mixtures [1]. Crystalline products can vary significantly in their physical properties depending on the method of production employed, with their critical quality attributes (CQAs) driven by the intended use of the material. Therefore, an in-depth understanding of crystallisation processes is required to target these attributes in a reliable and reproducible manner.

Continuous manufacturing (CM) has been employed for a number of years in various industries, such as food and petrochemicals [2]; however, batch manufacturing techniques still dominate the pharmaceutical industry [3]. The mechanisms of such processes are well documented, and have been honed by operators to produce products as close to specification as possible with the technology at hand [4]. Even so, challenges can present themselves, such as variation between batches and issues with scale-up [5]. CM attempts to address these issues and offer further advantages that batch manufacturing is not able to achieve.

There has been support by the pharmaceutical regulatory bodies for the industry to move away from a quality-by-testing (QbT) approach and adopt quality-by-design (QbD) manufacturing methods to ensure CQAs are consistently achieved [6], and CM is deemed a suitable method to provide this. Process analytical technology (PAT) lends itself well to this goal when incorporated into a continuous process, allowing for detailed real-time process information to be obtained that can be used to refine the production process [7]. This can result in reduced production costs and more environmentally friendly processes by minimising waste, which promote the adoption of CM [8].

In response to this demand, significant research on continuous crystallisation has been undertaken in recent years, with a variety of compounds, technologies and crystallisation methods having been demonstrated [9]–[11]. Although there are benefits

associated with continuous crystallisation over traditional batch methods, the pharmaceutical industry has been relatively slow to adopt them, attributable in part to the required investment in material, equipment and time to develop them [12]. To alleviate these challenges and mitigate risk, a systematic workflow has been developed to guide the development of continuous cooling crystallisation [13], with a similar undertaking for antisolvent crystallisation in development.

For any crystallisation process, it is imperative to understand the mechanisms by which crystals form and the factors that influence them. The following sections cover the fundamentals of crystallisation and the various platforms that can be utilised for crystallisation processes, with a focus on continuous crystallisation platforms and antisolvent crystallisation methods.

1.2 Solubility and Solvent Selection

The most common method of crystallisation in industrial application is from solution, where the solute is first dissolved in a solvent [14]. The amount of material that can dissolve in a solvent is determined by its solubility. Dissolution and crystallisation are governed by the laws of thermodynamics, and such processes only occur if the process is energetically favourable. The maximum amount of solute that can dissolve in a given solvent at a given temperature and pressure is a fixed value, at which point the solution is saturated and the solute is in equilibrium between the solid phase and the solution phase.

Solubility is predominantly dependent on the compound itself, the solvent or solvent mixture used to dissolve the compound, and the temperature of the system. Generally, an increase of temperature increases the solubility of a compound in a solvent, but this is not always the case [15]. For example, sodium chloride shows little temperature dependence on its solubility in water, and therefore a cooling crystallisation technique would be a poor choice for this compound. Some pharmaceutical compounds and their solubilities in ethanol, a commonly used solvent, are shown in Figure 1.1 to highlight this effect.

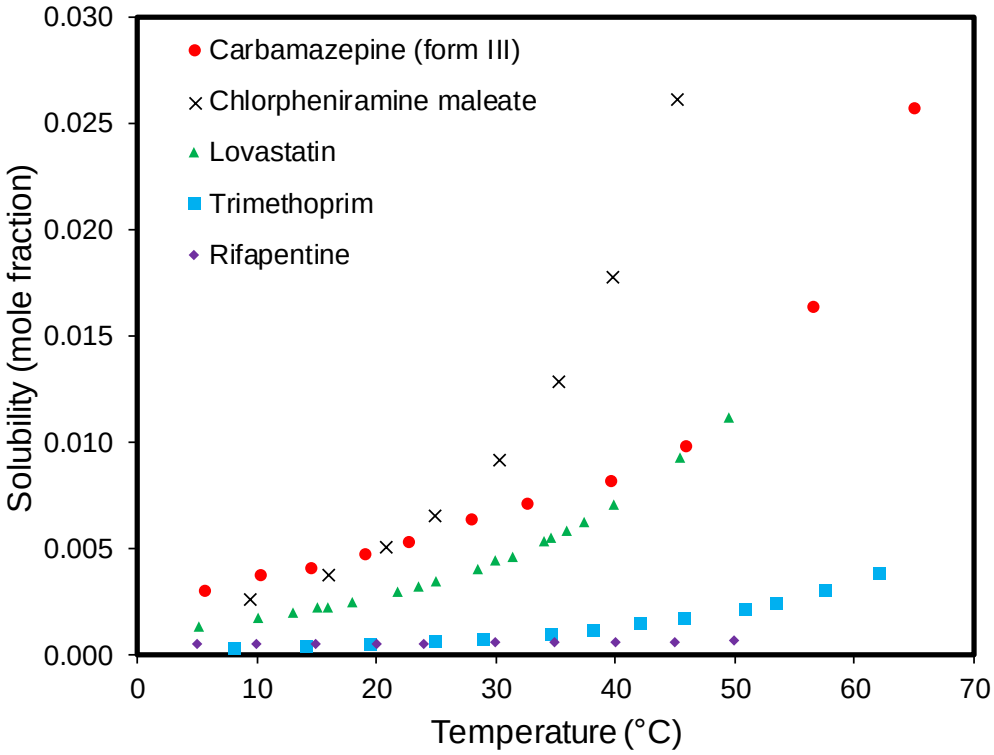

Figure 1.1. The solubility of various pharmaceutical compounds in ethanol. Data sourced from [16].

There are a multitude of solvents that can be used for crystallisation, but there are several practical aspects that can aid the selection process. Any prior knowledge of the solute and solvent system can significantly reduce the number of potential solvents. Some solvents can be readily discounted on account of their cost, environmental impact, reactivity, and potential toxicity for trace amounts in pharmaceuticals, amongst other factors [17]. Solvent screening may be performed to identify the most suitable solvent system based on the desired product outcomes such as polymorphism [18][18]. All of these aspects combined can determine which crystallisation techniques should be implemented.

1.3 Supersaturation

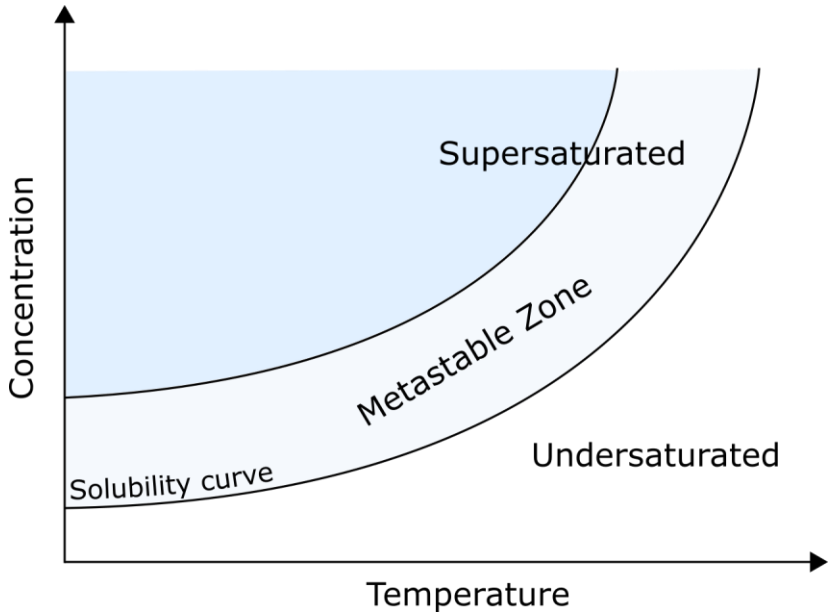

Figure 1.2: The saturation limits of a cooling crystallisation.

Supersaturation is produced when the concentration of a solute exceeds its solubility. To demonstrate this, a cooling crystallisation from solution is considered in Figure 1.2. There are three distinct zones highlighted. The first is the undersaturated region, whereby at a given temperature, the addition of solute would result in further dissolution. As an undersaturated solution is cooled, it crosses the solubility curve and becomes supersaturated. Upon reaching supersaturation, the compound first enters a metastable zone. In this region, nucleation will not occur, but crystals can grow if the solution is seeded. Beyond the metastable zone limit, there lies a region wherein crystals can form spontaneously following nucleation without external influence [19].

Unlike the solubility, which is a thermodynamic property, the metastable zone width (MSZW) is a kinetic property and can be modified, such as by the application of ultrasound [20]. This can have an effect on the probability of undesired nucleation, with a narrow MSZW being more difficult to control for when designing processes. The MSZW is often used to define a region suitable for seeded crystallisation [21], where seeding is used to prevent this undesired nucleation and affords greater control over crystal attributes.

The thermodynamic driving force for crystallising a substance can be represented by the difference in chemical potential between the solute in the supersaturated solution, μ_S', and the saturated solution, μ_S'' [22]:

$$\Delta\mu = \mu_S' - \mu_S'' \tag{1.1}$$

This is more commonly represented by the supersaturation ratio:

$$S = \frac{c}{c^*} \tag{1.2}$$

where c is the concentration, and c^* is the solubility. For a ratio less than one, the solution is undersaturated and crystallisation cannot occur. The limits of supersaturation vary depending on the compound and solvent system. Supersaturation can be generated by various methods, such as reducing the solute solubility in the system by cooling, addition of antisolvent, by increasing the solute concentration by the evaporation of solvent, or a combinatory approach. These are discussed in more detail in Section 1.7.

1.3.1 Mixing and Supersaturation

The magnitude of localised supersaturation can be influenced by the intensity of mixing within the system. For a cooling crystallisation process, temperature is typically controlled by heating/cooling jackets around a central vessel. Ideally, any temperature change would be instantaneously applied to every molecule in the vessel. In reality, there is a temperature gradient between the molecules in contact with the walls of the vessel and those in the bulk. Mixing minimises the presence of such a gradient, with a higher intensity tending towards the ideal.

Antisolvent crystallisation is highly dependent on mixing, and can influence the crystal size distribution (CSD) for antisolvent crystallisation [23]. There is high, localised supersaturation at the point where the solvent solution and antisolvent come into contact with one another, and this point varies depending on the mixing method employed. Consider a simple experiment where solvent and antisolvent are mixed by pouring a beaker of one into the other; there is little control over the mixing process, with wide variations in supersaturation across the total volume. To obtain nucleation

and crystal growth in a homogenous solution, and therefore maintain control over the product attributes, the mixing time of solvent and antisolvent should be shorter than the induction time [24].

The induction time is defined as the time between the generation of supersaturation and the formation of the first detectable crystal nucleus [25]. Induction time measurements are dependent on the techniques used, as this influences the ability to detect this first nucleus; probe-based methods would give more reliability than observation with the naked eye. There can also be variation in induction times due to the nature of nucleation, though with multiple experiments it is possible to determine the probability of nucleation over time under specific conditions [26].

The considerations for mixing will greatly influence the choice of crystallisation platform, as mixing intensity can alter the nucleation rate for both primary and secondary nucleation [27]. For the antisolvent crystallisation of benzoic acid in a stirred tank, the location of the addition of antisolvent has been shown to affect the MSZW [28]. Figure 1.3 shows that increased addition rate of antisolvent widens the MSZW where the antisolvent is added near the impellor. Increased impellor velocity also widens the MSZW in such a system, independent of addition rate. The error on the values is also relatively low, suggesting consistency in the system and giving good control over crystal properties.

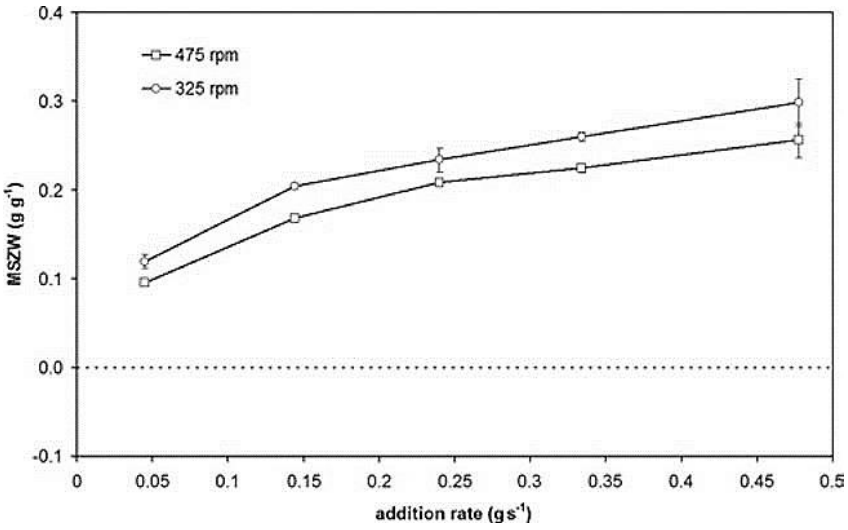

Figure 1.3: The variation in MSZW as a function of addition rate of antisolvent and impellor velocity with antisolvent addition near the impellor [28].

Figure 1.4 shows a narrower MSZW for all addition rates and impellor velocities when antisolvent is added near the wall of the vessel. The difference in MSZW is not as pronounced at low addition rates, but shows a greater dependence on impellor velocity at increased addition rates. There is significant error on the values, and such a system would not be suitable for a crystallisation process where narrow CSDs are desired.

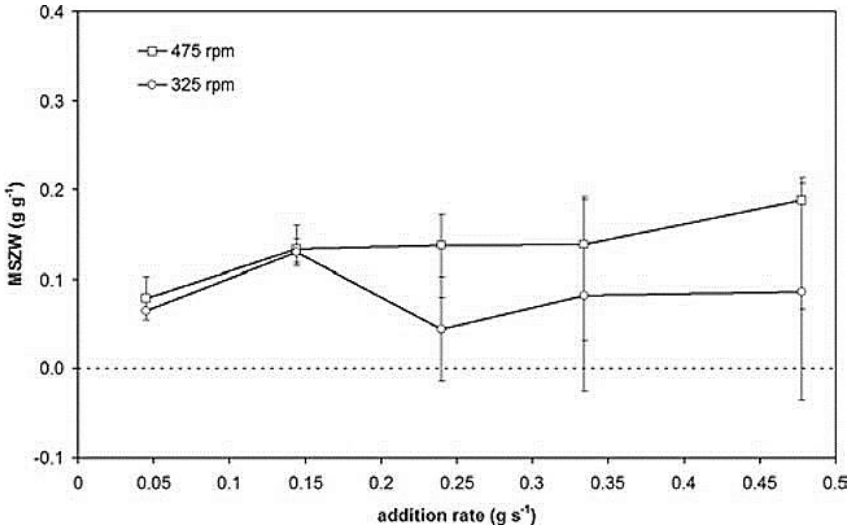

Figure 1.4: The variation in MSZW as a function of addition rate of antisolvent and impellor velocity with antisolvent addition near the vessel wall [28].

Various technologies and strategies have been developed that attempt to generate high supersaturations rapidly whilst also achieving thorough mixing to produce a crystal product with small size and a narrow CSD. Examples of these are confined impinging jets [29], T-mixers [30] and static mixers [9]. These mixers are reliant on their flow rates for mixing, with higher flow rates resulting in more thorough mixing. Further detail on crystallisation platforms and their mixing properties is given in Section 1.8.

1.4 Nucleation

The formation of a crystal in a supersaturated system requires a nucleation event, providing a surface upon which the crystal can grow via deposition of solute, and to progress the system towards equilibrium. A given mass of solute can crystallise into many small crystals, or fewer large crystals depending on the nucleation rate. Control of nucleation is a key step in the control of the overall crystal properties, number of

crystals, and CSD, and therefore the quality of the crystal product [31]. Nucleation can be categorised into primary or secondary, and is detailed in Figure 1.5.

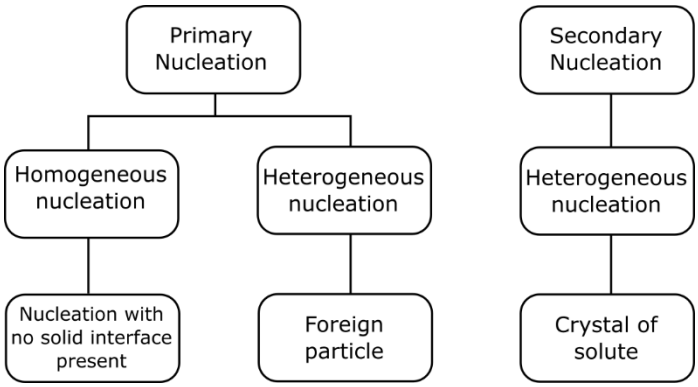

Figure 1.5: The different processes of nucleation. Adapted from [32].

1.4.1 Primary Nucleation

1.4.1.1 Homogeneous Primary Nucleation

This mode of nucleation occurs in a clear solution, with no external surface being provided, and relies on the formation of solute clusters within the solution. This process is described by Classical Nucleation Theory (CNT), which was first proposed by JW Gibbs in the latter part of the 19th century [33]. whereby it is assumed that clusters initially form by the addition of single units of solute, driven by supersaturation, in a process depicted by the schematic below:

$$A + A \longleftrightarrow A_2$$
$$A_2 + A \longleftrightarrow A_3$$
$$A_{n-1} + A \longleftrightarrow A_n$$

The majority of these clusters dissipate before they can grow to the required size, as the volume free energy ΔG_V must exceed the surface free energy ΔG_S. The solid state has greater stability than the liquid state, and so ΔG_V becomes negative, decreasing the free energy of the system. However, the free energy increases due to the presence of a solid/liquid interface at these clusters, the extent of which is proportional to their surface area. As shown in Figure 1.6, ΔG_S has a greater effect at small cluster radii, and so small clusters redissolve. Upon reaching a critical cluster size, r_c, the total free energy

reaches a maximum and the energy barrier for the formation of stable nuclei is overcome, making crystallization energetically favourable.

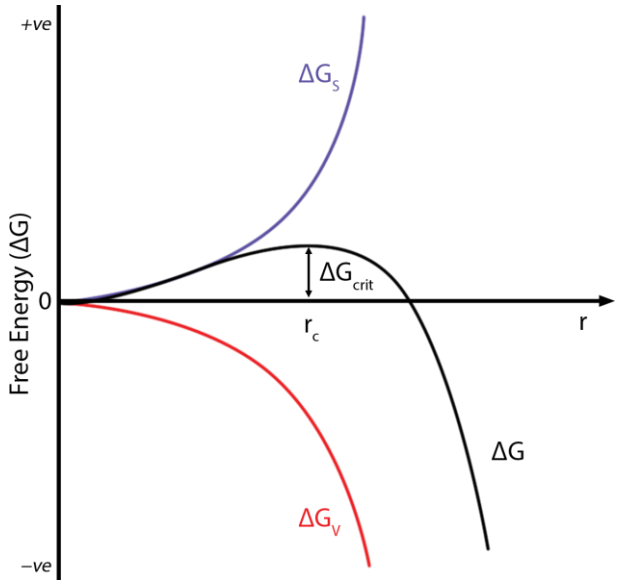

Figure 1.6: Energy diagram for formation of a critical nucleus. r_c must be exceeded for the free energy of the system to decrease [34].

The rate of nucleation, J, which represents the number of nuclei formed per unit time per unit volume, is expressed in the Arrhenius equation below:

$$J = A\exp\left(-\frac{\Delta G_{\text{crit}}}{kT}\right) \tag{1.3}$$

This can be rewritten by substituting a number of terms to obtain the following expression:

$$J = A\exp\left(-\frac{16\pi\gamma^3 v^2}{3k^3T^3(lnS)^2}\right) \tag{1.4}$$

By this equation, three variables affect the nucleation rate: the temperature, T; the supersaturation ratio, S; and the interfacial tension, γ. This suggests that an increase in temperature will increase the nucleation rate; however, increasing the temperature can also affect the supersaturation ratio for compounds that show temperature dependence

on solubility. Interfacial tension can be affected by the solvent composition and the presence of impurities [35], and the use of surfactants has been demonstrated to significantly affect crystallisation kinetics [36].

CNT has some limitations in that it assumes the critical clusters are uniform spheres; that the curvature of the cluster does not affect interfacial tension; and that the clusters grow by the addition of one unit at a time, ignoring the effect of the collision of clusters [37]. Nucleation rates measured experimentally differ from the predicted values by several orders of magnitude, which has been attributed to overestimation of the pre-exponential factor [31]. Thus, whilst CNT has been shown to have empirical application, nucleation theory continues to receive attention to better understand this complex phenomenon.

1.4.1.2 Heterogeneous Primary Nucleation

This mode of nucleation is defined as the generation of a solid phase that is induced by the presence of a surface other than a parent crystal. This surface can range from the walls of a crystallisation vessel to dust particles. The presence of interfaces initiates nucleation at lower supersaturations than are required for homogeneous nucleation. The free energy barrier for the formation of a critical nucleus by a heterogeneous pathway is therefore less than for homogeneous [34].

1.4.1.3 Two-Step Nucleation

CNT was initially developed to describe the condensation of droplets from a vapour, and although it has been assumed to be translatable to crystal nucleation, it is not an accurate descriptor. In recent years, a two-step nucleation theory has been developed. This theory describes the formation of liquid-like clusters of solute molecules, followed by reorganisation of these clusters into ordered crystal structures. This process was first observed for the formation of protein crystals, but has been suggested as a suitable descriptor for nucleation of small organic molecules [37]. The differences between these mechanisms are shown in Figure 1.7. CNT can result in the overestimation of the nucleation rate by orders of magnitude [31], but rate equations for two-step nucleation are not as well defined as those for CNT, and thus CNT is still the dominant mechanism for the quantification of nucleation processes.

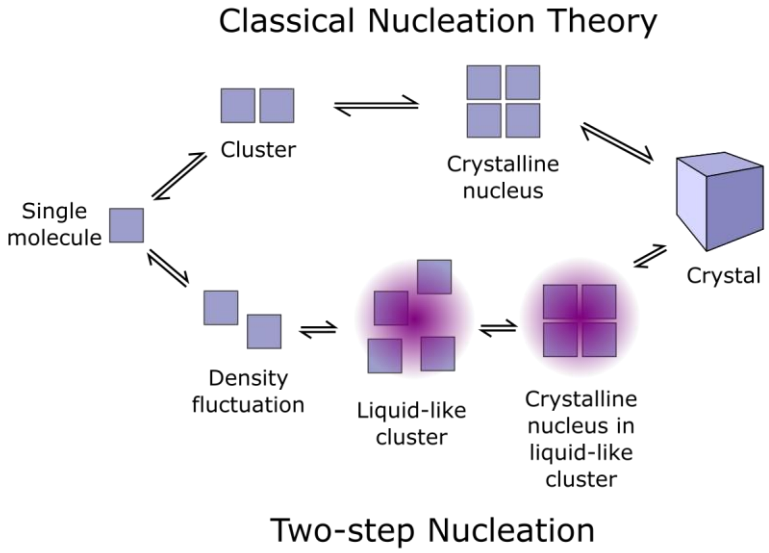

Figure 1.7. An overview of Classical Nucleation Theory and Two-step Nucleation. Adapted from [38].

1.4.2 Secondary Nucleation

Secondary nucleation is the process of nucleation occurring in the presence of existing crystals in solution. The two major mechanisms for the production of secondary nuclei are fluid shear and collision-based. These collision-based mechanisms can be further categorised: crystal-crystal collisions, whereby crystals in suspension collide directly and fragment; crystal-agitator collisions, where the crystals come into contact with a high-velocity agitator, which is typically an impeller in stirred tanks; and by crystal-wall collisions. All of these processes can result in small fractures and chips of material being produced that can result in the generation of fines and poor control over CSD. Collision-based mechanisms are the main consideration for industrial crystallisation processes [39].

Expressions for nucleation rates for both primary and secondary nucleation are highlighted in Table 1.1. These take into account a variety of mechanisms, the potential occurrence of which will be dependent on the system, and so consideration must be made as to which expression would most accurately represent the system it is used for.

Table 1.1. Summary of common nucleation expressions. Adapted from [40].

Nucleation	Expression	Comments	Reference
Primary	$B = k_B {S_A}^b$		[41]
Homogeneous	$B = k_B \exp\left(\frac{-16\pi\gamma^3\nu^2}{3k^3T^3(\ln(\sigma_s+1))^2}\right)$		[34]
Heterogeneous	$B = k_B \exp\left(\frac{-16\pi\gamma^3\nu^2 f(\varphi)}{3k^3T^3(\ln(\sigma_s+1))^2}\right)$	$f(\varphi)$ corrects for nucleation on non-crystal surfaces	[42]
Secondary	$B = k_B {S_A}^b \mu_2$		[43]
	$B = k_B {S_A}^b \mu_3$		[44]
	$B = k_B \exp\left(-\frac{\Delta E}{T}\right) {\sigma_s}^b \mu_3^k$	k_B is temperature dependent	[45]
	$B = k_B {\sigma_s}^b \mu_3 (L_{\min})^j$	$L_{\min}$ is the minimum size for a crystal to participate in collisions that produce secondary nucleation	[46], [47]
	$B = k_B {S_A}^b N^l \mu_2^j$	Includes crystal agitation and crystal-crystal effects	[48]
	$B = k_B {S_A}^b N^l \mu_3^j$		

Here, S_A represents the absolute supersaturation defined by $S_A = c - c^*$. Relative supersaturation is represented by σ_s and defined by $\sigma_s = \frac{c-c^*}{c^*}$.

1.5 Crystal Growth

After solute molecules have formed stable nuclei, these particles then undergo growth such that they reach a detectable size. Provided that these crystals are in the presence of a supersaturated solution, growth will occur. Figure 1.8 shows a simplified version of crystal growth at the molecular level, with molecular-level resolution shown in Figure 1.9. There are several proposed mechanisms for crystal growth [49], the most universally accepted of which is typically represented by two steps: diffusion of a solute molecule

from the bulk solution to the crystal surface, and integration of the solute molecule into the crystal structure. The attaching solute molecule is more likely to integrate at the kink site due to the potential to form more bonds to neighbouring molecules than elsewhere on the crystal surface, and conversely is more likely to leave this site upon dissolution [50].

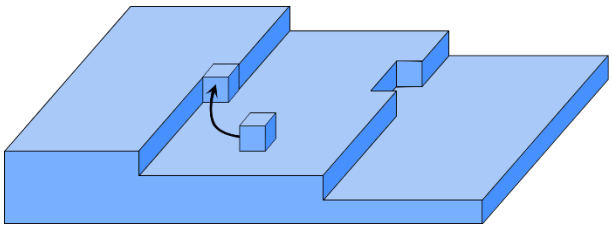

Figure 1.8: The molecular process of crystal growth. Steps and kinks are more energetically favourable locations for crystal growth. Adapted from [51]

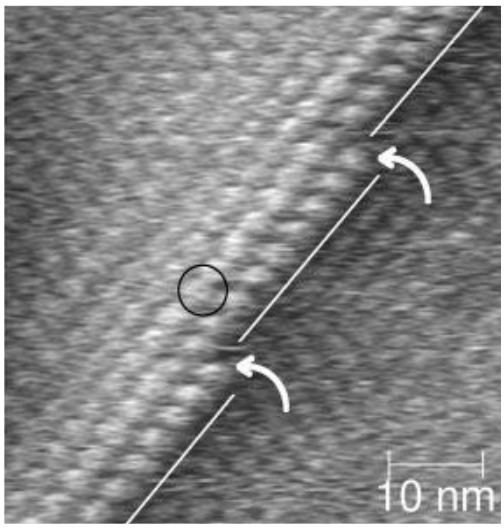

Figure 1.9: AFM image of an insulin crystal showing steps and kinks [52].

Crystal growth can be described in simple terms by the change in the size of the crystal over time and is represented by the size-independent growth rate expression in Table 1.2. There can be several factors that influence crystal growth, and expressions that incorporate those have also been developed and are shown in Table 1.2. Such expressions can be utilised in predicting the CSD of a process [53].

Table 1.2. Commonly used growth expressions.

Mechanism	Expression	Comments	Reference
Size-independent	$G = k_G {S_A}^g$		[54]
Size-dependent	$G = k_G {S_A}^g (1 + \gamma L)$ $G = k_G {S_A}^g (1 + \gamma L)^p$		[53], [55]
Power law	$G = k_G {S_A}^g L^p$		[53], [56], [57]
Burton, Cabrera and Frank (BCF)	$G = \frac{k_G}{k_{BCF}} {S_A}^2 \tanh\left(\frac{k_{BCF}}{\sigma_s}\right)$	Includes effects of surface defects	[58], [59]
Arrhenius type	$G = k_G \exp\left(-\frac{\Delta E_G}{RT}\right) {\sigma_s}^g$	Semi-empirical relationship; k_G is temperature dependent	[58]

The growth rate of a crystal determines the residence time required within a crystalliser to achieve a target size; a slow growth rate will require a longer residence time. This can be accommodated for by increasing the volume or decreasing the flow rate of continuous crystallisation processes. Consideration must then be made for the footprint of such crystallisers, and the effect on the housing of and initial outlay on equipment.

High supersaturation provides a greater driving force for growth, which can increase the rate of production. However, this can result in a lower quality product, such as crystals with inclusions of solvent [60]. This is not to be confused with the formation of solvates or hydrates, where solvent can be incorporated into the crystal structure. In the case of water as the solvent, these are referred to as hydrates; otherwise, the more generic term of solvates is used. Solvates are often undesirable, introducing issues with stability and potential toxicity for pharmaceutical products. Secondary processing can also be negatively affected by the presence of solvates [61].

Crystallisation close to a supersaturation ratio of 1 results in slower crystal growth, which in turn can improve the purity of the crystal product by minimising the aforementioned issues. Practically, there is a limit to the residence time one can provide

to a process. Maintaining crystallisation in the middle of the metastable zone is a suggested compromise between duration of operation and product quality [62].

1.6 Polymorphism and Solid Form

Polymorphism, with regards to crystal structure, is the ability for a compound to crystallise in more than one manner, the term being derived from the Greek *polus* meaning "many", and *morph* meaning "shape" [34]. There is no change in chemical composition, but the molecular packing can have a pronounced effect on the physical properties of the compound. A striking example that rather elegantly demonstrates just how different polymorphs can be is that of 5-methyl-2-[(2-notrophenyl)amino]-3-thiophenecarbonitrile, better known as ROY due to the red, orange and yellow crystals it can form, shown in Figure 1.10.

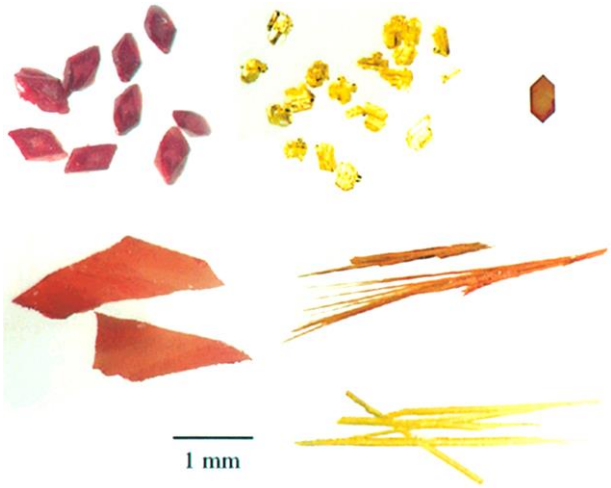

Figure 1.10: Polymorphs of ROY [63].

Polymorphism has been well documented, with one of the first recorded instances towards the end of the 18th Century by Klaproth, who discovered calcite and aragonite were both forms of calcium carbonate [64]. Compounds often display polymorphism, with evidence showing at least half of compounds that are screened for polymorphism display it [65]. . This is of particular importance in the manufacture of pharmaceuticals, as different polymorphs can exhibit varying bioavailability due to differing solubilities, and thus differing dissolution rates [66]. One of the most well-known instances of unwanted polymorphism within the pharmaceutical industry is associated with the antiviral drug ritonavir. The appearance of a new and more stable form (form II) of the

compound plagued production, requiring extensive review and modification of the manufacturing process [67]. The more stable form II had a lower bioavailability, and therefore was less effective than form I. Such occurrences demonstrate the need for extensive polymorph screening.

Ostwald's rule of stages states that the initial crystal form generated is the least stable form thermodynamically, with free energy closest to the original state [68]. This will then undergo transformation until the lowest free energy state is achieved and a stable polymorph is produced (Figure 1.11).

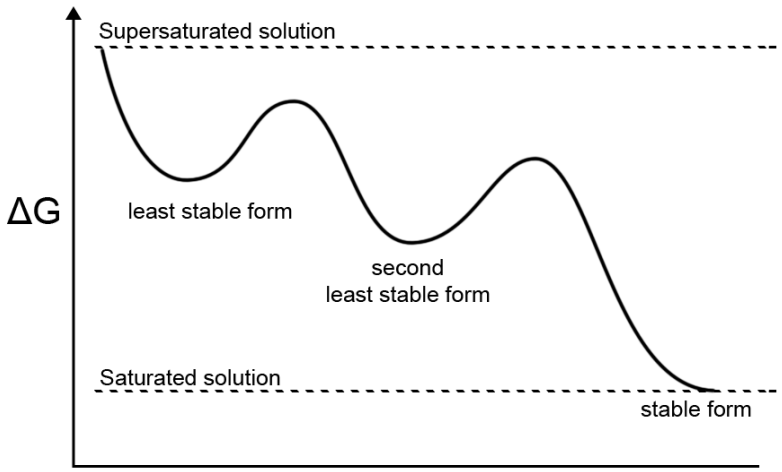

Figure 1.11. Energy states for a polymorphic system. Adapted from [69].

Depending on the stability of the compound and the desire for a metastable form, this may be preferable, as such crystals have greater solubility than their more stable counterparts; however, this may be at the expense of physical stability and affect product shelf life.

Polymorphism can significantly affect the formulation of active pharmaceutical ingredients (APIs). As exemplified in Figure 1.12, the stable monoclinic form I of paracetamol is not readily compressible into tablets due to the interdigitated nature of the molecular packing [70], whereas the metastable orthorhombic form II crystallises in flat hydrogen-bonded sheets [71], and is more amenable to direct compression.

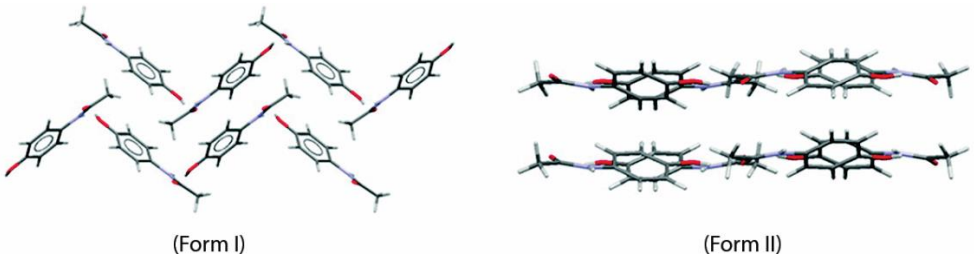

Figure 1.12: Crystal structures of the stable form I and metastable form II of paracetamol. Image adapted from [72]

Crystal structure prediction tools can be used to identify polymorphs that may not yet have been produced experimentally but are energetically feasible [73]. Some polymorphs can be very difficult to produce and require elaborate or novel methods to isolate them, such as the formation of carbamazepine form IV by spray drying [74].

1.7 Crystallisation Techniques

The method employed to crystallise a compound varies depending on the compound itself and the requirements for the product. For instance, one particular method may give the narrowest CSD, but may also give the lowest yield. If a solvent is required, the solvent properties also influence this decision. All crystallisation techniques rely on different approaches to generate supersaturation. The following section highlights the most commonly encountered crystallisation techniques.

1.7.1 Cooling Crystallisation

Manipulation of temperature is a common method of generating supersaturation to control crystallisation, often employed when the solubility of the compound is highly dependent on temperature, and when solubility is poor at low temperature. An undersaturated solution is cooled to the point that it becomes supersaturated, followed by either addition of seed crystals to grow them out, or by a further decrease in temperature to induce primary nucleation (Figure 1.13). Alternatives must be used for compounds that do not show such adequate temperature dependence, or that are very soluble at low temperatures.

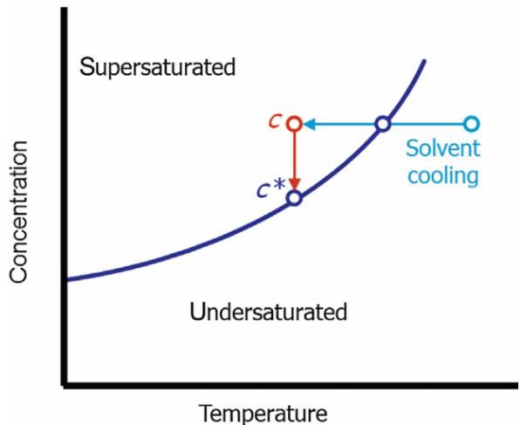

Figure 1.13: A representative phase diagram for cooling crystallisation [51].

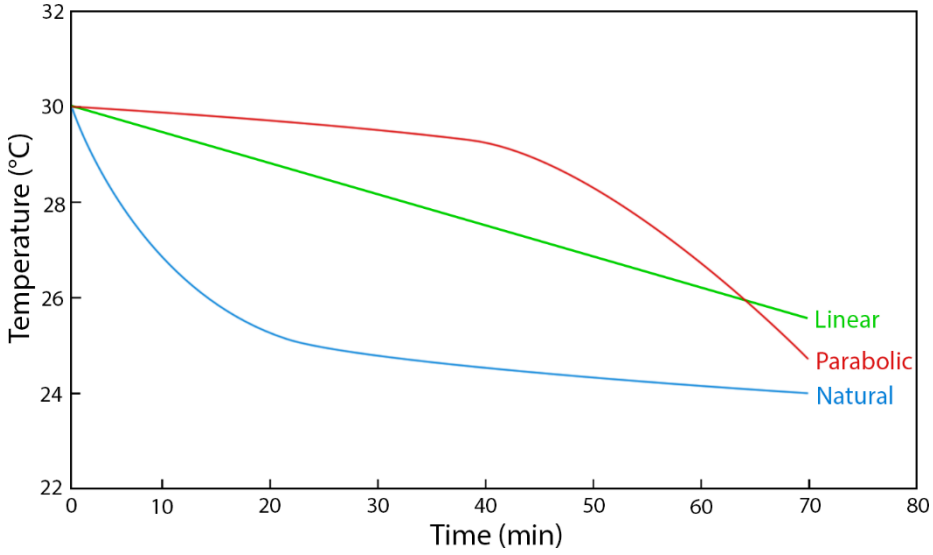

Figure 1.14: Various cooling profiles for seeded batch crystallisation from supersaturated K_2SO_4 solutions. Reproduced from [62].

Cooling profiles need to be considered when designing cooling crystallisation processes to achieve the most consistent crystal product. Three different cooling profiles used in a seeded cooling crystallisation are shown in Figure 1.14, which each produce different crystal growth rates and therefore affect the product quality. Crystals that grow quickly tend to be of a lower quality than those that grow slowly due to the potential inclusion of solvent and other impurities in the structure, and for undesired morphologies such as dendritic growth [62]. The rapid cooling displayed by the natural cooling profile generates a much higher supersaturation than linear or parabolic cooling and will result

in poor quality crystals. A linear cooling profile offers an improvement over natural cooling, but there will still be variable supersaturation during the crystallisation. Parabolic cooling profiles generate a constant supersaturation, and thus steady crystal growth and improved quality.

1.7.2 Evaporative Crystallisation

Evaporative crystallisation is a process which increases the concentration of the solution by evaporation of the solvent, either slowly by diffusion of solvent vapour from the liquid surface or more rapidly by boiling or pulling a vacuum. This increase in concentration then generates supersaturation as shown in Figure 1.15.

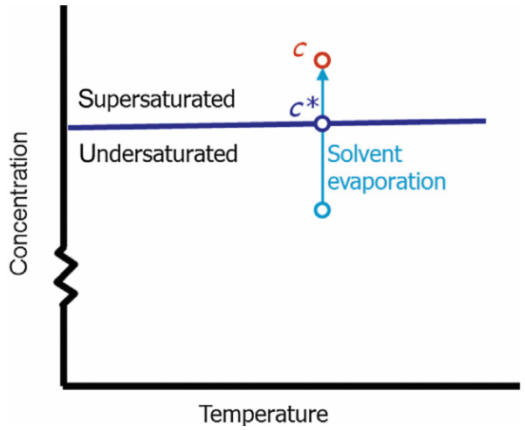

Figure 1.15: A representative phase diagram for evaporative crystallisation [51].

Evaporative crystallisation is not necessarily suitable for compounds that are liable to decomposition at elevated temperatures, depending on the threshold of this decomposition. The boiling point of the solvent can be controlled by altering the pressure of the system, which is of importance if the compound of interest has solubility limited to non-volatile solvents.

A compound whose solubility does not vary greatly with respect to temperature, for example sodium chloride, may be more suited to evaporative crystallisation. A suggested limit for the selection of evaporative crystallisation is if the solubility shows a temperature dependence of less than 0.005 g/g °C [75].

1.7.3 Melt Crystallisation

Melt crystallisation typically refers to crystallisation from a pure molten solid, in contrast to that of crystallisation from a solution. It is more commonly used as a purification technique, and very high purity crystals can be obtained [76].

As melt crystallisation does not require any solvent, this can be advantageous for reducing waste and eliminating the potential environmental hazards and cost associated with some solvents and their recovery. However, as the compound may well be produced by a chemical reaction using solvents to begin with, crystallisation from solution is often more practical.

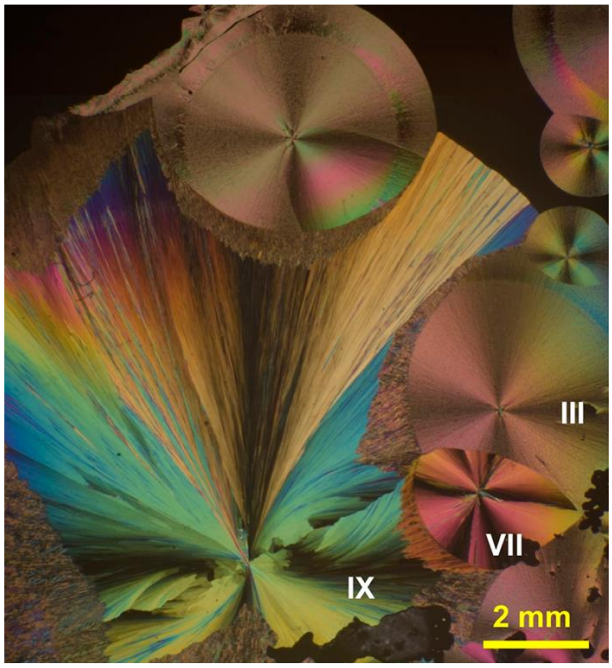

Figure 1.16. Paracetamol polymorphs produced from the melt [77].

Some elusive polymorphs of APIs have been reliably isolated by melt crystallization, such as paracetamol form III [78], where attempts to isolate this form from solution produce form I instead. This method has been used to identify new polymorphs [77].

1.7.4 Reactive Crystallisation

Reactive crystallisation, also referred to as precipitation, involves the mixture of two or more reagents to produce a chemical reaction such that the resulting product is poorly soluble. The product outcome of reactive crystallisation can be highly dependent on

the intensity of mixing. If reaction occurs before adequate mixing has been achieved, there can be localised regions of varying concentration, ultimately altering the product quality due to localized differences in nucleation and growth kinetics. Supersaturation can be controlled by varying the concentration of the reagents, with very high supersaturations possible.

1.7.5 Antisolvent Crystallisation

Compounds that are prone to thermal decomposition and show a poor temperature dependence on solubility are left with few other options for crystal growth. Antisolvent crystallisation is a method of producing crystals by mixing a solution of the compound to be crystallised and another fluid, so that the compound has a much lower solubility in the overall mixture. The balance of dilution and decrease in solubility determines the supersaturation. Antisolvent and cooling crystallisation are often combined in industry to increase the yield [79].

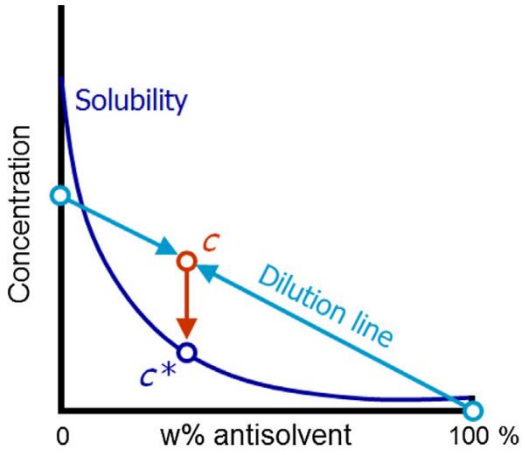

Figure 1.17: A representative phase diagram for antisolvent crystallisation [51].

The addition of antisolvent dilutes the overall solution. It is therefore necessary that the potential of the antisolvent to decrease the solubility overrides that of the dilution factor. This can be seen in Figure 1.17, where for regions of the curve c* above the dilution line, the system is undersaturated. This shows a critical ratio of solvent-antisolvent that must be reached before supersaturation is generated, which will differ between systems.

To generate supersaturation using an antisolvent, there are a number of ways it can be introduced. Typically, this is done by the addition of antisolvent to a solution, which normally has a greater volume than the antisolvent added. Alternatively, the solution

can be added to a large volume of antisolvent. This "reverse addition" generates very high supersaturation, and depending on the mixing conditions can produce a large number of small nuclei. In some cases with organic compounds, the generated supersaturation ratio can be so high that a metastable liquid-liquid phase separation forms, also known as oiling out, which is undesirable for ensuring product quality and purity [80]. Controlling supersaturation by the mixing of solvent and antisolvent and being aware of the limitations of the mixing in the platform affords better control over product outcome.

It is routine for pharmaceutical crystals produced by batch crystallisation methods to require milling. This serves to improve downstream processability by producing a more consistent CSD and can increase solubility of poorly soluble APIs by increasing their surface area. However, this process can result in reduced yields due to loss of material and can lead to surface defects on the crystals and even loss of crystallinity due to the high energies associated with the milling [81]. The potential to remove the milling process entirely from the supply chain of a pharmaceutical has benefits for manufacturers and consumers alike [82]. Antisolvent crystallisation offers a method for the generation of small crystals directly, without the need for extensive processing [83].

1.7.5.1 Solvent Recovery

Antisolvent crystallisation processes can require the processing of large volumes of solvent and antisolvent. The environmental impact of the use of some of these solvents can be of concern [84]. The solvent and/or antisolvent may also require non-renewable resources in their manufacture and may be expensive to produce and transport. In such cases, a recycling mechanism is desirable to minimise the effects of these factors. Recovery of the solvent and antisolvent assists in the self-containment of a crystalliser, which lends itself well to a continuous crystallisation platform.

There are a number of separation techniques that can be employed, and the selection of such a technique will depend on the properties of the solvent and antisolvent, once again highlighting the importance of solvent screening and selection. Chromatography is one of the mainstays of separation techniques in chemistry. A suitably designed chromatography column would be able to separate a mixture of various solvents and can be performed continuously, provided the integrity of the column is not

compromised over time. For a high throughput, this process may require a high pressure to operate.

Temperature-induced phase separation is one reported method of separating solvents. Diisopropylamine (DiPA) has been shown to be a suitable antisolvent for the crystallisation of sodium chloride (NaCl) from water [85], with DiPA reducing the solubility of NaCl, and showing a liquid-liquid phase separation near room temperature. Increased antisolvent fraction gave higher yields of NaCl, but the miscibility of the solvents increased as NaCl concentrations decreased, and the whole process had higher calculated operating costs than the standard evaporative technique. Several other potential methods could be investigated such as the use of membranes, distillation and liquid-solid separation.

1.8 Platforms for Continuous Crystallisation

1.8.1 Mixed Suspension Mixed Product Removal Crystalliser

The MSMPR crystallisers are a popular system for continuous crystallisation as they are easily adapted from existing STR technologies. They operate by the continuous feed of solvent-solute into the crystallisation vessel, whereupon it is mixed with the crystal suspension that is already within the vessel [51]. Supersaturation is then generated by the desired process, such as addition of antisolvent, and new crystal material is formed. Concurrently, a suspension of the MSMPR crystalliser contents can be fed into a second MSMPR crystalliser. Several MSMPRs can be connected together in a cascade, as shown in Figure 1.18. As the number of these vessels increases, the system likens to a plug flow reactor. There is a practical limit as to how many of these units can be connected in series, but a greater number potentially allows for greater control until diminishing returns and improved likelihood of failure of one of the units becomes a concern.

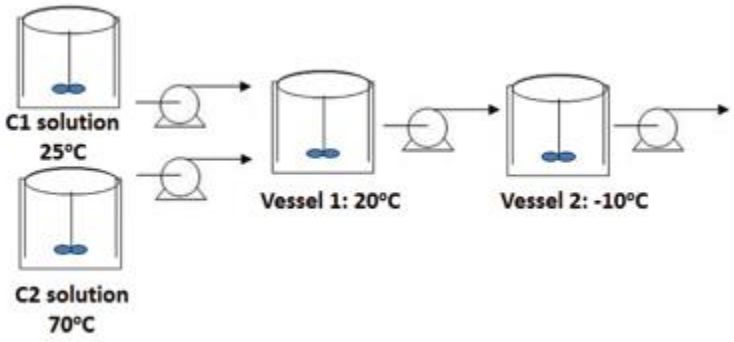

Figure 1.18: An example of an MSMPR cascade with temperature difference as the driving force of crystal growth [11].

One major advantage that MSMPR technology has over other technologies is that existing batch equipment can be readily converted, reducing the cost to industry. The platforms are readily accepting of PAT such as FBRM and process video microscopy (PVM) with little modification, compared to some PFRs that need large collars and additional sections to incorporate it. PAT can potentially be beneficial in an MSMPR system, as probes can act as baffles to improve mixing, whereas it is likely to impede mixing in a PFR.

1.8.2 Continuous Oscillatory Baffled Crystalliser

The Continuous Oscillatory Baffled Crystalliser (COBC) is a plug flow tubular reactor vessel with oscillatory motion superimposed on this net flow. The tube is typically smooth, with regularly spaced baffles that induce eddy currents, as shown in Figure 1.19. This vastly improves the mixing of the fluid within the sections compared to a regular pipe. These eddies in a standard temperature-controlled system ensure rapid and thorough heat transfer throughout the fluid. To achieve plug flow in a tubular reactor without the baffles in place, the reactor would have to operate at very high flow rates. The residence time of such a system is very low and impractical. COBCs allow longer residence times at a lower length-to-diameter ratio, which allows time for crystal growth [86].

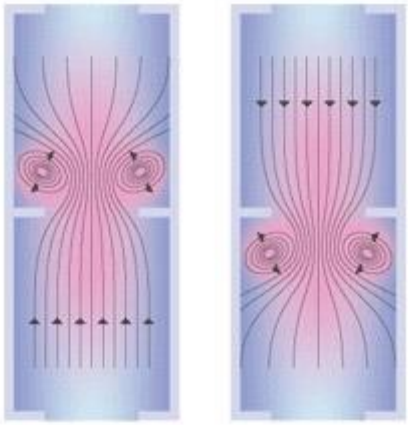

Figure 1.19: Eddies are generated as a result of oscillatory motion between the baffles of a COBC [87]

The fluid dynamics of a COBC are defined by the Strouhal number (*St*), net flow Reynolds number (Re_n) and oscillatory Reynolds number (Re_o), shown as Equations 1.5, 1.6 and 1.7 below:

$$St = \frac{D}{4\pi x_o} \tag{1.5}$$

$$Re_n = \frac{UD}{v} \tag{1.6}$$

$$Re_o = \frac{x_o \omega D}{v} \tag{1.7}$$

where $D$is the diameter of the reactor (m), U is the mean net flow velocity (m/s), v is the kinematic viscosity (m^2/s), $x_o$is the centre-to-peak oscillation amplitude (m) and $\omega$is the oscillation frequency (Hz).

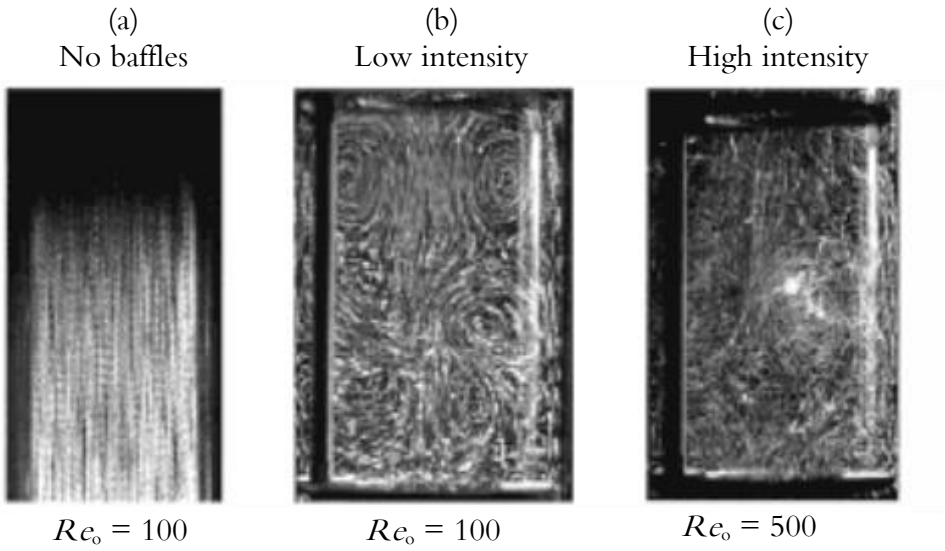

Figure 1.20. Oscillatory flow patterns in a COBC. (a) low Re_o, unbaffled tube. (b) low Re_o, baffles present. (c) high Re_o, baffles present. [86]

The Reynolds number describes how turbulent the fluid flow is within the reactor. As can be seen in Figure 1.20, an increase in Re_o results in greater turbulence, and therefore more thorough mixing. The Re_n and Re_o vary depending on the desired residence time within the system and the optimum mixing intensity, which may be limited by the attrition of crystals at high Reynolds numbers. Typically, COBCs are suited to long residence times, and as such the Re_n is usually low and Re_o relatively high to accommodate for this; as an example, Re_n = 80 and Re_o = 1000 were used for the crystallisation of α-lipoic acid:nicotinamide co-crystals [88]. The Strouhal number is a measure of the propagation of vortices generated by the presence of the baffles, and takes the unsteady flow that these generate into account [89].

For cooling crystallisations, this interaction is described well by the dimensionless Nusselt number (Nu), which gives the ratio of convective to conductive heat transfer across a boundary (in this case, the inner wall of the COBC):

$$Nu_t = \frac{h_t D}{k} \tag{1.8}$$

where D is the diameter of the reactor (m), k is the thermal conductivity of the fluid, and h_t is the heat transfer coefficient. The effect of the presence of baffles and oscillation

on mixing in a tube has been investigated previously [90]. As shown in Figure 1.21, an increase in net flow Reynolds number leads to an increase in Nusselt number, with a more pronounced change with the presence of baffles. Figure 1.22 shows an increased Nusselt number when oscillation is applied to the net flow, with a more pronounced effect with a higher Re_o. This shows there is a significant improvement in heat transfer in a tube with the presence of baffles and with oscillatory flow superimposed on the net flow, and a lesser improvement in heat transfer with increasing flow rate.

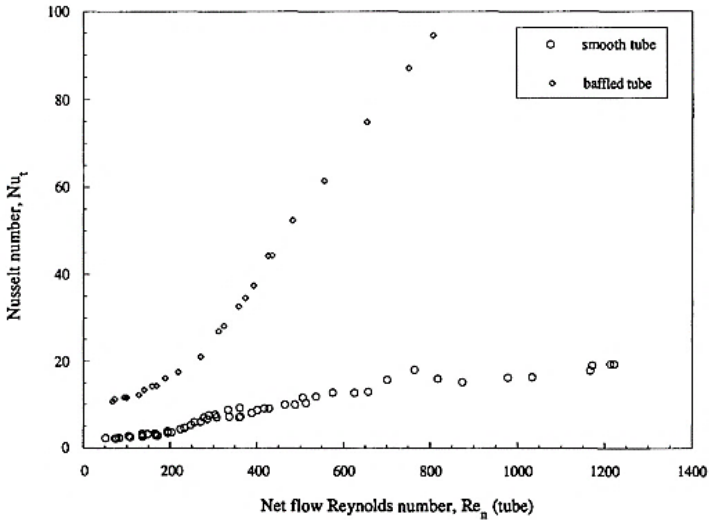

Figure 1.21: The heat transfer for a smooth tube and a baffled tube with non-oscillatory flow [90]

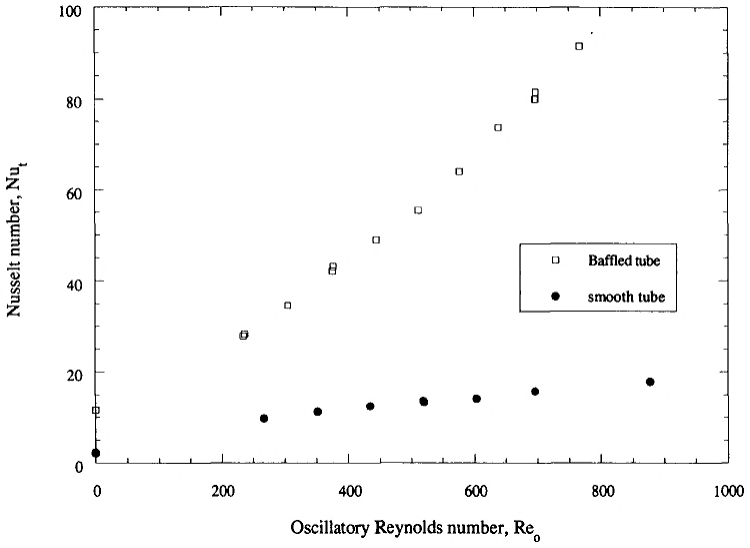

Figure 1.22: The heat transfer for a smooth tube and a baffled tube with oscillation superimposed on net flow (Re_n = 160, Sr = 0.16) [90]

A representation of a typical COBC is shown in Figure 1.23. In this diagram, there are bends present in the setup. These sections are subjected to different fluid mechanics than the straight sections, and so there is the potential for product variation to occur due to these sections. Whether these sections are jacketed or not can also affect the temperature profile. The significance of this is dependent on the type of crystallisation being performed. However, these bends are necessary to reduce the footprint of the reactor, and so an adequate trade-off between space and product control must be achieved. Practically, all lab scale COBC platforms are assembled with some number of these bends.

High supersaturations and poor temperature control can lead to fouling in such systems. In laboratory scale equipment, where the reactor is typically made of glass, this can be detected visually. In larger scale vessels operating at pressures unsuitable for glassware, and where robustness is required, this can be detected by pressure changes within the reactor [91].

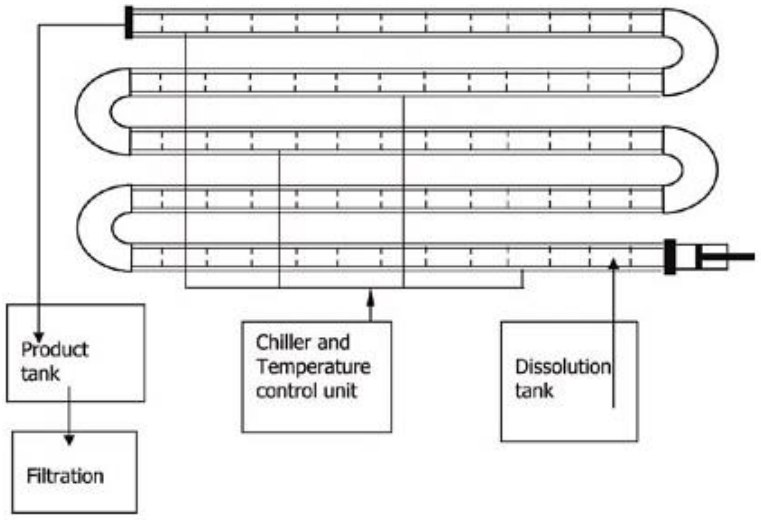

Figure 1.23: Schematic of a COBC [89].

An advantage of a COBC over a typical batch process is that due to the mechanics of the system, the reactor can be scaled up linearly to increase product output without affecting product quality by maintaining the Reynolds and Strouhal numbers. This is not possible in a batch process, where other factors become more prevalent and problems arise as the reactor size increases.

For cooling crystallisations in a COBC, maintaining a smooth cooling profile can prove challenging dependent on equipment design. Typically, step-wise temperature profiles are produced, based on the number of jackets and heater/chiller units present. In products with a narrow MSZW, the temperature difference between the jacketed sections could induce unwanted nucleation and fouling of the reactor. Due to this, primary nucleation followed by a suitable growth phase in a COBC can be difficult to achieve without fouling the walls of the reactor. An alternative is to use the COBC only for crystal growth by preparing a seed suspension externally, and then introducing this to the crystalliser. With suitable temperature control, this eliminates primary nucleation events. Smooth temperature profiles have been demonstrated in a COBC by use of a double jacket with countercurrent configurations [92], but increase the complexity of the platform over their single-jacket counterparts.

In order to test the suitability of a compound and solvent system for a COBC, it is possible to operate a smaller scale batch oscillatory baffled crystalliser (OBC) to mimic closely the conditions in a continuous platform. This allows for calculation of kinetic parameters without the inherent wastage of material associated with the larger volumes of a continuously operated COBC. Video imaging has been used in such a batch OBC in order to monitor the crystallisation process in real-time [93], and potentially allows for a feedback mechanism to maintain product specification.

There is only one known example of an experimental antisolvent crystallisation process in a COBC in the literature [94]. The schematic of the platform is shown in Figure 1.24, which was intended for the generation of seed crystals. Rapid desupersaturation was observed at a short distance from the mixing point.

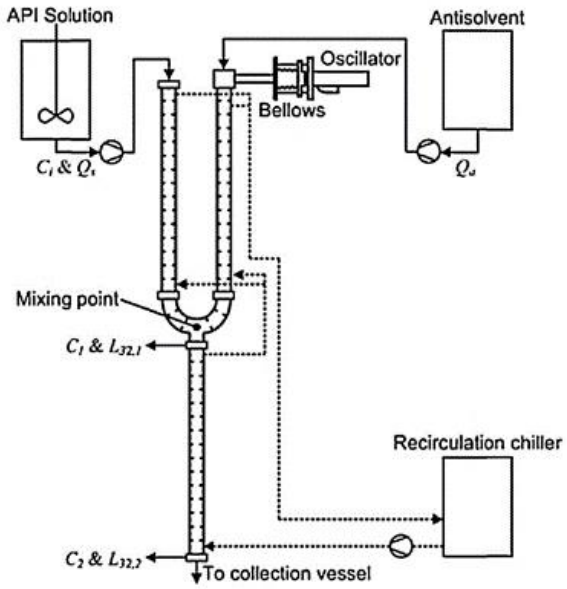

Figure 1.24: Antisolvent COBC setup for the generation of seed crystals [94].

For this setup, samples were taken every ten residence times until the reactor blocked or until depletion of the feed solution. The authors noted that steady state of solute concentration was reached at the two sampling locations C_1 and C_2 within ten residence times, and that this was consistent with other literature quoting 4 – 10 residence times [9]. A steady state of the mean crystal size was also reported to be achieved within ten residence times, but this mean size reduced towards the end of the reactor operation. Increasing the oscillation amplitude maintained steady state of concentration and mean crystal size for a greater number of residence times, but control was still lost. This improvement was attributed to more thorough mixing provided by the greater amplitude of oscillation. At optimal conditions, crystal size was maintained within ± 3.01 μm. Mean crystal sizes were lower upon an extended operation from 71.02 ± 3.28 μm to 44.63 ± 3.01 μm extended) which was attributed to the replacement of PVDF baffle inserts for integrated glass. This reduced surface roughness and therefore potential unwanted nucleation sites, and also removed the small gap present between the edge of the tube and the baffle inserts.

1.8.3 Static Mixer Crystalliser

Static mixers are designed for thorough mixing of fluids by the action of the fluid passing over a mixing element. Due to the nature of the static elements, the extent of mixing is determined by the flow velocity, with more thorough mixing at greater velocities.

This therefore reduces the residence time of these systems, and so they are therefore more suited to fast-growing crystals.

Operating static mixers at low flow rates can lead to sedimentation when mixing solid suspensions. A suggested workaround is to mount the reactor vertically, with a Re in the range 100-1000 [95]. The application of oscillation to the net flow with the use of static mixers, similar to the COBC, could be of interest. Control of heat transfer within static mixer systems is predominated by the flow velocity, and so may not be as suitable for cooling crystallisation as other technologies. However, for antisolvent crystallisation, rapid mixing is required before the onset of crystallisation for consistency in the product. These systems may be advantageous if temperature is to be kept constant. The effect of temperature versus flow rate on the crystal product in static mixer systems could be of interest. In such a system, there is the potential for secondary nucleation due to attrition of the crystal product by impacting on the leading edge of the mixing insert. This is clearly undesirable, as control over the CSD is lost. However, the extent of this attrition will correlate with flow rate and residence time employed.

Alvarez and Myerson investigated antisolvent crystallisation in a plug flow reactor, utilizing Kenics helical static mixers and varying the number of addition points of antisolvent [9], as detailed in Figure 1.25.

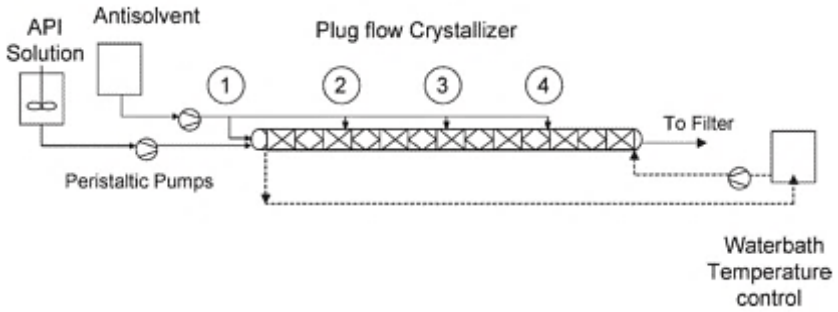

Figure 1.25: Antisolvent crystallisation in a plug flow crystalliser utilizing static mixer inserts [9].

The use of multiple addition points of antisolvent afforded control over crystal size. The effect of these injection points differed between the two compounds investigated. Flufenamic acid showed an increase in the mean crystal size as the number of antisolvent addition points increased, which can be seen in Figure 1.26. L-glutamic acid at first showed a decrease in mean crystal size, followed by an increase, implying the

mechanism of nucleation had a greater effect on this system than crystal growth. A potential method of expanding upon this work would be to increase the number of addition points of antisolvent and the mode by which it is introduced into the crystalliser.

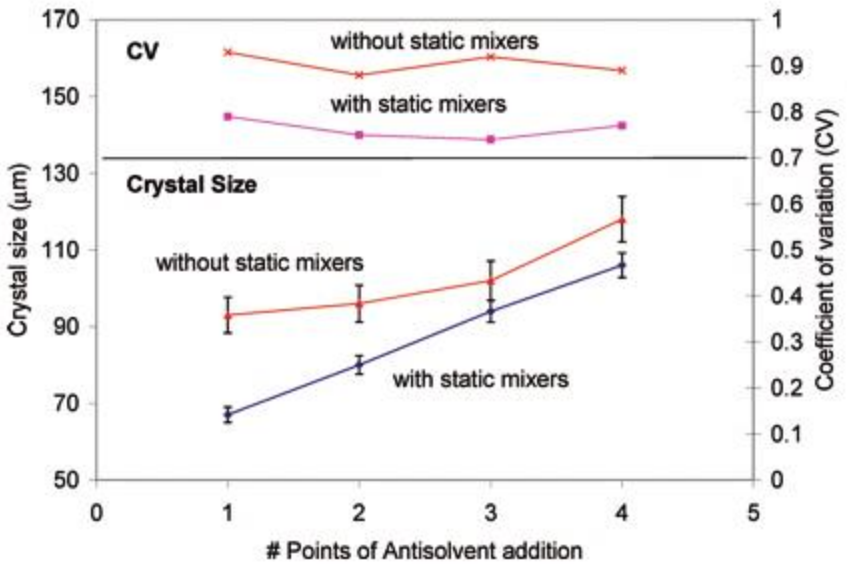

Figure 1.26: The influence of static mixers on the crystal size distribution of flufenamic acid.

The total volume of antisolvent introduced remained the same, but was split across one, two, three or four injection points. One injection point of antisolvent resulted in the generation of a large number of small crystals, due to the high supersaturation. Two injection points, and therefore 50% of the total volume of antisolvent introduced to the system, did not produce as high a supersaturation as in the case of one injection point. This was also the case for three and four injection points.

The influence of the static mixers themselves was compared to an empty pipe with no mixing elements, using flufenamic acid as the model compound. The results of this are shown in Figure 1.26, which show that the mean crystal size was much lower with static mixers. The removal of the mixing insert results in longer mixing times within the crystalliser. The results suggest that nucleation and crystal growth were already underway before the mixing of antisolvent and solvent had completed. The authors

reported a wider CSD in this case, which was in accordance with results from other sources [96], [97].

A reduced flow rate resulted in smaller crystals, contrary to their original expectations. A lower flow rate increases the residence time, and so would allow more time for crystal growth. Note was made to the importance of mixing intensity, with a higher intensity of mixing allowing for greater mass transfer and therefore larger crystals.

The crystal size distribution was measured using focus beam reflectance measurement (FBRM) for flufenamic acid and L-glutamic acid. FBRM devices for such work are probes that are mounted so that they make contact the crystal suspension itself. The probe uses a laser and scans the solution to measure the chord length of a crystal. The number of these measurements made by the probe gives the CSD. Mathematical modelling was applied to this crystallisation system, but both a plug flow model and axial dispersion model were unable to accurately describe the process.

1.9 Summary

Crystallisation of APIs are typically produced in batches by either cooling, antisolvent or reactive crystallisation. Batch crystallisation can result in high variability in the crystal product between batches. Continuous crystallisation can be utilised to target CQAs that are not achievable in batch processing.

Continuous crystallisation platforms generally consist of MSMPRs and PFRs, the selection of which is typically dependent on the process kinetics and the existing infrastructure. PFRs tend to be more suited to processes with shorter residence times. Of the available PFR technologies, COBCs have shown an ability to produce consistent crystal products compared to their stirred tank counterparts. There is limited work on antisolvent crystallisation using the COBC and scope to investigate its application further. Of particular interest is what are the limitations of such a process; which attributes is the technology suited to, and for which would an alternative be preferable.

The purpose of this research is to develop continuous antisolvent crystallisation in oscillatory baffled crystallisers to target various CQAs. The first chapter investigates different antisolvent addition strategies and various flow conditions in a COBC, covering a range of supersaturations. The second chapter considers an alternative OBC technology and its application in continuous antisolvent crystallisation, focusing on the product polymorphism. The last chapter utilises sequential parameter estimation to determine kinetic parameters from experiments in an MFOBC and applies them to the optimisation of multi-addition antisolvent crystallisations in a COBC.

2 Aims and Objectives

2.1 Aims

The intended aim of the research presented in this thesis is to develop the understanding and practical application of continuous antisolvent crystallisation in oscillatory baffled crystallisers. The goal is to utilise such crystallisers to demonstrate control over key crystal qualities, specifically crystal size and polymorphism. Three research areas addressed this, each demonstrating a different approach to continuous antisolvent crystallisation and control thereof in oscillatory platforms.

2.2 Objectives

Determine operational strategies for antisolvent crystallisations in a COBC.

- Construct a COBC with solution and antisolvent delivery ports.
- Vary the ratio of antisolvent to solution in the continuous crystallisation of anthranilic acid to achieve a range of supersaturations.
- Modify the flow velocities in the COBC to adjust residence time and local mixing conditions at point of contact of solution and antisolvent.
- Incorporate PAT to obtain real-time process information.

Demonstrate polymorph control in a continuous antisolvent crystallisation process utilising OBC technology.

- Design and construct a robust continuous crystallisation process utilising an MBOBC platform.
- Determine the effect of seeded and unseeded operation on polymorph dynamics.
- Determine the critical process parameters to allow for direct control over polymorph production.
- Investigate the steady state polymorphism and determine kinetic limits of the platform.

Develop an optimisation framework for continuous antisolvent crystallisation in a COBC.

- Determine growth and secondary nucleation kinetic parameters for the antisolvent crystallisation of anthranilic acid in a batch moving fluid oscillatory baffled crystalliser.
- Apply kinetic parameters to suggest optima for continuous antisolvent crystallisation in a COBC for targeted crystal product outcomes.

3 Materials and Methods

3.1 Materials

Anthranilic acid (*o*-aminobenzoic acid, CAS 118-92-3) of >98% purity was purchased from Acros Organics and Sigma-Aldrich. Ethanol (absolute, >99.8%, CAS 64-17-5) was obtained from VWR. Deionised water was produced in the laboratory via a Millipore Milli-Q Integral Water Purification System.

3.2 Methods

3.2.1 Solubility Measurements

3.2.1.1 Crystal16

The Crystal16 equipment was used to determine solubility based on turbidity measurements. An image of the Crystal16 is shown in Figure 3.1. The equipment consists of 16 wells that each hold a standard flat-bottomed HPLC vial of 1.5 ml volume and 11.5 mm diameter. Temperature control is provided by heating elements and Peltier modules. Stirring is provided by individually-controlled magnetic stirrers. The software interface allows for programmable heating and cooling cycles.

Figure 3.1. Crystal16 solubility measurement apparatus [98].

The experimental procedure involved placing a range of known masses of compound into the vials. Into these was then placed 1 ml of the desired ethanol and water solvent mixture, and a magnetic stirrer bar. Vials were capped with a screw top cap. Stirrer speed was set to 700 rpm. The following temperature profile was then set on the software interface:

Table 3.1. Temperature profile for Crystal16

Ramp to 63 °C @ 20 °C/min
Hold for 5 min @ 63 °C
Tune
Ramp to 5 °C @ - 0.5 °C/min
Hold for 30 min @ 5 °C
Ramp to 63 °C @ 0.5 °C/min
Hold for 30 min @ 63 °C
Ramp to 5 °C @ - 0.5 °C/min

3.2.1.2 Gravimetric Analysis

Gravimetric analysis was used to determine solubility by use of a custom water bath apparatus, shown in Figure 3.2. This consisted of a temperature-controlled water bath, beneath which was a 15-position magnetic stirrer plate. A heater/chiller unit maintained bath temperature in combination with two peristaltic pumps, one delivering water and the other for level control and recirculation to the heater/chiller unit. A calibrated thermometer submerged in the bath monitored the bath temperature directly. The setup had a lid to minimise evaporation of the bath water and thus reduce heat loss.

To measure the solubility, the solvents of interest were added to flasks and stirred for several hours to ensure they were at the desired temperature. To each of these was then added an excess of solid, which was stirred for three days to ensure equilibrium. Four samples of solutions from each water fraction were subsequently filtered over a 0.22 μm filter, weighed, and evaporated to dryness. The solubility was determined from the mass of the evaporated solvent and that of the remaining dry crystalline material.

Figure 3.2. Gravimetric solubility apparatus.

3.2.2 X-ray powder diffraction

Solid samples were analysed offline by X-ray powder diffraction (XRPD). Data was collected on a Bruker D8 Advance II diffractometer with Debye-Scherrer transmission geometry, monochromated Cu $K\alpha_1$ radiation at λ = 1.540596 Å, operating voltage of 40 kV and current of 50 mA, 1 mm anti-divergence slit, 2.5 ° Soller slits and Vantec 1D detector. Samples were lightly triturated to minimise any preferred orientation effects and mounted on a 28-well plate with X-ray transparent Kapton polyimide film of 7.5 μm thickness at ambient temperature. The plate was mounted on an automated x-y stage. Data was collected over a 2θ-range of 4 ° to 35 °, with a 0.017 ° step size and 1 second per step.

Data that was used for the preparation of a standard curve of polymorphic mass fractions was collected by XRPD on a Bruker D8 Advance II diffractometer with Debye-Scherrer transmission geometry, monochromated Cu $K\alpha_1$ radiation at λ =

1.540596 Å, operating voltage of 40 kV and current of 50 mA, 1 mm anti-divergence slit, 2.5 ° Soller slits, an 8 mm anti-scatter screen and LynxEye 1D detector. Samples were lightly triturated and placed within a 0.7 mm borosilicate glass capillary that was rotated for the duration of collection at ambient temperature. Data was collected over a 2θ-range of 5 ° to 35 °, with a 0.017 ° step size and 1 second per step.

3.2.3 Ultraviolet-visible Spectroscopy

Ultraviolet-visible (UV-vis) spectroscopy can be used as a method to measure the concentration of UV-absorbing compounds in solution. Measurements were performed using a Carl Zeiss MCS600 spectrometer with an attenuated total reflectance (ATR) probe of 6 mm diameter, allowing for in-line real-time concentration measurements in the batch OBC process. There are several advantages offered by ATR UV-vis spectroscopy over other means of measuring concentration. As no samples have to be taken, there is minimal interference with the system. The probe is suitable for use in slurries, as only the concentration of the solution is measured, making it ideal for crystallisation processes [99].

Anthranilic acid was determined to be suitably UV active upon initial testing with the apparatus and as reported elsewhere [100]. UV absorption is dependent on concentration and temperature, and so a calibration curve was produced from prepared standards that covered a range of ethanol/water mixtures and anthranilic acid concentrations. Temperature was maintained at 25 °C by use of a recirculating water bath connected to the jacket of the OBC in which the standards were placed, with temperature monitored directly in the solution by use of a thermocouple connected to a computer.

3.2.4 Microscopy

Crystal images were obtained with a Leica DM6000 FS optical microscope with 2.5x, 5x, 20x and 50x magnification objective lenses.

3.2.5 Particle Sizing

3.2.5.1 Laser Diffraction

Laser diffraction sizing measurements were taken using a Malvern Mastersizer 3000 with Hydro MV dispersant module and Hydro Sight imaging module, shown in Figure 3.3.

Samples were wetted with saturated solution and Tween 20 surfactant to aid dispersion, before being dispersed in saturated solution in the Hydro MV dispersion unit at 2000 rpm. Sample was added until the laser obscuration reached 10%. Six measurements were taken and averaged for each sample, providing a range of sizing statistical information.

Figure 3.3. Malvern Mastersizer 3000 instrument and modules [101].

3.2.5.2 Focused Beam Reflectance Measurement

Focused Beam Reflectance Measurement (FBRM) is a technique used to track particle size and number in real-time. The probe is inserted directly into the crystallisation process, where crystals flow past the probe window. The internal optics and mechanism, along with the measurement technique, are shown in Figure 3.4.

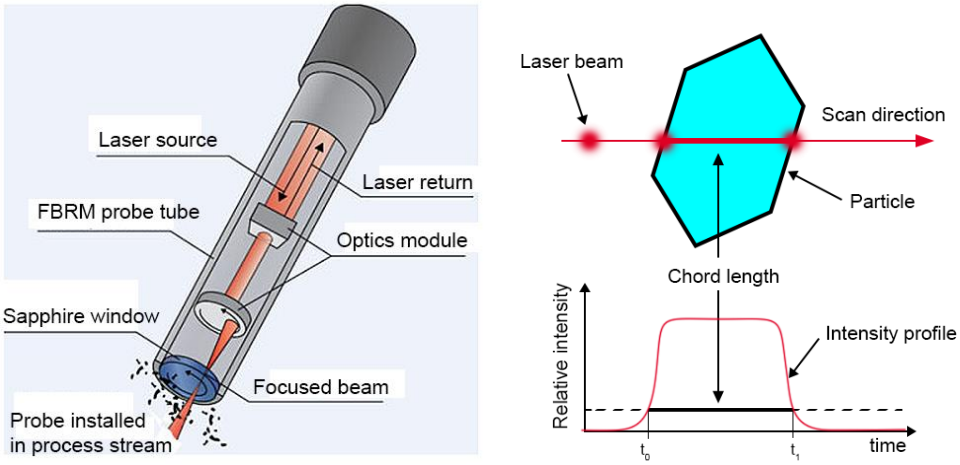

Figure 3.4. Cutaway view of the FBRM probe with illustration of measurement.

A laser is focused onto a sapphire window at the end of the probe. Rotating optics moving at 2 m/s rapidly scans particles as they flow past the face of the sapphire window. As the laser scans, these particles backscatter the laser light to a detector. The duration and number of backscattering events are measured, and the duration multiplied by the scan speed gives the length the laser traces across the particles, referred to as the chord length. Many of these chords are traced each second, which allows for a chord length distribution (CLD) to be reported in real time. In this work, FBRM was used to monitor process startup, from either seeded processes or to detect nucleation, and to determine steady-state operation. For processes operating with similar conditions, this allowed for direct comparison between CLDs to give an indication of process performance.

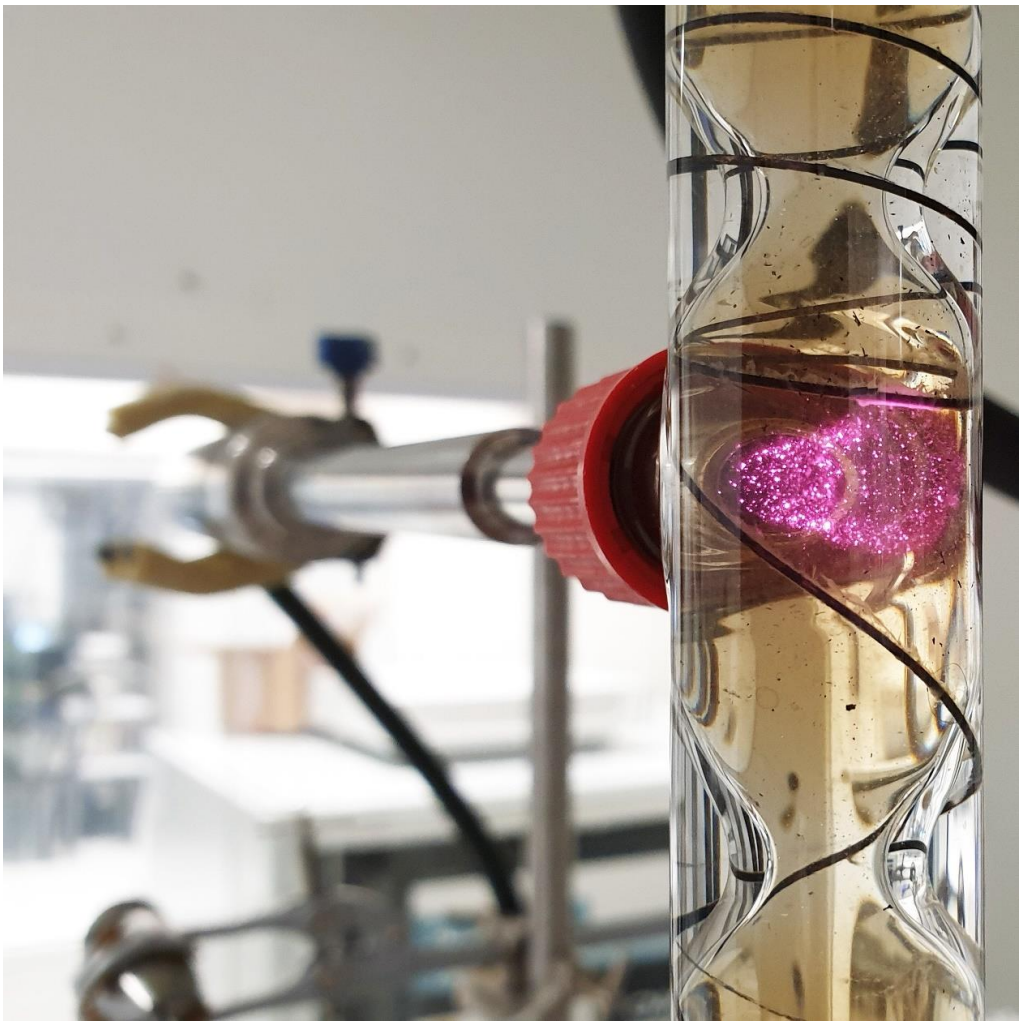

Figure 3.5. FBRM laser reflecting off particles in an OBC. The laser operates at 785 nm, which is invisible to the naked eye.

3.2.6 Sieving

Sieving is a technique used to break loose aggregates and produce seed material within a desired size distribution depending on the mesh sizes used. Seed material was prepared by the sieving of raw material from the chemical supplier. A sieve nest was assembled from test sieves consisting of 63, 125, 250 and 500 μm mesh sizes to give a range of size fractions. The sieves were arranged from smallest mesh size at the bottom to the largest mesh at the top, with a receiving cup at the base for any material less than 63 μm to be collected. The raw material was placed in the uppermost sieve, and a suitable vibration amplitude and duration were selected to prepare the sieve fractions.

Figure 3.6. Fritsch Analysette 3 Pro sieve shaker

3.2.7 Data Presentation and Analysis

All graphs presented in this thesis were produced from the raw data obtained from their respective instruments and processed using Microsoft Excel and Origin. XRPD patterns were analysed using DIFFRAC.EVA and Topas software. First-order derivatives of UV-vis spectra were calculated using Aspect Plus software.

4 Developing Antisolvent Crystallisations in a COBC

4.1 Introduction

The COBC has been studied extensively for application in cooling crystallisation [86],[89],[88]. Their good heat transfer capabilities, plug-flow characteristics and potential for long residence times are all desirable properties for controlling crystal growth. However, attempts at controlled primary nucleation within a COBC have been fraught with difficulties. To achieve primary nucleation, relatively high supersaturations are typically required, which in the case of a cooling crystallisation requires a large step change in temperature. As the heat exchange surface is the wall of the COBC, this can lead to encrustation. The build-up of crystalline material on the walls can impair heat transfer and occlude the vessel completely, necessitating the shutdown of the system entirely.

To alleviate such problems, seed crystals can be introduced to the system, providing surface area to consume supersaturation by growth on these seeds. The preparation of seed material in itself can be very involved and require many steps such as milling, sieving and washing [102]. There can also be issues with transferring seed material to the crystalliser such as blockage of the seed line. However, a process with controlled continuous nucleation would remove the necessity for separate seed production and resulting in a more elegant process overall.

Antisolvent crystallisations generate supersaturation by modifying solvent composition rather than temperature [103]. Typically, a saturated or near-saturated solution of a compound with a high solubility in a particular solvent is mixed with another solvent in which the compound is poorly soluble or insoluble. The solute has a lower solubility in this mixed solvent system. Upon mixing of solution and antisolvent, supersaturation is generated that depending on the level can result in rapid nucleation [80].

The degree of supersaturation, usually referred to as supersaturation ratio, can be controlled by various methods for antisolvent crystallisation. Commonly, this is achieved by adjusting the amount of antisolvent relative to the solution; however, the initial concentration of solute in solution can also be used to manipulate the supersaturation ratio. Certain systems will also possess a temperature dependence on solubility, allowing for combined antisolvent and cooling crystallisation for good

control over supersaturation and yield. These factors necessitate a significant amount of preliminary work to be performed in investigating suitable solvent systems and solubility screening before crystallisation can even be attempted. A thorough solvent screen can be complex and may be based on several factors, the details of which go beyond the scope of this thesis; however, well-miscible solvents with a large difference in solubility of the solute, low toxicity and low cost are usually the main considerations [104].

The residence time in a COBC is dependent on the length of the device and the total flow rate. Due to the modular nature of the platform, the length can be modified by the addition or removal of baffled sections. For cooling crystallisations, the residence time is constant across the entire length, determined by the total flow rate. During an antisolvent crystallisation, addition of antisolvent or solution leads to an increase in the total flow rate, and thus the residence time decreases. The platform could consist of multiple addition points, which would result in a cumulative increase in total flow rate after each antisolvent addition. Multiple additions would allow for greater control over supersaturation along the length of the COBC, similar to the principles of multiple small step changes in temperature for a cooling crystallisation versus fewer large steps. The ideal positions of these addition points and amount of solvent delivered would be dependent on the nucleation and growth kinetics of the system. Careful adjustment of supersaturation would be required to prevent multiple nucleation events, which would result in multi-modal particle size distributions, and to minimise detrimental effects on crystal habit, polymorphism or agglomeration for example.

The potential effect of a multi-addition process can be determined by using a single addition point and varying the conditions over multiple experiments. This chapter investigates the practical suitability of the COBC platform for unseeded antisolvent crystallisation of anthranilic acid. A DN15 COBC was constructed with an inlet for antisolvent and an inlet for feed solution. The solubility of the model compound anthranilic acid in an ethanol and water solvent system was determined. Antisolvent volume fraction, and thus the supersaturation ratio, was modified by adjusting the relative volume of antisolvent to feed solution. The residence time was controlled by adjusting the total flow rate. The temperature and oscillation frequency and amplitude were fixed for consistency to investigate effects produced by the other process variables.

4.1.1 Anthranilic Acid

Anthranilic acid (2-aminobenzoic acid, *o*-aminobenzoic acid), the chemical structure of which is shown in Figure 4.1, is used as a precursor in the synthesis of a variety of compounds, such as azo dyes, perfumes, and loop diuretics such as furosemide.

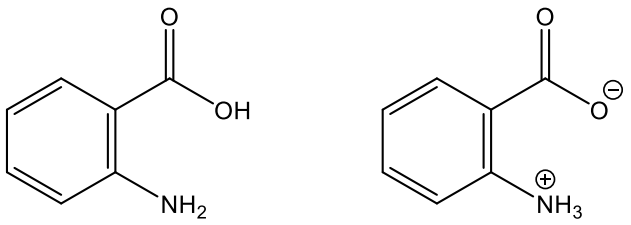

Figure 4.1. Structure of anthranilic acid showing the neutral (left) and zwitterionic (right) species.

Anthranilic acid has been well studied in batch antisolvent crystallisation from ethanol and water. Control over its polymorphism and differences in crystal morphology have been observed by varying the antisolvent volume fractions [24], [105]. The compound is known to crystallise into three polymorphs. Form I is thermodynamically stable at 25 °C and is enantiotropically related to forms II and III, which are both monotropically related [105]. Crystals and solutions of anthranilic acid are coloured and range from pale tan to brown, with some example crystals shown in Figure 4.2. Their XRPD patterns and crystal structures are shown in Figure 4.3 and Figure 4.4. Due to the existing body of work done with this compound and particular solvent system, and the relative safety and low cost of the materials, it was deemed a good candidate for continuous antisolvent crystallisation studies.

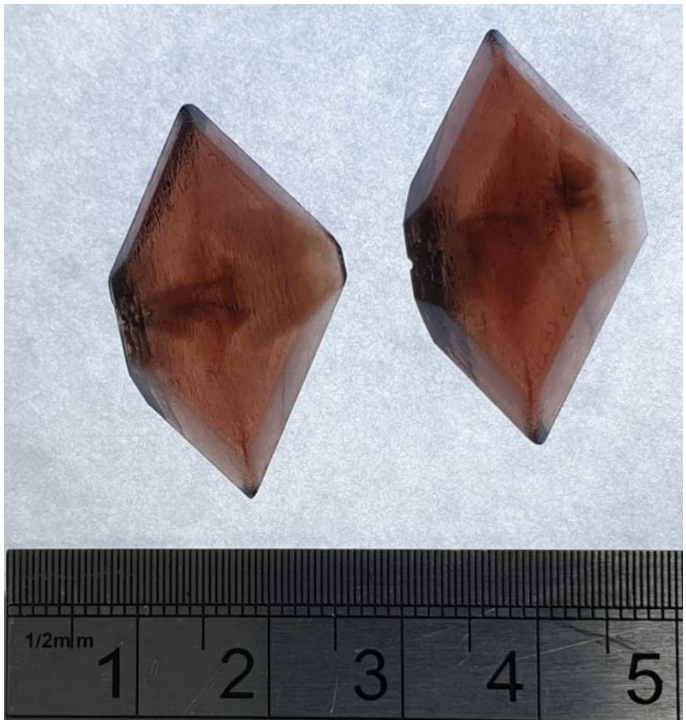

Figure 4.2. Large single crystals of anthranilic acid.

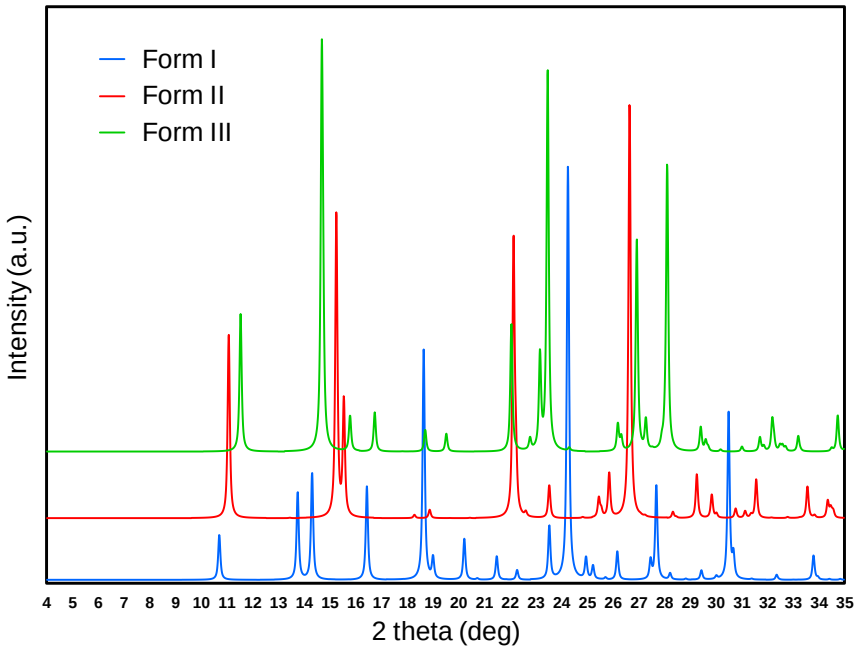

Figure 4.3. Simulated XRPD patterns from single-crystal data obtained from the Cambridge Structural Database [106] for form I (AMBACO01), II (AMBACO03) and III (AMBACO06).

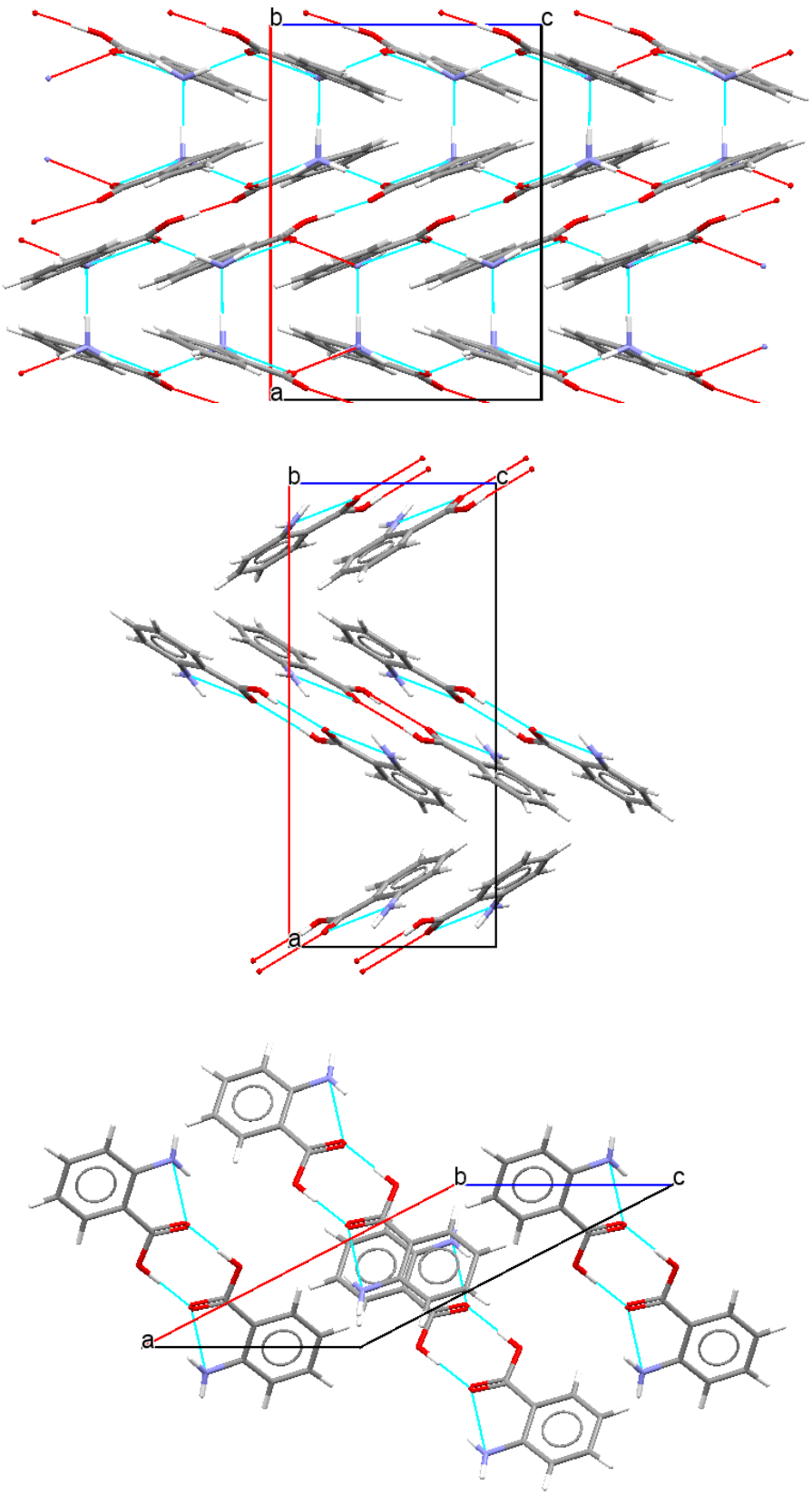

Figure 4.4. Crystal structures showing packing and hydrogen bonding for orthorhombic form I (top), orthorhombic form II (middle) and monoclinic form III (bottom) polymorphs of anthranilic acid.

4.2 Experimental

4.2.1 Isolation and Solubility of Anthranilic Acid Form I

The anthranilic acid raw material obtained from Acros Organics was determined to be a mixture of form II and III by XRPD. It was therefore necessary to prepare and isolate form I. This allowed solubility measurements to confirm those measured by Jiang et al. [24]. An excess of raw material was stirred in ethanol at 25 °C for one hour. The resulting solution was filtered over a 0.22 μm filter into a separate flask to ensure no undissolved material or solid impurities were carried over. The addition of the antisolvent (water) to give an antisolvent volume fraction, φ, of 0.7 yielded crystals within approximately 10 seconds. A sample of the solid was isolated and determined to be a mixture of forms II and III by XRPD. The suspension was stirred for 24 hours at ambient temperature, after which the remaining solid was filtered and dried, and shown to have transformed to form I by XRPD.

The solubility of form I was determined by the addition of an excess of this recrystallized material to 20 ml of varying ethanol/water mixtures, ranging from $\varphi = 0$ to $\varphi = 1$. The suspensions were stirred on a multi-position stirrer plate at 25 °C over three days, after which four samples of solutions from each water fraction were filtered over a 0.22 μm filter, weighed, and evaporated to dryness. The solubility was determined from the mass of the evaporated solvent and that of the remaining dry crystalline material.

The solubility was also measured using the Crystal16 platform. Vials were prepared with varying masses of anthranilic acid to cover a range of temperatures at which the solutions would become clear. To these were added 1 ml of ethanol/water mixtures ranging from $\varphi = 0$ to $\varphi = 1$. A temperature profile was set through the software interface to cycle the temperature as described in section 3.2.1.1. A laser measured the turbidity of the solution and was used to determine the solubility based on when the transmissivity reached 100%, i.e. a clear solution.

4.2.2 COBC Platform for Continuous Antisolvent Crystallisation

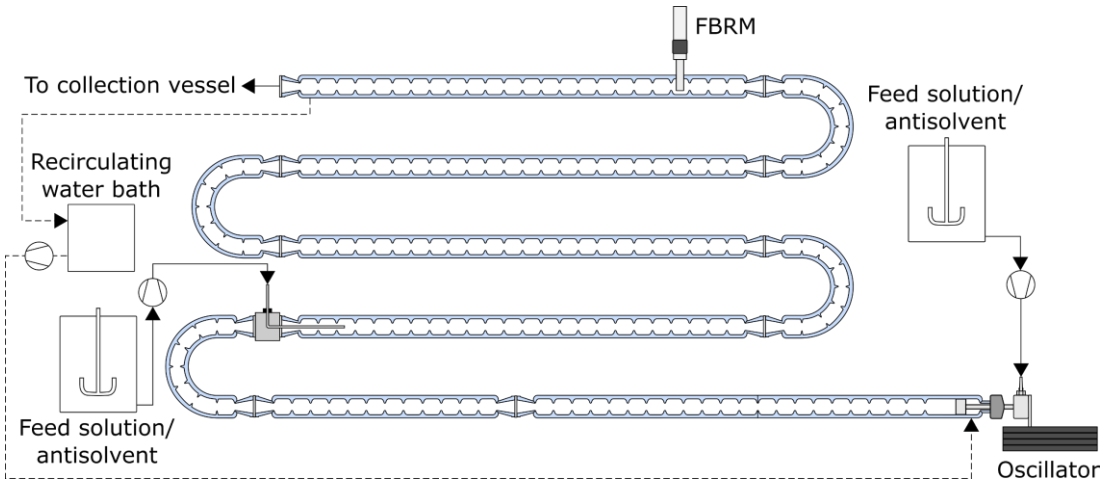

Figure 4.5. Schematic of the COBC setup for antisolvent crystallisation.

The crystallization platform was a DN15 NiTech COBC, shown in Figure 4.5. This consisted of jacketed glass straights and bends of 15 mm internal diameter, with integrated glass baffles and interconnecting polytetrafluoroethylene (PTFE) baffle caps between the joints to maintain the baffle geometry across connecting sections. The internal geometry of the COBC is shown in detail in Figure 4.6.

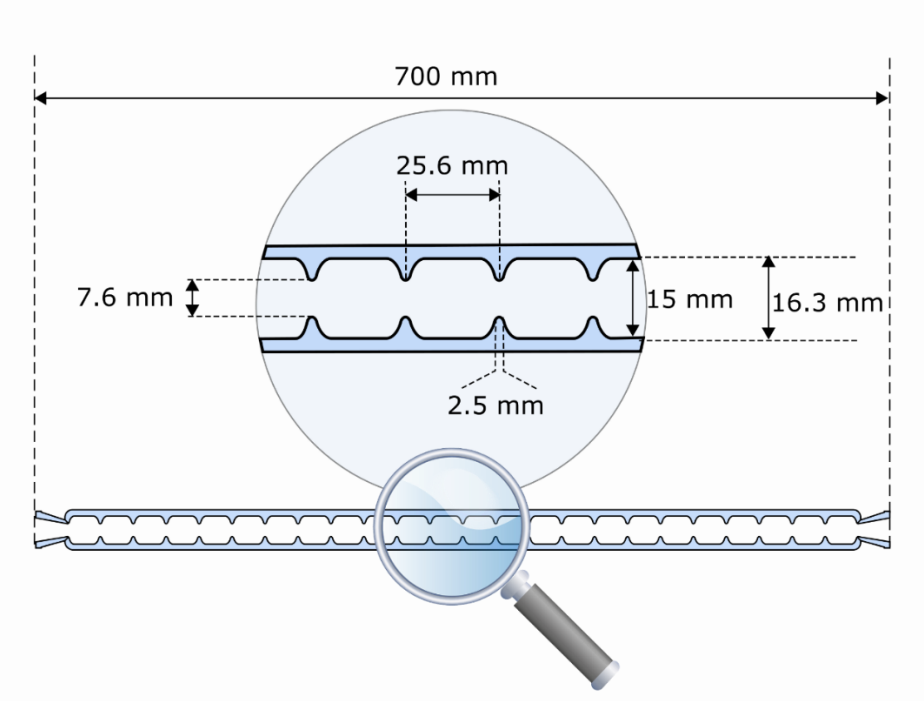

Figure 4.6. Internal geometry of the COBC.

Oscillations were provided by a polyether ether ketone (PEEK) piston, driven by linear motor at a frequency of 3 Hz and a centre-to-peak amplitude of 10 mm. These oscillatory conditions were selected such that particles were visibly well suspended and based on recommendation from other researchers with previous experience operating the apparatus. The COBC was pre-filled with either feed solution or antisolvent (water) depending on the mode of addition employed to remove any air in the system. The total volume of the COBC was approximately 830 ml, with the volume from the mixing location to the outlet approximately 600 ml. The temperature was maintained at 25 °C by a circulating water bath (Lauda ECO RE 620 G) connected to the integrated jacket of the glass sections.

A saturated solution of anthranilic acid in ethanol at 25 °C was used as the feed solution, which was prepared from recrystallized Form I material and held in a 5-litre jacketed stirred tank. Deionised water as antisolvent was held separately in a 5-litre jacketed stirred tank. These were fed into the COBC via peristaltic pumps (520 Du, Watson-Marlow) connected with Marprene thermoplastic elastomer tubing (3.2 mm internal diameter, 2.4 mm wall thickness). Four antisolvent volume fractions (φ) and varying flow rates were selected to cover a range of supersaturations and residence times, summarised in Table 4.1. Two modes of addition were investigated, herein referred to as "normal addition", where the feed solution is fed into the first inlet of the COBC by the oscillator and antisolvent via the second; and "reverse addition", where the positions are switched.

Table 4.1: Antisolvent volume fraction (φ), supersaturation ratio with respect to form I of anthranilic acid (S_I), and total flow rates for antisolvent crystallisation in the COBC.

φ	S_I	Total flow rate (ml/min)
0.4	1.2	100
0.5	1.5	100
0.6	2.2	25, 50, 100
0.8	4.1	50, 100

The startup and time to steady state of the process were determined using an in-line FBRM probe (ParticleTrack G400, Mettler Toledo). Solid samples were taken when the FBRM total counts were observed to plateau. These were filtered over a Büchner

funnel, washed with 25% ethanol (v/v), and dried over 24 hours at 40 °C. The concentration of the solution was determined gravimetrically by taking samples of filtered mother liquor at various time intervals.

4.2.3 Removal of Impurities from Raw Material

Initial experiments employed solutions prepared from the raw material directly. However, these solutions were cloudy even when undersaturated with respect to the anthranilic acid, and it became apparent that there was an insoluble component present. A sample of this impurity was isolated and analysed by XRPD, the results of which are shown in Figure 4.7.

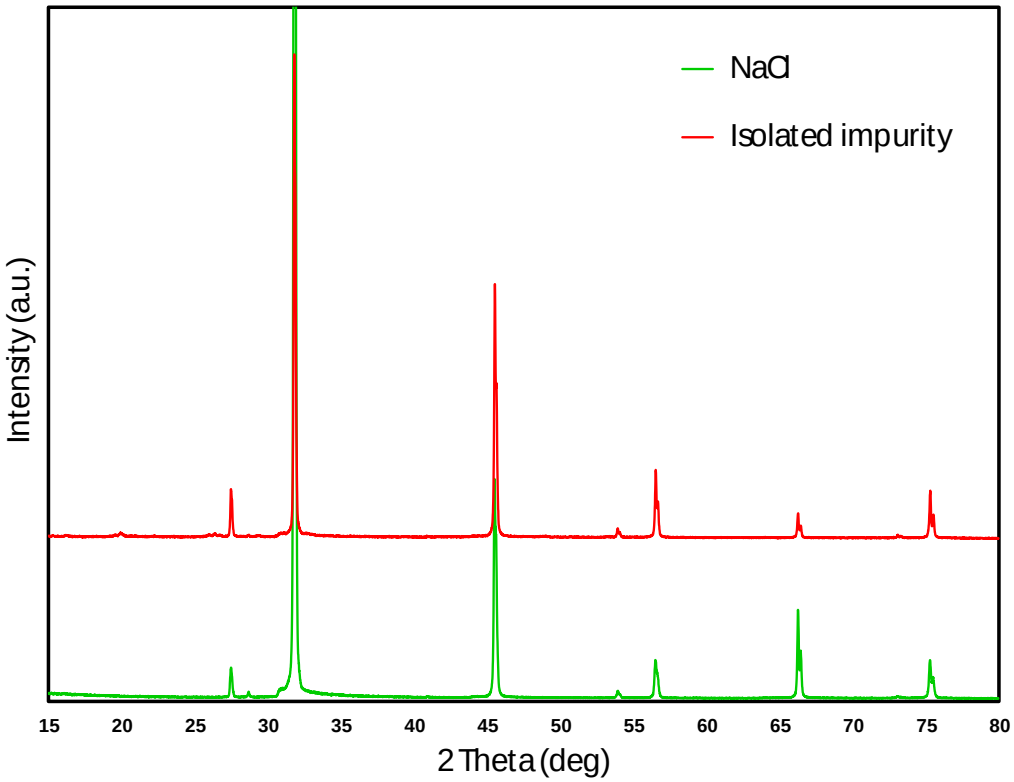

Figure 4.7. XRPD pattern for a known sample of NaCl and isolated impurity.

The first scan of this material was performed between 4 – 35 ° 2θ, which did not produce many peaks. This suggested the material may be inorganic, and a wider angle scan was performed up to 80 ° 2θ. Investigation into potential routes of industrial synthesis gave sodium chloride as a by-product. A sample of this was also analysed by XRPD, which matched the isolated impurity.

For experiments conducted by the normal addition mode, the solution containing these impurities was used for the crystallisation process. After concerns that these impurities may influence the crystallisation behaviour, it was decided to remove them. Attempts at filtration of these solutions using a Büchner funnel and typical filter papers proved challenging, as the papers would rapidly become clogged. Microscopy of the isolated impurities showed very fine particles, seen in Figure 4.8.

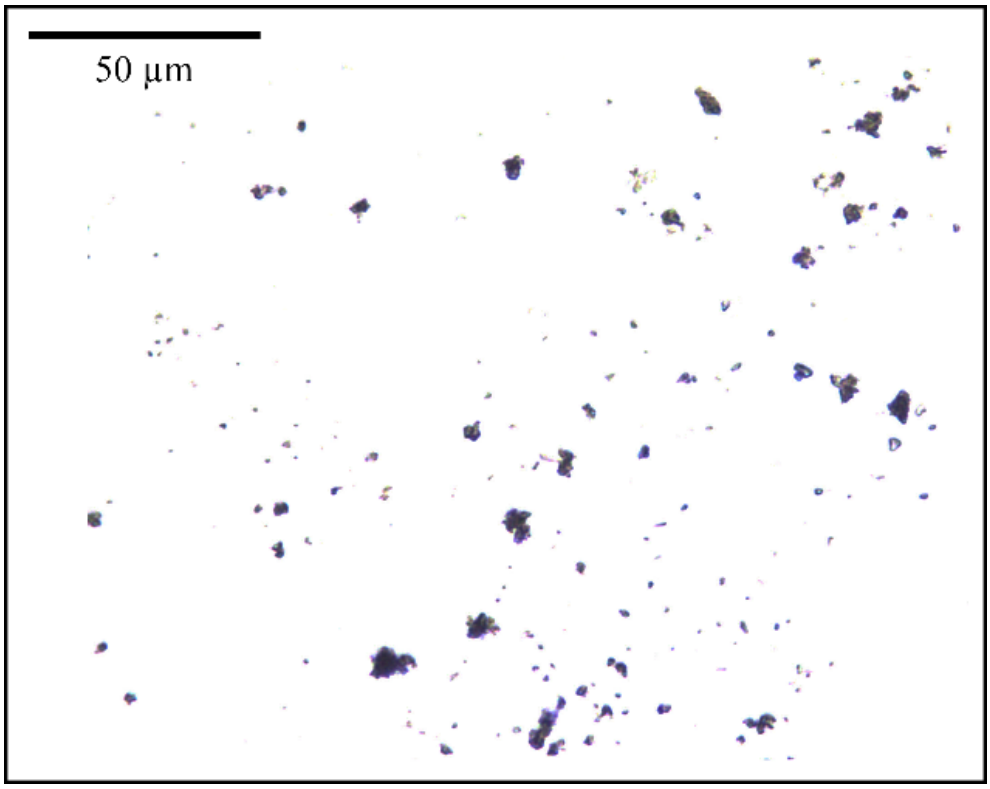

Figure 4.8. Isolated insoluble components from the anthranilic acid raw material.

A simple antisolvent crystallisation method was devised to recrystallise the material. A saturated solution was prepared in ethanol, to which a large volume of water antisolvent was added. This rapidly crystallised the anthranilic acid from solution. As the impurity had been determined to be sodium chloride, this excess of water served to dissolve these. The recrystallised material was dried thoroughly, and solutions prepared from it were clear.

4.3 Results and Discussion

4.3.1 Phase Diagram

The solubility data obtained by Crystal16 is shown in Figure 4.9, which covers the range of solvent compositions that were to be used experimentally. The majority of the data points appear consistent; however, this data was ultimately not used for generating the phase diagram. As described previously, the Crystal16 uses temperature cycling in conjunction with a turbidity measurement to determine at which temperature all material dissolves. This is dependent on the concentration prepared in each vial. The temperature profile that was used had an initial fast ramp to a high temperature to dissolve all material, followed by slow cooling to crystallise material and subsequently slow heating to measure the clear point. This method brings about uncertainty, as it is unknown as to which polymorph has crystallised in the vial, and so the clear point being measured could be that of a metastable form, the stable form, or a mixture. The gravimetric solubility measurements do not have this uncertainty, as the stable polymorph is present in excess.

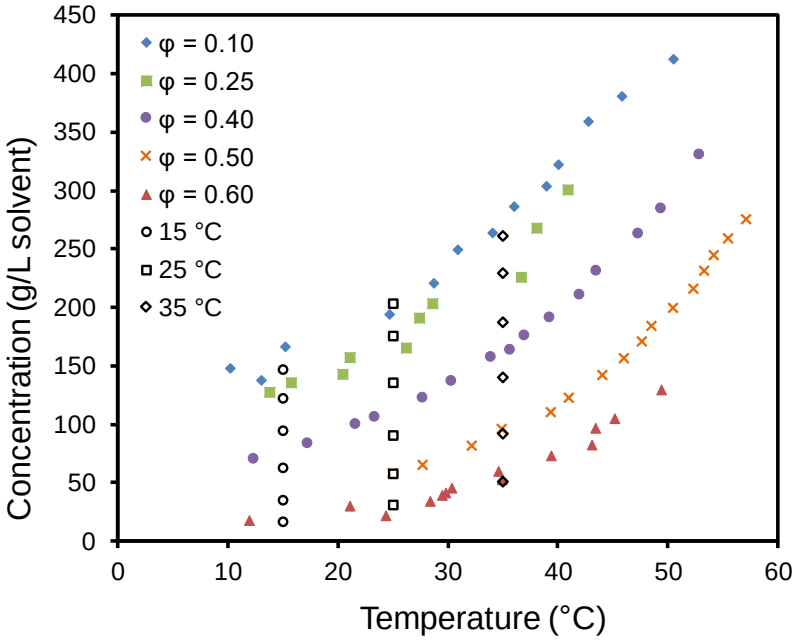

Figure 4.9. Crystal16 and gravimetric solubility measurements of anthranilic acid in an ethanol/water solvent system, covering a range of antisolvent (water) volume fractions (φ) and temperatures. Open markers represent gravimetric measurements at φ = 0.6 – 0.1.

Comparing the Crystal16 and the gravimetric data, there is good agreement at most antisolvent fractions with the exception of φ = 0.40, for which the Crystal16 measurements report a greater solubility than the gravimetric measurements. At this particular antisolvent fraction and under the conditions employed, it may be that a metastable polymorph is more prone to nucleate. Metastable zone width information could have been determined from the Crystal16; however, as it is a kinetic property and the Crystal16 is a vastly different system than the COBC, it was not reported.

The gravimetrically measured solubility of form I is shown in Figure 4.10 as blue diamonds and the blue curve c^*_I. The solubility of form II was not measured directly due to a reported rapid solvent-mediated transformation, which would not be suited to gravimetric measurement. It is instead approximated from the form I data based on a factor of 1.2 × the solubility of form I according to data reported by Jiang et al. [24]. This is represented by the red curve c^*_{II}.

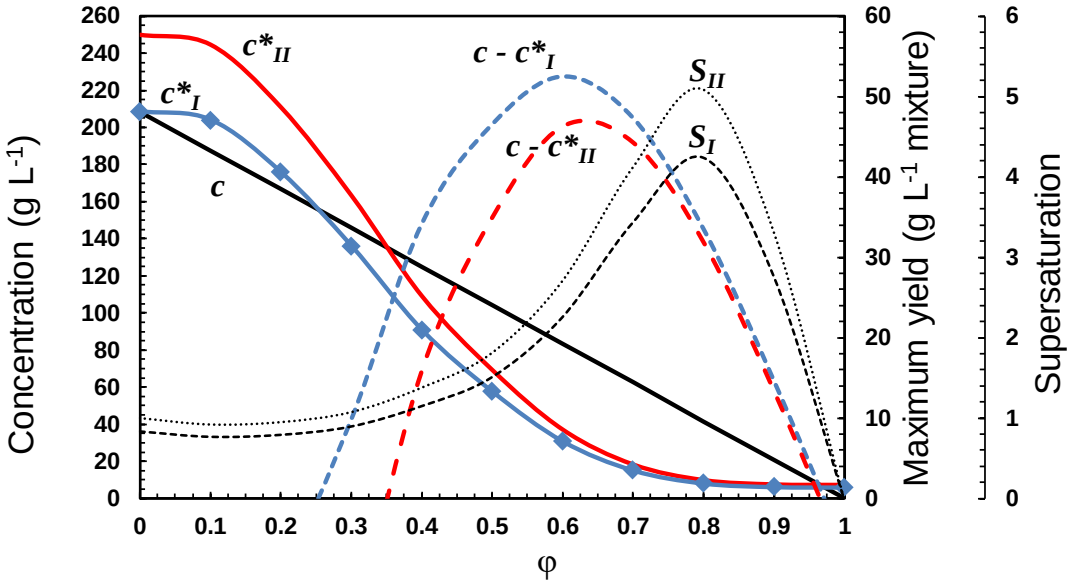

Figure 4.10. Solubility (c^*), dilution line (c), maximum yield ($c - c^*$) and supersaturation of anthranilic acid form I and II at 25 °C as a function of antisolvent (water) volume fraction (φ) in an ethanol/water solvent system.

The overall shape of the solubility curves c^* shows three phases: the initial phase, where at low water volume fractions there is little difference in overall solubility; a mid-phase where slight changes in water volume fraction give a significant reduction in solubility;

and a final region where large changes in water volume fraction give a negligible reduction in solubility.

Antisolvent crystallisations must achieve a compromise between reduced solubility in the mixed solvent versus the dilution of the system by the increase in volume. This is represented by the black dilution line *c*, which shows that the dilution effect is significant until $\varphi \approx 0.25$ for form I, after which the reduction of solubility becomes more significant. This remains the case until very high antisolvent volume fractions. As the continuous antisolvent experiments described were operated with only one antisolvent addition, it is also important to consider the yield of the process, shown by the dashed blue line $c - c^{\star}_{I}$ and dashed red line $c - c^{\star}_{II}$. The maximum obtainable yield in this system, in terms of mass of crystalline material per unit volume, is near $\varphi = 0.6$, and was selected for further investigation.

4.3.2 Modes of Addition of Antisolvent and Feed Solution

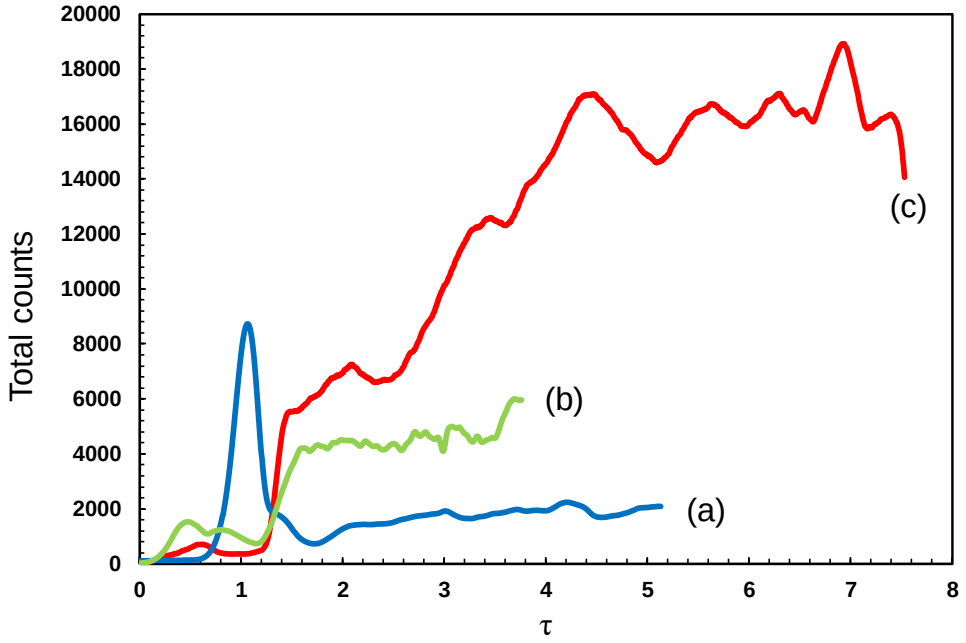

Figure 4.11. FBRM total counts as a function of number of residence times for varying total flow rates and antisolvent volume fractions. (a) $\varphi = 0.4$, 100 ml/min; (b) $\varphi = 0.4$, 50 ml/min; (c) $\varphi = 0.5$, 100 ml/min

As was stated in 4.2.3, the normal addition method was conducted using solutions prepared from the raw material directly. In these cases, the COBC was filled with feed solution well past the antisolvent inlet to ensure that when antisolvent delivery was

initiated there would be contact between feed solution and antisolvent at time zero, and the hydrodynamic environment should be consistent. The NaCl impurity in the solution feed was detected by the FBRM as a spike in total counts. This can be seen in Figure 4.11, where condition (a) shows a large increase in total counts, and a more significant spike than (b) or (c). The difference in these spikes is attributable to differences in the amount of feed solution that was pre-filled past the point of delivery of antisolvent, with a greater volume of feed solution pre-fill in (a), and a lower volume in (b) and (c).

The reduction in total counts after these spikes can be explained by two processes. One is that the addition of antisolvent dilutes the total number of these impurities per unit volume, which reduces the total counts observed. The other is that the addition of antisolvent dissolves the NaCl impurities. The impurity particles are typically < 10 μm in size, as seen from the scale bar in Figure 4.8, which would lend itself to rapid dissolution. The presence of these impurities may have an effect on the crystallisation behaviour, acting as sites for heterogeneous nucleation, and could alter crystal properties [107]. This is not to say the impurities have a detrimental effect on the process. From a purification perspective, the dissolution of impurities whilst simultaneously crystallising the target compound is desirable. However, such investigations were beyond the remit of this chapter.

Based on the FBRM total counts, (a) and (b) appeared to reach some sort of steady state after two residence times and fluctuated around mean values of 2000 and 4000, respectively. Condition (c) did not appear to reach a steady state, with significant fluctuation in total counts for the duration of the experiment. Both (b) and (c) had similar increases in total counts at approximately 1.2 τ. There may have been a similar occurrence for (a); however, the large spike in total counts from the NaCl impurity masked this.

There was localised fouling at the point of mixing of feed solution and antisolvent noted for each experiment. This in combination with the fluctuating results for (c) and the NaCl impurity prompted some adaptation of the setup. The feed solution and antisolvent addition ports were switched such that mixing would occur under a reverse addition method. To account for this change, the COBC was prefilled with antisolvent instead of feed solution. Anthranilic acid feed solutions were prepared with the NaCl

removed as described in 4.2.3. The following sections describe experiments conducted using the reverse addition method.

4.3.3 Effect of Total Flow Rate

Three different total flow rates were investigated at $\varphi = 0.6$. Their effect on the process startup and steady state is shown in Figure 4.12 and Figure 4.13. The end points of the traces are where the experiment was terminated either due to blockage from encrustation, and/or observation of insufficient particle suspension for continuation of the process. The FBRM traces show a rapid startup phase, reaching a plateau in the order of one residence time. The total counts are shown to increase as a function of increasing flow rate. This was accompanied by a reduction in the mean chord length, as shown in Figure 4.13. The mean chord length measurements all go through a maximum before settling to a steady value, suggesting that the environment during startup promotes a low number of relatively large crystals, before then moving to a steady state condition. If one considers the environment during startup, the feed solution encounters a large volume of antisolvent due to the pre-filling of the COBC, generating very high supersaturations and promoting rapid nucleation.

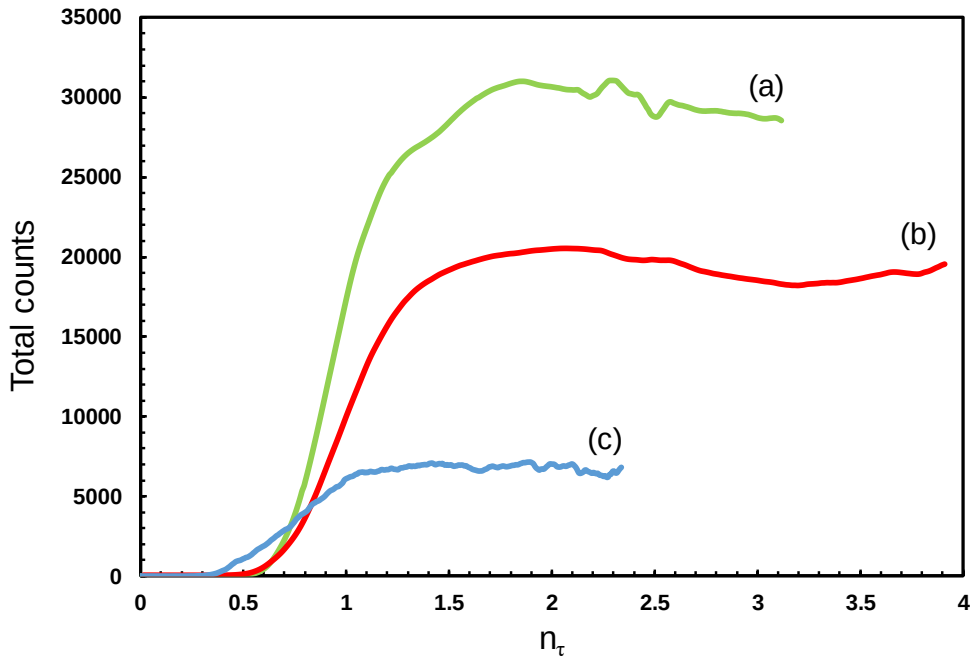

Figure 4.12. FBRM total counts as a function of number of residence times for varying total flow rates, $\varphi = 0.6$. (a) 100 ml/min; (b) 50 ml/min; (c) 25 ml/min

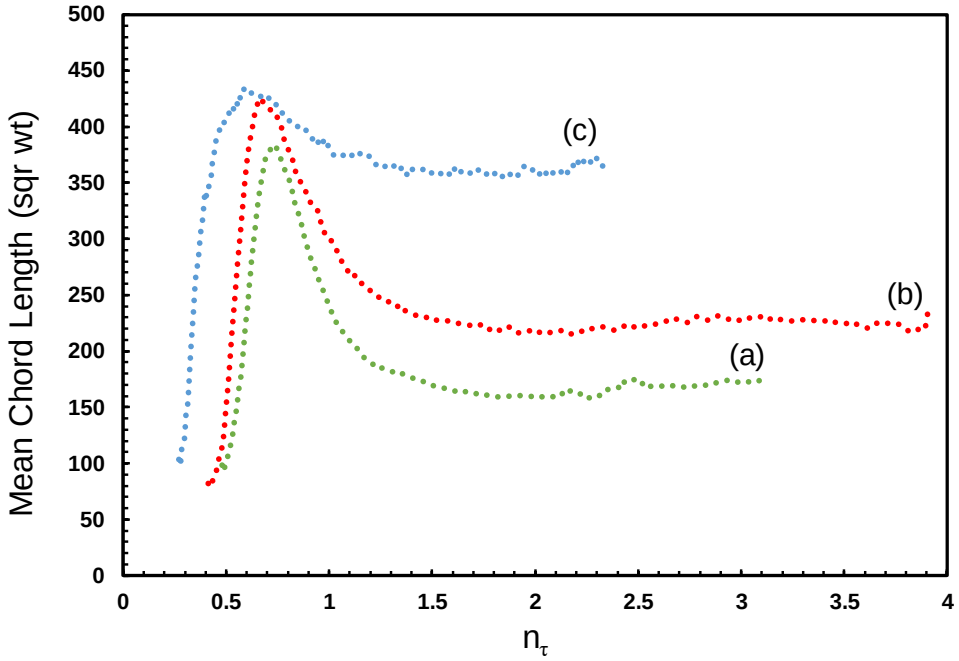

Figure 4.13. FBRM mean chord length (square-weighted) as a function of number of residence times for varying total flow rates, $\varphi = 0.6$. (a) 100 ml/min; (b) 50 ml/min; (c) 25 ml/min

The concentration of the mother liquor at the outlet sampled at steady FBRM total counts did not vary significantly between the three flow rates, at an average of 24.3 g/l. An equivalent mass of anthranilic acid had therefore crystallized in each condition investigated. There is a difference in residence time from the point of mixing to the FBRM versus point of mixing to the COBC outlet, which can be seen in the schematic in Figure 4.5, but this is relatively small at approximately 0.15 τ based on the lengths, and not expected to be significant. The measured concentration was lower than expected based on the solubility at $\varphi = 0.6$. Samples of the solid phase taken at steady state according to FBRM total counts were analysed by XRPD, shown in Figure 4.14. These patterns show only metastable form II had been produced at $\varphi = 0.6$ across three different flow rates. According to the phase diagram, the remaining solute concentration would be higher due to the increased solubility of form II compared to form I. This would require an increase from $\varphi = 0.6$ to $\varphi = 0.65$ to account for this difference. As the concentrations were roughly equal for the various total flow rates, this discrepancy appears to be systematic in nature.

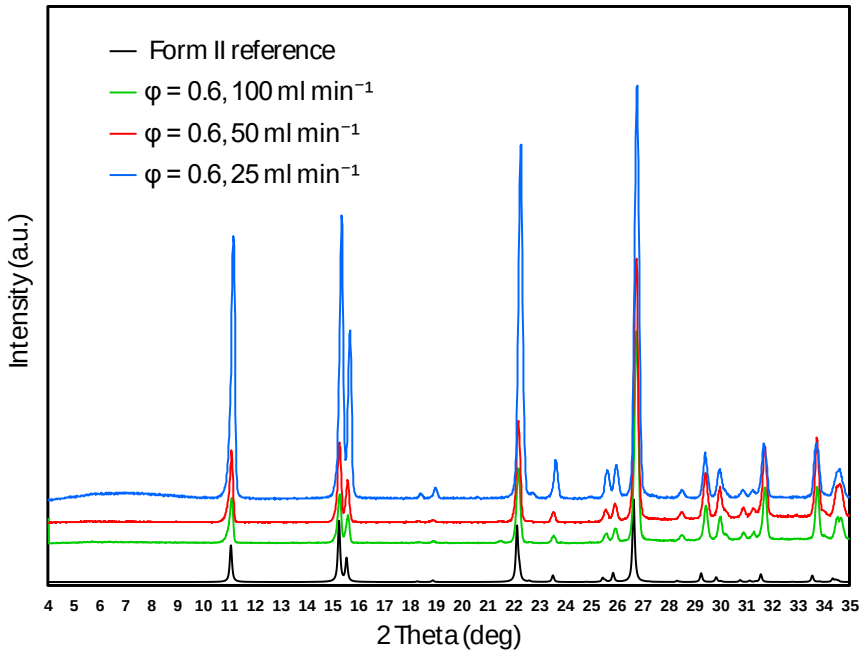

Figure 4.14. XRPD patterns for samples of anthranilic acid taken at steady state.

A rapid solvent-mediated transformation was reported for this system at comparable antisolvent fractions by Jiang et al. [24], with the first detection of form I at 8 minutes, and a complete transformation of form II to form I in 32 minutes at 25 °C and φ = 0.7. At higher flow rates, it may be that there is insufficient residence time for such a transformation to be observed, which may be the case for residence times of 6 and 12 minutes at flow rates of 100 and 50 ml/min. However, it would be expected that for the lowest flow rate of 25 ml/min, where the mean residence time is 24 minutes, at least some discernible amount of form I would have formed via solvent-mediated transformation.

The first particles detected by the FBRM at 25 ml/min arrived sooner than the other flow rates when plotted as a function of the number of residence times. In addition, particles were observed earlier than the expected residence time for all experiments, even if instantaneous nucleation were to occur at the point of mixing. This suggests the solid particles do not experience the same residence time as the liquid components, which has been demonstrated in a DN15 system [108]. Centre-to-peak amplitudes of 10 mm, as used in these experiments, are higher than the suggested optimum of approximately 2 mm, which would result in a large degree of axial dispersion for solids and would be more pronounced at lower net flow rates. The optimum operating

frequency and amplitude to minimise liquid axial dispersion is unlikely to be the same as the optimum for minimising solids dispersion. There will exist a set of conditions whereby the total dispersion of both liquid and solid components combined are at a minimum. Furthermore, the design of the inlets and the antisolvent fractions used will affect the velocity of flow from these locations. A narrow bore inlet tube will result in a high velocity stream that may further affect the disparity between axial dispersion coefficients for solid and liquid components. These conditions would require further targeted experiments to determine their effect.

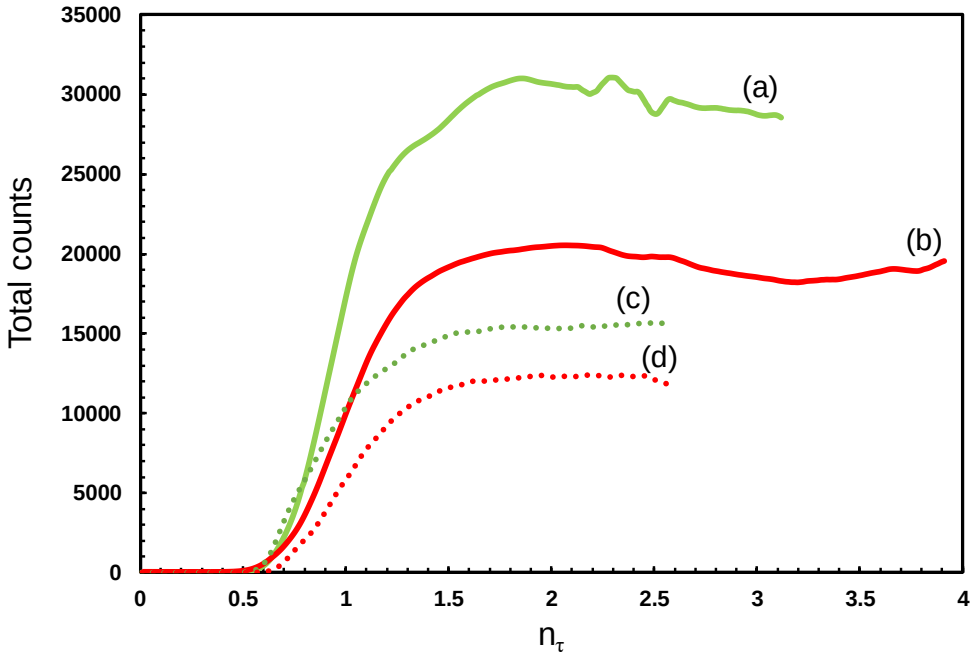

Figure 4.15: FBRM total counts as a function of number of residence times for (a) φ = 0.6, 100 ml/min; (b) φ = 0.8, 100 ml/min; (c) φ = 0.6, 50 ml/min; (d) φ = 0.8, 50 ml/min.

The trend of decreasing FBRM total counts with decreasing flow rate was also observed at φ = 0.8, as shown in Figure 4.15. The total counts for both flow rates at this higher antisolvent fraction were lower, which is expected based on the lower mass of crystals per unit volume that can be achieved at these conditions. The duration for which this process could be operated before critical fouling at the mixing point did not significantly change as a function of flow rate, in contrast to experiments at φ = 0.6, suggesting that the high supersaturation at φ = 0.8 was limiting.

An increase in particle size with an increase in mixing intensity has been reported in other systems. In the static mixer setup investigated by Alvarez and Myerson, mixing intensity is dependent on flow rate, and larger crystal sizes were observed as flow rate increased [9]. For the COBC setup investigated by Brown et al., increasing Re_O increased the mean particle size [94]. These suggest more intense mixing leads to larger crystal sizes, either due to improved suspension of large crystals that would otherwise settle in the crystalliser, or a more fundamental mechanism such as improved mass transfer. An increase in crystal size would have to be coupled with a decrease in the number of crystals if the mass of material crystallising remains constant, which can be deduced from the decrease in FBRM total counts (Figure 4.12) and increase in mean chord length (Figure 4.13) as total flow rate increases. The velocity of the inlet stream at the point of contact between solution and antisolvent therefore plays a significant role in the mixing in this system, with an apparent increase in mixing intensity with increased flow rate.

4.3.4 Effect of Antisolvent Fraction

The effect of varying antisolvent fractions at a fixed total flow rate on the FBRM total counts is shown in Figure 4.16. The lowest employed antisolvent fraction $\varphi = 0.4$ gave the lowest FBRM total counts value, which increased for $\varphi = 0.5$ and reached a maximum for $\varphi = 0.6$, before decreasing again for $\varphi = 0.8$.

All conditions were prone to fouling that ultimately required shutdown of the process, the extent of which appeared to correlate with the antisolvent fraction employed. This fouling was localised at the point of mixing of feed solution and antisolvent. Higher antisolvent fractions reduced the amount of time for the COBC to be completely occluded and/or sufficient liberated gas to accumulate to prevent adequate mixing and particle suspension, requiring shutdown. Considerable gas generation was observed, which can affect particle suspension. Increased antisolvent fractions may also result in a greater amount of gas liberation due to decreased gas solubility in the solvent mixture, which is described in more detail later in this chapter. It is likely a combination of these effects that result in the reduced duration of operation at higher antisolvent fractions.

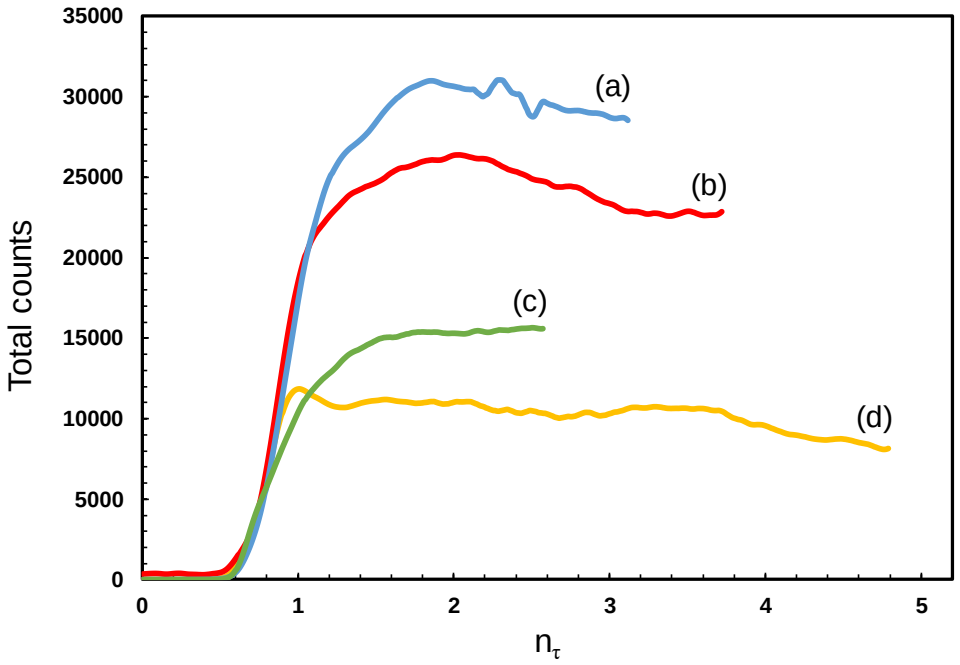

Figure 4.16. Total counts as a function of number of residence times for varying antisolvent fractions. (a) φ = 0.6; (b) φ = 0.5; (c) φ = 0.8; (d) φ = 0.4. Total flow rate = 100 ml/min.

The effect of antisolvent fraction on the mean chord length is shown in Table 4.2. The shortest chord length is found at φ = 0.6, where the total counts are greatest. There is a similar mean chord length for φ = 0.5, which combined with the lower total counts at this antisolvent fraction, agrees with the lower maximum yield per unit volume achievable at this antisolvent fraction.

Table 4.2. The median value of the mean chord length (square-weighted) for varying antisolvent fractions and corresponding S_{II}, 100 ml/min total flow rate.

φ	S_{II}	Mean Chord Length (square weighted) (μm)
0.4	1.0	229
0.5	1.3	186
0.6	1.8	175
0.8	3.4	265

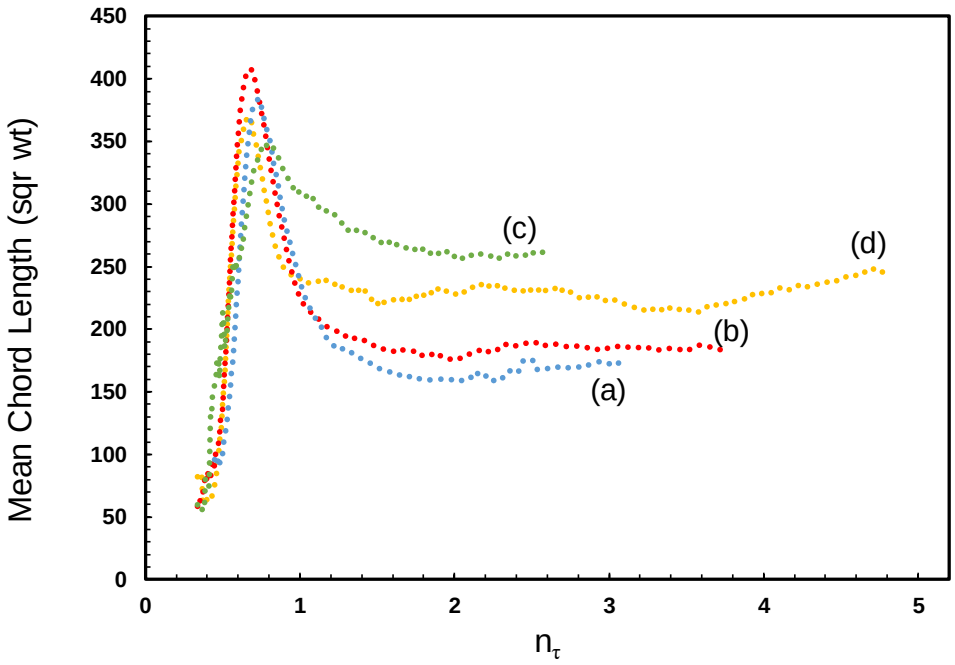

Figure 4.17. Mean chord length (square-weighted) as a function of number of residence times for varying antisolvent fractions. (a) $\varphi = 0.6$; (b) $\varphi = 0.5$; (c) $\varphi = 0.8$; (d) $\varphi = 0.4$. Total flow rate = 100 ml/min.

The crystalline material sampled during stable FBRM total counts for all samples was determined to be form II by XRPD. Of particular interest is the rapid startup and steady state achieved at $\varphi = 0.4$. At these conditions, $S_{II} = 1.0$, whereas $S_I = 1.2$. It would be expected that any crystalline material produced under these conditions would be form I, as the supersaturation ratio must be greater than 1 for crystallization to occur. Furthermore, the induction times at such supersaturations were measured to be between 15-95 minutes in batch antisolvent crystallizations [24]. The rapid startup in this case shows crystals have been produced in the order of seconds. The nucleation of form II and rapid startup are readily explained by the presence of antisolvent in the COBC prior to starting the flow of feed solution. The COBC needs to be pre-filled with a solvent prior to the flow of feed/antisolvent to purge any gases in the setup. If the COBC is filled with antisolvent, then as the feed solution flow is introduced, it will come into contact with a large volume of antisolvent, creating very high local supersaturations. If the target antisolvent fraction is relatively low, this will result in the supersaturation passing through a maximum before reaching the stable condition. In an unseeded process, this will generate nuclei very rapidly, with a much shorter induction time than the mixing time the process can provide. The process will ultimately reach a

steady state of concentration at the point of mixing, but by that point the presence of the initial nuclei may allow for secondary nucleation. This may be advantageous for low supersaturations by preventing long induction times and reaching a steady state of operation faster, but could alter the crystal properties. Pre-filling the COBC with solvent would provide a gradual increase in supersaturation as the antisolvent reaches the feed solution inlet. However, this introduces uncertainty around nucleation, and could result in no crystallization occurring in the crystalliser if the induction time is too long relative to the residence time.

4.4 Limitations of the Unseeded COBC

4.4.1 Fouling

Briggs et al. demonstrated that unseeded cooling crystallization of L-glutamic acid in a COBC resulted in significant encrustation on the walls of the crystallizer, which was alleviated with a seeding strategy [109]. In such a process, the walls of the COBC are where heat transfer occurs. As the antisolvent crystallizations were performed isothermally, it was not expected that encrustation would preferentially occur there. However, encrustation was localised around the L-shaped solvent inlet shown in Figure 4.18. The local supersaturation at the point of mixing will be very high, which may result in mixing times longer than induction times depending on the relationship between mixing offered from oscillatory conditions versus mixing due to the velocity of flows. The inlet is made of 316-grade stainless steel, compared to the rest of the COBC which is of glass construction. This may also contribute to the fouling observed due to differences in surface roughness and/or surface energy ofm the material of construction [110].

Figure 4.18. Localised fouling of the stainless steel inlet at the mixing location in the COBC.

Potential practical issues regarding fouling for unseeded continuous antisolvent crystallisation processes was identified by Su et al. who devised a model plug-flow crystallizer with optimised antisolvent additions with regards to the location and amounts of antisolvent [111]. It was noted that the model was particularly sensitive to the first antisolvent addition in an unseeded crystallisation and was important in determining the final crystal product qualities such as the CSD. Note was also made to the likelihood of fouling at this first mixing point should experiments be attempted to validate the model. Albeit not a direct comparison to their model parameters, the results of this work demonstrate this to be a real consideration. Further work on the use of models to aid the design of the process are present in Chapter 6.

4.4.2 Gas Solubilities and Degassing

There was a significant volume of gas being introduced to the COBC during the experiments. Initially, it was thought to be a leak at the mixing location; however, a thorough leak test showed this was not the case. Mixing ethanol and water solvents liberated gas. The solubility of atmospheric gases in ethanol is significantly greater than in water [112], [113], represented in Figure 4.19. The gas solubility data is given as the Ostwald coefficient for each respective gas, which is defined as the ratio of the volume of absorbed gas to the volume of the absorbing liquid [114].

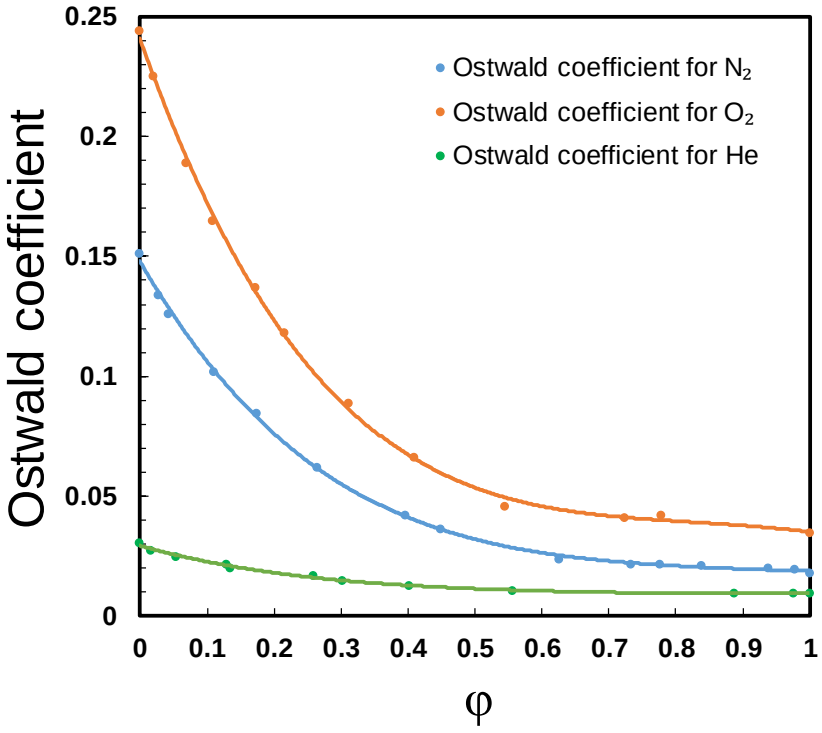

Figure 4.19. Ostwald coefficients for the solubility of nitrogen, oxygen and helium in ethanol and water mixtures. Data sourced from [112], [113], [115]

Hence, gas was being liberated due to the differences in gas solubility upon mixing feed solution and antisolvent. This may not normally be considered or evident in other platforms such as STRs, as any liberated gasses would escape to the head space of the vessel. Due to the design of the COBC, which operates as a near-closed system, the gas could not be readily purged from the vessel, and accumulated in various sections (Figure 4.20). This resulted in oscillation dampening, and therefore reduced efficiency of mixing within the vessel, which was observed by settling of particles. Furthermore, it has been demonstrated that gassing supersaturated solutions can decrease the induction time for nucleation compared to non-gassed solutions [116]. It cannot be ruled out that some form of this mechanism was taking place, but it was not investigated in this work.

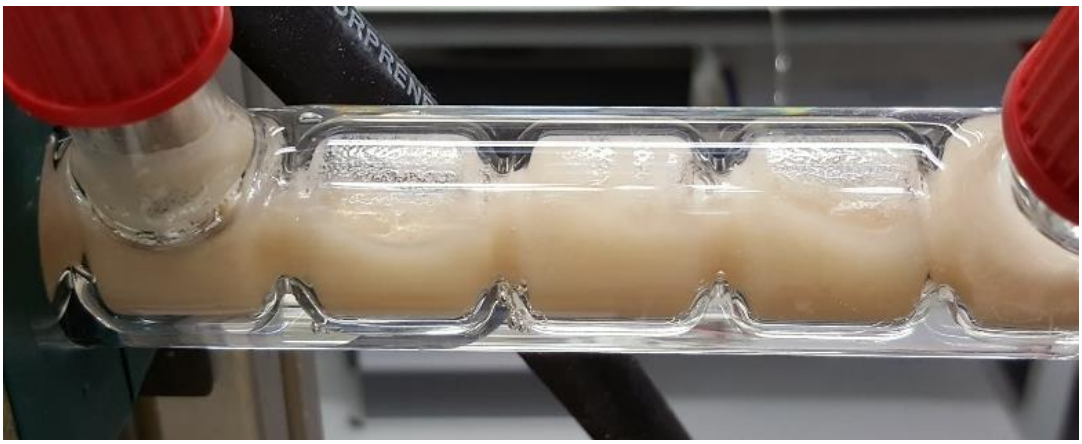

Figure 4.20. Accumulation of gas in the COBC during antisolvent crystallisation, resulting in oscillation dampening and reduced mixing.

To successfully perform continuous antisolvent crystallisations in the COBC, a degassing strategy would most likely have to be adopted to prevent the issues described above. There are various strategies to degas solvents. One is to sparge the solvent with an inert gas such as nitrogen, but this is typically done to remove oxygen in oxygen-sensitive processes, and as can be seen in Figure 4.19, there is still a reasonable degree of solubility for nitrogen in ethanol. Helium has a much lower solubility overall, and would be a reasonable option for degassing, but then one must consider other factors in the process. If ethanol was being used as antisolvent, then sparging would be a potential option, as the antisolvent could be degassed and then stored in a sealed vessel until which time it was required, and then a steady stream of helium gas could be introduced into the vessel when antisolvent delivery was required to prevent redissolution of nitrogen and oxygen. However, as ethanol is the solvent in this case, the compound needs to be added to the solvent and dissolved with agitation, thus increasing the difficulty of maintaining a degassed solution. Other methods involve freezing the solvent, applying a vacuum and then thawing the solvent, but this is rather labour and energy intensive for large quantities of solvent, and doesn't solve the issue of preventing redissolution of atmospheric gases when dissolving the compound.

Figure 4.21. An in-line degassing module. Vacuum is applied to the shell side and the liquid to be degassed flows through a bundle of silicone fibres.

Degassing is regularly used in high-performance liquid chromatography (HPLC) by use of an in-line degasser [117], which consists of a gas-permeable membrane across which a vacuum is applied. This draws the dissolved gas from the solvent, whilst the solvent itself cannot pass across the membrane. The extent of degassing is dependent on the membrane used, the residence time in the degasser and the vacuum applied. HPLC degassers operate with small volumes, and so for a continuous crystallisation process the flow rate would be too high for sufficient degassing. A higher capacity in-line degasser was sourced and is shown in Figure 4.21. It consists of a bundle of silicone fibres in a housing that allows a vacuum to be applied across the shell, operating like an HPLC degasser, but with a much higher throughput. The operation of this degasser was tested in the COBC, first with pure ethanol, and subsequently in crystallisations using solutions of anthranilic acid in ethanol. There was no gas liberation when testing this degasser in experiments under conditions where gas was previously observed. A quantified measurement of degassing was not made and issues with fouling were still present in the attempted crystallisations. Chemical compatibility must be considered when using such degassers, as some compounds and solvents can dissolve and degrade the membrane and housing materials, but it was sufficient for this system, and allowed for the in-line degassing of the feed solution directly.

4.4.3 Mixing Conditions

Due to the fixed geometry of the apparatus, the mixing conditions are not independent of net flow. At increasing flow rates of feed solution, the velocity of the liquid stream from the inlet increases. This will potentially produce a jet of liquid that will traverse several baffle spaces, and have a significant effect on the local mixing in this region.

There are several contributing factors to the mixing in this system. The oscillation frequency and amplitude provide mixing as described previously and well documented [10], [89]. The velocity of flow from the inlet has been shown to affect the crystal properties from the results described in this chapter. Characterisation of the mixing in the presence of multiple flows could be attempted by computational fluid dynamics studies by building upon those performed previously for oscillatory flow [118]–[120]. There would be additional complexity with factors such as the velocity and ratio of flow from the inlet vs flow in the COBC, the geometry and position of the inlet relative to baffle spacing and how the usual characteristics used to describe oscillatory mixing, i.e. $Re_{O,}$ Re_n and St, relate to these.

4.5 Summary

Antisolvent crystallization of anthranilic acid has been successfully demonstrated in a COBC. A more consistent process startup was observed in the case of the reverse addition method, reaching a steady state in the order of one residence time. The process rapidly desupersaturated, determined by the concentration of remaining solute in the mother liquor. This suggests a rapid growth rate due to the measured particle size compared to the residence time of the process. FBRM data suggests nucleation rate increases as the flow rate increases in this process. Metastable form II was consistently produced, even at relatively low supersaturations.

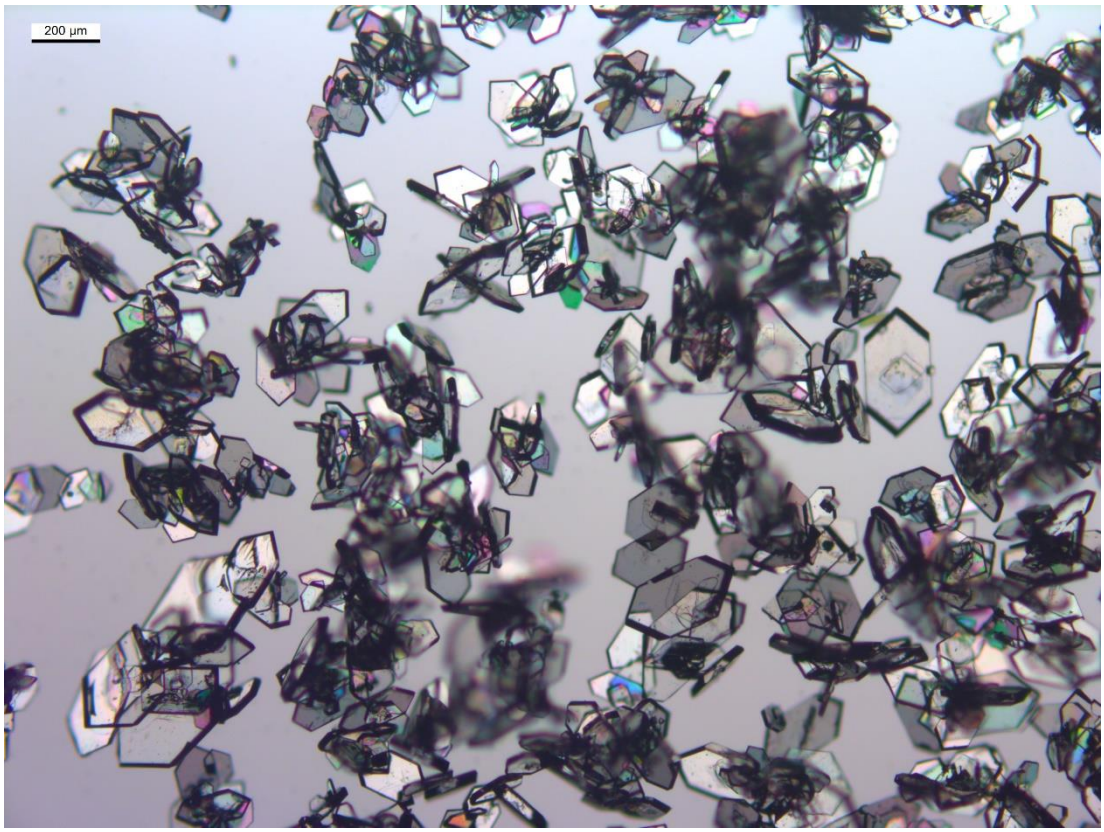

Figure 4.22. Crystals of anthranilic acid form II produced at S_I = 1.5

Antisolvent crystallization in a COBC is sensitive to a number of factors. Localised fouling occurred in all experiments, which needs to be addressed in future experiments with the COBC. Gas solubilities need to be taken into account when designing antisolvent processes in a COBC, due to their significant effect on the mixing and consequently particle suspension, and potentially nucleation. This could be remedied

by selecting a solvent/antisolvent pair that have similar gas solubilities, or by degassing solvents prior to introducing them to the COBC. A continuous in-line degassing strategy is presented to eliminate the effects of dissolved gases.

The normal addition mode has a very different startup strategy than the reverse addition. If one considers the environment at the point of contact of feed solution and antisolvent, as antisolvent flow is initiated it encounters a large volume of feed solution. The supersaturation ratio then dips as there is not a significant reduction in solubility until $\varphi = 0.25$. The supersaturation profile moves from low to high as the process stabilises at the target antisolvent fraction condition. This is in contrast to the reverse addition method, where the solution encounters a large volume of antisolvent. The supersaturation profile therefore goes through a maximum before reaching the target fraction. This maximum supersaturation ratio occurs around $\varphi = 0.8$, which explains why for all conditions in the reverse addition mode there was a consistent startup, and why metastable form II polymorph was the only form observed.

5 Polymorphism in a Continuous Antisolvent Crystallisation

5.1 Introduction

Polymorphism is one of the most important factors to control in the crystallisation of an API. Different polymorphs of a compound can exhibit differences in solubility, potentially affecting the bioavailability of the compound, and in cases where there is a narrow therapeutic window this could result in increased toxicity or an ineffective dose being administered. Changes in polymorphism can also affect the downstream processability of material through changes in shape or mechanical properties [121]. A thorough understanding of the polymorphic behaviour of a system can prevent unexpected manufacturing issues arising. It can also serve to protect intellectual property and extend financial viability, as different polymorphs can be patented separately [122].

Batch crystallisation studies have been conducted investigating their polymorph dynamics [123], [124]. Polymorph control may be employed in an unseeded process by several methods: careful control of supersaturation; by relying on a solvent-mediated transformation from a metastable to stable form; or by isolation of the crystal product before such a transformation can take place, but control of other attributes such as CSD and yield may be hindered by such methods. Crystallisation processes can control polymorphism by employing a seeding strategy and careful adjustment of supersaturation to prevent nucleation of an undesired form [125], which also provides control over CSD if the initial seed material has a narrow span.

For a continuous crystallisation process, nucleation must constantly take place if seed material is not being continuously provided, otherwise the seeds will be washed out of the crystalliser. Thus, seeding strategies that are traditionally adopted for batch crystallisations are not readily transferrable to continuous. A constant supply of seed material is often employed for continuous crystallisation processes [109][126]. This can require the preparation and isolation of significant amounts of seed material. To deliver the seeds to the continuous process, they are typically suspended in a saturated solution of the compound. This prevents the use of metastable polymorph as seed material, as the solution would be undersaturated with respect to a metastable form and result in dissolution of some seed material, and potential transformation of the seed. An antisolvent process opens an alternative seeding method in that seeds can be suspended in antisolvent. However, if the compound is not completely insoluble in the antisolvent, there can still be the potential for solvent-mediated transformation, albeit the rate of

transformation may be affected. The seed material may also be poorly wetting in the antisolvent, leading to difficulties in suspension and even dispersion of seed. An idealised process may involve a controlled continuous nucleation of seed material that has a specified and narrow CSD and the desired polymorph, that could then be fed into a growth unit to achieve control over the final product quality.

There has been investigation into polymorph-specific MSMPR crystallisations for enantiotropic systems [127], [128], which successfully controlled polymorphism and gave a high yield, but these involved a cooling crystallisation approach. This chapter investigates the polymorph dynamics in a continuous antisolvent crystallisation. Anthranilic acid in an ethanol and water solvent system are once again employed due to existing knowledge on the polymorphic behaviour [4],[5] and experience with the system from work in Chapter 4. The effect of residence time and antisolvent fraction on the polymorphism of anthranilic acid in an MBOBC is investigated experimentally. Seeded and unseeded startup strategies are employed to determine the effect of the initial seed condition on the evolution of the process.

5.2 Experimental

5.2.1 Moving Baffle Oscillatory Baffled Crystalliser (MBOBC)

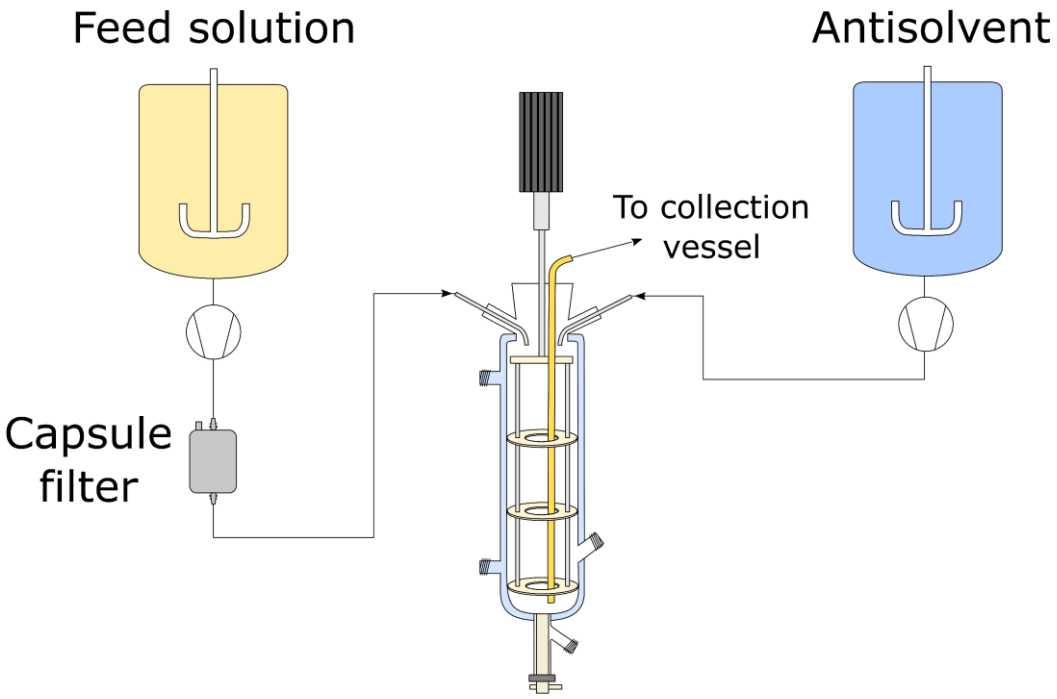

Figure 5.1. Schematic of the MBOBC setup used for antisolvent crystallisation studies.

The crystallisation platform used in these experiments is shown in Figure 5.1. This consisted of a jacketed vessel of approximately 250 ml maximum operating volume. Within this vessel was a string of three PEEK baffles connected with stainless steel threaded rods. The baffle string was driven by a linear motor that provided oscillations a frequency of 3 Hz and a centre-to-peak amplitude of 10 mm. The temperature was maintained at 25 °C by a circulating water bath (Lauda ECO RE 620 G) connected to the jacket. A side port allowed for incorporation of FBRM between the baffle spaces. The MBOBC vessel was selected as it was expected to be more robust than the COBC used in the previous chapter and not susceptible to the gas accumulation issues, which would allow it to perform as a continuous nucleation unit.

The experimental conditions used for the continuous antisolvent crystallisations in the MBOBC are detailed in Table 5.1.

Table 5.1. Experimental conditions for the MBOBC experiments

Temperature (°C)	Total flow rate (ml/min)	Mean residence time (min)	φ	S_I	Seed load, %	Seed polymorph
25	50	4	0.46	1.59	0	n/a
25	50	4	0.46	1.59	10	I
25	100	2	0.46	1.59	10	I
25	100	2	0.46	1.59	100	I
25	50	4	0.60	2.76	100	I
25	50	4	0.60	2.76	10	I
25	100	2	0.60	2.76	100	I
25	50	4	0.35	1.19	10	I
25	50	4	0.60	2.76	100	III

The MBOBC platform has been used previously for characterisation of mixing conditions and temperature control in a batch process that could be translated to COBC operation [129], but this is believed to be the first instance where it has been operated as an MSMPR crystalliser for antisolvent crystallisation. The MBOBC offers a different hydrodynamic environment than a conventional MSMPR stirred tank crystalliser, as mixing is provided by the oscillatory motion of a baffle string as opposed to an impeller. The shear rates will also differ between these systems, and is expected to have an effect on nucleation [130].

Due to the presence of impurities discussed in the previous chapter, a high-capacity capsule filter (Whatman) shown in Figure 5.2 was used to remove these in-line, eliminating the need to prepare recrystallised material. This filter consisted of PTFE membranes of 0.45 μm pore size within a robust polypropylene housing. The feed solution was comprised of anthranilic acid in 75% ethanol (v/v) saturated at 25 °C. This differs from the solution in Chapter 4, where 100% ethanol was used for the feed solution. This was decided upon as there is no generation of supersaturation until this point in the phase diagram (Figure 4.10); there is a reduction in gas solubility (Figure 4.19); and that the presence of water in solution may assist in dissolution of the NaCl impurities in the raw material and increase the lifespan of the filter.

Seed loading is defined by the ratio of the added seed mass, M_S, to the theoretical yield, Y_T, as determined from the concentration of the initial solution and solubility in the final solution after addition of antisolvent.

Figure 5.2. Filter capsule used for in-line filtration of impurities.

The feed solution and deionised water were held in 5-litre jacketed stirred tanks connected to circulating water baths (Lauda ECO RE 620 G). These were fed into the MBOBC via peristaltic pumps (520 Du, Watson-Marlow) fitted with Marprene thermoplastic elastomer tubing (3.2 mm internal diameter, 2.4 mm wall thickness). This tubing was connected to 316-grade stainless steel tubing of 1.6 mm internal diameter to maintain the feed and antisolvent inlet positions across all experiments. The outlet tubing also consisted of the same model of peristaltic pump and elastomer tubing material. The inlets were positioned above the operating liquid level of the vessel in an attempt to minimise any fouling that may occur on the steel, as this had been observed in the previous chapter where the inlet was in contact with solution at all times.

Initially, the tap at the bottom of the MBOBC was to be used as the outlet for the slurry. However, the geometry of the bottom of the vessel resulted in sedimentation of crystals at this location. The outlet tube was then placed inside the platform between the baffle spaces to prevent this sedimentation. The vessel was filled with various volumes of solvent to determine a suitable operating volume. If the liquid level is too low, there is significant splashing due to the top baffle disrupting the air-liquid interface. If it is too high, the suspension will not be adequately mixed. A volume of 200 ml was determined to provide minimal splashing and good particle suspension at the operating

frequency and amplitude. Degassing by the mixing of solvents was an issue in the previous chapter due to the geometry of the COBC. As the MBOBC is not a closed system, any gases liberated from mixing of the solvents could escape, and therefore did not hinder the process. The concentration of the solution was determined gravimetrically by taking samples of filtered mother liquor at various time intervals. FBRM was used to give an indication of the dynamics of solid in the process.

5.2.2 Solubility Data for Anthranilic Acid at Varying Temperature and Antisolvent Fraction

It has been shown that the solvent-mediated transformation of anthranilic acid form II to form I occurs at different rates depending on the temperature [105], with faster transformation at lower temperatures. This was considered as a potential control strategy for driving polymorphism to a particular form, and so additional solubility data was acquired for the system. Figure 5.3 shows the gravimetrically determined solubility for form I at 15, 25 and 35 °C. This strategy was ultimately not adopted, but the solubility data is included here for completeness.

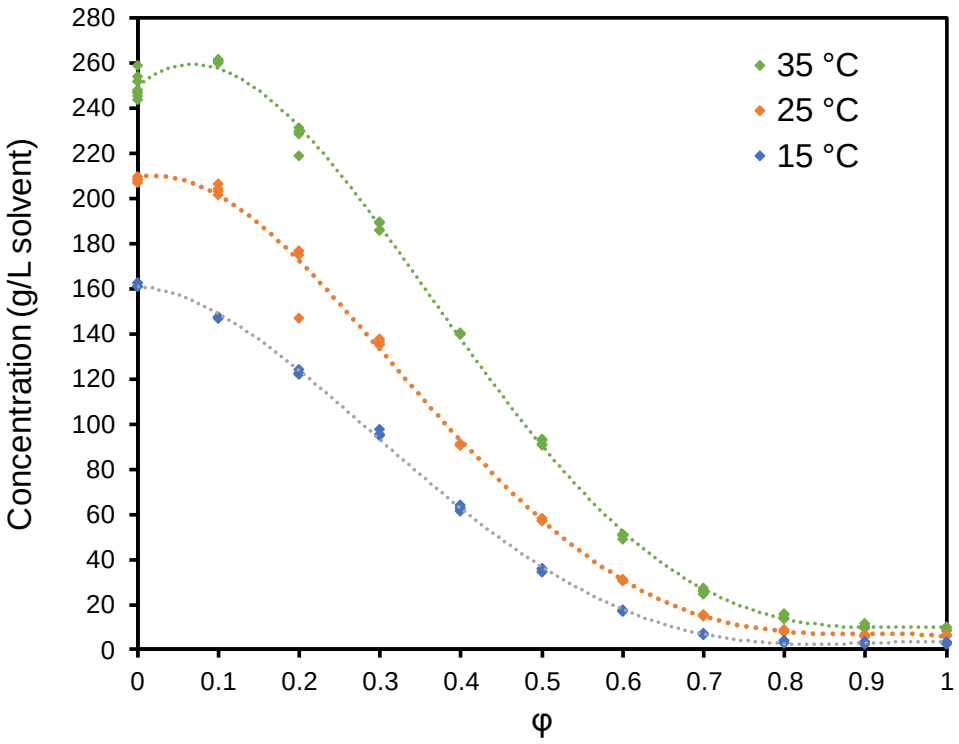

Figure 5.3. Gravimetric solubility data for anthranilic acid form I at 15, 25 and 35 °C across a range of antisolvent (water) volume fractions (φ).

5.2.3 Unseeded Startup Process Operation

For the unseeded process, the MBOBC was started as a batch antisolvent crystallisation. A solution of anthranilic acid with a concentration of 156 g per litre of 75% ethanol (v/v) and deionised water were flowed into the MBOBC to give $\varphi = 0.46$ at a total flow rate of 50 ml/min until the target volume of 200 ml was reached. The process was maintained as a batch until 20 minutes after nucleation was observed. Flow was then reinitiated, and the process operated as a continuous crystalliser with the outlet flow maintaining the 200 ml volume.

5.2.4 Seeded Startup Process Operation

For seeded experiments, the MBOBC was pre-filled with 200 ml of saturated solution of anthranilic acid. The concentration and antisolvent fraction of the pre-fill solutions varied depending on the experiment. They were prepared such that the antisolvent fraction was equal to that would be delivered in continuous flow during the experiment, and the concentration was equal to what would be the equilibrium concentration under these conditions. This ensured seed material would be suspended in saturated solution, and that the antisolvent volume fraction would be consistent for the whole experiment.

The anthranilic acid raw material from Acros Organics was a mixture of forms II and III, whereas form I was required for seeding. As an alternative to preparing form I seed material as was performed in section 4.2.1, form I raw material was ordered from Sigma-Aldrich. This was confirmed to be form I by XRPD as shown in Figure 5.4.

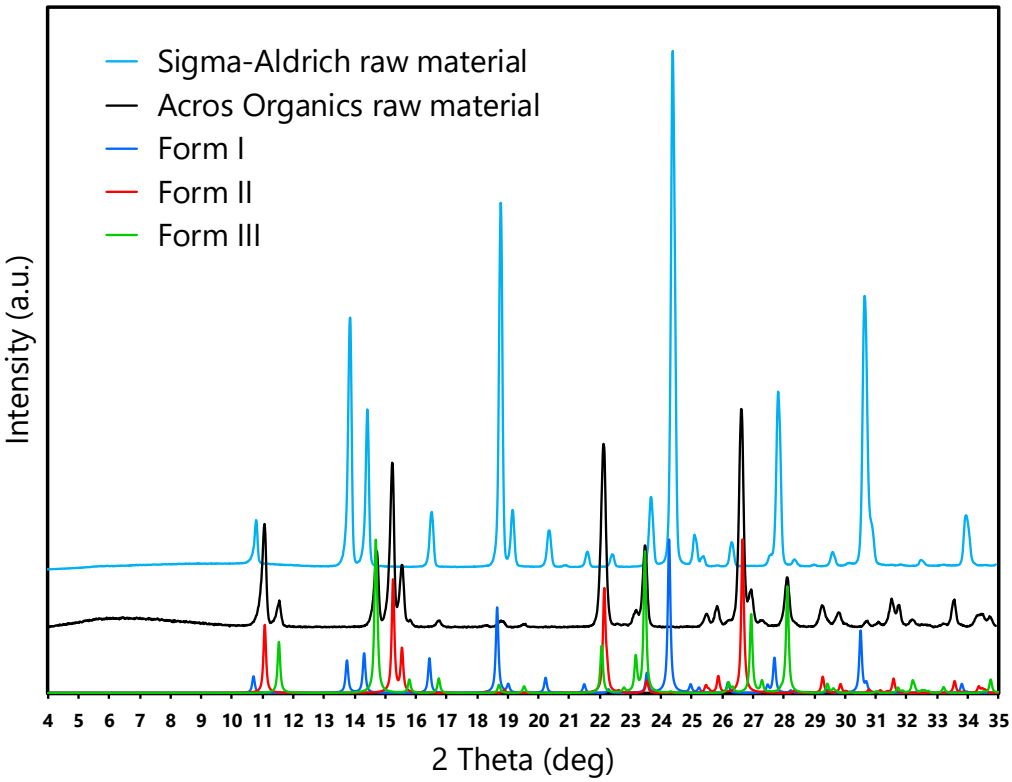

Figure 5.4. XRPD patterns of anthranilic acid raw material from different suppliers and reference patterns from the Cambridge Structural Database.

The required mass of seeds for each experiment were weighed from the anthranilic acid form I raw material directly. Seed material was then rapidly suspended in the solution, and inlet and outlet flows were initiated. The seeds were only provided as an initial bolus at the start of the experiment and were not continuously fed into the MBOBC.

5.2.5 Quantification of Polymorphic Content

As it was expected that some experiments may give a mixture of polymorphs, it was desired to be able to quantify the relative polymorphic content of each form in a sample. This was achieved by preparing standard samples of known mass fractions of each pure polymorph. Form I material was the previously tested raw material. Form II was a surplus sample from experiments in Chapter 4 that had been analysed by XRPD previously and reanalysed to confirm it had not undergone transformation in storage. Data was collected as described in Section 3.2.2. The pure polymorphs were lightly triturated separately in an agate pestle and mortar to minimise the effects of preferred orientation. These were then combined in separate vials to give 250 mg of mixed

component as detailed in Table 5.2. The mixtures were thoroughly blended to ensure homogeneity.

Table 5.2. Polymorphic mass fractions of form I and II for preparation of calibration line.

Mass fraction form I	Mass form I (mg)	Mass form II (mg)
1	250	0
0.8	200	50
0.6	150	100
0.4	100	150
0.2	50	200
0	0	250

Analysis of the blends by XRPD gave six diffraction patterns. From the peak height ratio of peaks characteristic to form I and form II, which occur at 24.28 ° and 26.58 ° 2θ respectively, versus the known mass fraction in each sample, a calibration line was prepared, depicted in Figure 5.5.

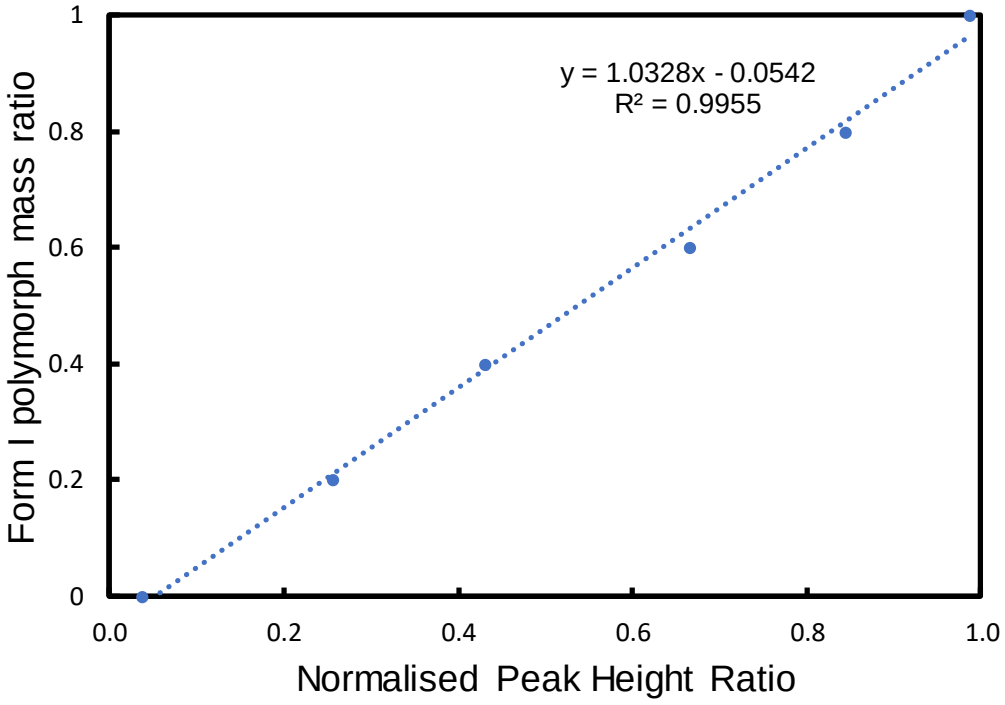

Figure 5.5. Calibration line for anthranilic acid polymorphic content based on ratio of XRPD peak height for form I (2θ = 24.28°) to form II (2θ = 26.58°).

5.3 Results and Discussion

5.3.1 Effect of Unseeded versus Seeded Startup

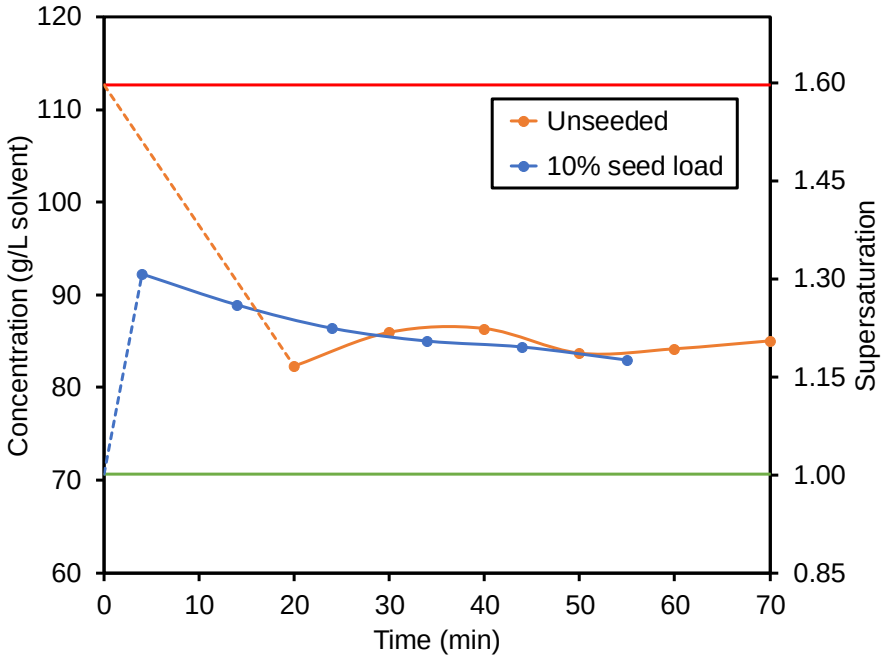

Figure 5.6. Concentration and S_I over time for φ = 0.46, 50 ml/min. Upper limit (red line): maximum possible concentration of mixture. Lower limit (green line): equilibrium concentration.

The concentration profiles of the seeded and unseeded experiments are shown in Figure 5.6. The upper red line shows the maximum achievable concentration of anthranilic acid in the solvent mixture after antisolvent has been added. This would be the concentration if no crystal growth or nucleation were to occur. The lower green line shows the concentration of anthranilic acid in the solvent mixture at equilibrium. Therefore, the difference between these two bounds is the maximum amount of anthranilic acid that could crystallise. The blue and orange lines that lie between these bounds represent the measured concentration. The dashed lines highlight the difference between the starting concentration of the process and the first measured concentration value. The unseeded process starts at a higher concentration, due to there being no pre-fill procedure and duration of batch operation in place for this condition. This higher concentration therefore produces a greater supersaturation ratio in the unseeded process

than is present in the seeded process. The concentrations of both processes then tend towards a similar value.

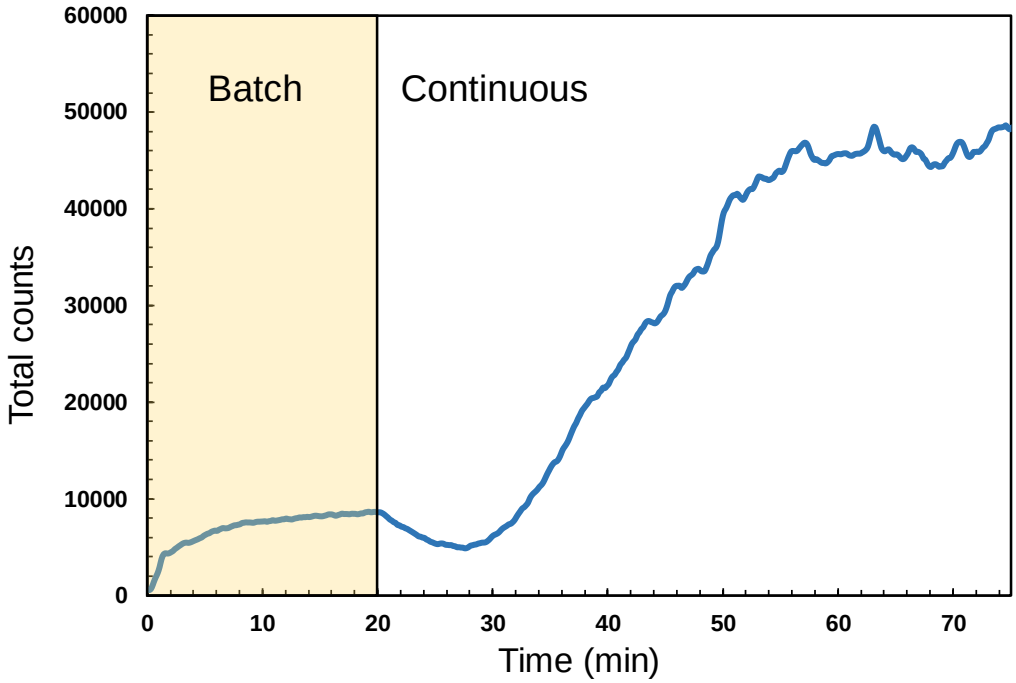

Figure 5.7. FBRM total counts for φ = 0.46, 50 ml/min, unseeded.

The FBRM data in Figure 5.7 shows the solid dynamics in this experiment. The process rapidly nucleates, as indicated by the initial spike in the FBRM total counts. The number of crystals then trends upwards for the duration of the batch phase of operation, albeit appearing to be approaching a plateau. After 20 minutes of batch operation, feed solution and antisolvent inlets and the outlet flows were initiated. There is a decrease in counts at this point, which is indicative of the displacement of material from the MBOBC. This decrease was then followed by a large increase in the total counts, and was also observed visually by a denser crystal slurry in the crystalliser. Continuous secondary nucleation is therefore taking place; otherwise, the decrease in counts that was observed when flow was initiated would have continued until there was no crystalline material remaining in the vessel.

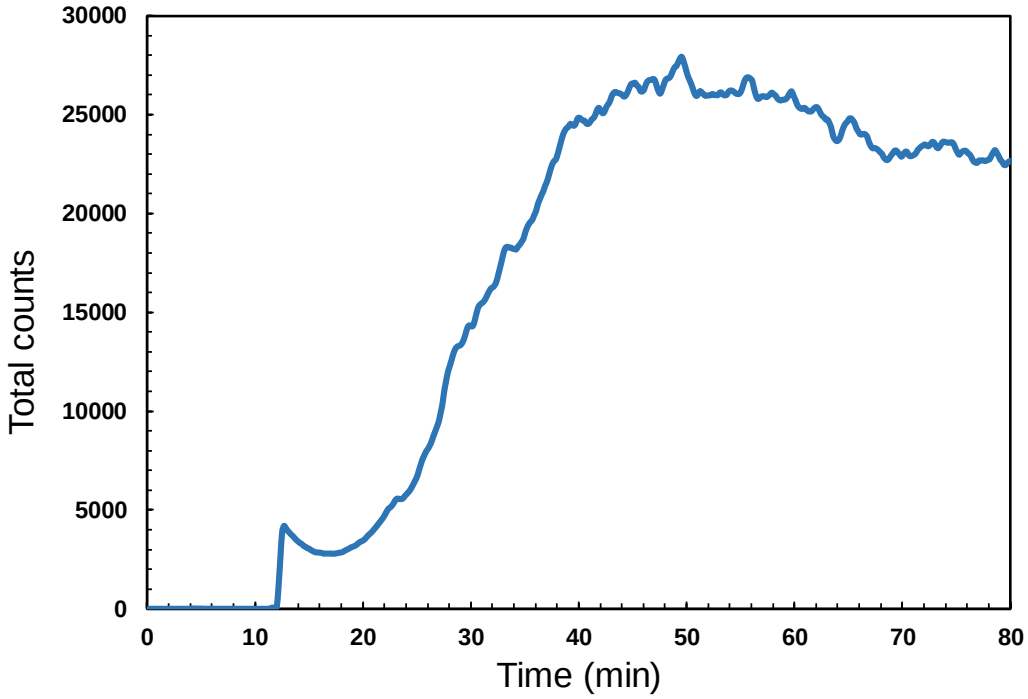

Figure 5.8. FBRM total counts for φ = 0.46, 50 ml/min, 10% seed load.

The point of addition of the seed material can be seen in the FBRM data in Figure 5.8. After the seeds were suspended, inlet and outlet flows were initiated. There is a decrease in total counts at this point, attributed to the washing out of crystals as was seen in the unseeded startup process in Figure 5.7. This was similarly followed by a large increase in counts.

It is important to note that due to the startup procedure for the unseeded process where the vessel was filled from empty, the solution was not well mixed until the liquid level reached the first baffle. Nucleation occurred rapidly and was observed before thorough mixing of the feed solution and antisolvent, and is likely due to high localised supersaturation at the point of contact. An alternative startup strategy for the unseeded condition would involve pre-filling the MBOBC with solvent or a saturated solution and operating in a continuous mode for a number of residence times until enough solution had been displaced to provide the target concentration. However, as there is no real-time concentration measurement in this case, it would have to be estimated when the target concentration had been reached before switching to batch mode and then back to continuous. It is also probable that nucleation would take place in this

startup phase. Therefore, the alternative startup with no pre-fill in the unseeded experiment was deemed a suitable compromise.

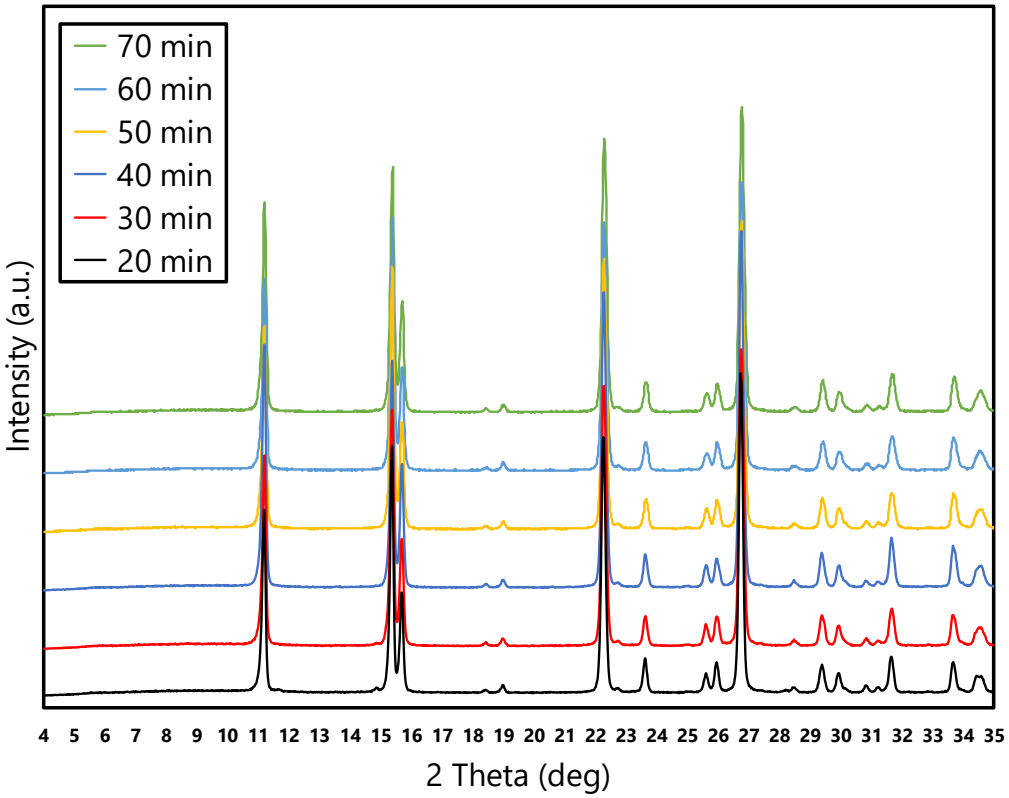

Figure 5.9. XRPD patterns for φ = 0.46, 50 ml/min, unseeded. The first sample at 20 minutes represents moving from the batch startup mode to continuous.

For the results of solid form from the unseeded condition in Figure 5.9, the first sample consisted of metastable form II polymorph, with form II being maintained for the duration of the experiment at over 13 residence times for continuous mode. Although the process had operated as a batch process at the start of the experiment, form I was not detected after 20 minutes, and so solvent-mediated transformation had not occurred. However, the lower measured concentration at 20 minutes vs the seeded experiment may suggest that the process was tending towards nucleation of stable form I before switching to continuous mode, and had batch operation been maintained for longer, form I may have nucleated.

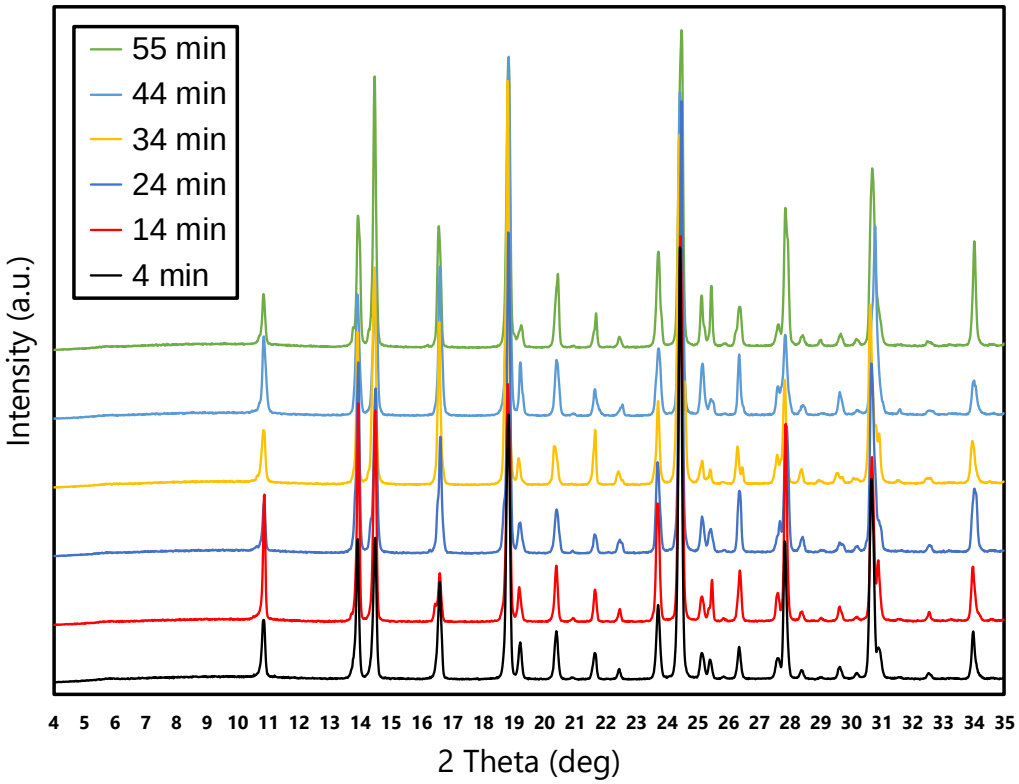

Figure 5.10. XRPD patterns for φ = 0.46, 50 ml/min, 10% seed load.

In contrast to the unseeded experiment, in the presence of seeds of form I there was no metastable form II observed for the duration of the experiment at approximately 17 residence times. Form I was the only polymorph produced, demonstrating the direct control expected and that there was a lack of any unwanted nucleation.

The results here are in agreement with observations in Chapter 4, such that in an unseeded continuous crystallisation process with sufficient supersaturation, form II will nucleate and be maintained. The concentration at the end of both experiments were equivalent, suggesting that there was a quasi-steady state production of form II, and that had form I nucleated or been added manually there may have been a shift from form II to form I production.

The presence of slight variation in the pattern in Figure 5.10 for the 55 minute sample at 14 ° and peak height at 25 ° across all samples could be attributed to the fast scan speed employed (1 sec/0.017 ° step), which would affect the resolution of peaks. A slower scan speed would have given higher resolution, but would have increased collection time significantly.

5.3.2 Effect of Flow Rate

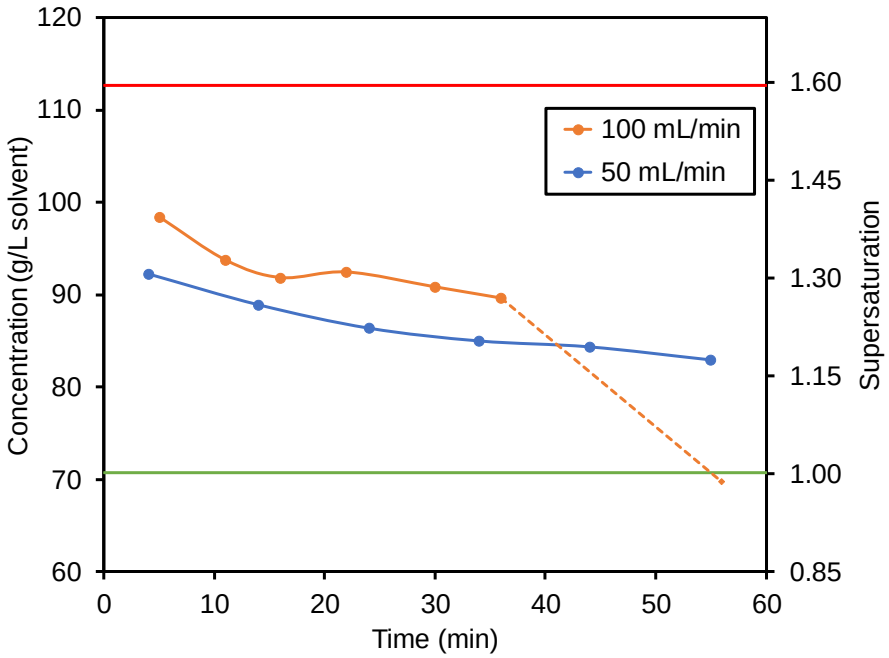

Figure 5.11. Concentration and S_I data for φ = 0.46, 10% seed load. Upper limit (red line): maximum possible concentration of mixture. Lower limit (green line): equilibrium concentration.

The residence time in the crystalliser was reduced from four minutes to two minutes by increasing the total flow rate from 50 to 100 ml/min. Initial seed loading and antisolvent volume fraction were kept constant at 10% and φ = 0.46 respectively. The concentration profiles are shown in Figure 5.11. At higher flow rates, the process operated at a higher concentration than the respective lower flow rate condition, and therefore a higher supersaturation, with an observed maximum of S_I = 1.34. This supersaturation therefore does have sufficient time to be consumed by either nucleation or growth. After the feed solution was depleted for the higher flow rate condition, flows were stopped and the unit operated as a batch process for 20 minutes, highlighted by the dashed orange line. The concentration then reaches the equilibrium concentration for form I.

The polymorphic outcome of the higher flow rate condition of 100 ml/min is shown in Figure 5.12. In comparison to the lower flow rate condition of 50 ml/min shown in Figure 5.10, where the polymorphism remains consistent across all samples as

form I, the presence of metastable form II is rapidly detected after the second sample. All subsequent samples in continuous operation show a mixture of forms I and II. Batch operation for 20 minutes shows only the presence of form I, and was therefore sufficient for solvent-mediated transformation of the form II material to form I.

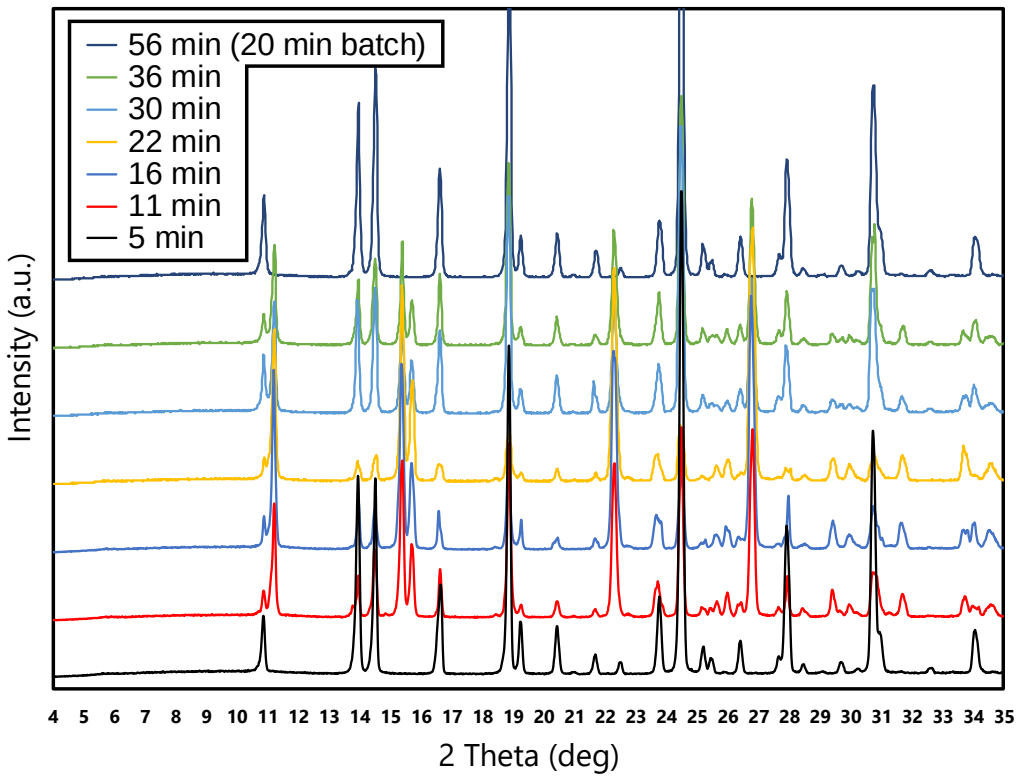

Figure 5.12. XRPD patterns for φ = 0.46, 100 ml/min, 10% seed load.

The quantified polymorphic fraction across the experiment is shown in Figure 5.13. This shows the rapid formation of form II in the process, contributing to roughly half the polymorphic content of the experiment just over five residence times into operation. This then increases to where near 80% of polymorph in the process is form II. This behaviour could be explained by a number of mechanisms, discussed below.

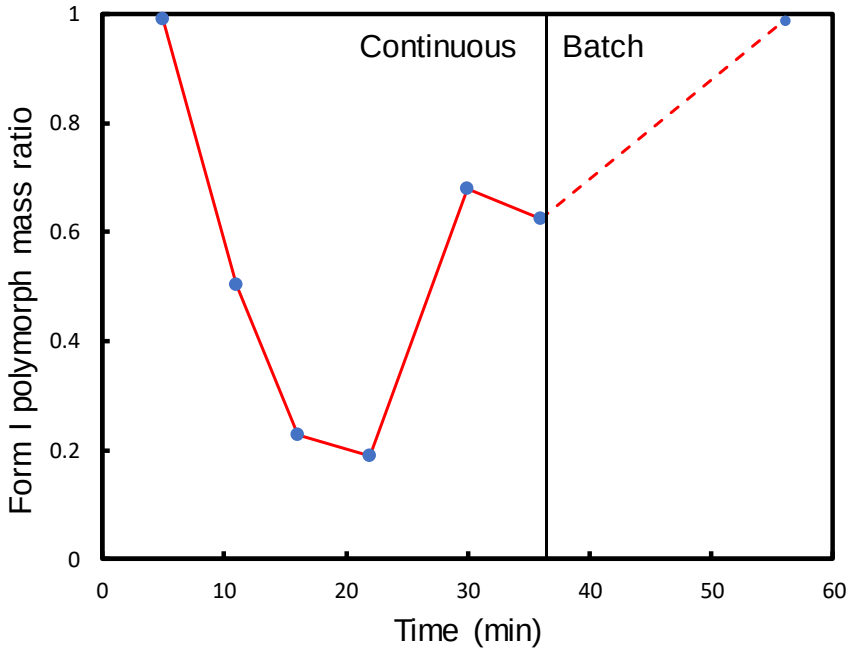

Figure 5.13. Polymorph dynamics in the continuous process between I and II.
φ = 0.46, 100 ml/min, 10% seed load

Clearly form II is produced by nucleation, as there are no form II seeds present at the beginning of the experiment. The reduction in percentage of form I could be attributed to the initial form I seed material washing out of the MBOBC; however, the amount of form I present does not reach zero, so form I nucleation must occur as the fraction of form I in the process then increases. This mechanism could be due to secondary nucleation of form I by the presence of form I seed, or by primary nucleation of form I; concomitant polymorphism in this system has been reported previously, and would be a likely explanation as to the mechanism occurring here [24]. However, in the unseeded experiment only form II was present, even when operating at lower supersaturations than in this instance, which removes the possibility of both the primary nucleation of form I and also a solvent-mediated transformation process, otherwise it would have been observed in that experiment. Therefore, it can be concluded that the mechanism responsible for the presence of form I is due to secondary nucleation from the initial seed.

Previous work by Jiang et al with this compound and solvent system identified regions of supersaturation whereby form I, II or a mixture could be obtained, as shown in Figure 5.14.

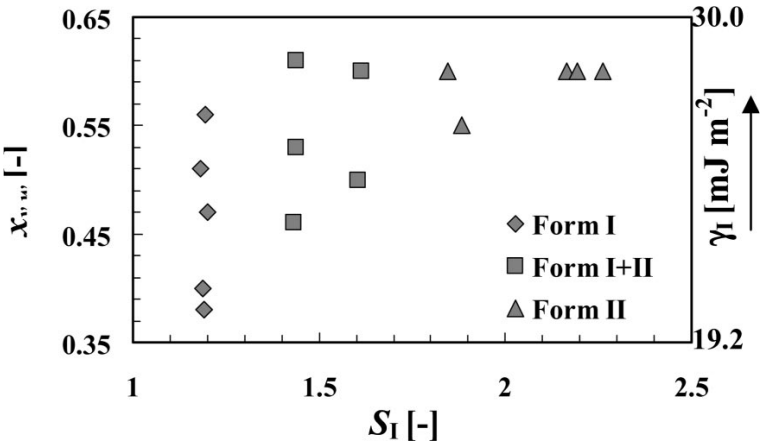

Figure 5.14. Polymorphs of anthranilic acid as a function of supersaturation and antisolvent volume fraction. Reproduced from [24].

The maximum observed supersaturation at the higher flow rate condition was $S_I = 1.34$ versus the lower flow rate condition $S_I = 1.23$. Based on the information in Figure 5.14 and from experimental data, this suggests the limit of supersaturation to produce only form I lies between these values. Therefore, to produce form I exclusively, one would have to ensure the supersaturation in the process did not exceed the threshold at which form II then nucleates. This could be achieved by operating with a longer residence time, such that the supersaturation has time to be consumed by growth of form I material. To produce form II exclusively, either an unseeded startup strategy, seeding with form II or short residence times would be required to prevent form I nucleating.

An alternative condition was investigated with a higher antisolvent fraction $\varphi = 0.60$, again with a 50 and 100 ml/min total flow rate and a 10% seed loading. Due to the higher antisolvent fraction, the pre-fill concentration was lower at 30.3 g/L. Concentration profiles for these experiments are depicted in Figure 5.15. As was the case with the lower antisolvent fraction condition, at higher flow rates the concentration remains higher than lower flow rates throughout the course of the continuous portion of the experiment. As in the previous condition, the unit was operated as a batch process for 20 minutes before the end of the experiment. The concentration then reaches the equilibrium concentration for form I within this time.

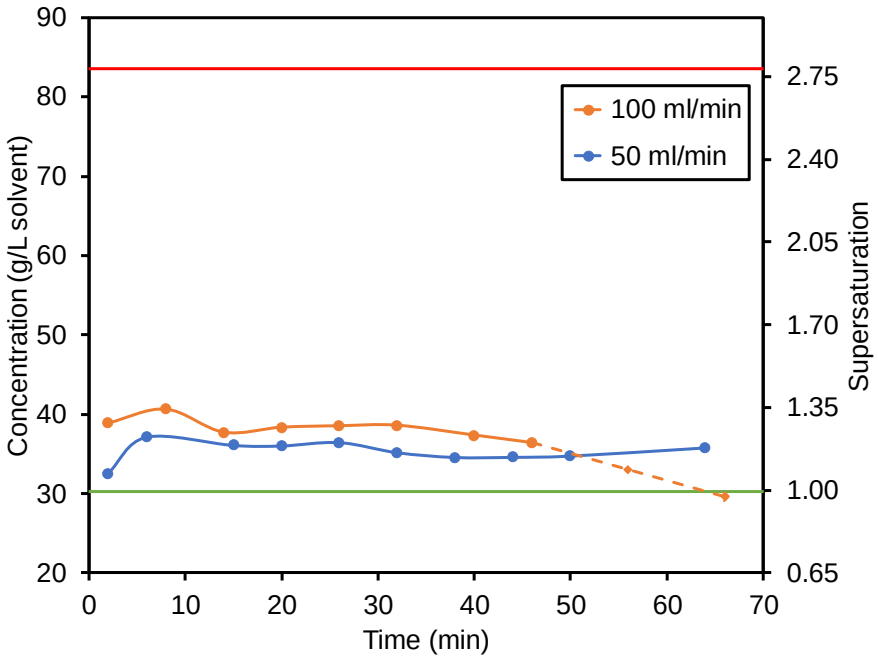

Figure 5.15. Concentration and S_I data for φ = 0.60, 10% seed load. Upper limit (red line): maximum possible concentration of mixture. Lower limit (green line): equilibrium concentration.

The polymorphic outcome of these higher antisolvent fraction experiments are shown in Figure 5.16 and Figure 5.17. The polymorphism at 50 ml/min is consistently form I for the duration of the experiment, approximately 16 residence times. As mentioned for Figure 5.10, the change in Figure 5.16 for the sample at 38 minutes at 14 ° can be attributed to the fast scan speed and slight variation in sample and plate preparation that can affect the resolution of peaks. With the rest of the pattern being consistent with other samples, this was not determined to be a significant enough difference to be of concern.

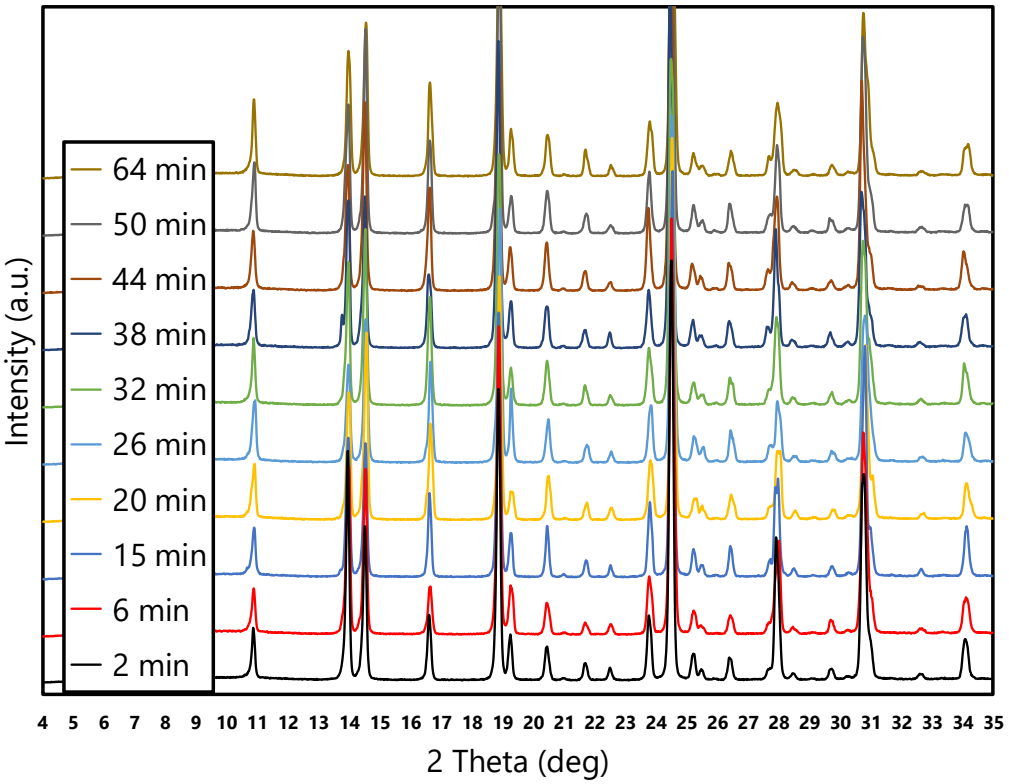

Figure 5.16. XRPD patterns for φ = 0.60, 50 ml/min, 10% seed load

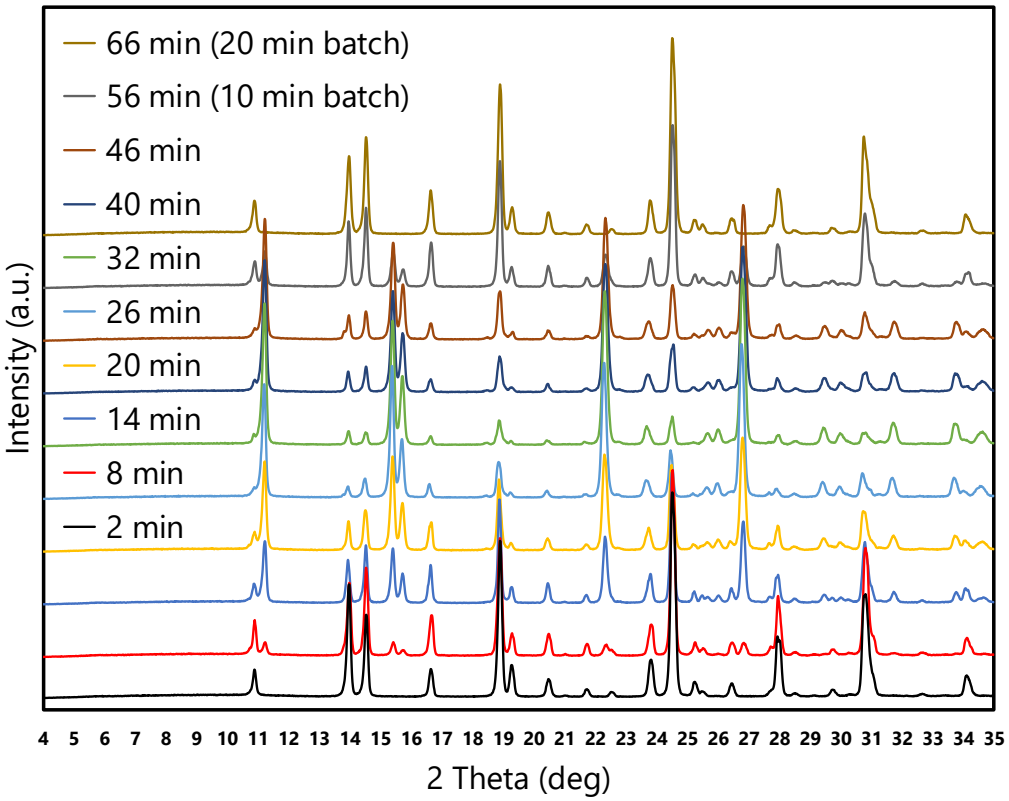

Figure 5.17. XRPD patterns for φ = 0.60, 100 ml/min, 10% seed load

At the higher flow rate of 100 ml/min, metastable form II is rapidly produced, being detected by the second sample at four residence times. The process then operates with a mixture of forms I and II present for the duration of the continuous portion of the experiment, 23 residence times. After the process moves from continuous to batch mode, there is a solvent-mediated transformation, and after 20 minutes all form II has transformed to form I.

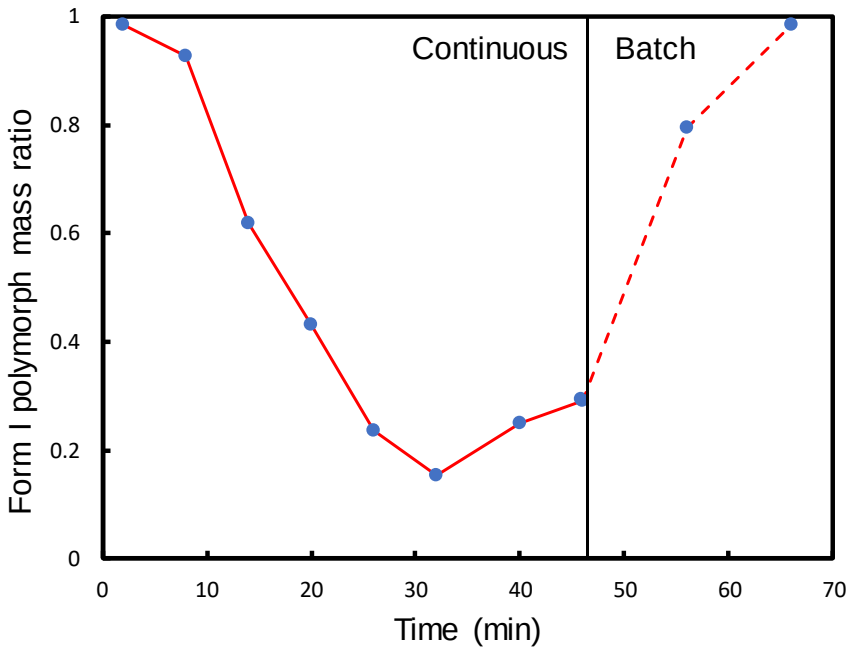

Figure 5.18. Polymorph dynamics in the continuous process;
φ = 0.60, 100 ml/min, 10% seed load.

The quantified polymorphic fraction for this condition is shown in Figure 5.18. As was observed in Figure 5.13 at φ = 0.46, there is a reduction in the mass fraction attributable to form I due to the nucleation of form II. This reduction in form I continues up to 32 minutes, which is equivalent to 16 residence times in this instance. Had there been no continuous nucleation of form I, it would be expected that a greater proportion of the initial seed material would have washed out of the MBOBC after this many residence times; therefore, even though there is a reduction in the amount of form I present relative to form II, there is still continuous secondary nucleation of form I occurring.

All continuous experiments performed at φ = 0.60 in Chapter 4 produced form II exclusively, at flow rates ranging from 25 to 100 ml/min. Batch antisolvent

crystallisations at comparable antisolvent fractions also produced form II exclusively [24]. However, it is not the antisolvent fraction, but the degree of supersaturation that determines which polymorphs will nucleate. The supersaturation ratio at the higher flow rate reaches its observed maximum at 4 residence times, with S_I = 1.34, which is when form II is first detected in Figure 5.17. It is possible that the supersaturation ratio between sampling times was even greater than this, but regardless, there was a point where sufficient supersaturation was generated to induce the nucleation of form II. The lower flow rate condition reaches an observed maximum supersaturation ratio of S_I = 1.23. There was insufficient supersaturation under the lower flow rate conditions to induce the nucleation of form II. Secondary nucleation induced by the presence of form I seed material is sufficient to maintain form I at low flow rates, but the secondary nucleation kinetics are not fast enough to overcome the increasing supersaturation at higher flow rates, and form II nucleates. As in the lower antisolvent fraction conditions, forms I and II are maintained throughout the experiment, implying that competing nucleation mechanisms are taking place.

5.3.3 Effect of Seed Polymorph

Form III polymorph of anthranilic acid had been previously isolated by solvent-mediated transformation from form I at elevated temperature described in [105]. A sample prepared by this approach was sieved to < 250 μm and used as seed material for the experiment described here. The earlier work all used form I seed material. Form III is a metastable polymorph, where the solubility lies between that of form I and II. It was hypothesised that the presence of form III seed, being more stable than that of form II, may promote secondary nucleation of form III and demonstrate a reliable method to produce this form.

Based on the success of the seeded experiment performed at 50 ml/min with φ = 0.60 at producing form I continuously with no form II present, and that higher flow rates had led to nucleation of form II, the lower flow rate condition was selected. Initially, a 10% seed loading of form III was used. However, upon attempting suspension of form III, the material rapidly dissolved. The solution that the seeds were introduced to was saturated with respect to form I, and therefore undersaturated with respect to form III. The MBOBC was flushed with fresh solution and a much more substantial seed loading of 100% was used. This would ensure that even though some

of the seed material would dissolve, there would be a significant amount of form III still present in suspension to promote secondary nucleation. An experiment was also carried out with a 100% seed loading of form I material at φ = 0.60 to make comparisons between the conditions with minimal variation.

The concentration profiles for the two different polymorph seeding experiments are shown in Figure 5.19. The first samples at two minutes correspond to half a residence time. The concentration for the form III seeded experiment is higher than that of the form I seed. This can be attributed to the dissolution of some form III material. The concentration then proceeds to decrease and reach a steady state, in contrast to that of form I that increases before reaching a steady state.

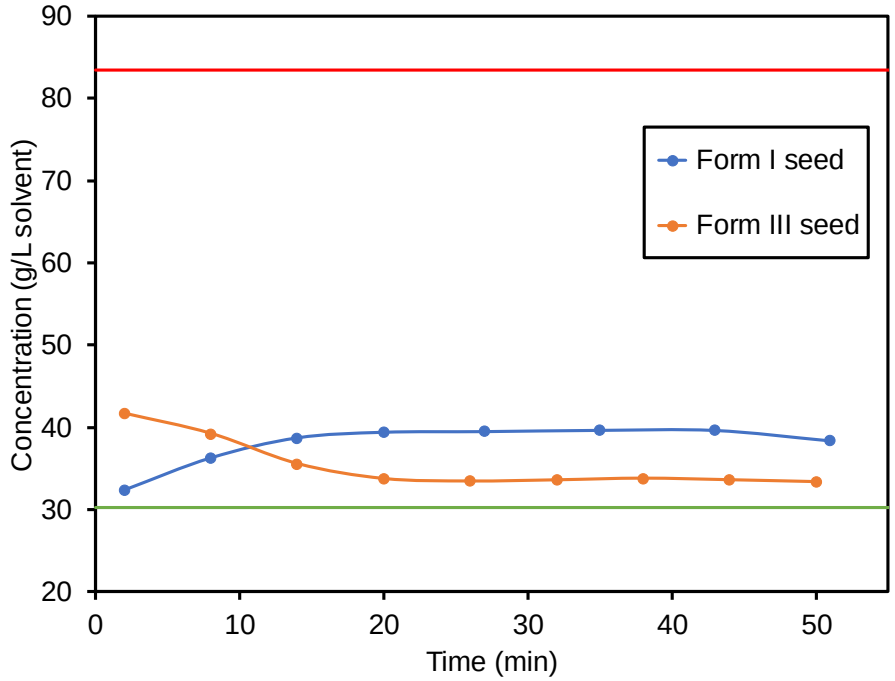

Figure 5.19. Concentration data for φ = 0.60, 50 ml/min, 100% seed load.
Upper limit (red line): maximum possible concentration of mixture.
Lower limit (green line): equilibrium concentration.

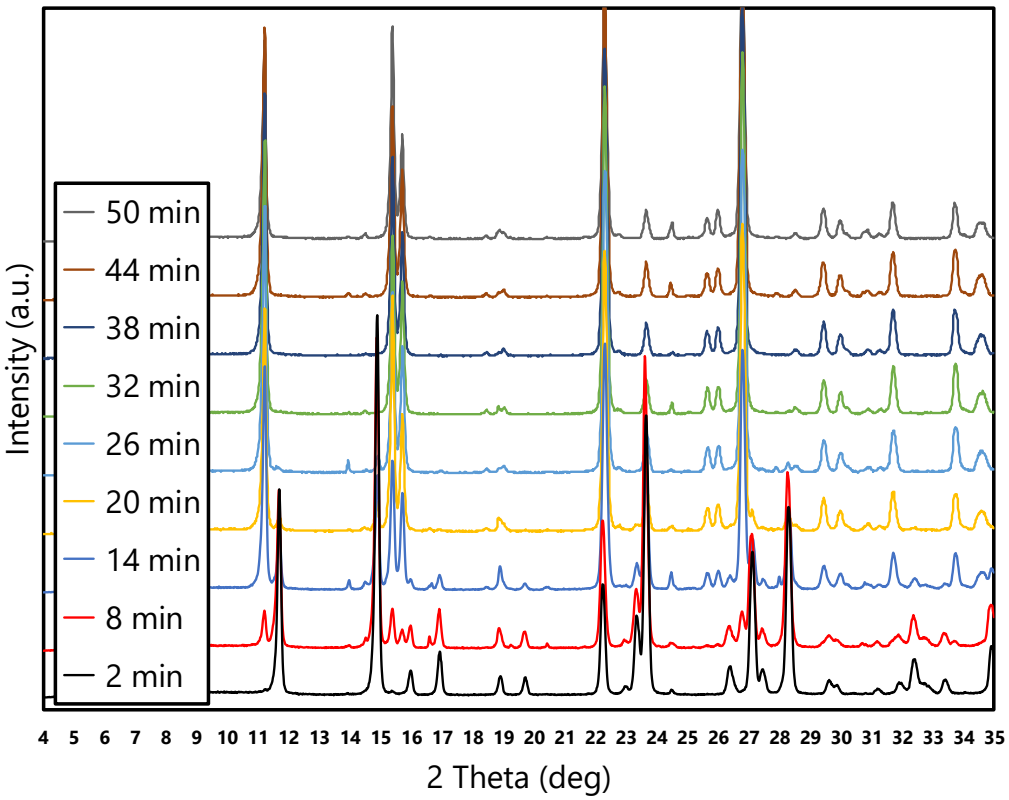

Figure 5.20. XRPD patterns for φ = 0.60, Form III seed, 50 ml/min, 100% seed load.

The polymorphic outcome of the form III seeded experiment is shown in Figure 5.20. From the first sample, only the presence of form III is detected. This is understandable, as there is still a significant amount of the initial seed material still present in the crystalliser. After two residence times, there is still form III present, but form II is now detected and has therefore nucleated. Form II then proceeds to become the dominant form for the remainder of the experiment. Form I was detected towards the end of the experiment, at approximately 5 wt %. There was no discernible form III present by the end of the experiment at over 12 residence times.

The presence of form III seed did not appear to promote secondary nucleation of form III, nor did it prevent the nucleation of form II. As the observed maximum concentration was greater for the form III seeded experiment, it is possible that form II was produced by primary nucleation. However, an alternate mechanism could be that form III seed material acts as a template for the secondary nucleation of form II, which has been reported in other systems [131].

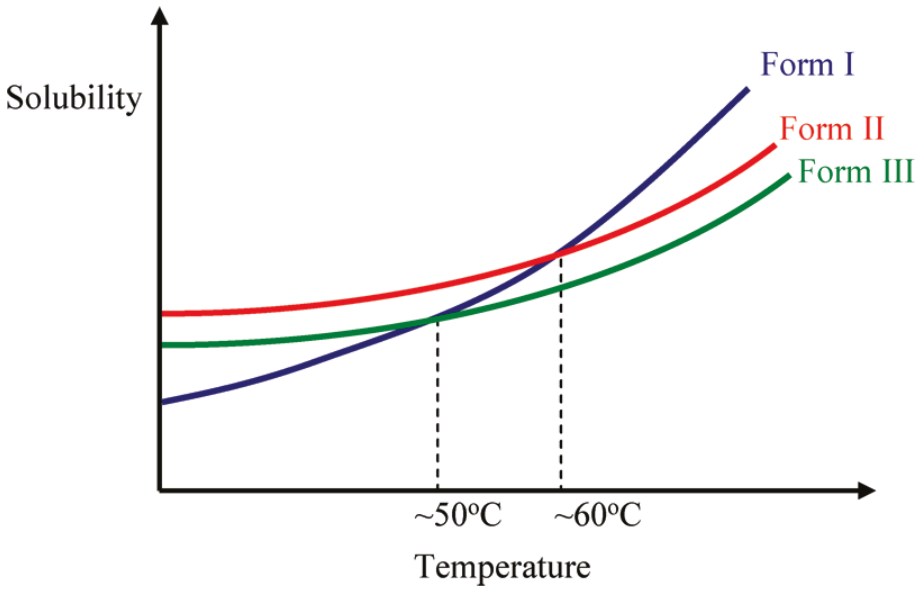

Figure 5.21. Relative solubility of the three polymorphs of anthranilic acid. Reproduced from [105].

Form III has reportedly an intermediate solubility, and therefore intermediate stability relative to form I and II at 25 °C, as depicted in Figure 5.21. This makes it difficult to target this form under the conditions tested. An alternative method that may prove more successful would involve performing the process at elevated temperature, where form III becomes the thermodynamically stable form.

5.4 Summary

Continuous antisolvent crystallisation of stable and metastable polymorphs of anthranilic acid have been demonstrated in an MBOBC for the first time. Control over polymorphism was achieved by varying residence time and initial seed polymorph within the crystalliser. Stable form I polymorph was produced exclusively when a seeded startup strategy was employed and residence times were sufficiently long. Metastable form II polymorph was produced exclusively with an unseeded startup strategy.

A mixture of stable and metastable polymorphs were produced when the residence time in the MBOBC was decreased by means of increasing flow rates of feed solution and antisolvent. Secondary nucleation kinetics were deemed insufficient to maintain the stable polymorph exclusively under these conditions. The MBOBC platform was demonstrated to operate as a robust continuous nucleation unit with polymorph selectivity. This continuous nucleation platform could be coupled with a growth unit to target other attributes such as CSD or yield that were not directly explored in this chapter.

6 Determination of Kinetic Parameters for the Optimisation of Continuous Antisolvent Crystallisations in a COBC

6.1 Introduction

It is essential for industrial crystallisation that the process is tightly controlled and monitored, to ensure the production of a crystal product with the necessary CQAs. In addition, there must be sufficient throughput such that the supply chain is not hindered. To ensure the necessary throughput whilst not having a detrimental effect on the product qualities, process optimisation strategies are developed, which typically involves a combination of PAT and mathematical modelling of processes [132]. When designing a crystallisation process, the CSD is the attribute that is most commonly desired to control, as it influences several downstream processes. The CSD is dependent on several mechanisms, such as nucleation, growth, attrition and agglomeration, which depending on how the process is designed can all occur concurrently during crystallisation.

The evolution of CSD throughout a crystallisation process can be described mathematically by the use of population balance equations (PBEs). There are generally two approaches to estimating model parameters. This can either be performed simultaneously, whereby all crystallisation phenomena occur at the same time and are fitted in one expression by using a least squares method [133]–[135]; or sequentially, whereby these phenomena are decoupled, allowing for independent determination of kinetic parameters [136], [137]. The first approach has disadvantages in that it produces numerical values for kinetic parameters without physical basis [138], which is undesirable if the model is to be used to inform crystallisation processes that have a broader range of operating conditions and target crystal attributes. Therefore, a sequential parameter estimation method is employed.

Previous chapters were focused primarily on polymorphism as the key product attribute. However, controlling other attributes such as the crystal size and yield are also critical to crystallisation processes. This chapter investigates the use of population balance models to optimise a continuous process for these attributes. Growth and secondary nucleation kinetics of anthranilic acid in ethanol and water solutions are estimated, achieved by isothermal seeded batch experiments in a moving fluid oscillatory baffled crystalliser (MFOBC). A sequential parameter estimation approach is taken to determine kinetic parameters by designing experiments that minimise the occurrence of multiple crystallisation phenomena, with the resultant data incorporated into the gPROMS FormulatedProducts 1.3 modelling platform to solve the PBEs.

6.2 Experimental Setup

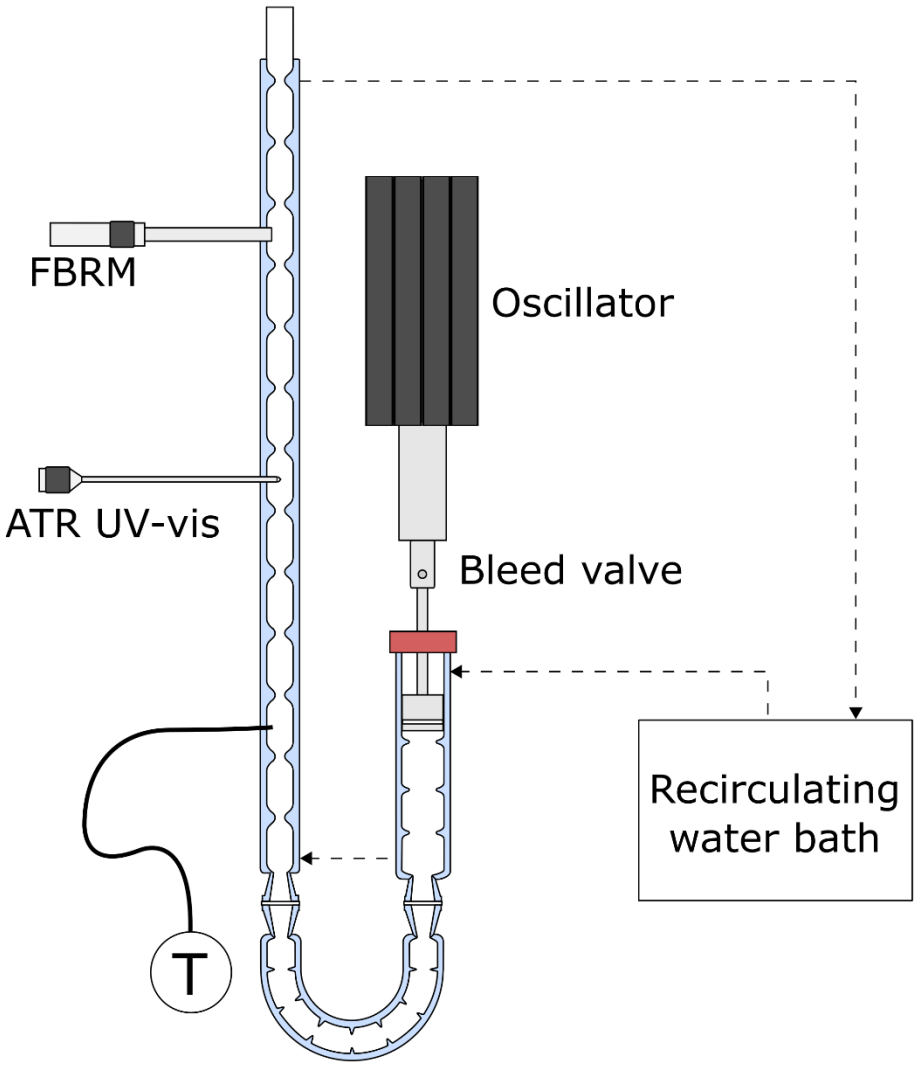

Figure 6.1. Batch moving fluid OBC for antisolvent crystallisation

The experimental apparatus is shown in Figure 6.1. Antisolvent crystallisation experiments were performed in an OBC of approximately 190 ml total operating volume. This consisted of a piston head in a DN22 section of OBC, connected to a DN15 baffled bend section, which in turn was connected to a DN15 straight section with ports that allowed for the incorporation of PAT. This straight section consisted of a different internal geometry than the other sections, the details of which are described in detail elsewhere [139], and was used due to the presence of these ports and the improved mixing and particle suspension characteristics over the previous DN15 baffle

design [140]. A recirculating water bath was connected to the integrated jacket to maintain temperature at 25 °C, which was monitored with a thermocouple mounted directly in the process. The bend section was not jacketed, but due to the majority of the equipment being jacketed and the process being operated near lab temperature and therefore no significant temperature differential, there was not expected to be any significant effect. Mixing was provided by a piston driven by a linear motor and a control box that allowed for modification of oscillation frequency and amplitude. A bleed valve facilitated filling of the OBC at the beginning of the experiment.

6.3 Experimental Procedure

6.3.1 Phase Diagram and Experimental Parameters

A number of concentrations of anthranilic acid solutions in various ethanol mass fractions were prepared as detailed in Table 6.1. This was achieved by the addition of the desired mass of compound, ethanol and deionised water to a flask and stirring at elevated temperature until the material had dissolved. The resulting solutions were filtered over a 0.45 μm filter to remove impurities that were present, resulting in clear coloured solutions. The phase diagram and intended experimental trajectory is shown in Figure 6.2. The highlighted rows in Table 6.1 and red dashed lines in Figure 6.2 show conditions that were originally intended, but had to be modified, the reasoning for which is described in detail in section 6.3.3.

Conditions were selected to maximise the effects of crystal growth over those of secondary nucleation by employing a relatively low power density and providing a high surface area by the use of a higher seed loading of small seeds. For experiments to maximise secondary nucleation, the seed loading was much lower, and the seed sizes and power densities were either equivalent to or greater than those for the growth experiments.

Power densities were calculated by the following equation:

$$\frac{P}{V} = \frac{2n\rho(x_o\omega)^3(1-\alpha^2/\alpha^2)}{3\pi {C_D}^2} \tag{6.0}$$

where n is the number of baffles per metre, ρ is the liquid density, $x_o$is the centre-to-peak oscillation amplitude (m), ω is the oscillation frequency (Hz), α is the free area as calculated by the orifice area divided by the tube area, and C_D is the discharge coefficient.

As the piston head was 22 mm in diameter, compared to the 15 mm of the rest of the apparatus, any set x_o on the control box of the piston would result in a higher x_o being provided to the DN15 sections. This was therefore accounted for to ensure the correct x_o in the DN15 sections were reported.

Table 6.1. Experimental process parameters for kinetic studies. Highlighted rows show originally intended experiments before these conditions were deemed unfeasible by preliminary experiments.

	#	Initial X_{EtOH} (g/g)	Initial c (g/g solution)	Mixed X_{EtOH} (g/g)	Mixed c (g/g solution)	c* (g/g)	c-c* (g/g)	(c-c*)/c* (g/g)	Seed loading	Seed D50 (μm)	f (Hz)	x_o (mm)	Power density (W/m^3)
Growth	1	0.60	0.067	0.60	0.0669	0.1044	-0.0375	-0.3591	-100%	90	4	5.4	1560
	2	0.90	0.190	0.60	0.1352	0.1044	0.0308	0.2954	10%	90	4	5.4	1560
	3	0.75	0.140	0.40	0.0799	0.0424	0.0375	0.8857	10%	90	4	5.4	1560
	3	0.75	0.140	0.50	0.0979	0.0706	0.0273	0.3863	10%	90	4	5.4	1560
	4	0.55	0.075	0.30	0.0424	0.0217	0.0207	0.9542	10%	90	4	5.4	1560
	4	0.55	0.075	0.36	0.0504	0.0331	0.0173	0.5222	10%	90	4	5.4	1560
	5	0.40	0.030	0.20	0.0152	0.0093	0.0059	0.6345	10%	90	4	5.4	1560
Secondary nucleation	6	0.90	0.190	0.60	0.1352	0.1044	0.0308	0.2954	1%	90	4	6.5	2695
	7	0.55	0.075	0.30	0.0424	0.0217	0.0207	0.9542	1%	166	4	6.5	2695
	7	0.55	0.075	0.36	0.0504	0.0331	0.0173	0.5222	1%	166	4	6.5	2695
	8	0.40	0.030	0.20	0.0152	0.0093	0.0059	0.6345	1%	110	4	6.5	2695
	9	0.90	0.190	0.60	0.1352	0.1044	0.0308	0.2954	1%	110	4	7.5	4280
	10	0.75	0.140	0.40	0.0799	0.0424	0.0375	0.8857	1%	110	4	5.4	1560
	10	0.75	0.140	0.50	0.0979	0.0706	0.0273	0.3863	1%	110	4	5.4	1560
	11	0.40	0.030	0.20	0.0152	0.0093	0.0059	0.6345	1%	166	4	7.5	4280
	12	0.40	0.030	0.20	0.0152	0.0093	0.0059	0.6345	1%	90	4	5.4	1560
	13	0.75	0.140	0.40	0.0799	0.0424	0.0375	0.8857	1%	90	4	7.5	4280
	13	0.75	0.140	0.50	0.0979	0.0706	0.0273	0.3863	1%	90	4	7.5	4280
	14	0.90	0.190	0.60	0.1352	0.1044	0.0308	0.2954	1%	166	4	5.4	1560

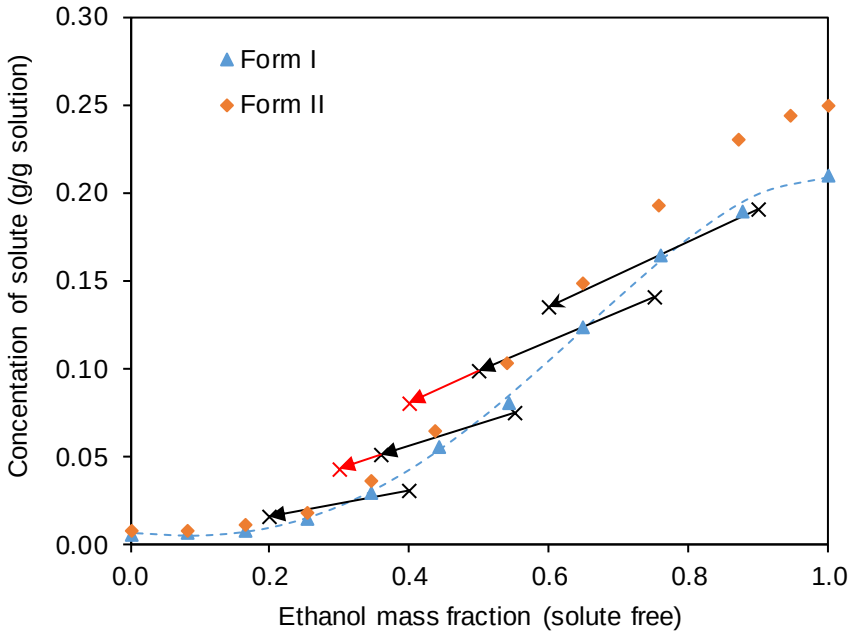

Figure 6.2. Phase diagram for anthranilic acid in an ethanol/water solvent system. Arrows show trajectory from undersaturation to supersaturation by addition of antisolvent. Red arrows show initially planned trajectory.

Seed material was prepared by the method described in section 3.2.6, and the resulting fractions are shown in Figure 6.3. Particle size distributions are shown in Figure 6.4. Seed loadings of 10% and 1% were selected to give high surface area where crystal growth was desired, and low surface area where secondary nucleation effects were targeted, respectively. Seed loading in this instance is defined by the ratio of the added seed mass, M_S, to the theoretical yield, Y_T, as determined from the concentration of the initial solution and solubility in the final solution after addition of antisolvent [141], and can be expressed as:

$$\text{Seed loading} = \frac{M_S}{Y_T} \times 100\ \% \qquad (6.1)$$

As can be seen from the fraction microscopy in Figure 6.3 and the tails in the PSDs in Figure 6.4, there are some fines in the larger sieve fractions. This could be due to a number of factors, such as the duration of sieving not being sufficient to ensure smaller particles can leave pass through the mesh, or attrition of larger crystals on the sieve itself.

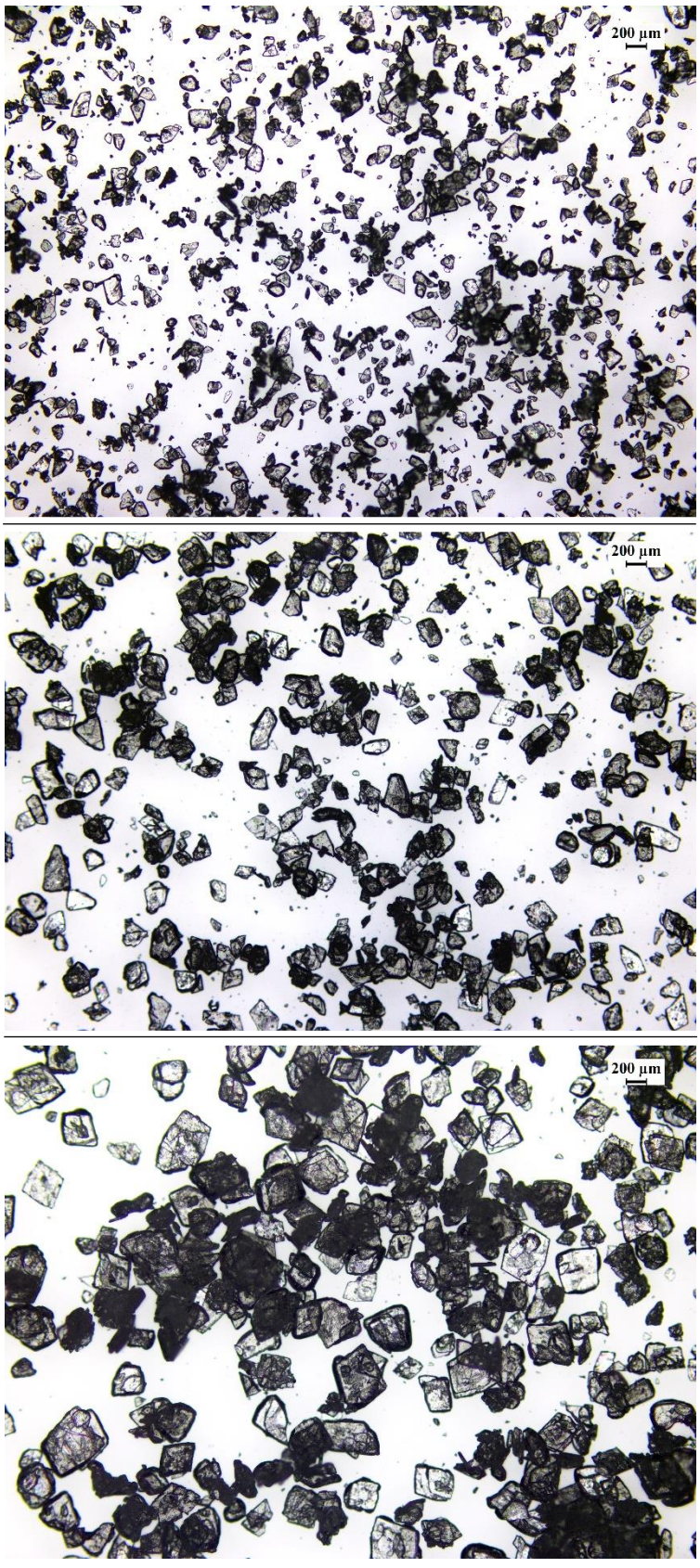

Figure 6.3. Sieved seed fractions of anthranilic acid form I.
0-63 µm (top), 63-125 µm (middle) and 125-250 µm (bottom).

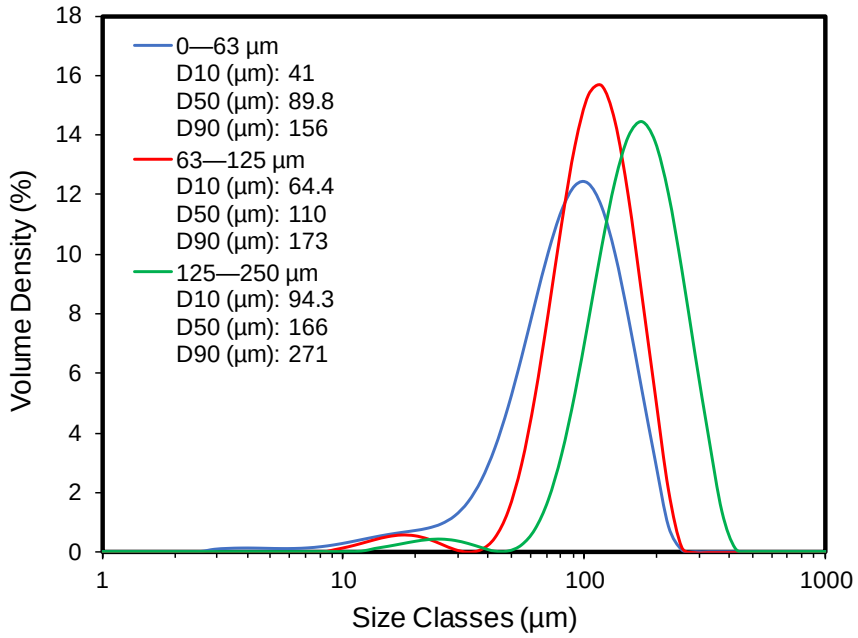

Figure 6.4. Particle size distributions for the three anthranilic acid sieve fractions.

6.3.2 Mixing and Addition Method

In an ideal scenario, the solution and antisolvent would be perfectly mixed, with the seed material evenly and instantaneously dispersed throughout the entire volume at the onset of the experiment. However, this is not practically possible, and so an addition strategy was devised that was deemed to have the fewest compromises. One consideration was the addition of solution to the OBC, followed by the required volume of antisolvent and seed material. However, the seed material is poorly wetting in water, and would result in difficulties transferring the entire mass of seed to the OBC. Other potential problems with mixing, gas bleeding and initial concentration measurements led to alternative addition strategies being considered. The strategy that was ultimately adopted was mixing the solution and antisolvent outwith the OBC, followed by addition of the majority of the resulting mixture to the OBC. Some solution was reserved to facilitate seed addition. This method ensured the ATR probe was submerged and gas at the piston head could be purged. Concentration measurements could then be made in the supersaturated solution for some initial data points. Seed material was then transferred to the OBC by suspension in the remaining solution volume. To ensure rapid mixing of solution and antisolvent, the solution was weighed in a 250 ml flask, and the antisolvent was weighed in a syringe, shown in

Figure 6.5. The action of depressing the plunger of the syringe rapidly mixed the solution and antisolvent, and ensured as much of the antisolvent as possible was added to the solution, compared to a different vessel where some antisolvent may not be transferred due to adhesion to the walls.

Figure 6.5. Seed, solution and antisolvent in preparation for mixing.

6.3.3 Induction Times and Modification of Initial Design Space

The addition method described in the previous section required a sufficiently long induction time such that primary nucleation would not occur in the resulting supersaturated solution before the seeds could be added. Therefore, a small-scale experiment was set up, shown in Figure 6.6, where the required solution and antisolvent masses were added to flasks with magnetic stirrers, with no seeds present. Induction times of less than five minutes were deemed necessary, which would allow sufficient time for the mixing of solution and antisolvent, transfer to the OBC and addition of seeds before primary nucleation would occur, with a few minutes of leeway. Although these induction times are effectively measured in an STR as opposed to an OBC, and will therefore be different across the platforms, they were assumed to be reasonably transferrable [142], [143]. Furthermore, particles were not observed when adding solution to the OBC in all cases, and the induction times measured represent a worst-case scenario, as in practice the solutions were not continuously stirred after

antisolvent was added and so would experience no shear from the action of a magnetic stirrer.

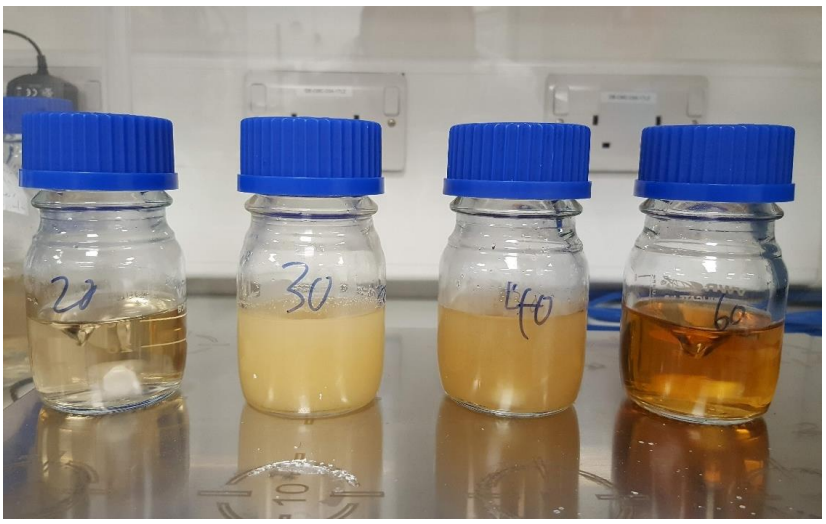

Figure 6.6. Induction time measurements for initial antisolvent fractions.
From left to right: X_{EtOH} = 0.2, 0.3, 0.4 and 0.6.

The original conditions showed induction times that were too short at X_{EtOH} of 0.3 and 0.4. As the starting solutions had already been prepared, it was necessary to reduce the ratio of antisolvent to solution in order to produce a lower supersaturation ratio in these conditions. Ethanol mass fractions were modified as detailed in Table 6.1 and Figure 6.2, being increased from X_{EtOH} = 0.3 and 0.4 to X_{EtOH} = 0.36 and 0.50, respectively. This in turn reduced $(c-c^{\star})/c^{\star}$ from 0.89 to 0.39 for X_{EtOH} = 0.50, and from 0.95 to 0.52 for X_{EtOH} = 0.36. Induction time measurements under these modified conditions showed no unwanted primary nucleation within the required time period.

6.3.4 UV-Vis Spectroscopy Calibration and Measurement

Different concentration measurement techniques were considered for the process, but as anthranilic acid has been shown to be UV active [100], ATR UV-vis was selected. This allowed for the acquisition of real-time concentration data that would give significantly more data than point samples by an offline technique. This also had the advantage that the potential for introducing disturbances by sampling was eliminated.

UV calibration was performed by preparing a range of concentrations of anthranilic acid in a range of ethanol mass fractions, and measuring the absorbance. An example of an unprocessed anthranilic acid spectrum is shown in Figure 6.7.

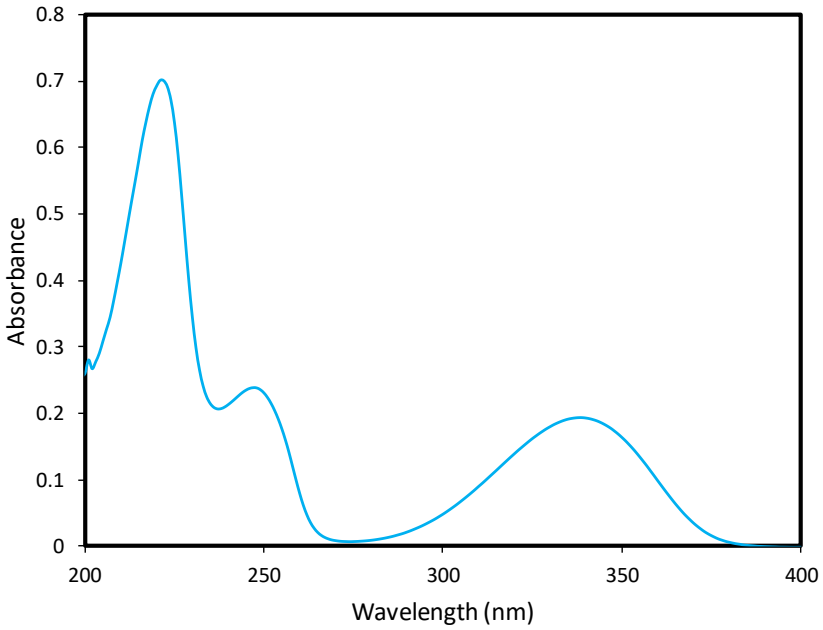

Figure 6.7. Representative unprocessed UV spectrum of anthranilic acid.

The UV spectrum shows three distinct absorbance peaks at 222, 248 and 340 nm. For development of a calibration model, the raw spectra were processed by taking the first order derivative over nine points to correct for any baseline drift, with an example shown in Figure 6.8.

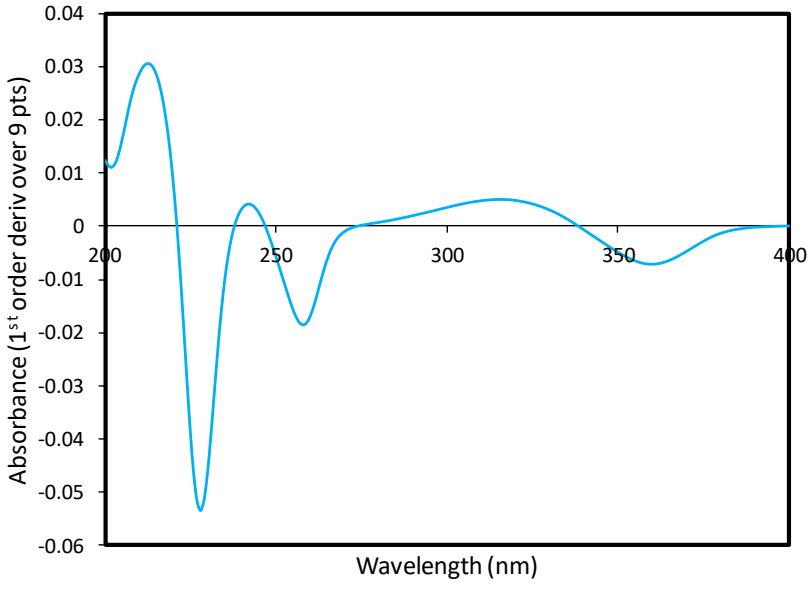

Figure 6.8. Representative first order derivative UV spectrum of anthranilic acid.

The derivatised UV spectrum of the UV spectra of anthranilic acid shows a maximum at 227 nm, and was therefore the wavelength that was selected for development of the calibration model. To develop the model, UV spectra were collected for a range of anthranilic acid concentrations in a range of ethanol mass fractions. This was performed in the same apparatus as in Figure 6.1, with the exception that the bottom bend section was replaced with a bend with an integrated tap. This facilitated draining solution from the apparatus between concentration measurements, whilst preventing disturbance of the optical fibres of the UV probe that could affect the calibration model.

For each ethanol mass fraction, six standards were prepared at varying anthranilic acid concentrations, corresponding to approximate supersaturation ratios of 0.6 – 1.1. The measurement method for each ethanol fraction consisted of washing through the apparatus with blank solvent of the appropriate ethanol fraction, followed by filling with this blank to submerge the ATR probe. The blank solvent was allowed to reach 25 °C before a reference spectrum was taken. This process was repeated with the anthranilic acid solutions, moving from the lowest to the highest concentration, and then repeated in its entirety for each new ethanol fraction. Spectra were collected with an integration time of 60 ms and 5 scans per measurement, with single measurements for developing the calibration model, and measurements every 10 seconds for the experiments.

6.3.5 Sizing by Laser Diffraction

Particle size was measured offline on a representative sample taken at the end of each experiment. The samples were filtered over a vacuum filter, washed with 20% ethanol (w/w) and dried over 24 h. The dried crystals were then characterised by laser diffraction as described in 3.2.5.1.

6.4 Formulation of the Population Balance Model

The modelling tool selected was gPROMS FormulatedProducts 1.3, a commercial software developed by Process Systems Enterprise Limited for the modelling of crystallisation and other pharmaceutical manufacturing processing with built-in population balance equations (PBEs). The numerical method implemented in gPROMS FormulatedProducts 1.3 to solve the PBE is the high-resolution finite volume scheme with flux-limited function (HRFVS-FL), which is described in detail elsewhere [144], [145].

For a batch crystallisation the population balance takes the form of:

$$\frac{dn}{dt} + \frac{dG}{dL} = B - D \tag{6.2}$$

where G is the linear growth rate, B the nucleation rate and D the crystal loss rate. In this specific case, as all experiments are to be seeded, primary nucleation is not considered. Therefore, B solely consists of secondary nucleation. These can be further defined by the appropriate kinetic models, described in the following sections.

6.4.1 Model Assumptions

The model makes the following assumptions:

- The contents of the crystalliser are uniform in space, i.e. the vessel is well mixed.
- The liquid and solid phases in the bulk are in thermal and mechanical equilibrium, i.e. at the same temperature and pressure.
- The liquid and solid phases are not in chemical equilibrium, i.e. different chemical compositions.
- All crystals are of the same shape and can be characterised by a chosen linear dimension, L.

6.4.2 Growth

Crystal growth is dependent on many factors such as supersaturation, temperature, size and more, and as such there is no single method of expressing growth rate that takes all these factors into account [34]. There are various growth rate expressions that could potentially be implemented, as detailed in Table 1.2. However, to facilitate solving the PBE, a size-independent growth rate expression was applied:

$$\mathrm{G} = k_G \left(\frac{c - c^*}{c^*}\right)^g \tag{6.3}$$

where k_G is the linear growth rate constant (m/s), (c-c*)/c* is the relative supersaturation, and g is the growth rate order. Terms k_G and g highlighted in blue in

Equation 6.3 are parameters to be estimated. A power law has been successfully implemented elsewhere to determine growth kinetic parameters for anthranilic acid in a water/IPA solvent system in the presence of additives, showing that this method is acceptable [146]. A simple generic expression was used initially; however, this could later be modified if other factors were determined to be significant, such as by incorporation a size-dependent growth factor.

6.4.3 Secondary Nucleation

Secondary nucleation is the process of nucleation influenced by the presence of existing crystals. As in the case of growth rate expressions, there are various secondary nucleation expressions that could potentially be implemented, as detailed in Table 1.1. A power law function was selected to simplify solving the PBEs:

$$B_{\text{sec}} = \exp(\ln k_B)\left(\frac{c - c^*}{c^*}\right)^n \varepsilon^a \rho^b \tag{6.4}$$

where B_{sec} is the secondary nucleation rate, k_B is the secondary nucleation rate constant, n is the secondary nucleation rate order, ε is the energy dissipation rate (W/kg), a is the energy dissipation rate order, ρ is the slurry density (kg/m^3), and b is the slurry density order. As stated previously, other crystallisation phenomena could be considered, such as primary nucleation and agglomeration. However, seeding allows primary nucleation to be ignored. Slurry density provides information on collision rates.

6.4.4 Solubility Expression

The solubility of anthranilic acid in ethanol and water mixtures was determined experimentally in section 4.3.1. Whereas the solubility was expressed in terms of volume fractions previously, here it is expressed as mass fractions to facilitate processing of data within this chapter. The solubility is described by a polynomial fitted to the experimentally determined solubility data:

$$c^* = -0.4453\, X_{\text{EtOH}}{}^3 + 0.8146\, X_{\text{EtOH}}{}^2 - 0.1677\, X_{\text{EtOH}} + 0.0103 \tag{6.5}$$

The fit is shown as the blue dashed line in Figure 6.2, and has good correlation ($R^2 = 0.9972$).

6.5 Results and Discussion

6.5.1 Growth Parameter Estimation

Crystal growth can be described as a two-step mechanism, consisting of diffusion of solute to the surface of a crystal, followed by the integration of solute into the crystal structure [147]. Dissolution is in effect the reverse of this process with no integration step, and can be used to determine the rate-limiting factor in crystal growth, i.e. limited by the diffusion of solute or the integration of solute to the crystal surface. A dissolution experiment was performed, the results of which are shown in Figure 6.9.

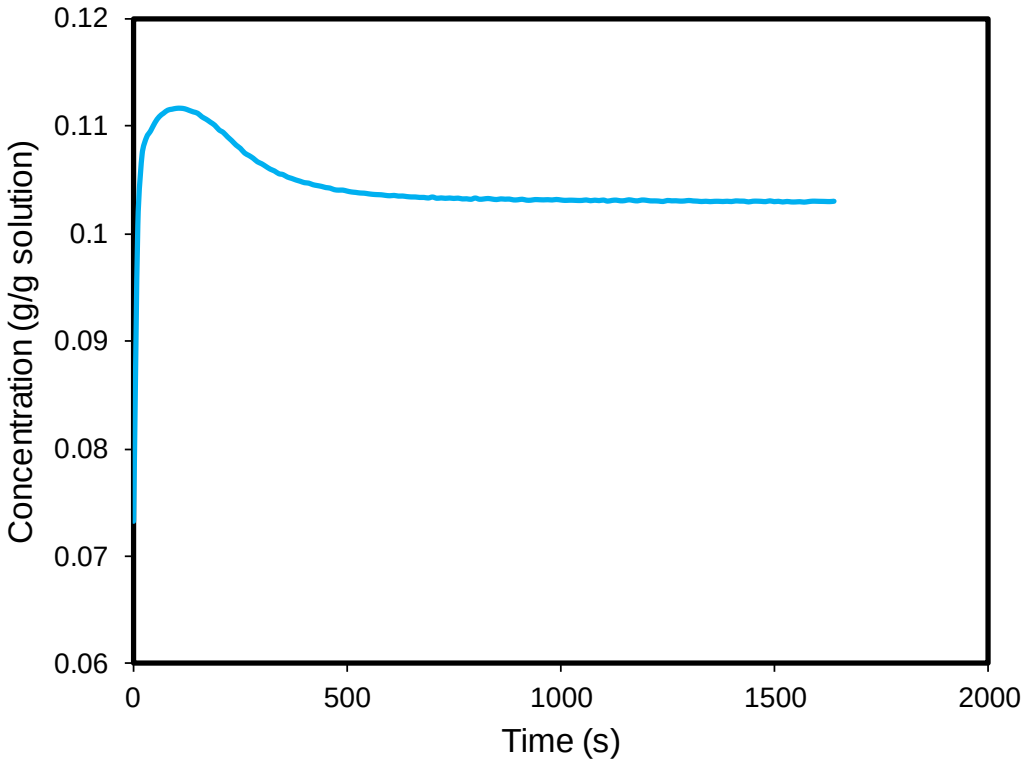

Figure 6.9. Concentration profile for mass transfer experiment 1.

If the rate of dissolution was slow, then the process would be limited by the diffusion of solute into the solvent and the concentration would increase slowly. However, the concentration increases rapidly, indicating mass transfer is rapid. Therefore, crystal growth is likely to be limited by surface integration.

The concentration goes through a maximum before reaching a stable value. This is due to the position of the UV probe in the apparatus relative to the location of solid

addition. The compound dissolves rapidly, which is observed as the spike in concentration. However, there exists a localised area of high concentration at the UV probe, due to the solute not having been completely dispersed throughout the total volume of the vessel. The observed reduction in concentration is where the distribution of solute occurs and reaches a steady value.

To estimate parameters for growth rates as per Equation 6.3, a number of experiments were performed as detailed in Table 6.1. The concentration profiles and the initial fits to the standard growth model are shown in Figure 6.10. Only the concentration data is fitted, with the CSD being measured but not fitted. Fitting is performed simultaneously over multiple experiments.

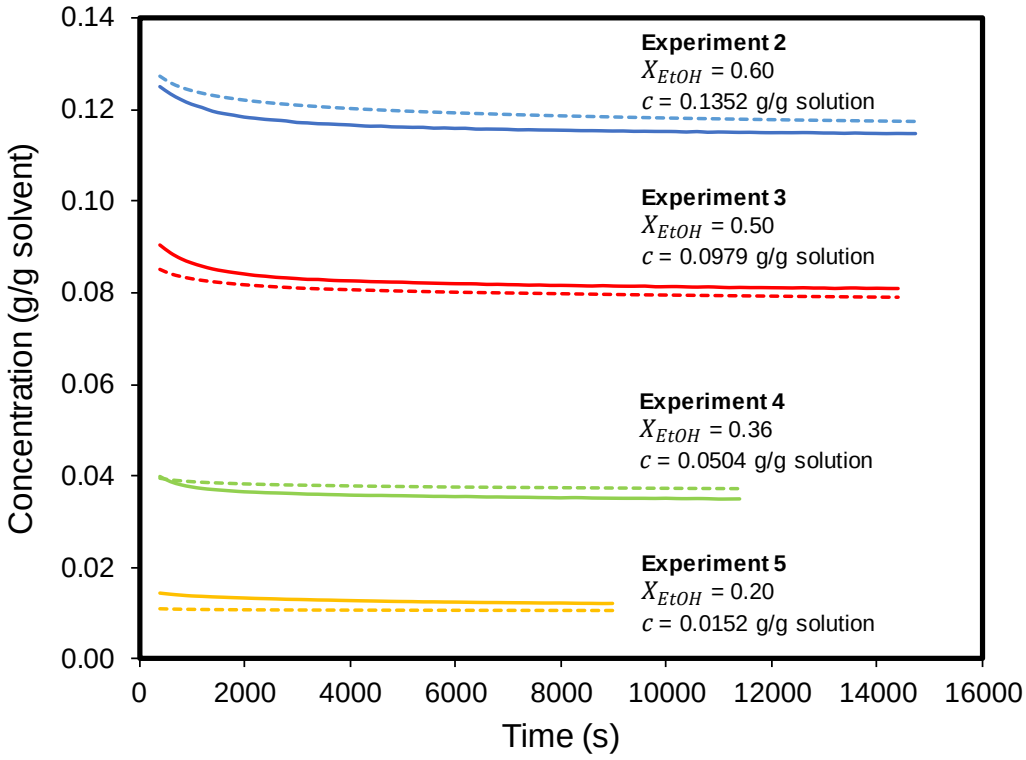

Figure 6.10. Measured (solid lines) and predicted (dashed lines) concentration profiles for growth rate experiments.

Each experiment shows a similar trend. Initially, there is a rapid reduction in concentration, which is attributable to the high supersaturation driving crystal growth. The rate of reduction of concentration then slows as the supersaturation is consumed, and the crystal growth rate decreases. The initial fits to the standard growth model are

not in good agreement with the measured values, and suggests that there are further factors that need to be incorporated into the growth model. Estimates of parameters are shown in Table 6.3.

A recent article noted that nucleation and growth kinetics were significantly affected by the solvent composition in a combined cooling and antisolvent crystallisation process [148], with inaccurate predictions when the kinetic dependence on solvent composition was neglected. Initially, k_g and g values were estimated to minimise the residuals across all four growth experiments between experimental and predicted values. However, if k_g and g were estimated to individual experiments, more acceptable residuals are obtained, the results of which are shown in Table 6.2 and Figure 6.11.

Table 6.2. Kinetic parameters from initial parameter estimation when fitted to individual experiments.

Experiment #	X_{EtOH}	S_I	k_G	$\ln k_G$	g
2	0.60	1.30	1.91×10^{-3}	-6.26	6.93
3	0.50	1.39	3.35×10^{-5}	-10.30	5.82
4	0.36	1.52	8.66×10^{-6}	-11.66	3.72
5	0.20	1.63	8.98×10^{-6}	-11.62	8.83

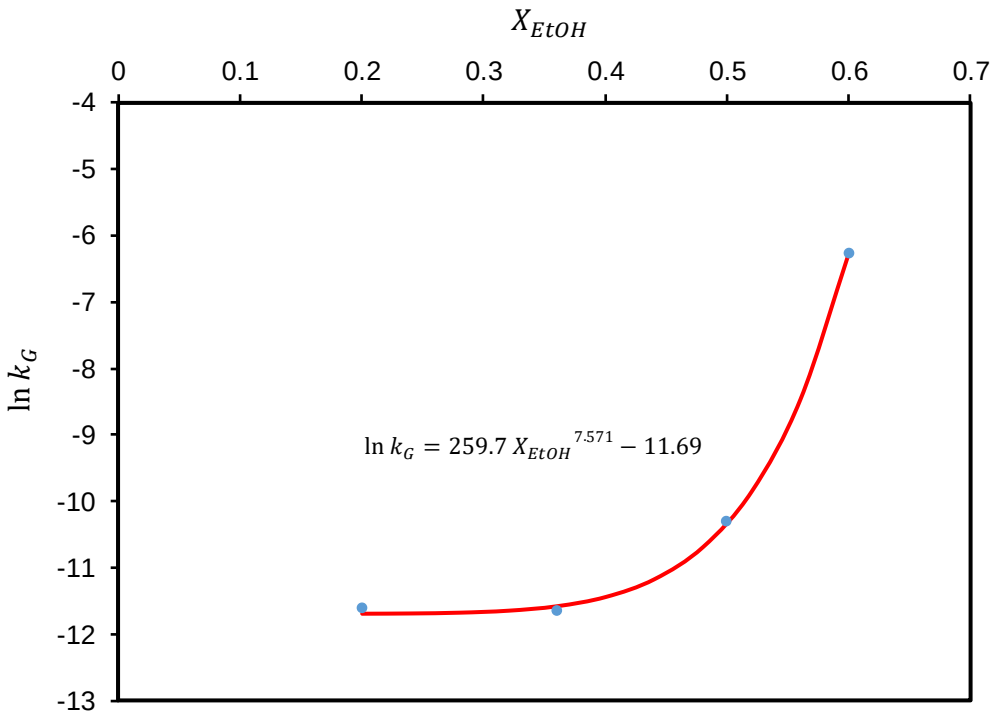

Figure 6.11. Growth rate constant as a function of ethanol mass fraction.

The values for g, ranging between 3.7 – 8.8 are high compared to other examples in the literature [149], [150], where it typically has values between 1 – 2. The high value may be attributed to the influence of S, which is also relatively high, ranging from S = 1.30 –1.63. Such high values of g may imply the surface integration step is severely limiting the growth rate [150].

If the growth rate expression was to be applied to an MSMPR cascade, no further processing would be required, as individual k_G values could be determined for each vessel in the cascade. However, in the case of a plug flow crystalliser, where in practical terms there is a degree of axial dispersion, there will not be discrete ethanol fractions, but rather a continuum of ethanol fraction across the length of the crystalliser.

Taking the solvent fraction into account, a modified growth rate expression based on Figure 6.11 was derived:

$$\mathrm{G} = k_G' \left(\frac{c - c^*}{c^*}\right)^g \tag{6.6}$$

$$k_G' = \exp\left(k_G {X_{\mathrm{EtOH}}}^{g2} - k_{G,0}\right) \tag{6.7}$$

where k_G' is the modified growth rate constant (m/s), X_{EtOH} is the solute-free ethanol mass fraction (g/g), $g2$ is the order of ethanol mass fraction, and $k_{G,0}$ represents the growth rate constant at zero ethanol fraction (m/s).

Using the redefined growth rate expression, parameter estimation was performed using initial guesses of k_G, $g2$ and $k_{G,0}$ of 259.7 m/s, 7.571 and 11.69 (m/s), respectively. The results of fitting with these parameters are shown in Figure 6.12, and the parameters themselves in Table 6.3. It is assumed that g is constant for fitting of Equation 6.6, but as stated previously, g may also be influenced by X_{EtOH} [148], [151].

Parameter estimation was carried out in gPROMS by minimising a maximum likelihood objective function as described in detail in [136]. The final product CSDs were not included in the fitting objective function; this consisted of only the concentration data.

Table 6.3. Growth kinetic parameters with and without solvent effects.

Parameters	No solvent effect; Equation 6.3	Solvent incorporated; Equation 6.6	Standard deviation
k_G	5.11163×10^{-3}	195.205	31.19
g	8.10739	4.66465	0.3165
$g2$	-	9.88023	4.223×10^{-4}
$k_{G,0}$	-	11.69	-
Residual	215857	192510	-

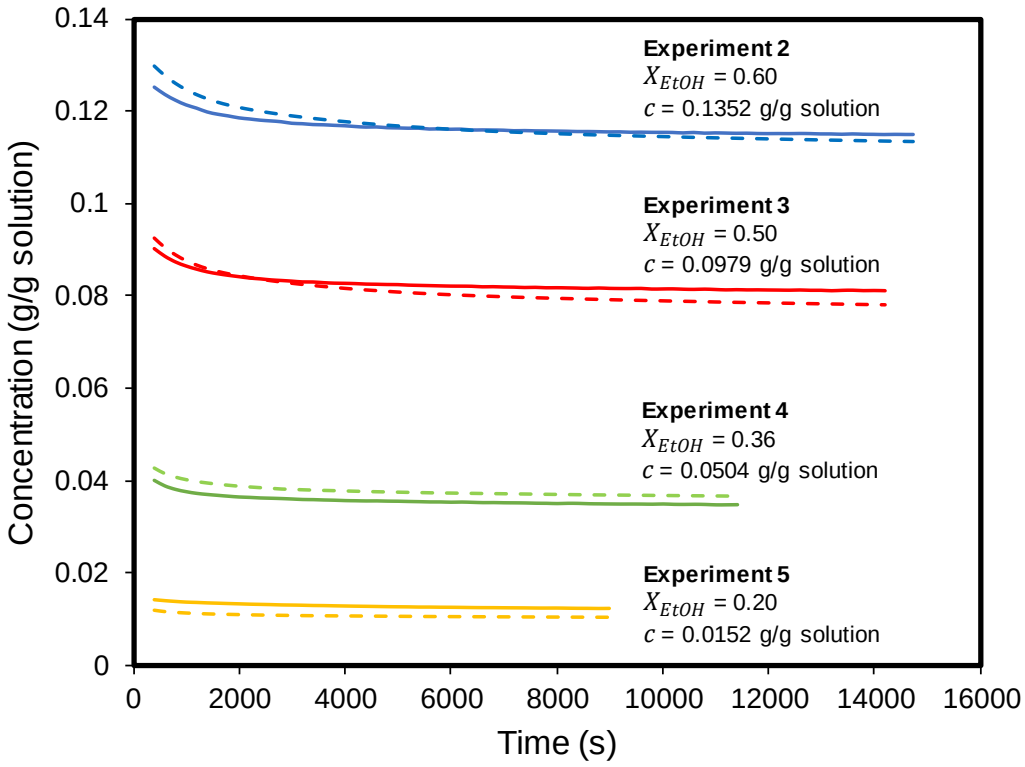

Figure 6.12. Measured (solid lines) and predicted (dashed lines) concentration profiles for growth rate experiments incorporating a solvent factor.

Qualitatively, these fits are somewhat improved. This is also reflected in the results of the goodness of fit test, where the weighted residual is reduced from 215857 to 192510. As an additional step to validate these expressions, comparisons were made between the measured and predicted product particle size distributions, shown in Figure 6.13 and Table 6.4.

(a

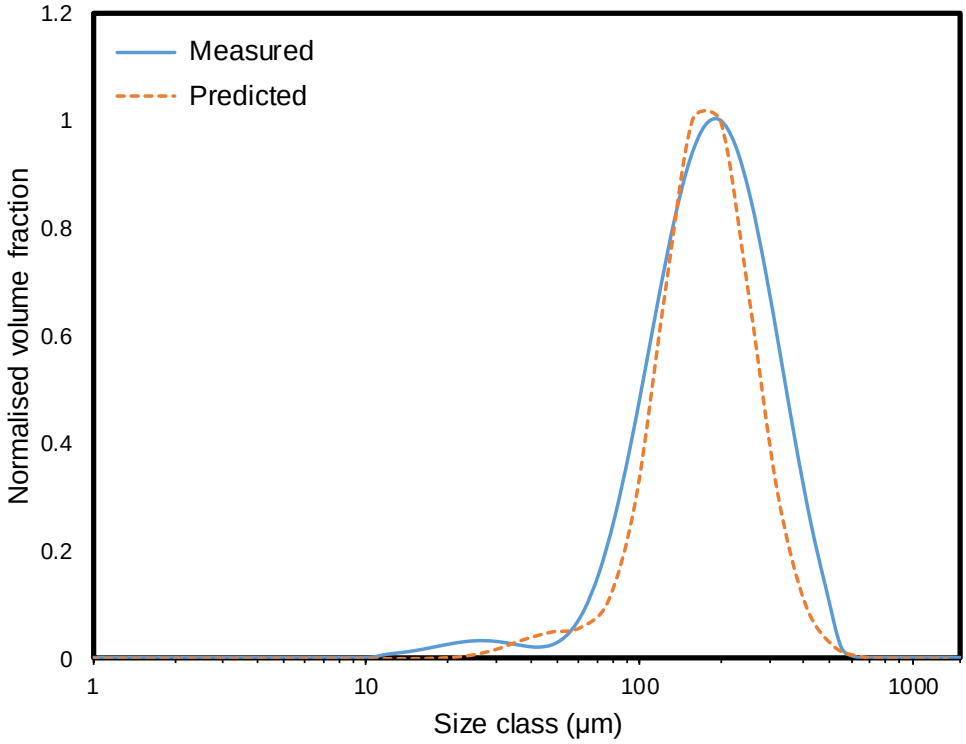

(b

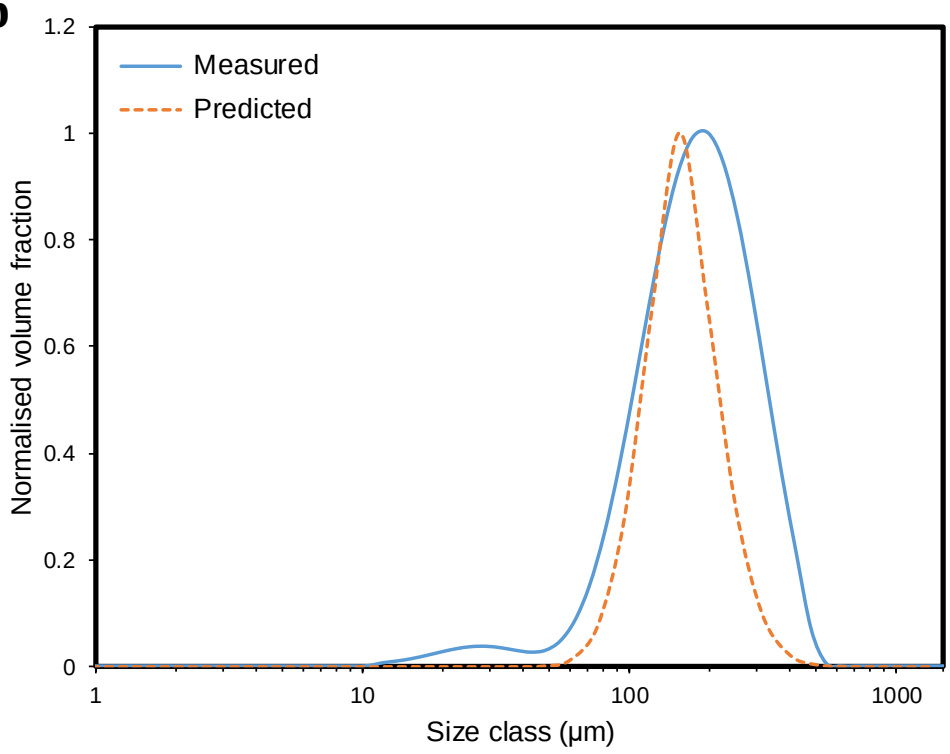

Figure continued →

(c

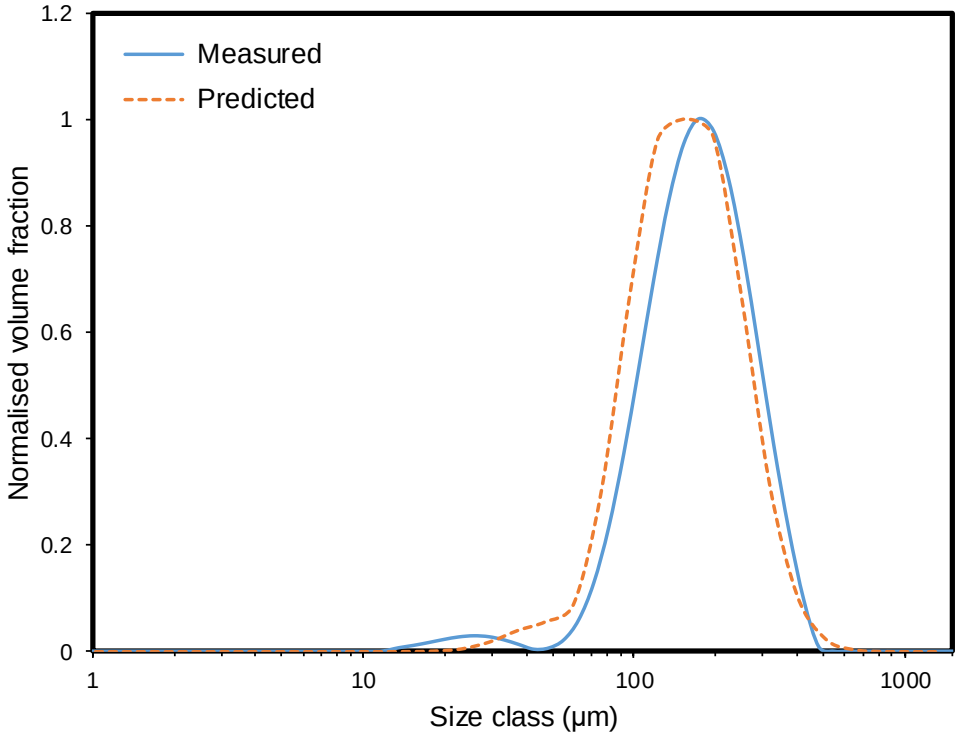

Figure 6.13. Measured and predicted CSDs for crystal growth from small seed. (a) X_{EtOH} = 0.6; (b) X_{EtOH} = 0.5; (c) X_{EtOH} = 0.36

Table 6.4. Measured and predicted growth CSDs for varying X_{EtOH}.

X_{EtOH}	Size Class	Measured (µm)	Predicted (µm)
0.6	D10	92.5	111
	D50	183	169
	D90	334	261
0.5	D10	90.9	111
	D50	180	170
	D90	321	263
0.36	D10	95.1	114
	D50	173	174
	D90	297	269

The fits of the predicted size distributions compared to the measured distributions show reasonable agreement. The measured size data for the condition X_{EtOH} = 0.2 is not available due to the crystals not being recovered from the experiment. The D10, 50 and 90 values in Table 6.4 when looked at in isolation do not appear to show good fits

in the case of X_{EtOH} = 0.5 and 0.36; however, when looking at the distribution curves in Figure 6.13, the measured particle size distributions (PSDs) have a tail towards the lower size region that will result in the size classes being shifted to lower sizes in comparison to the predicted PSDs. The model used to predict the PSD is a growth-only model, and does not take into account other effects that may be occurring during the crystallisation process that may result in the evolution of smaller crystals that could produce such a tail in the measured PSDs. Overall, the fits are reasonable, and as such this growth-only model is a satisfactory representation of the process.

6.5.1.1 Growth Parameter Uncertainty

The values reported in Table 6.3 are mean values as a result of fitting. However, these values will have variance associated with them. To investigate the impact of this, uncertainty analysis was performed on an arbitrarily selected experiment, which in this case was the experiment at X_{EtOH} = 0.6.

The variance-covariance matrix of the model parameters is shown in Table 6.5. This matrix contains an approximation of the variances and covariances of the estimated process model and variance model parameters and determines whether the parameters are varying together, or whether their values are independent of one another. This was produced using a built-in feature in gPROMS which takes the mean and variance of each individual parameter, and the covariance of the sum of the parameters.

Table 6.5. Variance-covariance matrix of growth kinetic parameters.

	k_G	g	$g2$
k_G	**973**		
g	9.85	**0.1**	
$g2$	-0.0734	-7.85×10^{-4}	$\mathbf{1.78\times10^{-5}}$

To highlight the attainable regions that these parameters could cover, scatter plots in Figure 6.14 show all possible combinations of these parameters. There is a high degree of correlation between k_G and $g2$, whereas k_G vs g and g vs $g2$ show poor correlation. Due to this correlation, further experimental work may be required to deconvolute this correlation. This could possibly be achieved by maintaining a constant X_{EtOH} whilst investigating different ranges of S.

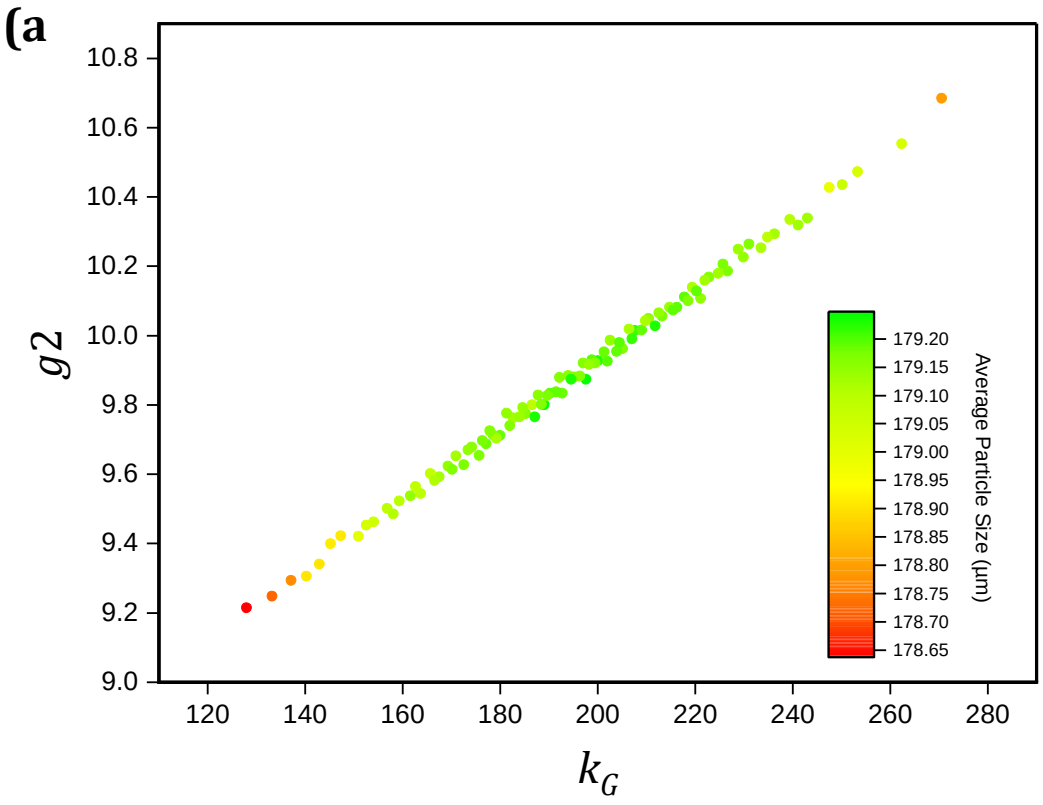

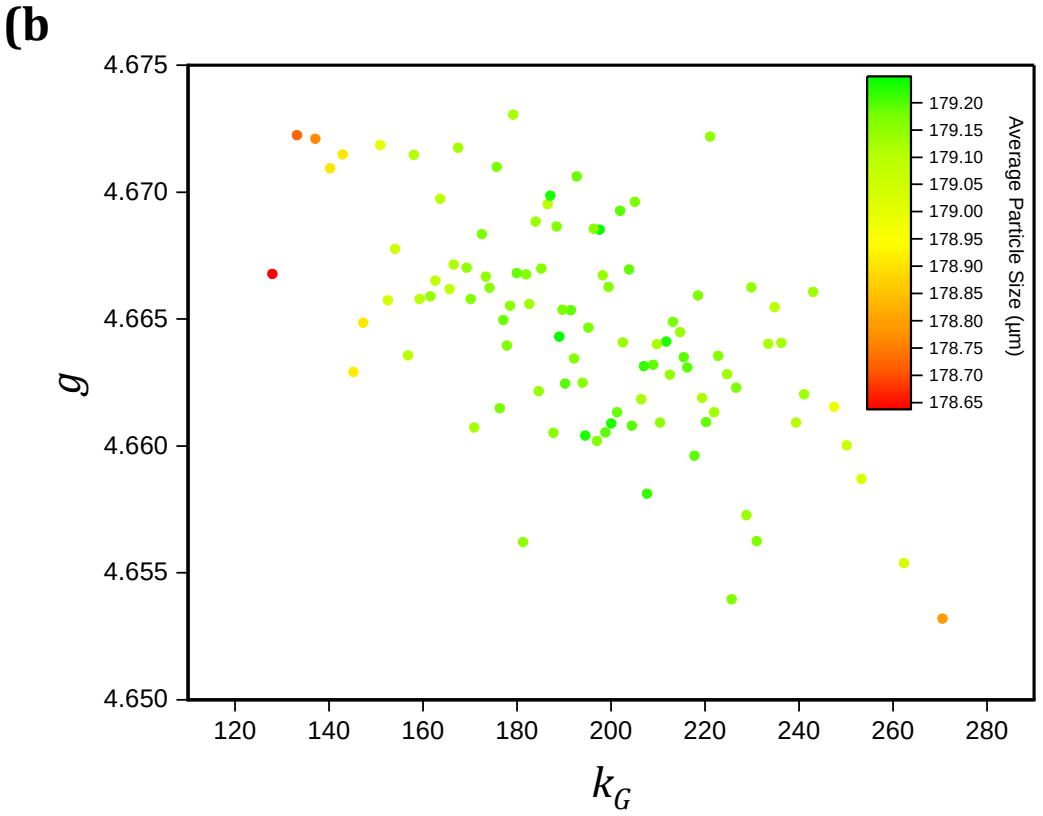

Figure continued →

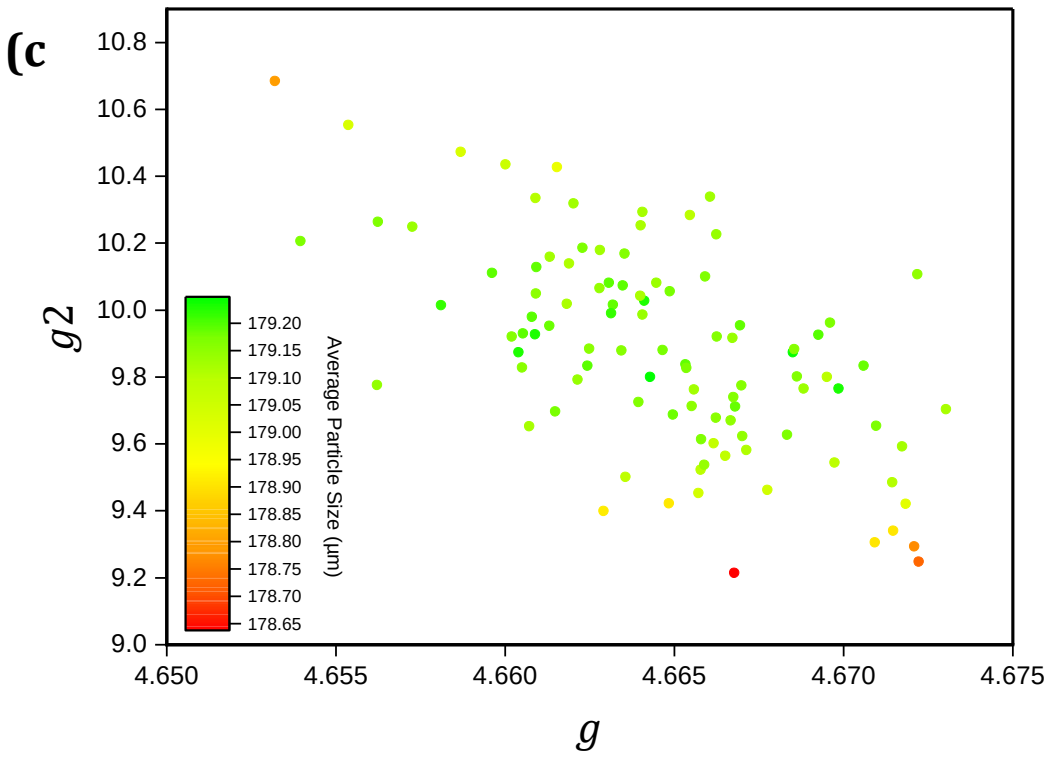

Figure 6.14. Scatter plots showing the correlation between model parameters at $X_{\mathrm{EtOH}} = 0.6$. (a) k_G vs $g2$; (b) k_G vs g; (c) g vs $g2$.

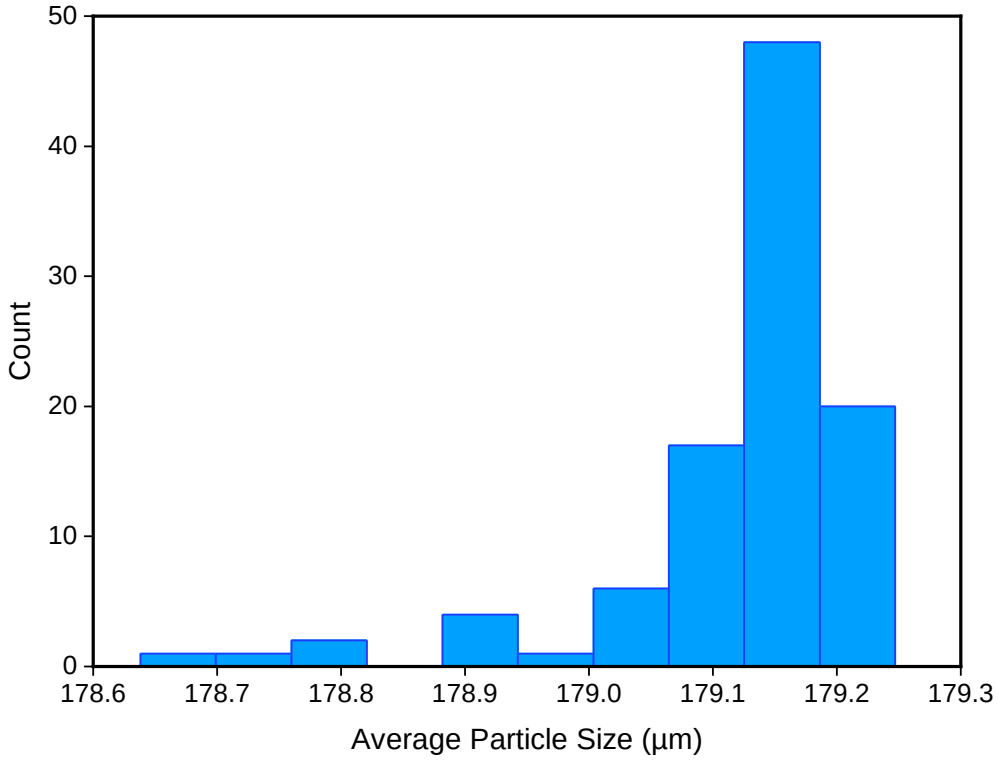

Figure 6.15. Histogram of PSD from predicted growth at $X_{\mathrm{EtOH}} = 0.6$.

The results of uncertainty analysis show that, despite variance within kinetic parameters, this variance leads to a narrow distribution of potential crystal sizes, as shown in Figure 6.15. Due to the correlation between k_G and $g2$, future experimental work might look to design experiments to decouple these parameters. Overall, the results of parameter estimation for growth rate kinetics look sufficient for starting secondary nucleation parameter estimation.

6.5.2 Secondary Nucleation Parameter Estimation

To estimate parameters for secondary nucleation rates as per Equation 6.4, a number of experiments were performed as detailed in Table 6.1. During parameter estimation, parameters for growth rate are also estimated; however, they are constrained by the mean and standard deviation of those parameters determined during growth rate parameter estimation as described in the previous sections. Due to concerns regarding data quality for concentration measurements made at lower ethanol fractions, only experiments 6, 9, 10 and 14 were used in parameter estimation.

The initial set of experiments that targeted crystal growth aimed to minimise the effects of secondary nucleation as these parameters were unknown initially. This was achieved by two methods. Firstly, the surface area for crystal growth was maximised by using a greater mass of seed and using the smallest sieve fraction. Secondly, the oscillation frequency and amplitude were set to the lowest values where adequate crystal suspension was observed, that is to say the lowest power density to provide a well-mixed system. The combination of these effects would minimise attrition in the growth experiments. In secondary nucleation experiments, where these effects were desired, power densities were increased, seed mass decreased and seed size increased significantly.

(a

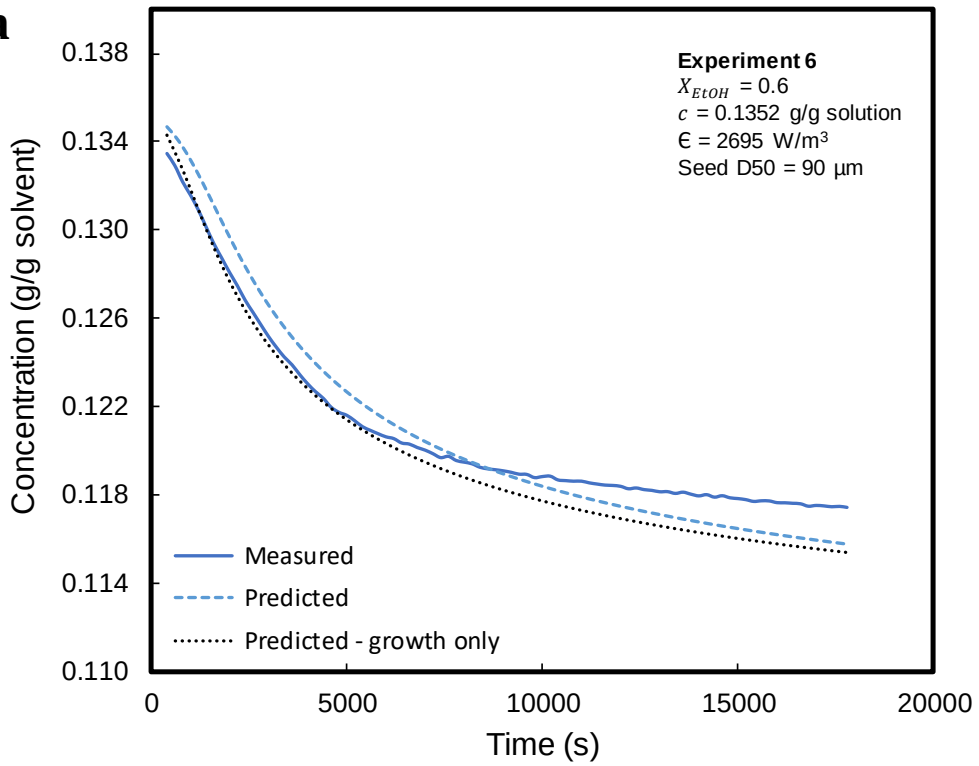

(b

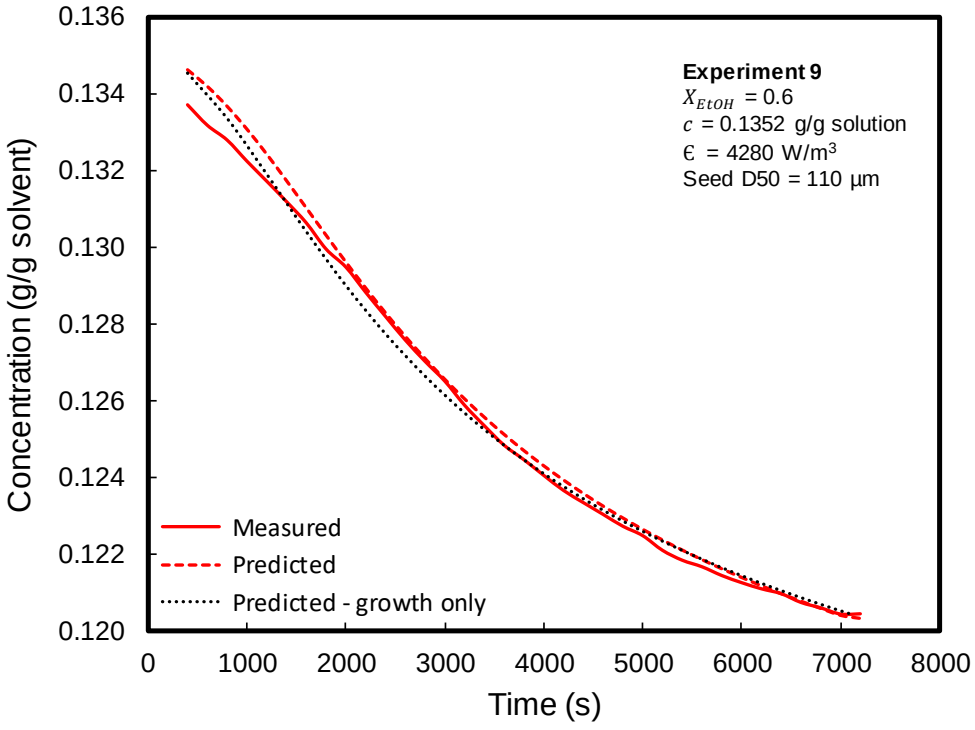

Figure continued →

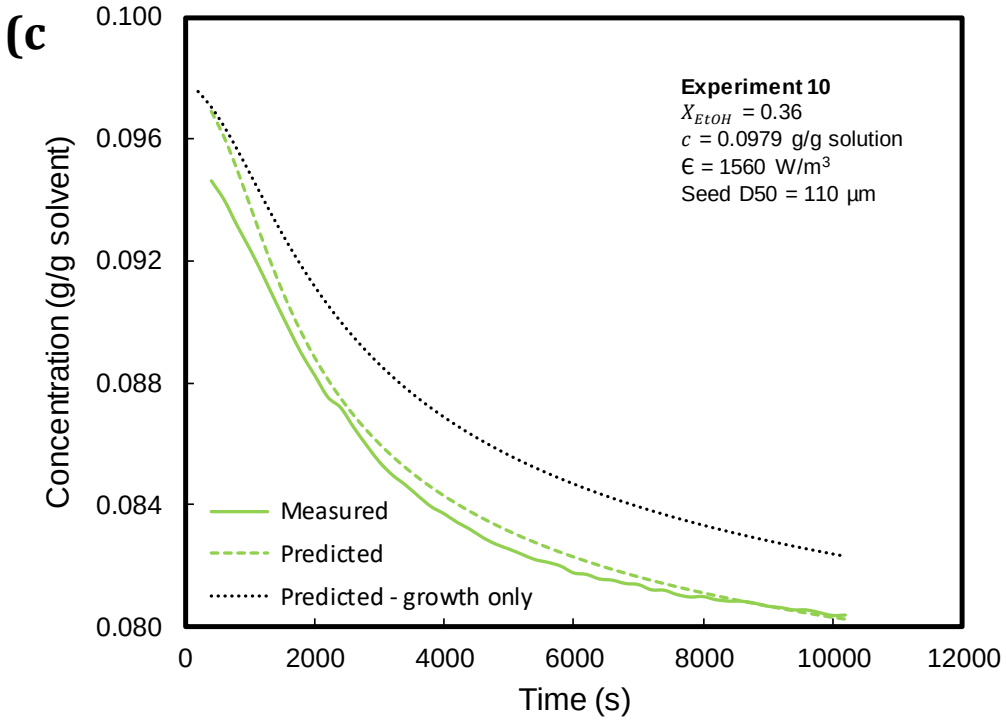

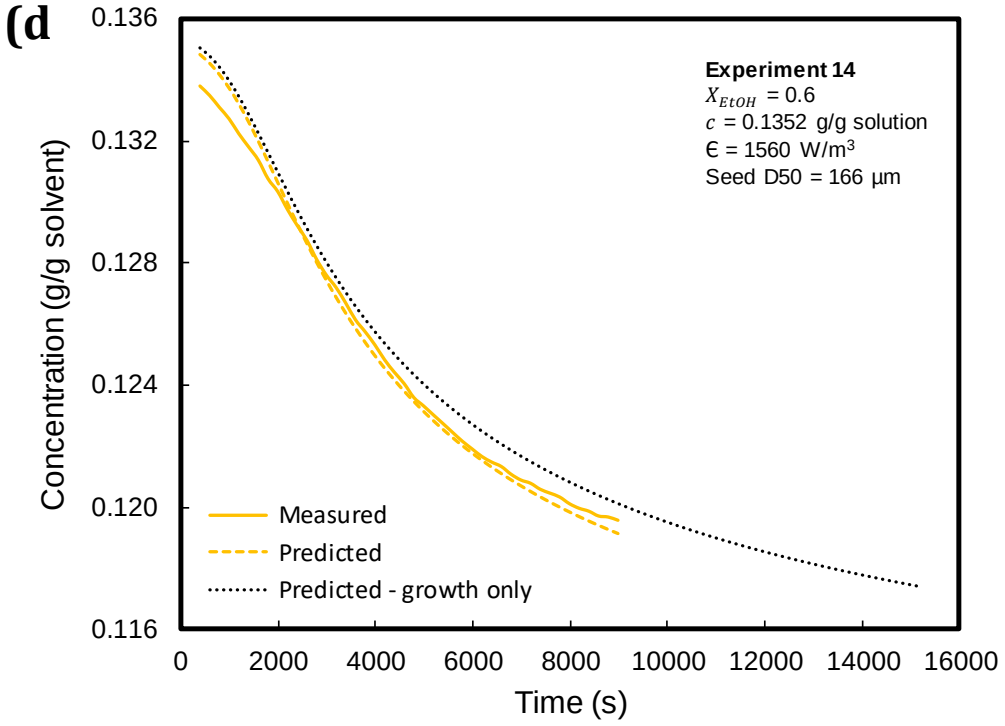

Figure 6.16. Concentration profiles for secondary nucleation rate experiments. Solid lines show measured concentrations. Dashed lines show predicted concentrations for a combined growth and secondary nucleation model. Dotted lines show predicted concentrations for a growth-only model.

The plots in Figure 6.16 show the measured and predicted concentration profiles for both a growth only model, and a model incorporating secondary nucleation parameters with the growth parameters. Figure 6.16a shows similar trends for both the growth-only and the secondary nucleation model predictions, but over a prolonged period, the measured concentration is higher than both predicted values. Figure 6.16b shows both a growth-only model and a secondary nucleation model predict the measured values well. The predicted concentration profile for combined growth and secondary nucleation appear to give higher concentrations than in the case of growth only; however, it is expected this is merely due to measurement error and that the measured and predicted values are equivalent.

The plots in Figure 6.16c shows a significant difference between the growth-only and the combined growth and secondary nucleation predictions, with the growth-only model being a poor representation of the process compared to the secondary nucleation model. As was seen in 6.5.1, and in Figure 6.11 specifically, growth rates were suppressed at lower ethanol fractions. In this case, where $X_{\mathrm{EtOH}} = 0.36$, the decrease in concentration cannot be attributed to growth alone. For Figure 6.16d, the secondary nucleation model once again gives comparable fits to the growth-only model.

Overall, the only condition whereby secondary nucleation parameters give any meaningful improvement in fits is in experiment 10. For experiment 9, where the power density is the largest, it would have been expected that secondary nucleation would have been much more significant. This suggests that, although equivalent power densities from stirred tanks were applied to the MFOBC, this factor alone is not sufficient to generate equivalent levels of secondary nucleation. This observation is supported by evidence in the literature that shows a greater degree of microstrain in the crystal structure of crystal products produced from impeller driven batch crystallisers (IDBCs) compared to an OBC at equivalent power densities, of a few orders of magnitude [152]. Much greater power densities would therefore be required to generate discernible levels of secondary nucleation on an attrition basis.

Table 6.6. Goodness of fit tests for growth-only and growth and secondary nucleation kinetic parameters. Highlighted cells are values that do not satisfy the null hypothesis for this test.

Kinetic parameters used	Experiment							
	6		9		10		14	
	χ^2	χ^2-critical	χ^2	χ^2-critical	χ^2	χ^2-critical	χ^2	χ^2-critical
Growth	209.24	108.65	4.80	47.40	1105.12	65.17	99.22	93.95
Growth and secondary nucleation	158.39	104.14	6.84	42.56	71.32	60.48	62.91	89.39

A growth-only model and a model that incorporates secondary nucleation parameters can be further differentiated by a chi-square goodness of fit test, the results of which are shown in Table 6.6. This is a statistical test that determines how well the model predictions fit the measured values by comparing the weighted residuals and the expected weighted residuals. Generally, this test takes the form of:

$$\chi^2 = \sum \frac{(\text{observed} - \text{expected})^2}{\text{expected}} \tag{6.8}$$

The null hypothesis for this test is that the difference between the weighted residual and the expected weighted residual is zero. If the χ^2-critical value is larger than the calculated χ^2 then the null hypothesis is rejected. The results of this test show that incorporating secondary nucleation parameters gives significant improvement to the predictions for experiment 14. The results for the other three experiments show a reduction in the residuals, although not sufficient to satisfy the null hypothesis, with experiment 9 having already satisfied the test under a growth only model.

(a

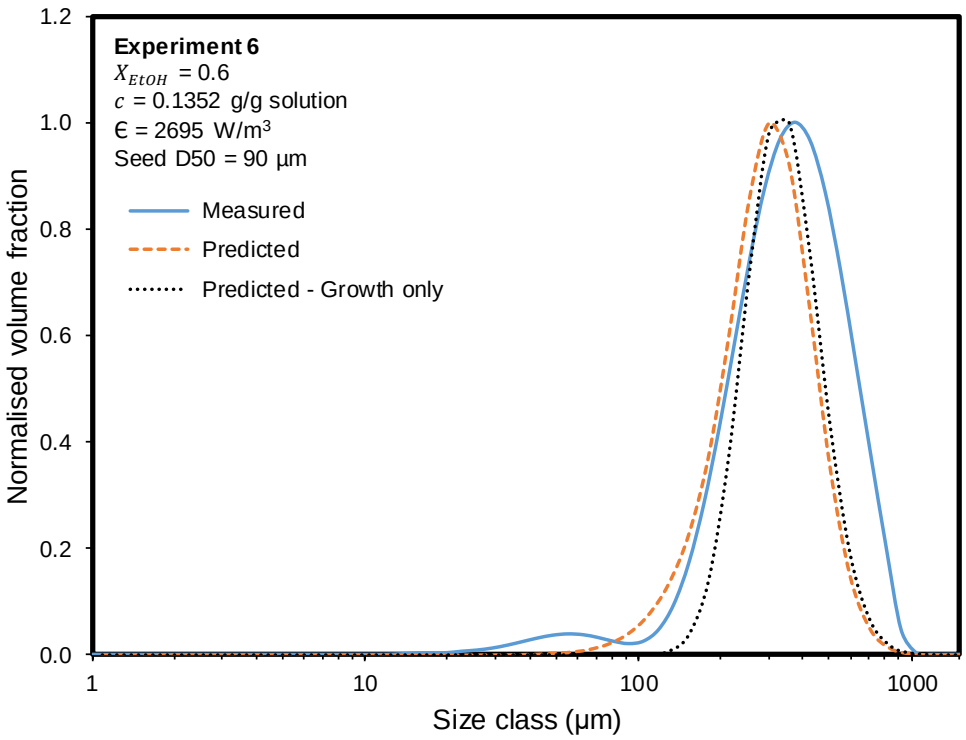

(b

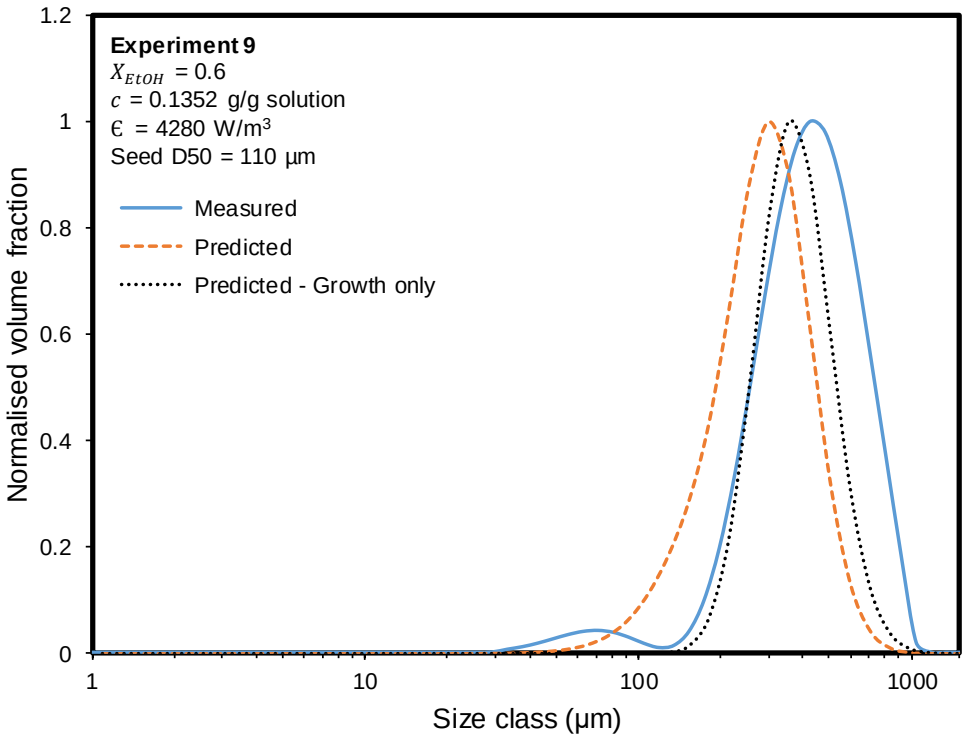

Figure continued →

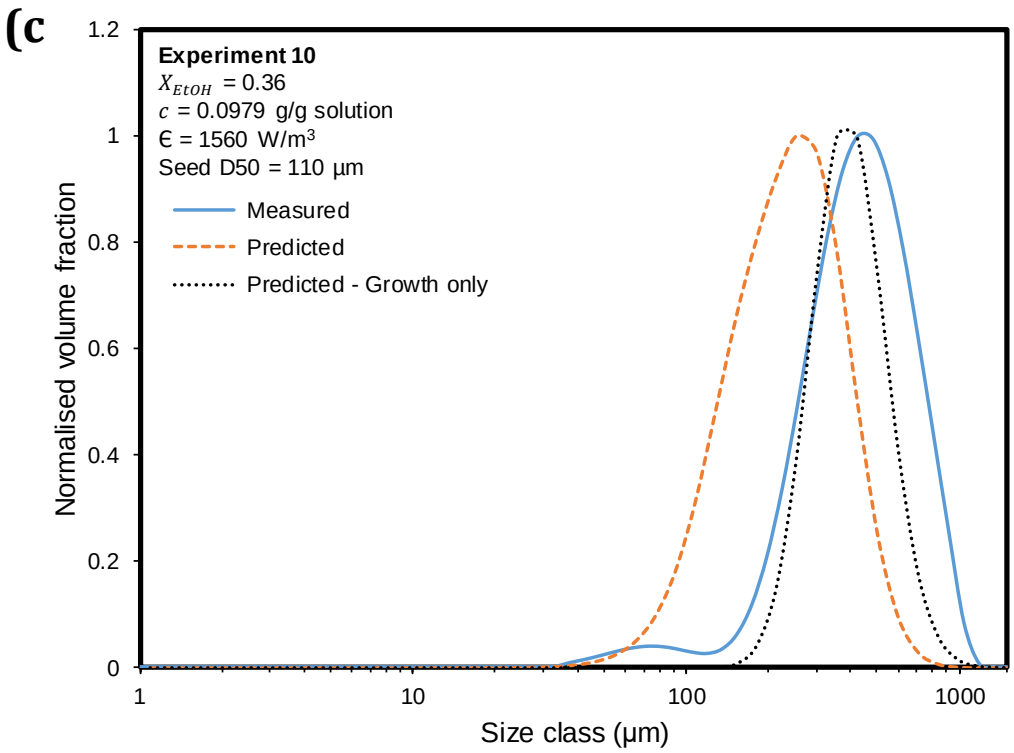

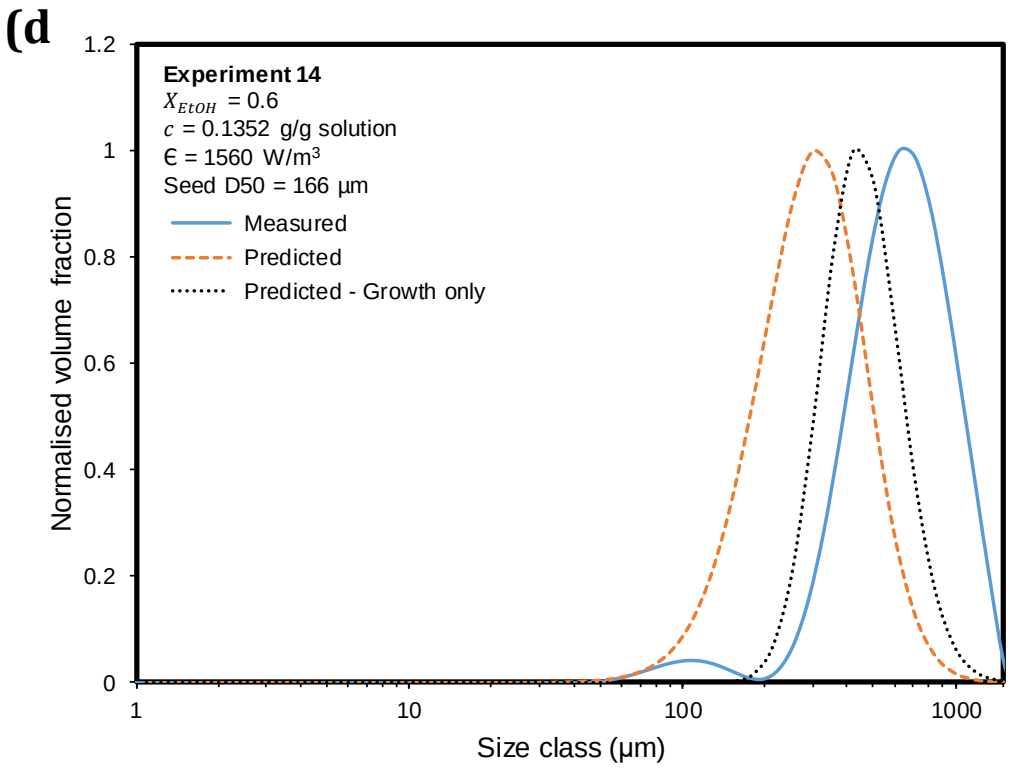

Figure 6.17. Measured and predicted PSDs for secondary nucleation experiments. Solid lines (blue) show measured PSDs. Dashed lines (orange) show predicted PSD for a combined growth and secondary nucleation model. Dotted lines (black) show predicted PSDs for a growth-only model.

Table 6.7. Measured and predicted PSDs for combined growth and secondary nucleation for varying ethanol mass fraction, seed size and power density.

Experiment	Size Class	Measured (μm)	Predicted – growth only (μm)	Predicted – growth and secondary (μm)
6	D10	187	223	168
	D50	357	334	296
	D90	620	506	470
9	D10	233	246	152
	D50	422	368	285
	D90	705	559	458
10	D10	230	261	118
	D50	431	391	234
	D90	735	592	412
14	D10	357	294	156
	D50	631	448	295
	D90	1040	699	515

The PSDs for the secondary nucleation experiments are shown in Figure 6.17 with key values tabulated in Table 6.7. For Figure 6.17a, both a growth-only and a secondary nucleation model gives PSDs that show a reasonable fit to the measured PSD; however, the secondary PSD has a wider span than the growth-only PSD that more closely resembles those of the measured PSD.

For the other three PSDs, there are more significant differences, with measured sizes all being larger than even a growth-only model predicts. Microscopy of the isolated crystal products are shown in Figure 6.18, and all show some degree of twinning, which would result in larger measured PSDs. Furthermore, due to the small amount of seed being added in these experiments, there is potential for variation in the seed material that could account somewhat for the observed shift in PSDs.

(a

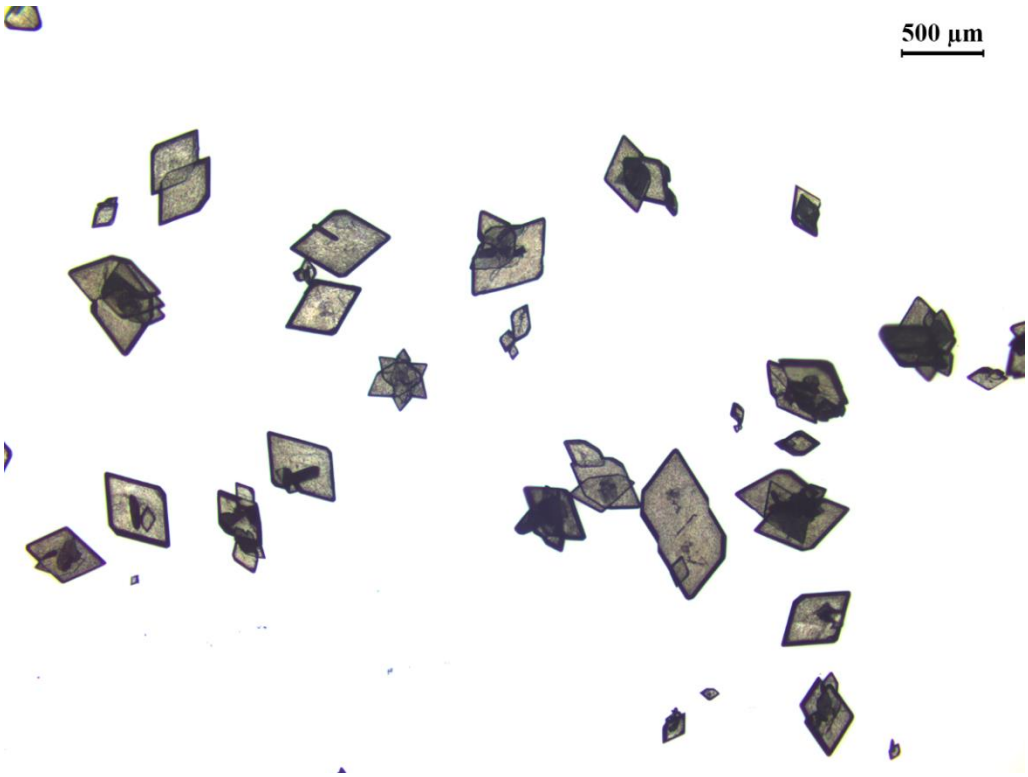

(b

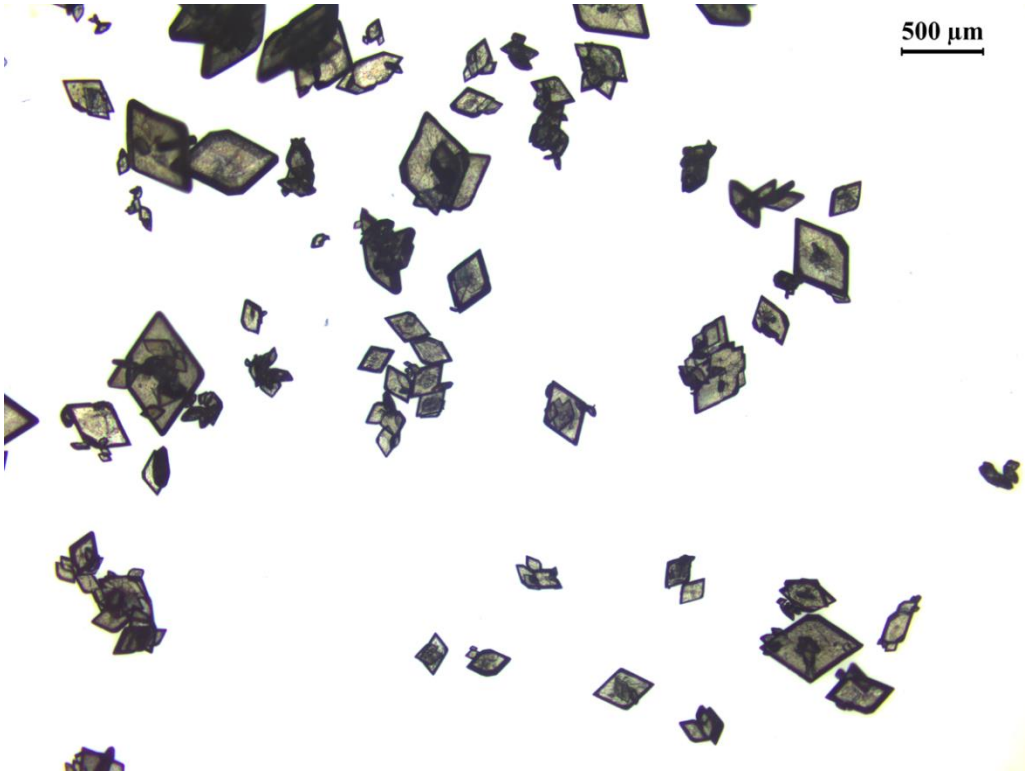

Figure continued →

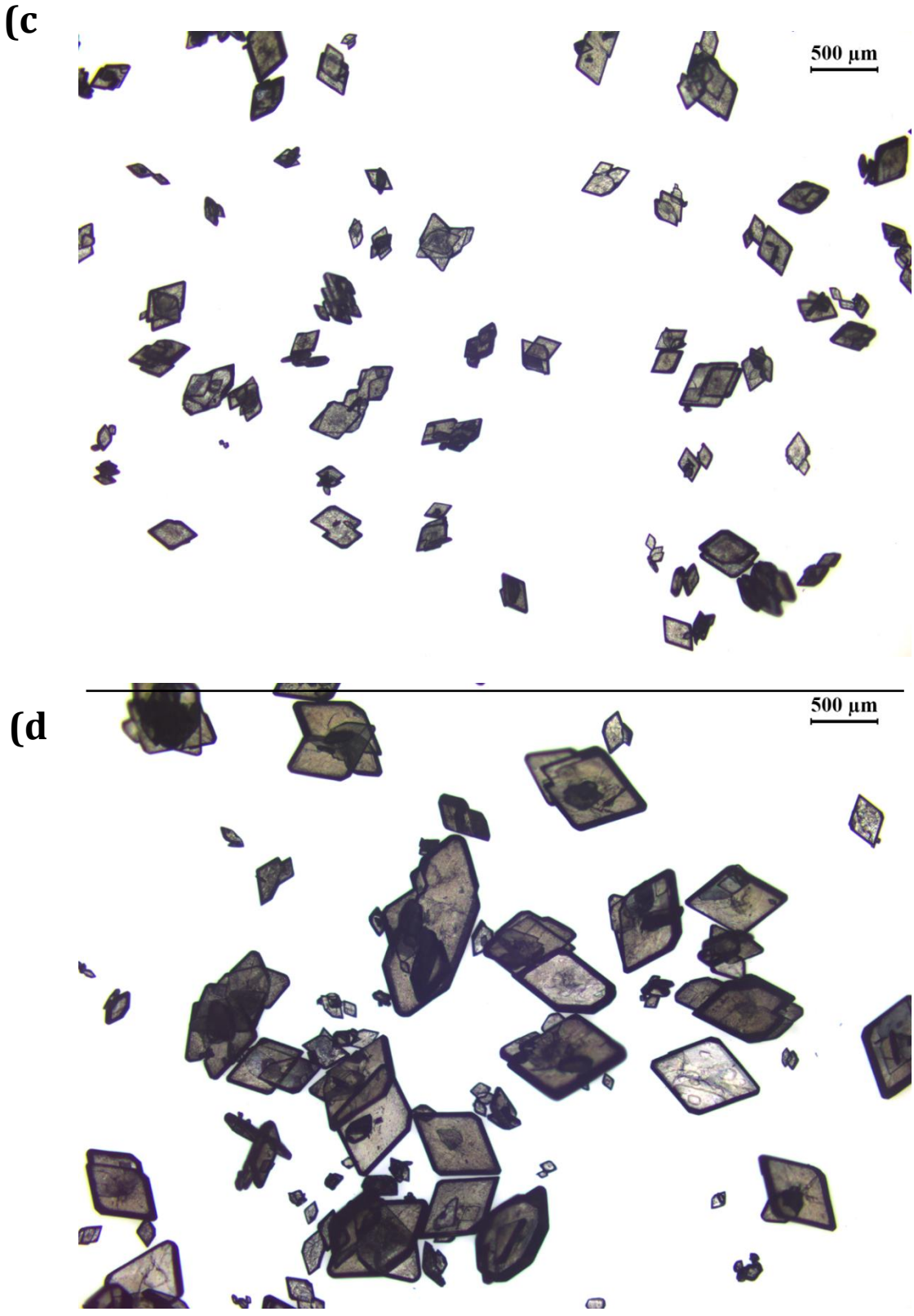

Figure 6.18. Microscopy of isolated crystal products from secondary nucleation experiments. (a) experiment 6; (b) experiment 9; (c) experiment 10; (d) experiment 14.

Mean values for the secondary nucleation kinetic parameters are shown in Table 6.8.

Table 6.8. Secondary nucleation kinetic parameters.

Parameter	Value	Standard Deviation
k_G	128.019	Not reported*
g	9.54405	0.349500
$g2$	4.65748	0.149800
$\ln k_B$	21.9416	1.52200
n	7	1.95
a	0.4	0.578500
b	0.300595	0.511700
Residual	299.457	-

$^\star k_G$ value at boundary set by growth parameter estimation

6.5.3 Secondary Nucleation Parameter Uncertainty

As was the case for the growth parameters in 6.5.1.1, values reported in Table 6.8 are mean values as a result of fitting and will have variance associated with them. Uncertainty analysis was performed on experiment 9 to determine its impact.

The variance-covariance matrix of the secondary nucleation kinetic parameters is shown in Table 6.9, containing an approximation of the variances and covariances of the estimated process model and variance model parameters.

Table 6.9. Variance-covariance matrix of secondary nucleation kinetic parameters

	g	$g2$	$\ln k_B$	n	a	b
g	**0.122**					
$g2$	-0.0504	**0.0224**				
$\ln k_B$	-0.184	0.0352	**2.32**			
n	0.0132	-0.0686	2.69	**3.80**		
a	0.131	-0.066	0.387	0.834	**0.335**	
b	-0.104	0.0329	0.435	0.502	-0.0076	**0.262**

To determine if there was any correlation between parameters, a correlation matrix was produced, shown in Table 6.10.

Table 6.10. Correlation matrix for secondary nucleation kinetic parameters.

	g	$g2$	$\ln k_B$	n	a	b
g	1					
$g2$	-0.963	1				
$\ln k_B$	-0.347	0.155	1			
n	0.0194	-0.235	0.907	1		
a	0.647	-0.761	0.44	0.739	1	
b	-0.584	0.43	0.558	0.503	-0.0257	1

The correlation matrix shows that g and $g2$ are highly correlated, which is undesirable, as it becomes less clear which parameter has an effect on the process when varied. Further experimentation would be preferred with experiments designed to decouple these parameters.

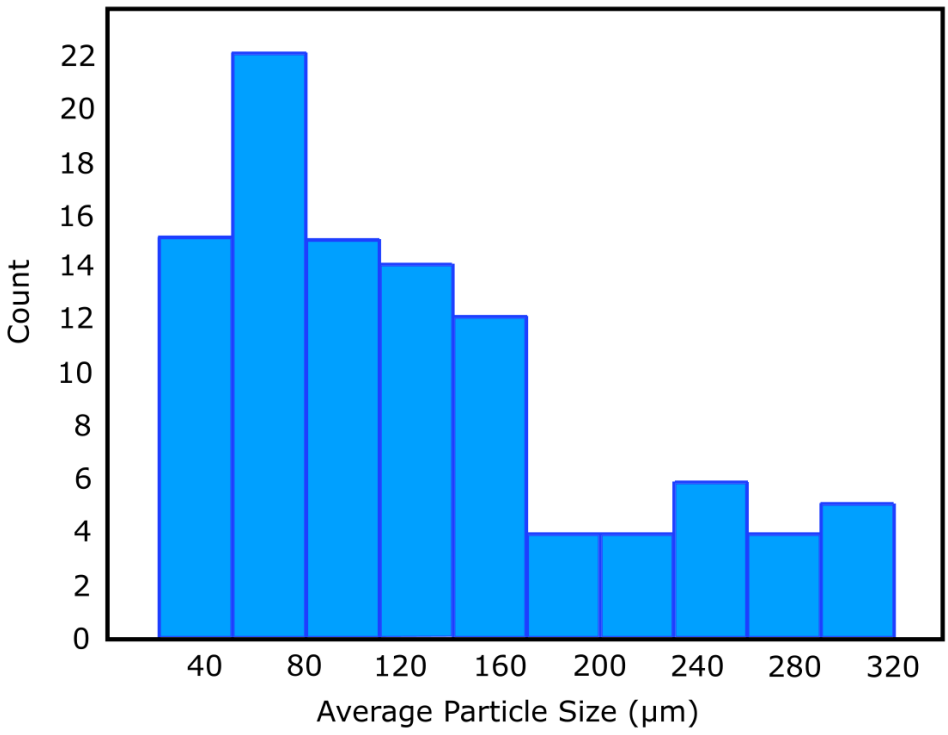

Figure 6.19. Histogram of the PSD from predicted secondary nucleation parameters from Experiment 9.

The histogram in Figure 6.19 shows a wide span of predicted crystal sizes, much wider than was observed in Figure 6.15 for a growth-only model. This is reflected by the large standard deviations for the secondary nucleation kinetic parameters in Table 6.8, and is apparent in the plots in Figure 6.16, as only experiment 10 shown in Figure 6.16c shows any significant improvement over a growth-only model. If time allowed, a future strategy may be to use the current model to plan experiments that give a high degree of secondary nucleation to reduce the standard deviation in the parameters.

6.5.4 Optimisation of a Multi-addition Plug Flow Antisolvent Process

The determined kinetic parameters were applied to optimise a continuous plug flow crystalliser. This work takes a similar approach to that performed previously for mathematical modelling of PFRs with antisolvent addition [9], [111]; however, the kinetic parameters in those setups will differ to those reported here due to variations between the platforms. Furthermore, primary nucleation is not considered, as experience from Chapter 4 and other research [109] has shown there can be significant practical limitations in the operation of unseeded COBCs, and therefore the focus will be on the optimisation of seeded processes.

The population balance equation described in Equation 6.2 represents that of a batch crystalliser. For a plug flow crystalliser operating at steady state, the PBE can be represented as [94], [153]:

$$u_x \frac{\delta n}{\delta x} + G \frac{\delta n}{\delta L} = 0 \tag{6.9}$$

where u_x is the average fluid velocity, n is the number density, x is the length along the crystalliser, G is the crystal growth rate, and L is the crystal size.

The model crystalliser consisted of a DN15 NiTech COBC of 30 m length, a schematic of which is shown in Figure 6.20. The internal geometry was as described in Figure 4.6. The COBC was discretised into fifteen axial points. As no direct correlation between frequency, amplitude, flow rate and axial dispersion have been demonstrated, an axial dispersion coefficient of 1×10^{-5} m^2/s was assumed. Power density was set to 1.5597 W/kg, which corresponds to the lowest power density tested. The feed composition was fixed at 10 g/min flow rate, with mass fractions of ethanol, anthranilic

acid and water at 0.5374, 0.1044 and 0.3582, respectively. Seed material had a D50 of 50 μm, with standard deviation of 25 μm. A seed loading of 1% (based on a maximum theoretical yield of solid) was employed, which corresponded to a seed flow rate of 7.9 mg/min. Ethanol mass fractions were constrained such that the sum of the three antisolvent additions were less than or equal to 18 g/min, corresponding to a final $X_{\mathrm{EtOH}} \geq 0.2$, as this was the range within which the kinetic parameters were determined, and therefore the range in which they would remain valid.

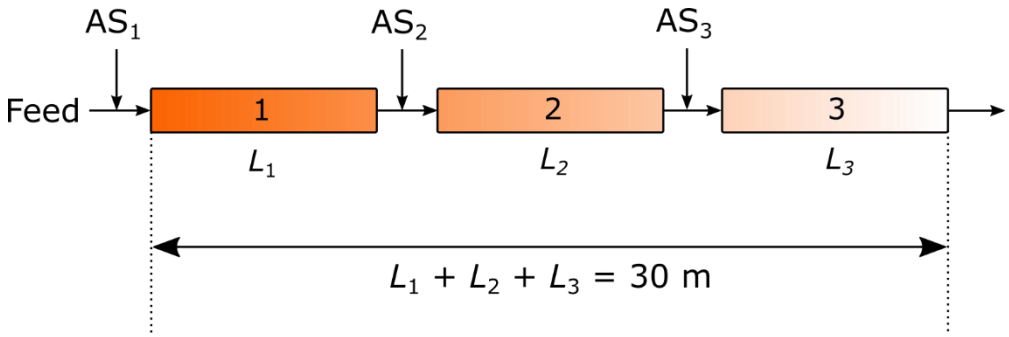

Figure 6.20. Schematic of a 30 m COBC with multiple antisolvent additions.

Initial optimisations were performed for three equally spaced antisolvent additions at 10 m intervals. Later optimisations incorporated variable position of these additions. The antisolvent flow rates, residence times and summarised results for each optimisation case are detailed in Table 6.11. Case A is a baseline case where antisolvent additions were equal across all three inlets.

Table 6.11. Summary of optimisation cases for antisolvent crystallisation in a 30 m COBC.

Case	Objective	Constraints	Segment	Length (m)	AS flow rate (g/min)	τ (min)	Total flow rate (ml/min)	Yield %	D4,3 (μm)	CV (μm)
A	n/a	$X_{\mathrm{EtOH}} \geq 0.2$	1	10	5.97	111	15.97	–	–	–
			2	10	5.97	81	21.93	–	–	–
			3	10	5.97	63	27.90	96.6	287.2	58.3
B	Maximise Yield	$X_{\mathrm{EtOH}} \geq 0.2$	1	10	4.92	118	14.92	–	–	–
			2	10	11.67	66	26.59	–	–	–
			3	10	1.27	63	27.86	97.0	281.1	56.1
C	Maximise D4,3	$X_{\mathrm{EtOH}} \geq 0.2$	1	10	12.66	78	22.66	–	–	–
			2	10	1.97	72	24.63	–	–	–
			3	10	3.09	64	27.72	96.8	314.1	61.9
D	Minimise CV	$X_{\mathrm{EtOH}} \geq 0.2$	1	10	2.11	146	12.11	–	–	–
			2	10	2.11	124	14.22	–	–	–
			3	10	11.95	68	26.17	96.2	241.8	46.1
E	Maximise D4,3	$X_{\mathrm{EtOH}} \geq 0.2$; $S_{\mathrm{II}} \leq 1$ in segment 1	1	10	0.48	169	10.48	–	–	–
			2	10	12.57	77	23.05	–	–	–
			3	10	3.53	66	26.58	96.5	314.0	61.9
F	Maximise D4,3	$X_{\mathrm{EtOH}} \geq 0.2$; $S_{\mathrm{II}} \leq 1$ in segment 1 and 2	1	10	1.73	151	11.73	–	–	–
			2	10	0.51	144	12.23	–	–	–
			3	10	12.09	73	24.32	95.7	252.5	51.6
G	Maximise Yield	$X_{\mathrm{EtOH}} \geq 0.2$	1	6.95	2.00	102	12.00	–	–	–
			2	3.23	10.45	25	22.45	–	–	–
			3	19.57	5.43	124	27.88	97.2	256.0	53.7
H	Maximise D4,3	$X_{\mathrm{EtOH}} \geq 0.2$; $S_{\mathrm{II}} \leq 1$ in segment 1	1	5.14	0.60	86	10.60	–	–	–
			2	16.07	12.35	124	22.95	–	–	–
			3	8.74	6.64	52	29.59	96.7	323.2	61.3

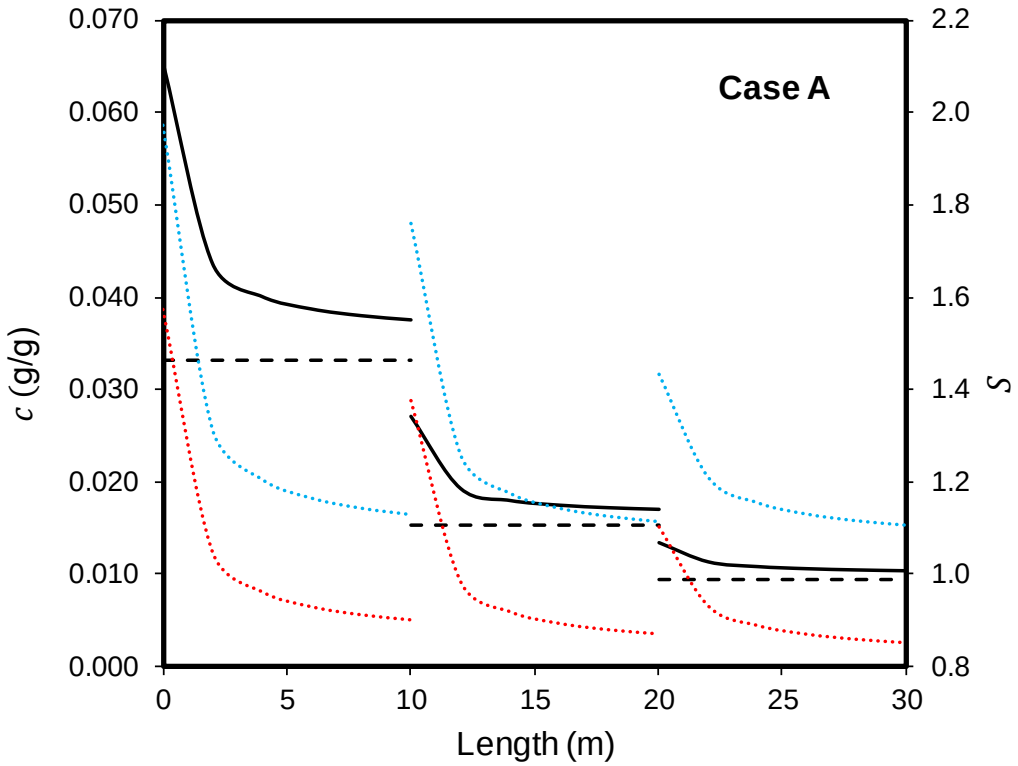

Figure 6.21. Results of unoptimised antisolvent addition at three equally spaced positions in a COBC, constrained on X_{EtOH}. Solid lines: c. Dashed lines: $c^{\star}$. Blue (upper) dotted line: S_{I}. Red (lower) dotted line: S_{II}.

The results of an unoptimized process are shown in Figure 6.21. As all of the optimisations are based on a seeded process, there is no reliance on primary nucleation, and therefore no associated induction time. This explains how the supersaturation starts to be consumed immediately compared to results by Su et al. [111], whereby in their case the first antisolvent addition did not significantly reduce the concentration, and where the second addition generated very high levels of supersaturation that likely would result in additional nucleation events. However, the first antisolvent addition in this case does generate quite significant levels of supersaturation that also give a similar result. No kinetics are assumed for form II as this form is not desired. Here, S_{II} is included to show the maximum S_{II} that can be obtained, and how control over polymorphism could be lost in an unoptimized case by driving S too high and resulting in the nucleation of form II.

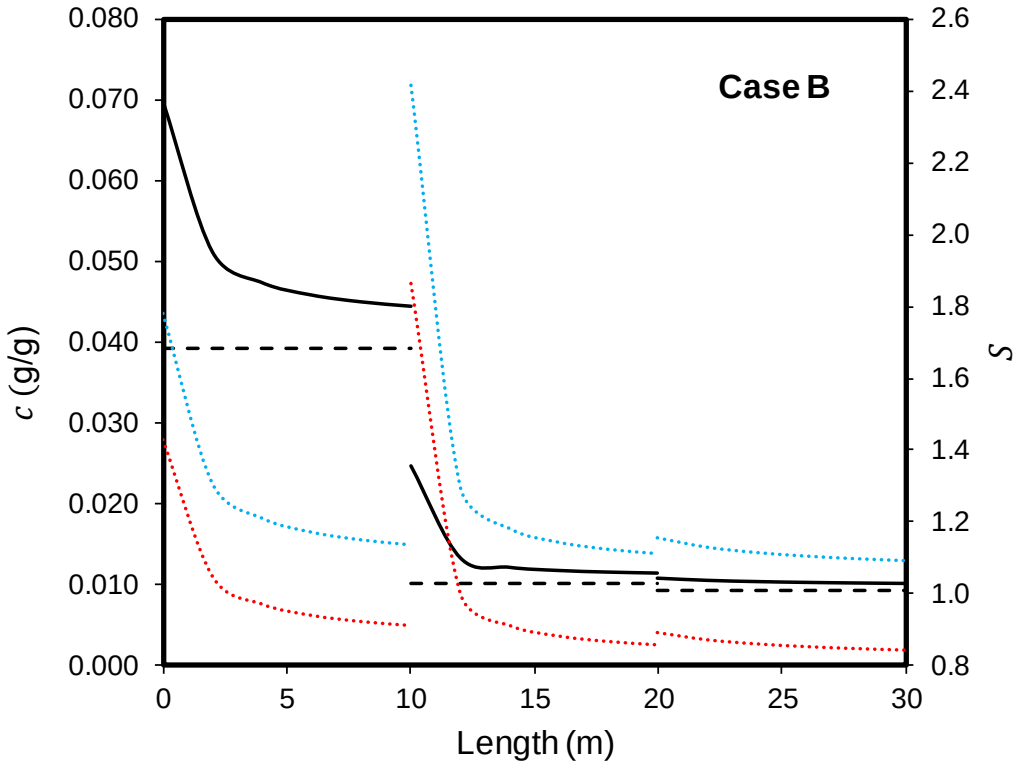

Figure 6.22. Optimisation results for maximum yield with antisolvent addition at three equally spaced positions in a COBC, constrained on X_{EtOH}. Solid lines: c. Dashed lines: $c^{\star}$. Blue (upper) dotted line: S_{I}. Red (lower) dotted line: S_{II}.

The results of optimisation for maximum yield in Figure 6.22 show the first antisolvent addition is comparable to that of the unoptimized condition. There is a greater amount of antisolvent added in the second addition point, but by 12 m supersaturations are similar, with S_{I} = 1.30 for Case B versus S_{I} = 1.26 for Case A. Consequently, the last antisolvent addition does not generate much additional supersaturation due to the constraints on the final ethanol fraction.

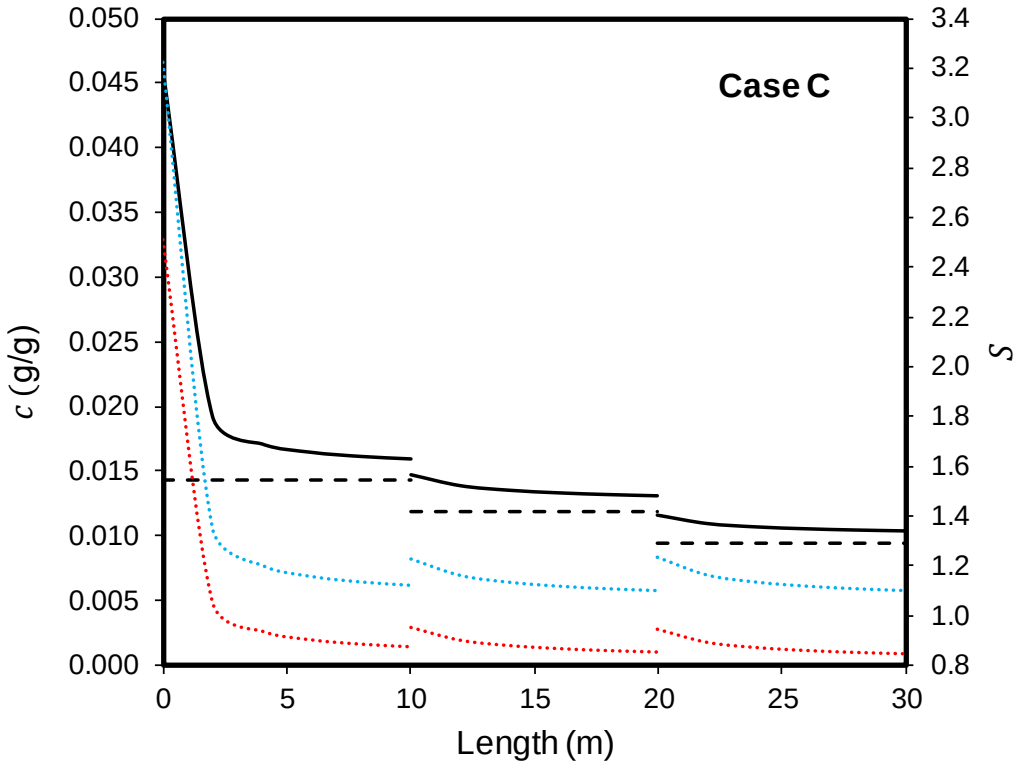

Figure 6.23. Optimisation results for maximum D4,3 with antisolvent addition at three equally spaced positions in a COBC, constrained on X_{EtOH}. Solid lines: c. Dashed lines: $c^{\star}$. Blue (upper) dotted line: S_{I}. Red (lower) dotted line: S_{II}.

Optimisation for maximum size is shown in Figure 6.23, and immediately noticeable is the high degree of supersaturation generated by the first antisolvent addition. One would be concerned that in practice, the low seed loading would not provide sufficient surface area to prevent uncontrolled nucleation, particularly of metastable form II. At the first point of mixing of feed solution and antisolvent, i.e. length 0, S_{I} = 3.2 and S_{II} = 2.5. Although not directly comparable due to being different crystallisation platforms, the induction times at such supersaturations have been measured to be in the order of seconds [24], and would likely occur here. This configuration also gives the shortest overall residence times due to the addition of the majority of antisolvent at the beginning of the process. Subsequent antisolvent additions provide a much less aggressive level of additional supersaturation.

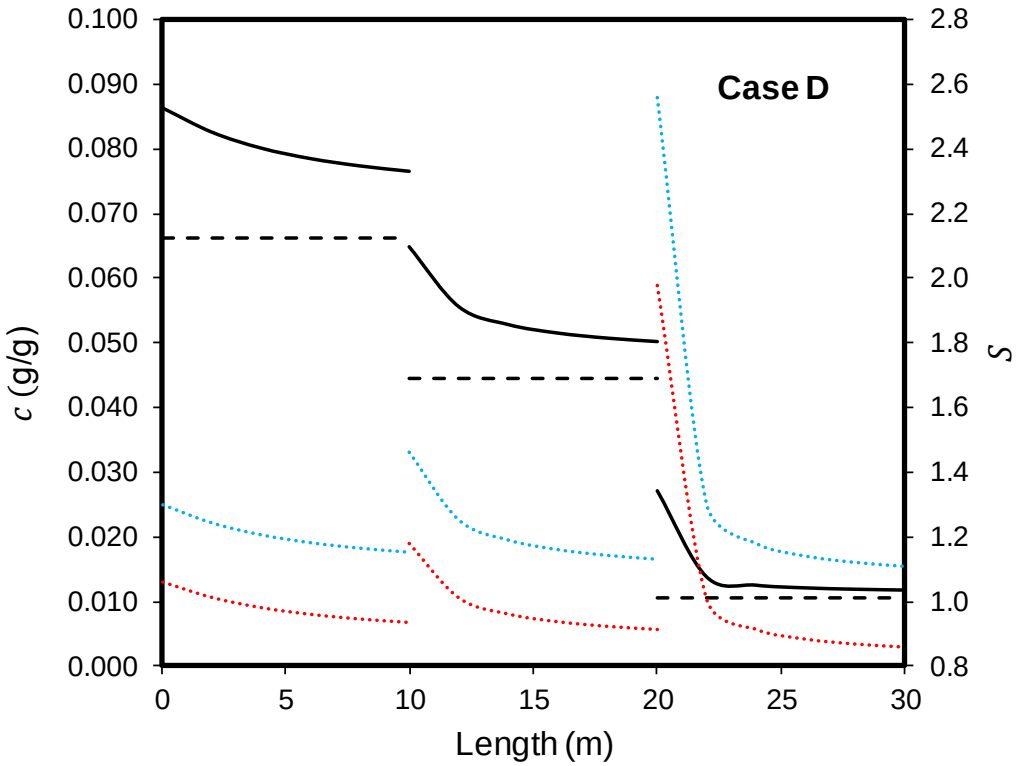

Figure 6.24. Optimisation results for minimum coefficient of variation with antisolvent addition at three equally spaced positions in a COBC, constrained on X_{EtOH}. Solid lines: c. Dashed lines: $c^{\star}$. Blue (upper) dotted line: S_{I}. Red (lower) dotted line: S_{II}.

Optimisation for minimum coefficient of variation (CV) is shown in Figure 6.24. This case provides equal masses of antisolvent in the first and second sections, with the majority of the antisolvent being delivered in the final section; this increase in supersaturation in the final section is offset by the increased surface area from crystal growth in the previous two sections, such that the potential for additional nucleation events is reduced, compared to if the increased supersaturation occurred in the first section. The supersaturation ratio in this last section does reach S_{II} = 2.0

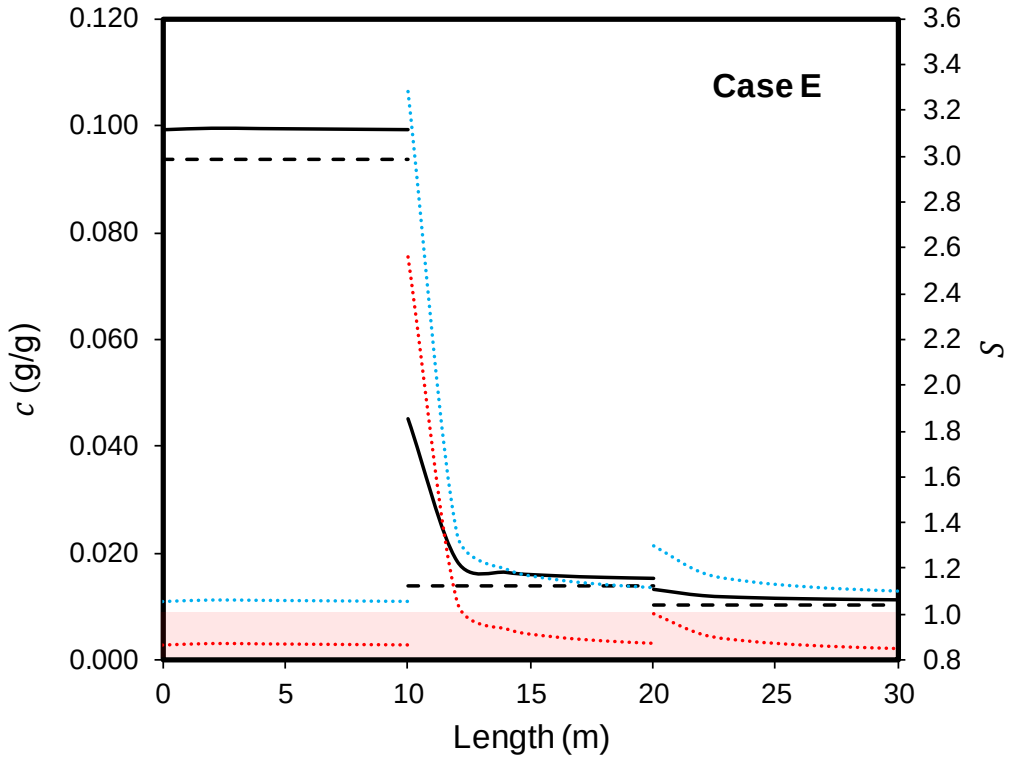

Figure 6.25. Optimisation results for maximum D4,3 with antisolvent addition at three equally spaced positions in a COBC, constrained on X_{EtOH} and S_{II} in first segment. Solid lines: c. Dashed lines: $c^{\star}$. Blue (upper) dotted line: S_{I}. Red (lower) dotted line: S_{II}.

Optimisation for maximising D4,3 with the additional constraint on S_{II} in the first stage is shown in Figure 6.25, and results in barely any antisolvent being added to the first stage. This would be desirable to prevent unwanted nucleation and fouling in the first section of the process, where it is most sensitive to large spikes in supersaturation due to having the lowest surface area of crystals of any part of the process. However, this supersaturation constraint effectively offsets the antisolvent addition to the second stage, and the high supersaturation here would likely result in unwanted nucleation and fouling. From a practical perspective, such a small amount of antisolvent will likely result in little growth in this first section. There is the potential for more antisolvent to be added whilst maintaining $S_{\mathrm{II}} \leq 1$, as the maximum in the first section is only $S_{\mathrm{II}} = 0.87$.

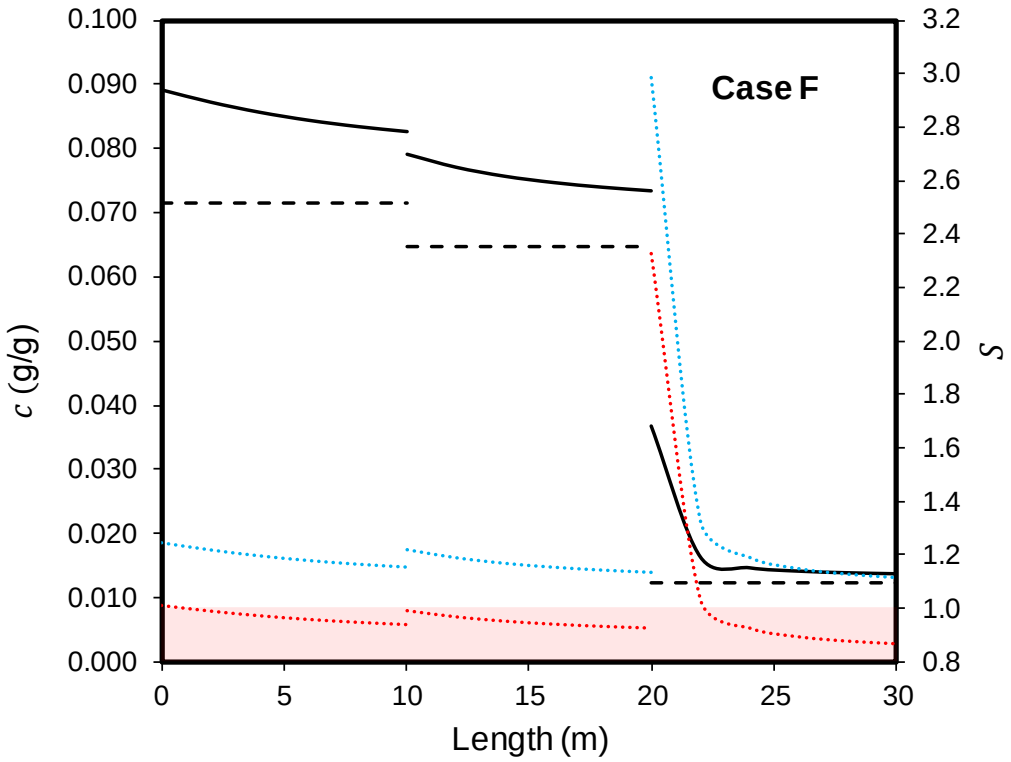

Figure 6.26. Optimisation results for maximum D4,3 with antisolvent addition at three equally spaced positions in a COBC, constrained on X_{EtOH} and S_{II} in first and second segment. Solid lines: c. Dashed lines: $c^{\star}$. Blue (upper) dotted line: S_{I}. Red (lower) dotted line: S_{II}.

Figure 6.26 shows the application of further constraint to the process, limiting S_{II} in the second stage as well as the first. This has the effect of preventing the possibility of nucleation of form II, but at the expense of increased residence times in these stages. This case also helps to highlight how small amounts of antisolvent can greatly reduce the solubility when operating in critical regions of the phase diagram. As was observed for Case E, the constraints on S_{II} shifts the remaining antisolvent addition to the next unconstrained addition point, where S_{II} then exceeds 1. However, the maximum S_{II} is lower in this case than the others, and it is possible that by this stage, due to growth afforded by the first two stages, that there will be a significant enough surface area for crystal growth that additional nucleation events will be minimised.

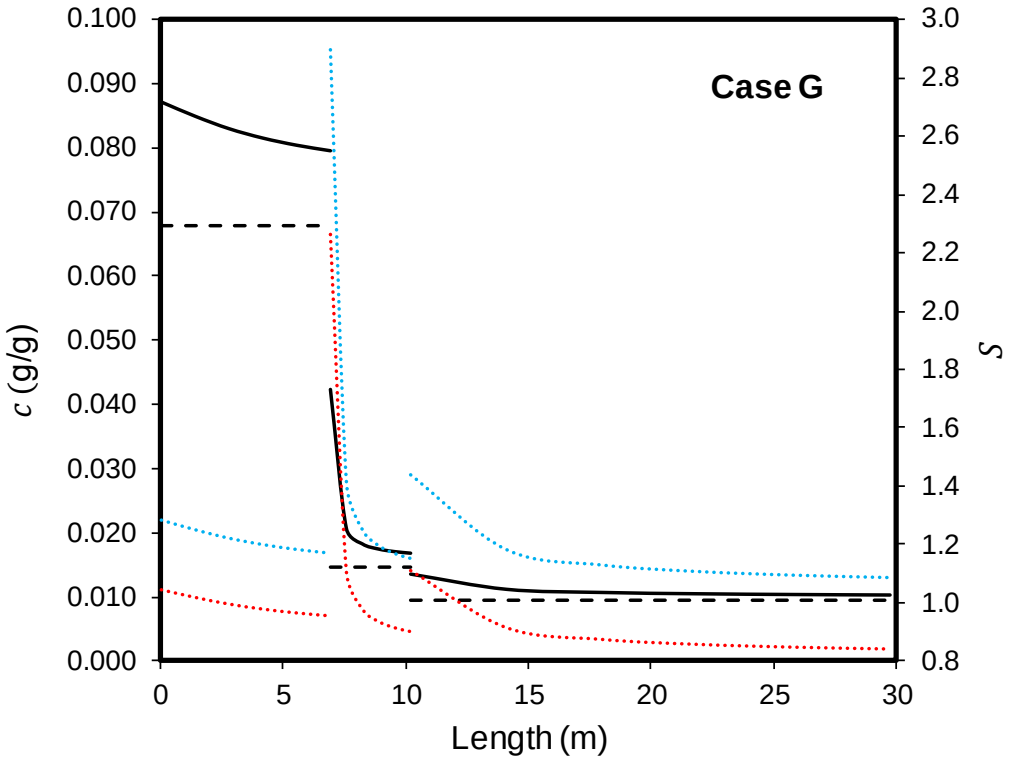

Figure 6.27. Optimisation results for maximum yield for three antisolvent addition points at variable positions in a COBC, constrained on X_{EtOH}. Solid lines: c. Dashed lines: $c^{\star}$. Blue (upper) dotted line: S_{I}. Red (lower) dotted line: S_{II}.

Optimisation results for maximising yield with varying segment length is depicted in Figure 6.27. For this case, a significant amount of antisolvent is added in the second stage. As observed in other cases where S_{II} was not constrained, this leads to large increases in supersaturation, which has practical implications regarding nucleation and the propensity for fouling in the crystalliser at the antisolvent addition points. Due to the variable length, the residence time in the second stage is also comparatively short at 25 minutes. The supersaturation is consumed rapidly within this time, and so optimisation that incorporates variable length reduces the amount of wasted length, whereby there is a low amount of supersaturation for crystal growth, and particles are merely being suspended until reaching the next antisolvent addition point.

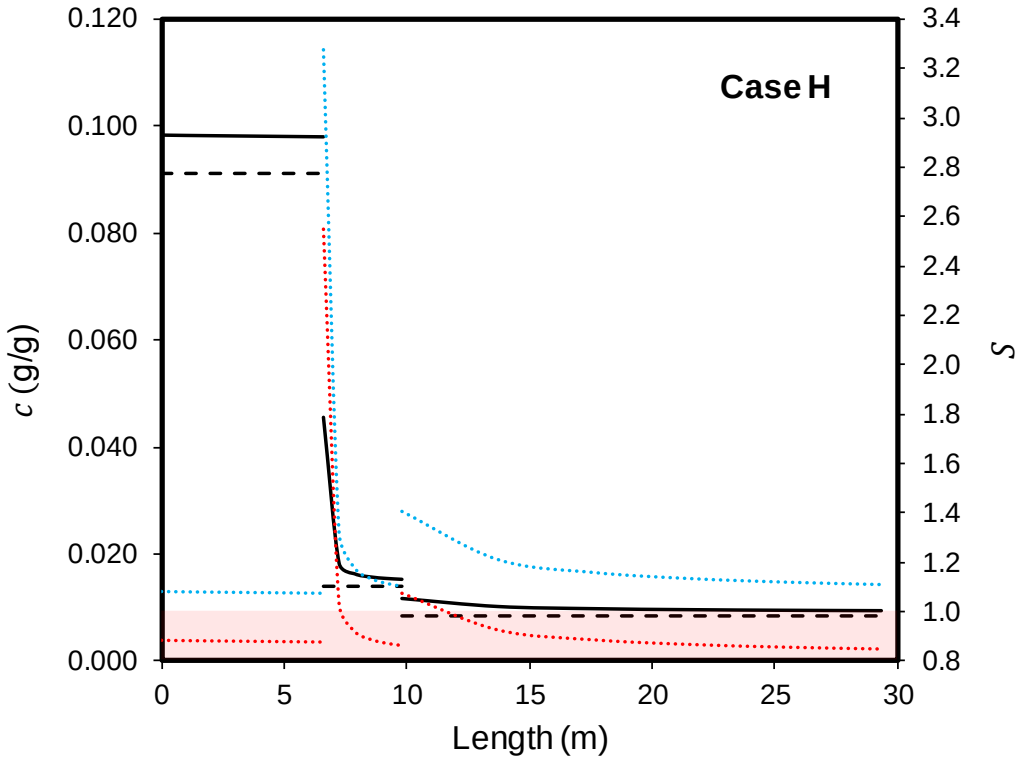

Figure 6.28. Optimisation results for maximum D4,3 for three antisolvent addition points at variable positions in a COBC, constrained on X_{EtOH} and S_{II} in first segment. Solid lines: c. Dashed lines: $c^{\star}$. Blue (upper) dotted line: S_{I}. Red (lower) dotted line: S_{II}.

The final optimisation case shown in Figure 6.28 attempts to maximise D4,3 with varying segment length, and also incorporates constraints on S_{II} in the first stage. This case gave the largest size of all cases where maximum D4,3 was targeted, with a final size of 323.2 μm compared to 314.0 μm for Case E and 314.1 μm for Case C, respectively. As was observed for Case E, the supersaturation in the first stage is relatively low when constrained, only reaching a maximum $S_{\mathrm{II}} = 0.88$ in this stage, before spiking to $S_{\mathrm{II}} = 2.55$ in the second stage. This raises similar concerns regarding the potential for further nucleation and fouling in this second stage.

An additional optimisation was performed for variable length and constraints on S_{II} in stages one and two. However, the reported values from this case did not appear to give a significant improvement over Case F with equal length segments. This could either be due to the lengths in Case F already being the optimum, which is improbable, or an issue with the optimiser in this case under the given decision variables.

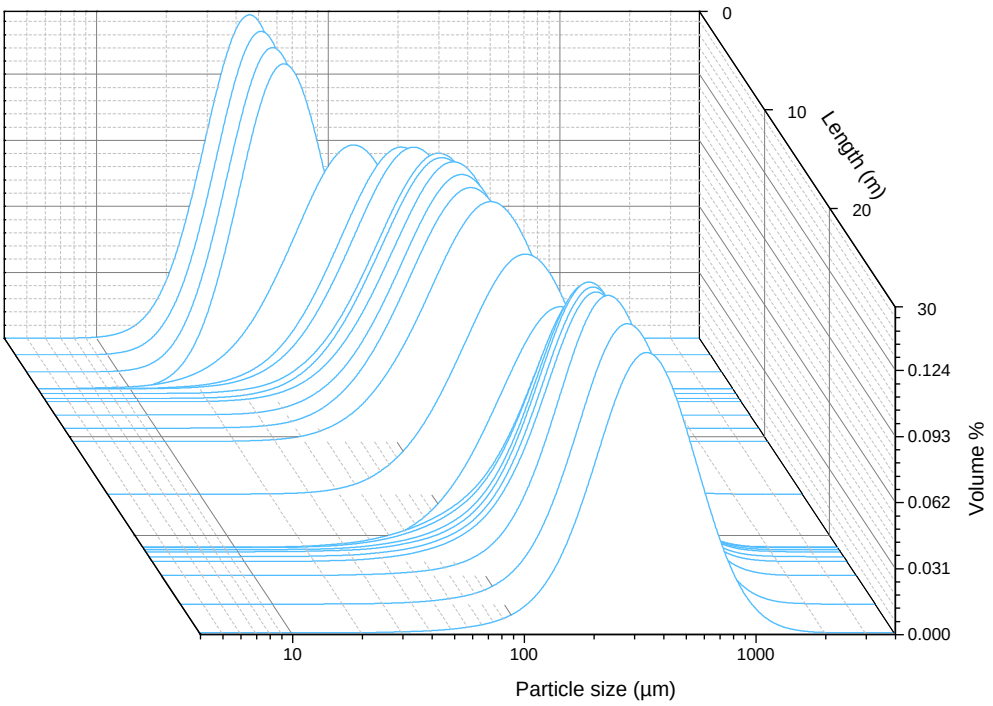

Figure 6.29. Waterfall plot showing the evolution of PSD along the length of the COBC for Case H.

Figure 6.29 uses Case H to demonstrate how PSD changes along the length of the COBC. As there is not much antisolvent added in the first segment, the PSD does not show any significant change. Addition of antisolvent in the second segment gives a rapid increase in crystal size, followed by modest increase as the remaining supersaturation is consumed. The antisolvent addition in the third segment generates additional supersaturation, but results in consistent growth, in contrast to the rapid increase in size as was observed between segments one and two.

6.5.5 Limitations of the Optimisation

For the experimental conditions investigated, the results suggest they were not ideal for maximising the effects of secondary nucleation, as was demonstrated by similar predicted concentration profiles for growth-only models versus those incorporating secondary nucleation. Additional experiments would preferably have been performed that would attempt to maximise the effects of secondary nucleation.

There are several other factors could have been considered, but limits were set based on what was deemed practically feasible. There were no terms to incorporate

agglomeration or twinning into the model, and as there was some observation of these effects in the crystal products, further investigation into this would have likely yielded more accurate model representations of the process.

As was described in detail in Chapter 4, fouling is known to be a potential issue, and with some of the supersaturations suggested by the optimisation cases, it is probable that it would occur. To determine whether this would be the case, a series of experiments could be performed to investigate the suggested conditions from these optimisations, and whether they would be practically implementable. Data from these experiments could then be used to set more informed limits to supersaturation ratios.

The determined kinetics apply over the majority of the length of the COBC multi-addition optimisations, but there are regions where S is much higher than those used experimentally. The maximum S achieved in experiments was S_I = 1.63, whereas in some cases where S is unconstrained, it reaches a maximum of S_I = 3.28. To optimise a process where the kinetics would apply across wider ranges of S, experiments would have to be performed at these high S to determine them; however, this is impractical experimentally due to issues surrounding primary nucleation at high S as was highlighted in Table 6.1. One would therefore have to apply tighter constraints on the maximum S to ensure the kinetics were applicable over the entire length of the COBC.

There are many more variables that could have been explored, such as other seed loadings, total flow rates, lengths and residence times. However, these can be somewhat constrained based on practical knowledge of the system. For example, if attempting to maximise yield, an increase in 1 μm would not be worth another 10 m in length. Other factors begin to have an effect, such as pressure drop along the length of the COBC causing a loss in particle suspension, which would have a much more significant effect on the process overall. Optimisations for a 30 m COBC were chosen as that is a physical platform that has been used previously; however, more significant differences may have become apparent had the maximum length been reduced to 20 m.

6.6 Summary

Growth and secondary nucleation kinetic parameters have been determined for antisolvent crystallisations of anthranilic acid, by means of isothermal seeded batch experiments in an MFOBC. Ethanol mass fraction, power density and seed loading were varied to provide a range of conditions. In-line concentration and offline PSD measurements were used to determine growth and secondary nucleation rate as a function of ethanol mass fraction and supersaturation. The determined kinetic parameters were then used in rate expressions to develop kinetic models of the process.

The initial growth model did not contain a factor for ethanol mass fraction, and the resulting predictions gave a moderately poor fit to the experimentally measured values. These were improved by the incorporation of a factor for ethanol mass fraction.

Secondary nucleation was investigated using lower seed loadings than the cases for growth, and by varying power density by altering the amplitude of oscillations. The results did not show significant improvement over a growth-only model at higher ethanol fractions. At lower ethanol mass fractions, the secondary nucleation model gave improved predicted fits to the experimental values.

The determined kinetic parameters were used to develop an optimisation strategy for a continuous antisolvent crystallisation in a 30 m DN15 COBC with three antisolvent addition ports. Several optimisation cases were considered to maximise yield, maximise D4,3 and to minimise CV. This was achieved by applying constraints to X_{EtOH} and S_{II}, and by varying the positions of antisolvent additions. The results of these optimisations provide the first continuous multi-addition antisolvent crystallisation process in a COBC based upon experimentally determined kinetic rate parameters and form a basis upon which such crystallisations can be developed.

7 Conclusions and Future Work

7.1 Conclusions

The overall aim of this thesis was to develop continuous antisolvent crystallisation processes of anthranilic acid in oscillatory baffled crystallisers (OBCs) to demonstrate how they can be utilised to control crystal attributes. Two platforms were selected for investigation, consisting of a moving baffle (MBOBC) and a fixed baffle (COBC) construction. A variety of experimental approaches were taken to modify the crystallisation behaviour in these systems.

Chapter 4 utilised a COBC platform and investigated the effect of varying the addition method of antisolvent, the flow rate of solution and antisolvent, and the total residence time in the COBC. There was inconsistency observed in the process startup as monitored by in-situ FBRM when the antisolvent was introduced to the COBC which was pre-filled with a solution of anthranilic acid in ethanol. This was attributed to the gradual increase in supersaturation this mode of addition produced. The process was operated in a controlled manner without seeds, therefore relying upon primary nucleation generating the surface area necessary to deplete supersaturation. This was the case for all antisolvent fractions, and hence supersaturations, used for this startup method. When the addition points were reversed, such that solution was introduced to a COBC that was pre-filled with antisolvent, a much more consistent process startup for all antisolvent fractions and flow rates investigated was achieved. The supersaturation ratio always reaches a maximum by this method, rapidly inducing nucleation. The antisolvent fraction itself did not have an effect on the polymorphism observed in the crystal products, and metastable form II polymorph of anthranilic acid was consistently obtained.

By reducing the flow rate of antisolvent and feed solution, the residence time in the fixed volume COBC could be increased whilst maintaining the same antisolvent fraction. The longest residence time used in the experiments still produced metastable form II polymorph, which showed that a residence time of 24 minutes was not sufficient for the process to undergo solvent-mediated transformation. The concentration of the mother liquor at the outlet was consistent when the process was at steady state for all flow rates at the specified antisolvent fractions, which demonstrated that the process rapidly desupersaturated in the length of COBC used for these experiments.

Adjusting the antisolvent fraction whilst maintaining the same total flow rate resulted in variations in the total number of crystals produced and the size of those crystals. The number and size of crystals followed the trend of the maximum yield per unit volume, represented by $c-c^{\star}$, with the highest yielding condition producing the greatest number of crystals with the smallest size. The practical limitations of the process were also dependent on the antisolvent fraction, and the rate of fouling and gas liberation was observed to be faster at higher supersaturations for operating an unseeded antisolvent crystallisation process.

Whilst it might be beneficial if the consistent environment in a COBC could be exploited to control primary nucleation, this proved to be unachievable. Based on the operational issues encountered with fouling, it is recommended that a seeding strategy be adopted as is suggested for cooling crystallisations [129]. Gas liberation can be mitigated either by making it a point of consideration during the solvent selection process, or by incorporating a degassing strategy into the process design.

The use of an MBOBC as a robust platform for continuous nucleation and polymorph control was demonstrated in Chapter 5. Due to the design of the MBOBC, whereby solution and antisolvent delivery is provided by two separate inlets above the liquid level, it is much less sensitive to the fouling issues observed in the COBC. The polymorphic outcome of the process was found to be dependent on several factors. When the platform was started without seeds present, the polymorph produced was form II, consistent with observations in Chapter 4. When seeds of the stable form I polymorph were present at startup, the process either produced form I exclusively when the residence time was 2 minutes, or a mixture of forms I and II when the residence time was 4 minutes. This observation was made for both $\varphi = 0.46$ and $\varphi = 0.60$. The presence of a mixture of stable and metastable polymorphs after several residence times leads to the conclusion that both forms are continuously nucleating. By arresting flow and operating as a batch vessel, mixtures of forms I and II underwent transformation to form I within 20 minutes.

Control over polymorphism is of significant interest to both industry and academia, owing to the differences in physical properties different forms can exhibit [154]. The ability to produce desired polymorphs on demand reproducibly has been demonstrated for continuous cooling crystallisations [127], [155]. This work has contributed towards

the understanding of how composition and flow can impact polymorphism and allow for polymorph control in continuous antisolvent crystallisation.

Chapter 6 detailed the determination of kinetic parameters for crystal growth and secondary nucleation for seeded antisolvent crystallisation of anthranilic acid in a batch MFOBC. The population balance models developed were improved upon by the incorporation of an additional solvent factor. The model was parameterised and validated using methods described in Chapter 6, and then used for the digital design of a multi-addition antisolvent crystallisation in a 30 m COBC. Several conditions suggested to maximise or minimise a range of commonly desired outcomes, such as yield and CSD. Constraints were applied to ethanol mass fraction to operate within the regions where the kinetic parameters determined from the batch process would remain valid, and in some cases constraints were also applied to the supersaturation ratio that would prevent the nucleation of an undesired polymorph.

The ability to predict process outcomes with the aid of modelling tools is highly desirable for the pharmaceutical industry, where their implementation can significantly reduce material cost and development time. This work has further developed the principles outlined in the work by Su et al. [111] by coupling the mathematical modelling of a plug flow crystalliser with experimentally determined kinetic rate parameters.

7.2 Future Work

7.2.1 Fouling Mitigation Strategies

During all continuous crystallisations performed in the COBC, there was some degree of fouling observed at the point of mixing of feed solution and antisolvent. There are several potential methods that could be employed to mitigate this fouling issue. As it was observed that fouling predominantly occurred on the steel inlet itself as shown in Figure 4.18, various other materials of construction could be investigated, as material of construction has been shown to affect the propensity for fouling [156]. In addition, the application of durable protective coatings or films could be investigated, such as PTFE as used for heat exchangers [157].

The most obvious strategy would be to perform seeded crystallisations, as this reduces the need to operate with the high supersaturations required to induce primary nucleation and relies on growth and/or secondary nucleation that best occur at lower supersaturation. However, this introduces additional steps in the preparation of seed material, and continuous transfer of seed from a seed vessel to the COBC. If primary nucleation could be controlled in a COBC, such that the produced material was of the desired polymorph and small size to allow for further crystal growth if desired, this would be advantageous. Localised sonication, for example, could be incorporated at the first point of mixing, which could promote nucleation at lower supersaturations [20] and help to minimise fouling. Other in-situ methods of seed generation could be explored such as laser-induced nucleation [158].

Seed generation could be explored by using an external continuous seed generating unit that then feeds into the COBC, similar to that shown in Figure 7.1. The apparatus shown in that figure was constructed and crystallisations performed; however, similar issues with fouling were encountered at the point of mixing and this line of investigation was not pursued further. Modification of the unit or use of a different compound and solvent system may prove more successful.

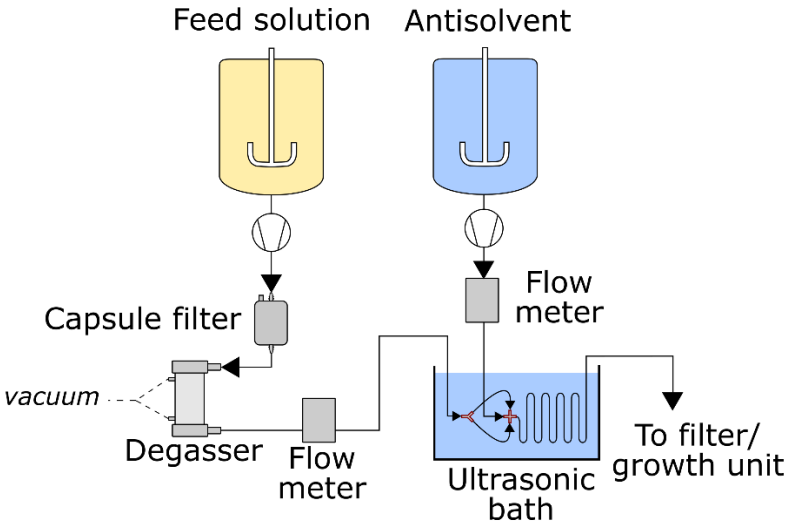

Figure 7.1. Proposed continuous nucleation unit to feed into the COBC.

7.2.2 Alternative Methods of Generating Supersaturation

All experiments reported in this thesis were performed isothermally to investigate antisolvent effects in isolation. A combination of cooling and antisolvent crystallisation is often used to increase the yield of a process, and can also assist in targeting CQAs over the use of either technique separately [159]. Further development of these combined approaches would be beneficial and the jacketed COBC is well-suited to deliver this.

The COBC has recently been utilised to perform both the synthesis and seeded cooling crystallisation of paracetamol in a single platform [160]. Owing to the similarities between antisolvent crystallisation and reactive crystallisation, there is scope to develop such processes to further streamline crystallisation.

7.2.3 Dissolved Gas Effects

Gas solubility and potential methods to reduce the amount of dissolved gas has already been discussed in detail in 4.4.2; however, investigation was not carried out into the effect these dissolved gases may have on the system itself, nor any quantification of the extent of degassing required. These could be more thoroughly investigated in a systematic way to inform crystalliser selection or the requirements for pre-processing of solvents.

The method to approach dissolved gas effects may differ in the case of the MBOBC due to the head space of air compared to the near-closed COBC. The MBOBC therefore allows for both the dissolution of gas from the atmosphere into the solvent, and for any gas liberated from the mixing of solvents to escape the MBOBC. The rate of gas dissolution or liberation will be dependent on several factors, such as the relative solubilities of gases in various solvent and antisolvent compositions, and on the residence time in the MBOBC. The gas solubility may not matter if operating the MBOBC as a single unit or in a cascade, but if the unit were coupled to a COBC, these effects would need consideration.

7.2.4 Alternative Techniques for Targeting Polymorphs

Experiments performed in Chapter 5 resulted in the production of two of the reported three forms of anthranilic acid. Attempts to produce form III continuously at 25 °C by seeding with form III proved unsuccessful, which is understandable as form I is thermodynamically stable at this temperature, and form II is metastable with a lower stability than form III, which makes it difficult to target form III without producing form II instead. Due to their enantiotropic relationship, form III becomes more stable than form I above approximately 53 °C [105]. As continuous crystallisation of form I was demonstrated at 25 °C, this opens up the possibility of performing experiments at elevated temperature in an attempt to continuously produce form III via direct nucleation, which would result in the ability to produce any of the forms in desired quantities on demand. Furthermore, form I could be targeted as a metastable polymorph at elevated temperature in a similar manner to the method used to produce form II at 25 °C.

Unseeded experiments in Chapter 4 only resulted in form II being produced. Even with the longest residence time employed of 24 minutes, there was no stable form I detected, whereas some form I was expected to result from a solvent-mediated transformation based on previous research with this compound [24]. A potential strategy for targeting form I in the COBC other than by seeding with it directly would be to attempt a controlled solvent-mediated transformation from form II. This could be achieved by adjusting the residence time in the COBC such that complete transformation of form II to form I would occur.

7.2.5 Local Mixing versus Overall Mixing and Dispersion Effects

It was determined in Chapter 4 that the local mixing at the point of contact between solution and antisolvent in the COBC had a significant effect on the crystallisation. The mixing provided by oscillations was fixed by using one frequency and amplitude throughout. The mixing effects were therefore dependent on the velocity of flow of solution and antisolvent, and their relative flow rates. With antisolvent processes being highly sensitive to mixing conditions [23], further investigation into the mixing offered by oscillations versus the local mixing would be warranted. This could be achieved by performing experiments at fixed antisolvent compositions and flow rates, and varying the oscillation frequency and amplitude. Furthermore, varying flow rates at constant supersaturations could be investigated by adjusting the concentration of the solution and the solvent compositions.

Although not investigated here, the design of the addition points themselves may have an effect on the product outcome. An L-shaped inlet was designed and selected such that antisolvent or solution would be delivered into a well-baffled region, in comparison to a simple straight piece inserted into a collar that would have experienced a different hydrodynamic environment to the majority of the COBC. This also had the advantage of being able to visualise the mixing of solution and antisolvent at first contact that would otherwise have been obscured by the collar of the inlet. Further considerations could be made to the inlet shape, diameter, and overall design.

Work by Kacker, Regensburg and Kramer [108] describes studies into the residence time distribution of solid and liquid phases in the COBC, and draws conclusions that optimal conditions for minimising axial dispersion for solids is not necessarily the same as for liquid components under the same frequency and amplitude of oscillation. This poses some implications for antisolvent crystallisation, as for each addition of antisolvent into the process, the flow rate increases and therefore the residence time decreases. This will affect the plug-flow behaviour of the system. This may warrant investigation to identify operational ranges for which axial dispersion for both solid and liquid phases is minimised whilst maintaining particle suspension and providing adequate mixing.

7.2.6 Development of the Multi-addition COBC

The work described in Chapter 6 could be further developed by utilising a wider range of power densities to target secondary nucleation kinetics. Experimental validation of the optimisation strategies would provide added confidence in the ability of the PBE model to accurately predict the process outcomes. Further developing optimisation strategies with different constraints on the total length of the COBC would allow for the minimum footprint of the platform to be achieved whilst maximising performance.

Utilising a different compound and solvent system for which kinetic parameters have also been determined would be beneficial to see how optimisation strategies differ based on kinetics. Primary nucleation was not considered due to the practical issues surrounding it, but if they could be alleviated by means described previously, there may be scope for its consideration here. The optimisation of a combined cooling and antisolvent crystallisation process, whilst not without its challenges computationally and experimentally, would represent a significant development to this platform.

7.3 Overall Conclusions

This work has developed continuous antisolvent crystallisation in oscillatory baffled crystallisers, demonstrating the application of these platforms beyond seeded cooling crystallisations. OBCs are well-suited for polymorph control, being able to operate at steady states whilst producing stable or metastable polymorphs. This is especially applicable to systems with relatively fast transformation kinetics, where an MSMPR may be less suitable due to longer residence times they typically employ.

Unseeded operation of the COBC can result in challenges surrounding encrustation and therefore is not recommended. Liberation of dissolved gases can affect the mixing in the COBC and therefore consideration must be taken over the solvent system and relative gas solubilities in solvent mixtures for antisolvent crystallisation.

As with all antisolvent processes, careful control of supersaturation is required to maintain the desired CQAs of the crystal products. The modular nature of the COBC makes it highly customisable to the crystallisation process. By combining knowledge of the thermodynamics of the crystallisation system, practical points of consideration of the platform, PAT capabilities, and the development of kinetic models, OBCs can be a useful addition to a crystal manufacturing portfolio.

8 References

[1] J. Chen, B. Sarma, J. M. B. Evans, and A. S. Myerson, "Pharmaceutical Crystallization Published as part of the Crystal Growth & Design 10th Anniversary Perspective," *Cryst. Growth Des.*, vol. 11, pp. 887–895, 2011.

[2] Stephen Byrn *et al.*, "Achieving Continuous Manufacturing for Final Dosage Formation: Challenges and How to Meet Them," *J. Pharm. Sci.*, vol. 104, no. 3, pp. 792–802, 2015.

[3] D. Zhang, S. Xu, S. Du, J. Wang, and J. Gong, "Progress of Pharmaceutical Continuous Crystallization," *Engineering*, vol. 3, no. 3, pp. 354–364, 2017.

[4] S. Rohani, S. Horne, and K. Murthy, "Control of product quality in batch crystallization of pharmaceuticals and fine chemicals. Part 1: Design of the crystallization process and the effect of solvent," *Org. Process Res. Dev.*, vol. 9, no. 6, pp. 858–872, 2005.

[5] I. R. Baxendale *et al.*, "Achieving Continuous Manufacturing: Technologies and Approaches for Synthesis , Work-Up and Isolation of Drug Substance," *White Pap.*, pp. 1–19, 2014.

[6] G. Allison *et al.*, "Regulatory and Quality Considerations for Continuous Manufacturing," *J. Pharm. Sci.*, vol. 104, no. 3, pp. 803–812, 2015.

[7] K. A. Powell, A. N. Saleemi, C. D. Rielly, and Z. K. Nagy, "Monitoring Continuous Crystallization of Paracetamol in the Presence of an Additive Using an Integrated PAT Array and Multivariate Methods," *Org. Process Res. Dev.*, vol. 20, no. 3, pp. 626–636, 2016.

[8] C. Badman and B. L. Trout, "Achieving Continuous Manufacturing," *J. Pharm. Sci.*, vol. 104, no. 3, pp. 779–780, 2015.

[9] A. J. Alvarez and A. S. Myerson, "Continuous plug flow crystallization of pharmaceutical compounds," *Cryst. Growth Des.*, vol. 10, pp. 2219–2228, 2010.

[10] N. E. B. Briggs, U. Schacht, V. Raval, T. McGlone, J. Sefcik, and A. J. Florence, "Seeded Crystallization of β- L -Glutamic Acid in a Continuous Oscillatory Baffled Crystallizer," *Org. Process Res. Dev.*, vol. 19, no. 12, pp. 1903–1911, 2015.

[11] J. L. Quon, H. Zhang, A. Alvarez, J. Evans, A. S. Myerson, and B. L. Trout, "Continuous crystallization of Aliskiren hemifumarate," *Cryst. Growth Des.*, vol. 12, pp. 3036–3044, 2012.

[12] K. Robinson, "Continuous manufacturing: the facts and the future," *Manufacturing Chemist*, 2019. [Online]. Available: https://www.manufacturingchemist.com/news/article_page/Continuous_manufacturing_the_facts_and_the_future/150919. [Accessed: 19-Sep-2019].

[13] C. J. Brown *et al.*, "Enabling precision manufacturing of active pharmaceutical ingredients: workflow for seeded cooling continuous crystallisations," *Mol. Syst. Des. Eng.*, vol. 3, no. 3, pp. 518–549, 2018.

[14] A. M. Schwartz, *Handbook of Industrial Crystallization - Chapter 01 - Solutions and solution properties*. 2002.

[15] D. J. Kirwan and C. J. Orella, *Handbook of Industrial Crystallization - Chapter 11 - Crystallization in the pharmaceutical and bioprocessing industries*, 2nd ed. Butterworth-Heinemann, 2002.

[16] A. Jouyban, *Handbook of Solubility Data for Pharmaceuticals*. CRC Press, 2009.

[17] A. T. Karunanithi, L. E. K. Achenie, and R. Gani, "A computer-aided molecular design framework for crystallization solvent design," *Chem. Eng. Sci.*, vol. 61, no. 4, pp. 1247–1260, 2006.

[18] M. Allesø, J. Rantanen, J. Aaltonen, C. Cornett, and F. Van Den Berg, "Solvent subset selection for polymorph screening," *J. Chemom.*, vol. 22, no. 11–12, pp. 621–631, 2008.

[19] I. Taimni, "The Viscosity of Saturated Solutions," *J. Phys. Chem.*, vol. 32, no. 4, pp. 604–615, 1922.

[20] K. a. Ramisetty, A. B. Pandit, and P. R. Gogate, "Ultrasound-assisted antisolvent crystallization of benzoic acid: Effect of process variables supported by theoretical simulations," *Ind. Eng. Chem. Res.*, vol. 52, pp. 17573–17582, 2013.

[21] A. R. Parsons, S. N. Black, and R. Colling, "Automated Measurement of Metastable Zones for Pharmaceutical Compounds," *Chem. Eng. Res. Des.*, vol. 81, no. 6, pp. 700–704, Jul. 2003.

[22] J. Nývlt, O. Söhnel, M. Matachová, and M. Broul, *The kinetics of industrial crystallization*, vol. 32, no. 7. New York: Elsevier, 1986.

[23] X. Y. Woo, R. B. H. Tan, P. S. Chow, and R. D. Braatz, "Simulation of mixing effects in antisolvent crystallization using a coupled CFD-PDF-PBE approach," *Cryst. Growth Des.*, vol. 6, pp. 1291–1303, 2006.

[24] S. Jiang, J. H. ter Horst, and P. J. Jansens, "Concomitant Polymorphism of o-Aminobenzoic Acid in Antisolvent Crystallization," *Cryst. Growth Des.*, vol. 8, no. 1, pp. 37–43, 2008.

[25] S. a. Kulkarni, S. S. Kadam, H. Meekes, A. I. Stankiewicz, and J. H. Ter Horst, "Crystal nucleation kinetics from induction times and metastable zone widths," *Cryst. Growth Des.*, vol. 13, pp. 2435–2440, 2013.

[26] C. Brandel and J. H. ter Horst, "Measuring induction times and crystal nucleation rates," *Faraday Discuss.*, vol. 179, no. 0, pp. 199–214, 2015.

[27] C. J. Callahan and X. W. Ni, "An investigation into the effect of mixing on the secondary nucleation of sodium chlorate in a stirred tank and an oscillatory baffled crystallizer," *CrystEngComm*, vol. 16, no. 4, pp. 690–697, 2014.

[28] D. O'Grady, M. Barrett, E. Casey, and B. Glennon, "The Effect of Mixing on the Metastable Zone Width and Nucleation Kinetics in the Anti-Solvent Crystallization of Benzoic Acid," *Chem. Eng. Res. Des.*, vol. 85, pp. 945–952, 2007.

[29] C. P. Fonte, M. A. Sultan, R. J. Santos, M. M. Dias, and J. C. B. Lopes, "Flow imbalance and Reynolds number impact on mixing in Confined Impinging Jets," *Chem. Eng. J.*, vol. 260, pp. 316–330, 2015.

[30] M. Ståhl, B. L. Åslund, and Å. C. Rasmuson, "Reaction crystallization kinetics of benzoic acid," *AIChE J.*, vol. 47, no. 7, pp. 1544–1560, Jul. 2001.

[31] P. G. Vekilov, "Nucleation," *Cryst. Growth Des.*, vol. 10, no. 12, pp. 5007–5019, Nov. 2010.

[32] W. Beckmann, *Crystallization: Basic Concepts and Industrial Applications*. 2013.

[33] J. W. Gibbs, "On the equilibrium of heterogeneous substances," *Am. J. Sci.*, vol. s3-16, no. 96, pp. 441–458, 1878.

[34] J. W. Mullin, *Crystallization*, Fourth. Butterworth-Heinemann, 2001.

[35] J. W. Russo and M. M. Hoffmann, "Influence of typical impurities on the surface tension measurements of binary mixtures of water and the ionic liquids 1-butyl-3-methylimidazolium tetrafluoroborate and chloride," *J. Chem. Eng. Data*, vol. 55, no. 12, pp. 5900–5905, 2010.

[36] H. Goswami and J. R. Seth, "Influence of Surfactant on Crystallization Kinetics of Stearic Acid," *Ind. Eng. Chem. Res.*, vol. 58, no. 18, pp. 7661–7669, May 2019.

[37] D. Erdemir, A. Y. Lee, and A. S. Myerson, "Nucleation of crystals from solution: Classical and two-step models," *Acc. Chem. Res.*, vol. 42, no. 5, pp. 621–629, 2009.

[38] R. J. Davey, S. L. M. Schroeder, and J. H. Ter Horst, "Nucleation of organic crystals - A molecular perspective," *Angew. Chemie - Int. Ed.*, vol. 52, no. 8, pp. 2167–2179, 2013.

[39] S. G. Agrawal and A. H. J. Paterson, "Secondary Nucleation: Mechanisms and Models," *Chem. Eng. Commun.*, vol. 202, no. 5, pp. 698–706, 2015.

[40] E. Aamir, "Population Balance Model-Based Optimal Control of Batch Crystallisation Processes for Systematic Crystal Size Distribution Design by," 2010.

[41] J. W. Mullin and J. Nývlt, "Programmed cooling of batch crystallizers," *Chem. Eng. Process.*, vol. 26, pp. 369–377, 1971.

[42] O. Söhnel and J. Garside, *Precipitation: basic principles and industrial applications*. Oxford: Butterworth-Heinemann, 1992.

[43] J. Garside and R. J. Davey, "Secondary contact nucleation: Kinetics, growth and scale-up," *Chem. Eng. Commun.*, 1980.

[44] S. T. Dunham, I. Clejan, and A. H. Gencer, "Accurate and efficient modeling of nucleation and growth processes," *Mater. Sci. Eng. A*, vol. 238, no. 1, pp. 152–159, 1997.

[45] J. E. Helt and M. A. Larson, "Effects of temperature on the crystallization of potassium nitrate by direct measurement of supersaturation," *AIChE J.*, vol. 23, no. 6, pp. 822–830, 1977.

[46] A. Chianese, F. Di Berardino, and A. G. Jones, "On the effect of secondary nucleation on the crystal size distribution from a seeded batch crystallizer," *Chem. Eng. Sci.*, vol. 48, no. 3, pp. 551–560, 1993.

[47] H. B. Matthews, S. M. Miller, and J. B. Rawlings, "Model identification for crystallization: Theory and experimental verification," *Powder Technol.*, vol. 88, no. 3, pp. 227–235, 1996.

[48] D. B. Patience, "Crystal Engineering through Particle Size and Shape Monitoring, Modeling, and Control," University of Wisconsin-Madison, 2002.

[49] R. S. Feigelson, "1 - Crystal Growth through the Ages: A Historical Perspective," in *Handbook of Crystal Growth (Second Edition)*, Second Edi., T. Nishinaga, Ed. Boston: Elsevier, 2015, pp. 1–83.

[50] J. J. De Yoreo and P. G. Vekilov, "Principles of crystal nucleation and growth," *Rev. Mineral. geochemistry*, vol. 54, no. 1, pp. 57–93, 2003.

[51] J. H. Ter Horst, C. Schmidt, and J. Ulrich, *Springer Handbook of Crystal Growth*, 2nd ed., vol. 39, no. 5. Elsevier B.V., 2010.

[52] D. K. Georgiou and P. G. Vekilov, "A fast response mechanism for insulin storage in crystals may involve kink generation by association of 2D clusters," *Proc. Natl. Acad. Sci. U. S. A.*, vol. 103, no. 6, pp. 1681–1686, 2006.

[53] J. Garside and S. J. Jančić, "Prediction and measurement of crystal size distributions for size-dependent growth," *Chem. Eng. Sci.*, vol. 33, no. 12, pp. 1623–1630, 1978.

[54] J. R. Beckman and A. D. Randolph, "Crystal size distribution dynamics in a classified crystallizer: Part II. Simulated control of crystal size distribution," *AIChE J.*, vol. 23, no. 4, pp. 510–520, 1977.

[55] R. A. Granberg and Å. C. Rasmuson, "Crystal growth rates of paracetamol in mixtures of water + acetone + toluene," *AIChE J.*, vol. 51, no. 9, pp. 2441–2456, 2005.

[56] J. Garside, "Advances in the characterization of crystal growth," *AIChE Symp. Ser.*, vol. 240, pp. 23–38, Jan. 1984.

[57] J. Garside, "Industrial crystallization from solution," *Chem. Eng. Sci.*, vol. 40, no. 1, pp. 3–26, 1985.

[58] J. B. Rawlings, S. M. Miller, and W. R. Witkowski, "Model Identification and Control of Solution Crystallization Processes: A Review," *Industrial and Engineering Chemistry Research*, vol. 32, no. 7. pp. 1275–1296, 1993.

[59] P. A. Larsen, D. B. Patience, and J. B. Rawlings, "Industrial crystallization process control," *IEEE Control Syst. Mag.*, vol. 26, no. 4, pp. 70–80, 2006.

[60] J. W. Kim, J. K. Kim, H. S. Kim, and K. K. Koo, "Characterization of liquid inclusion of rdx crystals with a cooling crystallization," *Cryst. Growth Des.*, vol. 9, no. 6, pp. 2700–2706, 2009.

[61] S. Boothroyd, A. Kerridge, A. Broo, D. Buttar, and J. Anwar, "Why Do Some Molecules Form Hydrates or Solvates?," *Cryst. Growth Des.*, vol. 18, no. 3, pp. 1903–1908, 2018.

[62] J. Ulrich and C. Strege, "Some aspects of the importance of metastable zone width and nucleation in industrial crystallizers," *J. Cryst. Growth*, vol. 237–239, no. 1-4 III, pp. 2130–2135, 2002.

[63] L. Yu *et al.*, "Thermochemistry and conformational polymorphism of a hexamorphic crystal system," *J. Am. Chem. Soc.*, vol. 122, no. 4, pp. 585–591, 2000.

[64] P. Chaudhari, P. Uttekar, N. Waria, and a. Ajab, "Study of Different Crystal Habits Formed by Recrystallization Process and Study Effect of Variables," *Res. J. Pharm. Tech.*, vol. 1, no. 4, pp. 381–385, 2008.

[65] A. J. Cruz-Cabeza, S. M. Reutzel-Edens, and J. Bernstein, "Facts and fictions about polymorphism," *Chemical Society Reviews*. 2015.

[66] A. Gavezzotti and G. Filippini, "Polymorphic Forms of Organic Crystals at Room Conditions: Thermodynamic and Structural Implications," *J. Am. Chem. Soc.*, vol. 117, no. 49, pp. 12299–12305, 1995.

[67] J. Bauer *et al.*, "Ritonavir: An extraordinary example of conformational polymorphism," *Pharm. Res.*, vol. 18, no. 6, pp. 859–866, 2001.

[68] R. A. Van Santen, "The Ostwald step rule," *J. Phys. Chem.*, vol. 88, no. 24, pp. 5768–5769, 1984.

[69] E. H. Lee, "A practical guide to pharmaceutical polymorph screening & selection," *Asian J. Pharm. Sci.*, vol. 9, no. 4, pp. 163–175, 2014.

[70] M. Haisa, S. Kashino, R. Kawai, and H. Maeda, "The Monoclinic Form of p-Hydroxyacetanilide," *Acta Crystallogr.*, vol. 32, pp. 1283–1285, 1976.

[71] M. Haisa, S. Kashino, and H. Maeda, "The Orthorhombic Form of p-Hydroxyacetanilide," *Acta Crystallogr.*, vol. 30, pp. 2510–2512, 1974.

[72] L. H. Thomas, C. Wales, L. Zhao, and C. C. Wilson, "Paracetamol form II: An elusive polymorph through facile multicomponent crystallization routes," *Cryst. Growth Des.*, vol. 11, no. 5, pp. 1450–1452, 2011.

[73] S. L. Price, "From crystal structure prediction to polymorph prediction: Interpreting the crystal energy landscape," *Phys. Chem. Chem. Phys.*, vol. 10, no. 15, pp. 1996–2009, 2008.

[74] R. A. Halliwell *et al.*, "Spray Drying as a Reliable Route to Produce Metastable Carbamazepine Form IV," *J. Pharm. Sci.*, vol. 106, no. 7, pp. 1874–1880, 2017.

[75] H. J. . Kramer, S. K. Bermingham, and G. M. van Rosmalen, "Design of industrial crystallisers for a given product quality," *J. Cryst. Growth*, vol. 198–199, pp. 729–737, Mar. 1999.

[76] J. Ulrich and T. Stelzer, "Melt Crystallization," in *Crystallization: Basic Concepts and Industrial Applications*, 2013, pp. 289–304.

[77] A. G. Shtukenberg *et al.*, "Melt Crystallization for Paracetamol Polymorphism," *Cryst. Growth Des.*, vol. 19, no. 7, pp. 4070–4080, 2019.

[78] J. C. Burley, M. J. Duer, R. S. Stein, and R. M. Vrcelj, "Enforcing Ostwald's rule of stages: Isolation of paracetamol forms III and II," *Eur. J. Pharm. Sci.*, vol. 31, no. 5, pp. 271–276, 2007.

[79] C. Lindenberg, "Optimizing the precipitation of organic compounds," ETH Zürich, 2009.

[80] W. Genck, "Make The Most of Antisolvent Crystallization," 2010. [Online]. Available: http://www.chemicalprocessing.com/articles/2010/210/.

[81] Z. H. Loh, A. K. Samanta, and P. W. Sia Heng, "Overview of milling techniques for improving the solubility of poorly water-soluble drugs," *Asian J. Pharm. Sci.*, vol. 10, no. 4, pp. 255–274, 2014.

[82] M. Midler, P. D. Liu, E. L. Paul, M. Futran, and E. F. Whittington, "A crystallization method to improve crystal structure and size," 18-Dec-1991.

[83] S. Khan, M. De Matas, J. Zhang, and J. Anwar, "Nanocrystal preparation: Low-energy precipitation method revisited," *Cryst. Growth Des.*, vol. 13, no. 7, pp. 2766–2777, 2013.

[84] M. Uusi-Penttilä and K. A. Berglund, "Spectroscopic monitoring of environmentally benign anti-solvent crystallization," *J. Cryst. Growth*, vol. 166, no. 1–4, pp. 967–970, 1996.

[85] T. G. Zijlema, R. M. Geertman, G.-J. Witkamp, G. M. van Rosmalen, and J. de Graauw, "Antisolvent Crystallization as an Alternative to Evaporative Crystallization for the Production of Sodium Chloride," *Ind. Eng. Chem. Res.*, vol. 39, no. 5, pp. 1330–1337, 2000.

[86] A. P. Harvey, M. R. Mackley, and P. Stonestreet, "Operation and Optimization of an Oscillatory Flow Continuous Reactor," *Ind. Eng. Chem. Res.*, vol. 40, pp. 5371–5377, 2001.

[87] NiTech Solutions, "The generation of eddies as a result of oscillatory motion between the baffles of a COBC," 2015. [Online]. Available: www.nitechsolutions.co.uk.

[88] L. Zhao *et al.*, "From discovery to scale-up: α-lipoic acid : nicotinamide co-crystals in a continuous oscillatory baffled crystalliser," *CrystEngComm*, vol. 16, no. 26, p. 5769, 2014.

[89] S. Lawton, G. Steele, P. Shering, L. Zhao, I. Laird, and X. W. Ni, "Continuous crystallization of pharmaceuticals using a continuous oscillatory baffled crystallizer," *Org. Process Res. Dev.*, vol. 13, no. 6, pp. 1357–1363, 2009.

[90] M. R. Mackley and P. Stonestreet, "Heat transfer and associated energy dissipation for oscillatory flow in baffled tubes," *Chem. Eng. Sci.*, vol. 50, no. 14, pp. 2211–2224, 1995.

[91] C. S. Polster *et al.*, "Pilot-Scale Continuous Production of LY2886721: Amide Formation and Reactive Crystallization," *Org. Process Res. Dev.*, vol. 18, pp. 1295–1309, 2014.

[92] H. Siddique, C. J. Brown, I. Houson, and A. J. Florence, "Establishment of a Continuous Sonocrystallization Process for Lactose in an Oscillatory Baffled Crystallizer," *Org. Process Res. Dev.*, vol. 19, no. 12, pp. 1871–1881, 2015.

[93] C. J. Brown and X. Ni, "Online evaluation of paracetamol antisolvent crystallization growth rate with video imaging in an oscillatory baffled crystallizer," *Cryst. Growth Des.*, vol. 11, no. 3, pp. 719–725, 2011.

[94] C. J. Brown, J. A. Adelakun, and X. Ni, "Characterization and modelling of antisolvent crystallization of salicylic acid in a continuous oscillatory baffled crystallizer," *Chem. Eng. Process. Process Intensif.*, vol. 97, pp. 180–186, 2015.

[95] W. F. C. Van Wageningen, D. Kandhai, R. F. Mudde, and H. E. a Van Den Akker, "Dynamic flow in a kenics static mixer: An assessment of various CFD methods," *AIChE J.*, vol. 50, no. 8, pp. 1684–1696, 2004.

[96] M. Raphael, "Sunflower Protein Precipitation in a Tubular Precipitator," *Can. J. Chem. Eng.*, vol. 77, no. 4, pp. 470–483, 1995.

[97] A. J. Mahajan and D. J. Kirwan, "Rapid precipitation of biochemicals," *Journal of Physics D: Applied Physics*, vol. 26, no. 8B. pp. B176–B180, 1999.

[98] "Crystal16." [Online]. Available: https://www.crystallizationsystems.com/crystal16. [Accessed: 28-Dec-2018].

[99] P. Billot, M. Couty, and P. Hosek, "Application of ATR-UV spectroscopy for monitoring the crystallisation of UV absorbing and nonabsorbing molecules," *Org. Process Res. Dev.*, vol. 14, no. 3, pp. 511–523, 2010.

[100] O. K. Abou-Zied, B. Y. Al-Busaidi, and J. Husband, "Solvent effect on anthranilic acid spectroscopy," *J. Phys. Chem. A*, vol. 118, no. 1, pp. 103–109, 2014.

[101] "Mastersizer 3000." [Online]. Available: https://www.malvernpanalytical.com/en/products/product-range/mastersizer-range/mastersizer-3000. [Accessed: 28-Dec-2018].

[102] E. Aamir, Z. K. Nagy, and C. D. Rielly, "Evaluation of the effect of seed preparation method on the product crystal size distribution for batch cooling crystallization processes," in *Crystal Growth and Design*, 2010, vol. 10, no. 11, pp. 4728–4740.

[103] C. P. M. Roelands, S. Jiang, M. Kitamura, J. H. Ter Horst, H. J. M. Kramer, and P. J. Jansens, "Antisolvent crystallization of the polymorphs of L-histidine as a function of supersaturation ratio and of solvent composition," *Cryst. Growth Des.*, 2006.

[104] H. Modarresi, E. Conte, J. Abildskov, R. Gani, and P. Crafts, "Model-based calculation of solid solubility for solvent selection - A review," *Ind. Eng. Chem. Res.*, vol. 47, no. 15, pp. 5234–5242, 2008.

[105] S. Jiang, P. J. Jansens, and J. H. ter Horst, "Control over polymorph formation of o-aminobenzoic acid," *Cryst. Growth Des.*, vol. 10, pp. 2541–2547, 2010.

[106] C. R. Groom, I. J. Bruno, M. P. Lightfoot, and S. C. Ward, "The Cambridge structural database," *Acta Crystallogr. Sect. B Struct. Sci. Cryst. Eng. Mater.*, 2016.

[107] J. Ulrich and P. Frohberg, "Problems, potentials and future of industrial crystallization," *Front. Chem. Sci. Eng.*, vol. 7, no. 1, pp. 1–8, 2013.

[108] R. Kacker, S. I. Regensburg, and H. J. M. Kramer, "Residence Time Distribution of Dispersed Liquid and Solid Phase in a Continuous Oscillatory Flow Baffled Crystallizer," *Chem. Eng. J.*, vol. 317, pp. 413–423, 2017.

[109] N. E. B. Briggs, U. Schacht, V. Raval, T. McGlone, J. Sefcik, and A. J. Florence, "Seeded Crystallization of β- L -Glutamic Acid in a Continuous Oscillatory Baffled Crystallizer," *Org. Process Res. Dev.*, vol. 19, no. 12, pp. 1903–1911, 2015.

[110] C. Tachtatzis *et al.*, "Image-based monitoring for early detection of fouling in crystallisation processes," *Chem. Eng. Sci.*, pp. 1–9, 2015.

[111] Q. Su, B. Benyahia, Z. K. Nagy, and C. D. Rielly, "Mathematical Modeling, Design, and Optimization of a Multisegment Multiaddition Plug-Flow Crystallizer for Antisolvent Crystallizations," *Org. Process Res. Dev.*, vol. 19, no. 12, pp. 1859–1870, 2015.

[112] R. Battino, T. R. Rettich, and T. Tominaga, "The Solubility of Oxygen and Ozone in Liquids," *Journal of Physical and Chemical Reference Data*, vol. 12, no. 2. pp. 163–178, 1983.

[113] R. Battino, T. R. Rettich, and T. Tominaga, "The Solubility of Nitrogen and Air in Liquids," *Journal of Physical and Chemical Reference Data*, vol. 13, no. 2. pp. 563–600, 1984.

[114] A. E. Markham and K. A. Kobe, "The solubility of gases in liquids," *J. Phys. Chem.*, pp. 519–588, 1941.

[115] H. Yamamoto, J. Tokunaga, and K. Ichikawa, "Solubility of Helium in Methanol + Water, Ethanol + Water, l-Propanol + Water, and 2-Propanol + Water Solutions at 25 "C," *J. Chem. Eng. Data*, vol. 39, no. 1, pp. 155–157, 1994.

[116] T. Kleetz, G. Pätzold, G. Schembecker, and K. Wohlgemuth, "Gassing Crystallization at Different Scales: Potential to Control Nucleation and Product Properties," *Cryst. Growth Des.*, vol. 17, pp. 1028–1035, 2017.

[117] J. W. Dolan, "Mobile-Phase Degassing: What, Why and How," *LCGC North Am.*, vol. 32, no. 7, pp. 482–487, 2014.

[118] X. Ni, H. Jian, and A. . Fitch, "Computational fluid dynamic modelling of flow patterns in an oscillatory baffled column," *Chem. Eng. Sci.*, vol. 57, no. 14, pp. 2849–2862, Jul. 2002.

[119] H. Jian and X. Ni, "A Numerical Study on the Scale-Up Behaviour in Oscillatory Baffled Columns," *Chem. Eng. Res. Des.*, vol. 83, no. 10, pp. 1163–1170, Oct. 2005.

[120] M. Manninen, E. Gorshkova, K. Immonen, and X.-W. Ni, "Evaluation of axial dispersion and mixing performance in oscillatory baffled reactors using CFD," *J. Chem. Technol. Biotechnol.*, vol. 88, no. 4, pp. 553–562, Apr. 2013.

[121] A. Y. Lee, D. Erdemir, and A. S. Myerson, "Crystal Polymorphism in Chemical Process Development," *Annu. Rev. Chem. Biomol. Eng.*, vol. 2, no. 1, pp. 259–280, 2011.

[122] R. Tandon, N. Tandon, and R. K. Thapar, "Patenting of polymorphs," vol. 7, pp. 59–63, 2018.

[123] S. Ferguson, G. Morris, H. Hao, M. Barrett, and B. Glennon, "Characterization of the anti-solvent batch, plug flow and MSMPR crystallization of benzoic acid," *Chem. Eng. Sci.*, vol. 104, pp. 44–54, 2013.

[124] J. Cornel, C. Lindenberg, and M. Mazzotti, "Quantitative application of in-situ ATR-FTIR and Raman spectroscopy in crystallization processes. Submitted to Industrial &," *Ind. Eng. Chem. Res. Chem. Res.*, vol. 47, pp. 4870–4882, 2008.

[125] W. Beckmann, "Seeding the Desired Polymorph: Background, Possibilities, Limitations, and Case Studies," *Org. Process Res. Dev.*, vol. 4, no. 5, pp. 372–383, 2000.

[126] R. J. P. Eder *et al.*, "Continuously seeded, continuously operated tubular crystallizer for the production of active pharmaceutical ingredients," *Cryst. Growth Des.*, vol. 10, pp. 2247–2257, 2010.

[127] T.-T. C. Lai, S. Ferguson, L. Palmer, B. L. Trout, and A. S. Myerson, "Continuous Crystallization and Polymorph Dynamics in the L-Glutamic Acid System," *Org. Process Res. Dev.*, vol. 18, pp. 1382–1390, 2014.

[128] T.-T. C. Lai, J. Cornevin, S. Ferguson, N. Li, B. L. Trout, and A. S. Myerson, "Control of Polymorphism in Continuous Crystallization via Mixed Suspension Mixed Product Removal Systems Cascade Design," *Cryst. Growth Des.*, vol. 15, no. 7, pp. 3374–3382, 2015.

[129] N. E. B. Briggs, "Polymorph Control of Pharmaceuticals within a Continuous Oscillatory Baffled Crystalliser," University of Strathclyde, 2015.

[130] H. Yang, X. Yu, V. Raval, Y. Makkawi, and A. Florence, "Effect of Oscillatory Flow on Nucleation Kinetics of Butyl Paraben," *Cryst. Growth Des.*, vol. 16, pp. 875–886, 2016.

[131] E. S. Ferrari and R. J. Davey, "Solution-mediated transformation of α to β L-glutamic acid: Rate enhancement due to secondary nucleation," *Cryst. Growth Des.*, vol. 4, no. 5, pp. 1061–1068, 2004.

[132] N. A. Mitchell, "Numerical Modelling of Cooling Crystallisation: Process Kinetics to Optimisation," 2012.

[133] A. Tadayon, S. Rohani, and M. K. Bennett, "Estimation of nucleation and growth kinetics of ammonium sulfate from transients of a cooling batch seeded crystallizer," *Ind. Eng. Chem. Res.*, vol. 41, no. 24, pp. 6181–6193, 2002.

[134] Q. Hu, S. Rohani, and A. Jutan, "Modelling and optimization of seeded batch crystallizers," *Comput. Chem. Eng.*, vol. 29, no. 4, pp. 911–918, 2005.

[135] C. Himawan and G. J. Witkamp, "Crystallization kinetics of MgSO4·12H2O from different scales of batch cooling scraped crystallizers," *Cryst. Res. Technol.*, vol. 41, no. 9, pp. 865–873, 2006.

[136] J.-F. Pérez-Calvo, S. S. Kadam, and H. J. M. Kramer, "Determination of Kinetics in Batch Cooling Crystallization Processes - A Sequential Parameter Estimation Approach," *AIChE J.*, vol. 62, no. 11, pp. 3992–4012, 2016.

[137] A. H. Bari and A. B. Pandit, "Sequential Crystallization Parameter Estimation Method for Determination of Nucleation, Growth, Breakage, and Agglomeration Kinetics," *Ind. Eng. Chem. Res.*, vol. 57, no. 5, pp. 1370–1379, 2018.

[138] K. Wohlgemuth and G. Schembecker, "Modeling induced nucleation processes during batch cooling crystallization: A sequential parameter determination procedure," *Comput. Chem. Eng.*, vol. 52, pp. 216–229, 2013.

[139] L. N. Ejim *et al.*, "A factorial approach to understanding the effect of inner geometry of baffled meso-scale tubes on solids suspension and axial dispersion in continuous , oscillatory liquid – solid plug flows," *Chem. Eng. J.*, vol. 308, pp. 669–682, 2017.

[140] N. E. B. Briggs, "Polymorph Control of Pharmaceuticals within a Continuous Oscillatory Baffled Crystalliser," 2015.

[141] O. Narducci, A. G. Jones, and E. Kougoulos, "Crystal Product Engineering in the Seeded Cooling Crystallization of Adipic Acid from Aqueous Solution," *Org. Process Res. Dev.*, vol. 15, pp. 974–980, 2011.

[142] C. M. Chew and R. I. Ristic, "Crystallization by oscillatory and conventional mixing at constant power density," *AIChE J.*, vol. 51, no. 5, pp. 1576–1579, 2005.

[143] Y. C. Liu *et al.*, "A comparative study of continuous operation between a dynamic baffle crystallizer and a stirred tank crystallizer," *Chem. Eng. J.*, vol. 367, no. February, pp. 278–294, 2019.

[144] S. Qamar and G. Warnecke, "Numerical solution of population balance equations for nucleation, growth and aggregation processes," *Comput. Chem. Eng.*, vol. 31, no. 12, pp. 1576–1589, 2007.

[145] S. Qamar, G. Warnecke, and M. P. Elsner, "On the solution of population balances for nucleation, growth, aggregation and breakage processes," *Chem. Eng. Sci.*, vol. 64, no. 9, pp. 2088–2095, 2009.

[146] E. Simone, M. V. Cenzato, and Z. K. Nagy, "A study on the effect of the polymeric additive HPMC on morphology and polymorphism of ortho-aminobenzoic acid crystals," *J. Cryst. Growth*, vol. 446, pp. 50–59, 2016.

[147] J. Garside, "The concept of effectiveness factors in crystal growth," *Chem. Eng. Sci.*, vol. 26, no. 9, pp. 1425–1431, 1971.

[148] J. M. Schall, J. S. Mandur, R. D. Braatz, and A. S. Myerson, "Nucleation and Growth Kinetics for Combined Cooling and Antisolvent Crystallization in a Mixed-Suspension, Mixed-Product Removal System: Estimating Solvent Dependency," *Cryst. Growth Des.*, vol. 18, no. 3, pp. 1560–1570, 2018.

[149] C. T. Óciardhá, N. A. Mitchell, K. W. Hutton, and P. J. Frawley, "Determination of the crystal growth rate of paracetamol as a function of solvent composition," *Ind. Eng. Chem. Res.*, vol. 51, no. 12, pp. 4731–4740, 2012.

[150] A. Lynch, L. Jia, M. Svärd, and Å. C. Rasmuson, "Crystal Growth of Salicylamide in Organic Solvents," *Cryst. Growth Des.*, vol. 18, no. 12, pp. 7305–7315, 2018.

[151] T. Kodera, M. Kobari, and I. Hirasawa, "Modeling and Growth Kinetics of Antisolvent Crystallization Applied to the Pharmaceutical Industry," *Chem. Eng. Technol.*, vol. 42, no. 7, pp. 1458–1465, 2019.

[152] R. I. Ristic, "Oscillatory mixing for crystallization of high crystal perfection pharmaceuticals," *Chem. Eng. Res. Des.*, vol. 85, no. 7 A, pp. 937–944, 2007.

[153] B. J. Ridder, A. Majumder, and Z. K. Nagy, "Population Balance Model Based Multi-Objective Optimization of a Multi-Segment Multi-Addition (MSMA) Continuous Plug Flow Antisolvent Crystallizer," *Ind. Eng. Chem. Res.*, vol. 53, pp. 4387–4397, 2014.

[154] R. Censi and P. Di Martino, "Polymorph impact on the bioavailability and stability of poorly soluble drugs," *Molecules*, vol. 20, no. 10, pp. 18759–18776, 2015.

[155] Z. Gao, Y. Wu, J. Gong, J. Wang, and S. Rohani, "Continuous crystallization of α-form L-glutamic acid in an MSMPR-Tubular crystallizer system," *J. Cryst. Growth*, vol. 507, no. June 2018, pp. 344–351, 2019.

[156] F. A. Mabbott, "Towards understanding fouling mechanisms in continuous crystallisation processes," 2017.

[157] Q. Zhao, Y. Liu, C. Wang, S. Wang, and H. Müller-Steinhagen, "Effect of surface free energy on the adhesion of biofouling and crystalline fouling," *Chem. Eng. Sci.*, vol. 60, no. 17, pp. 4858–4865, 2005.

[158] A. J. Alexander and P. J. Camp, "Non-photochemical laser-induced nucleation," *J. Chem. Phys.*, vol. 150, no. 4, 2019.

[159] Y. Yang and Z. K. Nagy, "Model-based systematic design and analysis approach for unseeded combined cooling and antisolvent crystallization (CCAC) systems," *Cryst. Growth Des.*, vol. 14, no. 2, pp. 687–698, 2014.

[160] M. Jiang and X. W. Ni, "Reactive Crystallization of Paracetamol in a Continuous Oscillatory Baffled Reactor," *Org. Process Res. Dev.*, vol. 23, pp. 882–890, 2019.